



THE UNIVERSITY *of* EDINBURGH

This thesis has been submitted in fulfilment of the requirements for a postgraduate degree (e. g. PhD, MPhil, DClinPsychol) at the University of Edinburgh. Please note the following terms and conditions of use:

- This work is protected by copyright and other intellectual property rights, which are retained by the thesis author, unless otherwise stated.
- A copy can be downloaded for personal non-commercial research or study, without prior permission or charge.
- This thesis cannot be reproduced or quoted extensively from without first obtaining permission in writing from the author.
- The content must not be changed in any way or sold commercially in any format or medium without the formal permission of the author.
- When referring to this work, full bibliographic details including the author, title, awarding institution and date of the thesis must be given.

Towards Improved Logarithmic Descriptions of High Energy Processes Involving Jets in Hadron Colliders

Conor Elrick



Doctor of Philosophy
The University of Edinburgh
June 2023

Abstract

The total cross section for QCD processes at the LHC can be expanded perturbatively in the QCD coupling, α_s , and then approximated by performing calculations in quantum field theory to a fixed order. However, in the presence of a large separation of energy scales, the convergence of this perturbative expansion is known to be damaged as higher order corrections in α_s become more significant. High Energy Jets (HEJ) is a resummation framework designed to include contributions from high energy logarithms in the ratio of centre of mass energy to the transverse scale of particle produced to all orders in perturbation theory. These logs can become significant at the LHC and future colliders, and are significantly enhanced by the requirement of a large dijet invariant mass or large rapidity separation common in vector boson fusion/scattering (VBF/VBS) selection cuts.

The work collected together in this thesis was done to extend the HEJ description of high energy collisions; both adding support for new, experimentally relevant processes at leading-log (LL) accuracy and improving the understanding of the currently supported processes. We present the first calculation of the leading log description of same-sign WW boson production plus jets at the LHC, which is important as a necessary background processes for vector boson scattering and which has high energy logarithms which are directly enhanced by VBS cuts. We compare the HEJ LL result to that of pure next-to-leading order and with next-to-leading order matched parton shower using the setup of a recent CMS experimental analysis.

We then present results from studies looking at the impact of higher order corrections for two ongoing ATLAS experimental analyses. The setup of these analyses have directly lead to improvements in the HEJ description of both pure QCD jets and W plus jets which we describe in detail. Finally, we present a look ahead to the impact on the perturbative expansion of QCD at future colliders

with a higher centre of mass energy, where we expect the impact of higher energy logarithms to be increasingly significant.

Lay Summary

When differences arise between what we predict with theory and what we see in experimental data at the Large Hadron Collider (LHC), the most interesting outcome is the possibility of new physics. This could lead to the discovery of new particles and interactions, fundamentally changing how we view the universe. It is important then to be able to describe the currently known interactions as accurately as possible so that any differences are not simply due to the shortcomings of the theoretical descriptions.

The standard method for making theoretical predictions is to approximate a result as a sum of terms where the first term in the sum is called the “lowest order” approximation and is typically the simplest to compute. Each successive term in the sum should be much smaller than those which came before, and including more of these “higher order” corrections term by term should lead to a more accurate prediction. However when using this method to describe particle collisions, we sometimes find that these higher order corrections are not small compared to the lowest order approximation and can end up changing the calculated result dramatically.

High Energy Jets (HEJ) is a framework designed to produce accurate theoretical predictions for particle collisions by including significant parts from all of the higher order corrections and has previously been shown to have good agreement with data for certain experimental setups and measurements. In particular, experimental studies of Vector Boson Scattering (VBS) looking at particle collisions where there are two W (or Z) bosons produced as intermediate particles. In such studies, the choice of setup can end up increasing these higher order corrections leading to a need for an alternative description.

The work collected together in this thesis was done to extend the HEJ description of high energy collisions; both adding support for new, experimentally relevant

processes and improving the understanding of the currently supported processes. We present a calculation of same-sign WW boson production plus jets at the LHC, which has higher order corrections which are directly enhanced by VBS cuts on the particles involved. We compare the **HEJ** result to that from standard methods using the setup of a recent CMS experimental analyses.

We then present results from studies looking at the impact of higher order corrections for two ongoing ATLAS experimental analyses. The setup of these analyses have directly lead to improvements in the **HEJ** description of both pure QCD jets and W plus jets which we describe in detail. Finally, we present a look ahead to the impact of higher order corrections at future colliders with a higher collision energy, where we expect the impact of higher order corrections to be increasingly significant.

Declaration

I declare that this thesis was composed by myself, that the work contained herein is my own except where explicitly stated otherwise in the text, and that this work has not been submitted for any other degree or professional qualification except as specified.

Parts of this work have been published in [1, 2].

(Conor Elrick, June 2023)

Acknowledgements

There are a number of people I would like to thank for their support over the course of the of my PhD, most recently in the thesis writing stage but more generally in the studies presented in this document. Firstly, I would like to express my sincere thanks to my supervisor Jennifer Smillie for all of their input and sharing their physical insights in all the work presented here and in our own discussions.

Secondly I would like to extend my thanks to all of the people who have been part of the HEJ collaboration during my time as a PhD student. Thank you to Jeppe Andersen as well as to post docs Emmet Byrne, Bertrand Duclou  , Andreas Maier, Graeme Nail and Andreas Papaefstathiou for all their inputs and guidance over the past few years.

Two of my fellow PhD students within HEJ I would also like to thank here are J  r  my Paltrineri and Hitham Hassan for being excellent colleagues and always having time to discuss ongoing issues.

Thanks to members of the ATLAS collaboration for sharing details of their ongoing analyses presented in chapters 5 and 6.

The predictions presented in chapters 4 to 7 were produced using resources from PhenoGrid which is part of the GridPP Collaboration[3, 4].

Contents

Abstract	i
Lay Summary	iii
Declaration	v
Acknowledgements	vi
Contents	vii
List of Figures	xi
List of Tables	xx
1 Introduction	1
2 Theoretical framework of modern particle physics	4
2.1 Foundations of Quantum Chromodynamics	4
2.1.1 From Yang-Mills theory to the QCD Lagrangian.....	4
2.1.2 Feynman Rules for QCD	6
2.1.3 Running of the coupling	6
2.1.4 Spinor-Helicity notation	9
2.2 Fundamental results from Electroweak Theory	12

2.3	Framework for computation of theoretical predictions at fixed order.....	15
2.3.1	Fixed order technology.....	15
2.3.2	Quantifying the structure of the Proton with Parton Distribution Functions	19
2.3.3	Jet clustering and infrared safety.....	21
2.4	Moving to Next-to-leading order accuracy predictions.....	22
2.5	All order corrections with Parton Showers	23
2.5.1	Matching and merging	26
3	QCD physics in the high energy limit: An overview of the High Energy Jets framework	30
3.1	Regge limits.....	30
3.1.1	Regge limit of scattering amplitudes	33
3.2	High Energy Jets	35
3.2.1	Leading log description	35
3.2.2	Motivating the Lipatov Vertex for real emissions.....	36
3.2.3	A brief aside on BFKL resummation	40
3.2.4	Motivating the Lipatov Ansatz for virtual corrections	41
3.2.5	HEJ resummation.....	43
3.3	Summary of HEJ formalism and performing resummation with the HEJ2 software package.....	44
3.4	NLO bin-by-bin matching	49
4	Leading Log description of same-sign WW pair production + jets	52
4.1	Vector Boson Scattering and unitarity	53
4.2	Same-Sign WW production in VBS studies.....	56

4.3	Construction of the HEJ leading log amplitude for same-sign WW production.....	57
4.3.1	Matching to Fixed Order.....	61
4.3.2	Impact of interference terms.....	62
4.3.3	A comment on opposite-sign WW production	63
4.4	Impact of Leading-Logarithm corrections.....	63
4.5	Impact of NLO matching.....	71
4.6	Conclusions and future work.....	77
5	High Energy predictions for QCD jets at LHC: A study with ATLAS R_{32} team	79
5.1	Measurements of experimental interest.....	79
5.1.1	The quantity R_{32}	79
5.1.2	Profiles of average number of jets	81
5.2	Experimental and simulation setups	82
5.3	Logarithmically accurate predictions with High Energy Jets.....	83
5.3.1	Lower energy jet contributions.....	85
5.4	Comparison of fixed order and HEJ results	86
5.4.1	Comparison of R_{32} Measurements.....	86
5.4.2	Comparison of differential distributions for R_{32}	87
5.4.3	Comparison of differential distributions for average number of jets	89
5.5	Final thoughts and conclusions.....	93
6	High energy predictions for Vector Boson plus jets at LHC: A study with ATLAS_MET_JETS analysis team	94
6.1	Setup of the experimental measurement	94

6.2	Initial HEJ2 predictions for ATLAS_MET_JETS analysis	97
6.3	HEJ Resummation with heterogeneous jet samples	100
6.3.1	Classifying additional FKL emissions	100
6.3.2	Numerical testing of the HEJ descriptions	102
6.3.3	Correct treatment of non-FKL events	106
6.3.4	Full breakdown of best ATLAS_MET_JETS description	109
6.3.5	Quantitative changes to the jet rates	110
6.4	Comparison of HEJ and multijet merged predictions for selected experimental observables	111
6.5	Conclusions and summary of ATLAS_MET_JETS study	119
7	Impact of high energy resummation at a future circular collider	120
7.1	Considerations on construction of a future circular collider	120
7.2	Impact of HEJ resummation at large centre-of-mass energies	121
7.3	Conclusions and final remarks	126
8	Summary and future studies	127
A	Spinor representations	131
B	Full collection of predictions for the ATLAS_MET_JETS analysis	133
	Bibliography	147

List of Figures

2.1	Summary of different measurements of α_s as a function of the energy scale Q . As the energy scale increases and the length scale decreases the strength of the coupling is also reduced. Reproduced from 2021 revision of Particle Data Group summary of QCD [5]. .	8
2.2	Plots showing the NNPDF4.0 fits for the structure of the proton at (a) low (b) high energy scales as a function of momentum fraction x . Taken from reference [6].	19
2.3	Display of a CMS event that occurred in 2016, with two very high energy jets (> 3 TeV) depicted as orange cones. Taken from reference [7].	21
2.4	Diagrams of the splitting functions. Taken from reference [8]. . . .	24
2.5	(a) Example born level process. (b) Example process which can be reached by both a hard emission from an NLO calculation and from a parton shower algorithm.	25
2.6	Diagrammatic representation of towers of matrix elements calculated at NLO which are combined into one inclusive MEPS@NLO sample. Taken from a talk by Stefan Höche [9].	29
3.1	Example phase space explorer plot comparing leading order (Madgraph) and the high energy limit given in eq. (3.16) as a function of rapidity separation Δy	34
3.2	Diagrams which contribute to the process $qQ \rightarrow qqQ$ at leading order. (a) shows the 4 possible places where an extra emission (red) can be emitted off of a quark leg and (b) contains the 3 gluon vertex contribution.	36
3.3	The one loop corrections to the gg scattering amplitude that contribute at leading logarithm.	41
3.4	Diagram representing the standard HEJ use case. Taken from reference [2].	45

3.5	$2 \rightarrow n$ scattering (a) in an FKL configuration (b) expressed as a factorised amplitude in the HEJ formalism	47
4.1	Five processes contributing to longitudinally polarised W scattering $W_L^+ W_L^- \rightarrow W_L^+ W_L^-$ at leading order (a) Involving the $4 - V$ vertex (b,c) Involving an intermediate Z boson or photon (d,e) Involving an intermediate Higgs boson	53
4.2	Three processes contributing to $pp \rightarrow jjW^\pm W^\pm$ at (a) $\mathcal{O}(g_w^4)$, (b) $\mathcal{O}(g_w^2 g_{HWW}^2)$, (c) $\mathcal{O}(g_w^2 g_s^2)$	56
4.3	Schematic illustration of the current, $j_\mu^W(p_i, p_o, p_\ell, p_{\bar{\ell}})$, defined in Eq. (4.12) to describe the production of a W boson from a quark line with an off-shell gluon (shown as a zigzag line).	57
4.4	Phase space explorer plots for $uc \rightarrow W^+ W^+ + n$ jets for (a) 3 jets and (b) 4 jets.	59
4.5	Plot of cross section versus ΔR for $pp \rightarrow W^+ W^+ + 2j$ using an example experimental setup. In red is the full HEJ amplitude, in blue the interference term from exchanging the two W bosons have been removed and in orange, the subdominant WW configuration is removed.	62
4.6	Two processes contributing to the amplitude $pp \rightarrow jj\ell\bar{\ell}\nu_\ell\bar{\nu}_\ell$, involving (a) $W^+ W^-$ bosons (b) ZZ bosons.	63
4.7	Exclusive jet rates for $pp \rightarrow W^\pm W^\pm + \geq 2j$, (a) without and (b) with additional VBS cuts. In this figure and the remaining figures in this chapter, the bands shown are scale variation bands obtained from varying the renormalisation and factorisation scales around the central value.	66
4.8	Exclusive jet rates for $pp \rightarrow W^\pm W^\pm + \geq 2j$ where the jet isolation cut has been removed, (a) without and (b) with additional VBS cuts.	67
4.9	The differential distribution in the pseudorapidity separation of the two leading jets in $pp \rightarrow W^\pm W^\pm + \geq 2j$, (a) without and (b) with additional VBS cuts.	68
4.10	The differential distribution in the transverse momentum of the hardest jet in $pp \rightarrow W^\pm W^\pm + \geq 2j$, (a) without and (b) with additional VBS cuts.	68
4.11	The differential distribution in the invariant mass of the two leading jets in $pp \rightarrow W^\pm W^\pm + \geq 2j$, (a) without and (b) with additional VBS cuts.	69

4.12	The differential distribution in the invariant mass of the two charged leptons in $pp \rightarrow W^\pm W^\pm + \geq 2j$, (a) without and (b) with additional VBS cuts.	70
4.13	The differential distribution in the Zeppenfeld variable for the electron in $pp \rightarrow W^\pm W^\pm + \geq 2j$, without and with additional VBS cuts.	70
4.14	The (a) differential distribution in the pseudorapidity separation of the two leading jets in $pp \rightarrow W^\pm W^\pm + \geq 2j$ without additional VBS cuts. The HEJ result here has been matched to NLO using the procedure outlined in section 3.4. (b) ratio $\frac{\sigma_{2\text{-jet}}^{\text{NLO}}}{\sigma_{2\text{-jet}}^{\text{HEJ@NLO}}}$ and (c) ratio $\frac{\sigma_{2\text{-jet}}^{\text{HEJ}}}{\sigma_{2\text{-jet}}^{\text{HEJ@NLO}}}$	72
4.15	Reweight factors for dijet rapidity separation in single W plus jets production, taken from reference [10]	73
4.16	The (a) differential distribution in the hardest jet transverse momentum in $pp \rightarrow W^\pm W^\pm + \geq 2j$ without additional VBS cuts. The HEJ result here has been matched to NLO using the procedure outlined in section 3.4. (b) ratio $\frac{\sigma_{2\text{-jet}}^{\text{NLO}}}{\sigma_{2\text{-jet}}^{\text{HEJ@NLO}}}$ and (c) ratio $\frac{\sigma_{2\text{-jet}}^{\text{HEJ}}}{\sigma_{2\text{-jet}}^{\text{HEJ@NLO}}}$	74
4.17	Reweight factors for hardest jet transverse momentum in single W plus jets production, taken from reference [10]	74
4.18	The (a) differential distribution in the dijet invariant mass of the two leading jets in $pp \rightarrow W^\pm W^\pm + \geq 2j$ without additional VBS cuts. The HEJ result here has been matched to NLO using the procedure outlined in section 3.4. (b) ratio $\frac{\sigma_{2\text{-jet}}^{\text{NLO}}}{\sigma_{2\text{-jet}}^{\text{HEJ@NLO}}}$ and (c) ratio $\frac{\sigma_{2\text{-jet}}^{\text{HEJ}}}{\sigma_{2\text{-jet}}^{\text{HEJ@NLO}}}$	75
4.19	Reweight factors for dijet invariant mass in single W plus jets production, taken from reference [10]	75
4.20	The (a) differential distribution in the invariant mass of the two charged leptons in $pp \rightarrow W^\pm W^\pm + \geq 2j$ without additional VBS cuts. The HEJ result here has been matched to NLO using the procedure outlined in section 3.4. (b) ratio $\frac{\sigma_{2\text{-jet}}^{\text{NLO}}}{\sigma_{2\text{-jet}}^{\text{HEJ@NLO}}}$ and (c) ratio $\frac{\sigma_{2\text{-jet}}^{\text{HEJ}}}{\sigma_{2\text{-jet}}^{\text{HEJ@NLO}}}$	76
5.1	Plot of the rapidity separation between the two hardest jets for 2 jet fixed order sample split into three regions: (0, 5.2), (5.2, 7.9), (7.9+).	83

5.2	HEJ2.1 includes support for resumming unordered emissions where one parton is emitted outside of the forward backwards rapidity range of the quarks.	84
5.3	Two processes involving $q\bar{q}$ vertices that contribute to next-to-leading logarithm which are included in the HEJ resummation. . .	85
5.4	Plot of R_{32} as a function of jet rapidity separation between jets for (a) hardest two jets (b) most forward and backward jets. In red is the HEJ result at LL with some NLL corrections included, in blue ratio of R_{32}^{LO} defined in eq. (5.2) and in yellow the ratio R_{32}^{NLO} defined in eq. (5.4). The NLO lines have an adjusted binning in the large rapidity regions to account for poor statistics.	88
5.5	Plot of R_{32} as a function of dijet invariant mass between jets for (a) hardest two jets (b) jet pair with the largest invariant mass. In red is the HEJ result at LL with some NLL corrections included, in blue ratio of R_{32}^{LO} defined in eq. (5.2) and in yellow the ratio R_{32}^{NLO} defined in eq. (5.4). The NLO lines have an adjusted binning in the large invariant mass regions to account for poor statistics.	89
5.6	Plot of R_{32} as a function of sum of transverse momenta of the hardest two jets, H_{T2} , for (a) $60 \text{ GeV} < p_{3;\perp} < 0.05H_{T2}$ (b) $0.05H_{T2} < p_{3;\perp} < 0.1H_{T2}$ (c) $0.1H_{T2} < p_{3;\perp} < 0.2H_{T2}$ (d) $0.2H_{T2} < p_{3;\perp} < 0.3H_{T2}$ (e) $0.3H_{T2} < p_{3;\perp} < 0.4H_{T2}$ (e) $0.4H_{T2} < p_{3;\perp} < 0.5H_{T2}$. In red is the HEJ result at LL with some NLL corrections included, in blue ratio of R_{32}^{LO} defined in eq. (5.2) and in yellow the ratio R_{32}^{NLO} defined in eq. (5.4).	90
5.7	Plot of average number of jets as a function of jet rapidity separation between jets for (a) hardest two jets (b) most forward and backward jets. In red is the HEJ result at LL with some NLL corrections included and in yellow the NLO mean number of jets defined in eq. (5.7). The NLO lines have an adjusted binning in the large rapidity regions to account for poor statistics.	91
5.8	Plot of average number of jets as a function of dijet invariant mass between jets for (a) hardest two jets (b) jet pair with the largest invariant mass. In red is the HEJ result at LL with some NLL corrections included and in yellow the NLO mean number of jets defined in eq. (5.7). The NLO lines have an adjusted binning in the large rapidity regions to account for poor statistics.	92
5.9	Plot of average number of jets as a function of the sum of the transverse momenta of the hardest two jets, H_{T2} . In red is the HEJ result at LL with some NLL corrections included and in yellow the NLO mean number of jets defined in eq. (5.7).	92

5.10	Plot of average number of jets as a function of the angular separation of the hardest two jets. In red is the HEJ result at LL with some NLL corrections included.	93
6.1	Tables outlining the experimental setup for the large missing p_{\perp} study focusing on selection cuts to (a) jets (b) leptons	95
6.2	Plot of cross section as function of dijet invariant mass from a study of Higgs Boson plus jets comparing HEJ with vector boson fusion and gluon fusion calculated at NLO. Reproduced from reference [11].	96
6.3	Plots of the cross section as a function of dijet angular separation highlighting the contribution of lepton isolation cuts in (a) electron channel (b) muon channel.	98
6.4	Example fixed-order event jets with one jet passing the $p_{\perp} > 110$ GeV requirement and one passing the $p_{\perp} > 50$ GeV requirement. .	99
6.5	Example correction to the born level event (fig. 6.4) with an additional emission above 30 GeV between jets.	100
6.6	Diagrams indicating the regions of phase space where HEJ will produce extra emissions, Starting from the fixed order input in fig. 6.4, resummation is allowed in the grey shaded area when the jet p_{\perp} in the HEJ config is set to (a) 30 GeV (b) 50 GeV.	101
6.7	Diagrams showing an extra emission outside of the rapidity region between the hardest jets at (a) 30 GeV (b) 50 GeV. Allowing the third jet to have a low p_{\perp} will lead to a divergence which is not currently cancelled in the HEJ procedure due to missing virtual corrections.	101
6.8	Code snippet from the modified ATLAS_MET_JETS analysis which restricted the sample to only include events where the outer jets in rapidity are above 50 GeV and at least one is above 110 GeV. .	102
6.9	Combined two and three-jet exclusive jet rates from HEJ2, reweighing the FKL events and discarding everything else. The N GeV line uses a fixed order sample at N GeV and has the HEJ resummation jets at N GeV. (a) Uses a modified version of the ATLAS_MET_JETS analysis, with the jet cut adjusted (b) Requires that the outer jets in rapidity satisfy the cuts on the two jet sample.	103
6.10	Combined $\sigma_{2j}^{exc} + \sigma_{3j}^{exc}$ jet rates against configuration options for 10, 30 and 50 GeV jets. The FKL, FKL+UNO and FKL+QQBAR differ only in the 3j contribution, whereas there are contributions from non-resummable events to both the 2j and 3j rate.	104

6.11	Combined $\sigma_{2j}^{exc} + \sigma_{3j}^{exc}$ jet rates against configuration options for 10, 30 and 50 GeV jets with the additional requirement that the third hardest jet be between the two hardest jets in rapidity. The FKL, FKL+UNO and FKL+QQBAR differ only in the 3j contribution, whereas there are contributions from non-resummable events to both the 2j and 3j rate.	106
6.12	Table of exclusive 3j rates using the <code>ATLAS_MET_JETS</code> analysis with modified p_{\perp} in jet clustering.	106
6.13	Example 3j unordered events, with the cut on the third jet being (a) lower than that of the other jets, leading to an impact factor with non-uniform cuts, (b,c) the same as the other jets, leading to an impact factor with uniform jet p_{\perp} cuts.	107
6.14	Combined $\sigma_{2j}^{exc} + \sigma_{3j}^{exc}$ jet rates against configuration options for 10, 30 and 50 GeV jets using the breakdown of HEJ configurations in section 6.3.4. The FKL, FKL+UNO and FKL+QQBAR differ only in the 3j contribution, whereas there are contributions from non-resummable events to both the 2j and 3j rate.	110
6.15	Plot of the ratio $\frac{\sigma_{2\text{-jet}}^{\text{NLO}}}{\sigma_{2\text{-jet}}^{\text{HEJ@NLO}}}$ for one identified electron in the final state in the 2 jet region for (a) hardest jet transverse momentum (b) second hardest jet transverse momentum (c) missing transverse momentum.	112
6.16	Plot of the ratio $\frac{\sigma_{2\text{-jet}}^{\text{HEJ}}}{\sigma_{2\text{-jet}}^{\text{HEJ@NLO}}}$ for one identified electron in the final state in the 2 jet region for (a) hardest jet transverse momentum (b) second hardest jet transverse momentum (c) missing transverse momentum.	113
6.17	Plot of the total cross section as a function of number of jets for the <code>ATLAS_MET_JETS</code> study comparing HEJ and <code>MEPS@NLO</code> with one identified charged lepton in the final state. Decay is in the electron channel and in the 2j region.	113
6.18	Plot of the total cross section as a function of dijet angular separation for the hardest two jets in the <code>ATLAS_MET_JETS</code> study comparing HEJ and <code>MEPS@NLO</code> with one identified charged lepton in the final state. Decay is in the electron channel and in the 2j region.	114
6.19	Plot of the total cross section as a function of dijet rapidity separation for the <code>ATLAS_MET_JETS</code> study comparing HEJ and <code>MEPS@NLO</code> in the VBF region with leptonic decay into muon + neutrino in the VBF region.	115

6.20	Plot of the total cross section as a function of the transverse momentum of the (a) hardest jet (b) second hardest jet for the <code>ATLAS_MET_JETS</code> study comparing <code>HEJ</code> and <code>MEPS@NLO</code> with one identified charged electron in the final state. Decay is in the electron channel and in the 2j region.	116
6.21	Plot of the total cross section as a function of the transverse momentum of the (a) hardest jet (b) second hardest jet for the <code>ATLAS_MET_JETS</code> study comparing <code>HEJ</code> and <code>MEPS@NLO</code> with two identified charged electrons in the final state. Decay is in the electron channel and in the 2j region.	117
6.22	Plot of the total cross section as a function of the missing transverse momentum for the <code>ATLAS_MET_JETS</code> study comparing <code>HEJ</code> and <code>MEPS@NLO</code> with (a) one (b) two identified charged lepton in the final state. Decay is in the 2j region.	117
6.23	Plot of the total cross section as a function of the dijet invariant mass for the <code>ATLAS_MET_JETS</code> study comparing <code>HEJ</code> and <code>MEPS@NLO</code> with one identified charged lepton in the final state. Decay is in the electron channel and in the 2j region.	118
7.1	Plot of two, three and four jet rates in leading log resummed <code>HEJ</code> prediction for W plus jets where jets are clustered at $R = 0.4$. The red line is at $\sqrt{s} = 13$ TeV with jets counted above 30 GeV, whilst the other lines are at $\sqrt{s} = 100$ TeV with jets counted above (dark blue) 30 GeV (yellow) 60 GeV (light blue) 80 GeV.	123
7.2	Plot of transverse momentum of the hardest jet in leading log resummed <code>HEJ</code> prediction for W plus jets where jets are clustered at $R = 0.4$. The red line is at $\sqrt{s} = 13$ TeV with jets counted above 30 GeV, whilst the other lines are at $\sqrt{s} = 100$ TeV with jets counted above (dark blue) 30 GeV (yellow) 60 GeV (light blue) 80 GeV.	124
7.3	Plot of invariant mass between the hardest two jets in leading log resummed <code>HEJ</code> prediction for W plus jets where jets are clustered at $R = 0.4$. The red line is at $\sqrt{s} = 13$ TeV with jets counted above 30 GeV, whilst the other lines are at $\sqrt{s} = 100$ TeV with jets counted above (dark blue) 30 GeV (yellow) 60 GeV (light blue) 80 GeV.	125
7.4	Plot of rapidity separation between the hardest two jets in leading log resummed <code>HEJ</code> prediction for W plus jets where jets are clustered at $R = 0.4$. The red line is at $\sqrt{s} = 13$ TeV with jets counted above 30 GeV, whilst the other lines are at $\sqrt{s} = 100$ TeV with jets counted above (dark blue) 30 GeV (yellow) 60 GeV (light blue) 80 GeV.	125

B.1	Plot of the total cross section as a function of number of jets for the ATLAS MET JETS study comparing HEJ and MEPS@NLO with one identified charged lepton in the final state. Decay is in the (a) electron channel, 2j region (b) muon channel, 2j region (c) electron channel VBF region (d) muon channel, VBF region	134
B.2	Plot of the total cross section as a function of number of jets for the ATLAS MET JETS study comparing HEJ and MEPS@NLO with two identified charged leptons in the final state. Decay is in the (a) electron channel, 2j region (b) muon channel, 2j region (c) electron channel VBF region (d) muon channel, VBF region	135
B.3	Plot of the total cross section as a function of dijet angular separation for the ATLAS MET JETS study comparing HEJ and MEPS@NLO with one identified charged lepton in the final state. Decay is in the (a) electron channel, 2j region (b) muon channel, 2j region (c) electron channel VBF region (d) muon channel, VBF region	136
B.4	Plot of the total cross section as a function of dijet angular separation for the ATLAS MET JETS study comparing HEJ and MEPS@NLO with two identified charged leptons in the final state. Decay is in the (a) electron channel, 2j region (b) muon channel, 2j region (c) electron channel VBF region (d) muon channel, VBF region	137
B.5	Plot of the total cross section as a function of dijet rapidity separation for the ATLAS MET JETS study comparing HEJ and MEPS@NLO in the VBF region with leptonic decay into (a) electron + neutrino (b) muon + neutrino (c) electron + antielectron (d) muon + antimuon	138
B.6	Plot of the total cross section as a function of the transverse momentum of the hardest jet for the ATLAS MET JETS study comparing HEJ and MEPS@NLO with one identified charged lepton in the final state. Decay is in the (a) electron channel, 2j region (b) muon channel, 2j region (c) electron channel VBF region (d) muon channel, VBF region	139
B.7	Plot of the total cross section as a function of the transverse momentum of the hardest jet for the ATLAS MET JETS study comparing HEJ and MEPS@NLO with two identified charged leptons in the final state. Decay is in the (a) electron channel, 2j region (b) muon channel, 2j region (c) electron channel VBF region (d) muon channel, VBF region	140

B.8	Plot of the total cross section as a function of the transverse momentum of the second hardest jet for the ATLAS MET JETS study comparing HEJ and MEPS@NLO with one identified charged lepton in the final state. Decay is in the (a) electron channel, 2j region (b) muon channel, 2j region (c) electron channel VBF region (d) muon channel, VBF region	141
B.9	Plot of the total cross section as a function of the transverse momentum of the second hardest jet for the ATLAS MET JETS study comparing HEJ and MEPS@NLO with two identified charged leptons in the final state. Decay is in the (a) electron channel, 2j region (b) muon channel, 2j region (c) electron channel VBF region (d) muon channel, VBF region	142
B.10	Plot of the total cross section as a function of the missing transverse momentum for the ATLAS MET JETS study comparing HEJ and MEPS@NLO with one identified charged lepton in the final state. Decay is in the (a) electron channel, 2j region (b) muon channel, 2j region (c) electron channel VBF region (d) muon channel, VBF region	143
B.11	Plot of the total cross section as a function of the missing transverse momentum for the ATLAS MET JETS study comparing HEJ and MEPS@NLO with two identified charged leptons in the final state. Decay is in the (a) electron channel, 2j region (b) muon channel, 2j region (c) electron channel VBF region (d) muon channel, VBF region	144
B.12	Plot of the total cross section as a function of the dijet invariant mass for the ATLAS MET JETS study comparing HEJ and MEPS@NLO with one identified charged lepton in the final state. Decay is in the (a) electron channel, 2j region (b) muon channel, 2j region (c) electron channel VBF region (d) muon channel, VBF region	145
B.13	Plot of the total cross section as a function of the dijet invariant mass for the ATLAS MET JETS study comparing HEJ and MEPS@NLO with two identified charged leptons in the final state. Decay is in the (a) electron channel, 2j region (b) muon channel, 2j region (c) electron channel VBF region (d) muon channel, VBF region	146

List of Tables

2.1	Relevant QCD Feynman Rules	7
2.2	Relevant Electroweak Feynman Rules involving W bosons	14
3.1	Implemented processes and higher-order logarithmic corrections in HEJ. The “pure LL” column lists processes implemented in the HEJFOG. The NLL columns include both pure NLL and NLL matched to LO.	46
4.1	The selection cuts used in the analysis where the lepton cuts apply only to the charged leptons. The last three rows define the additional VBS cuts.	65
4.2	This table gives the total cross section calculated with the new HEJ2 LO + LL predictions in this paper compared to the result at NLO accuracy, both before and after the VBS cuts given in the text.	65
5.1	Precision wish list for jet final states, taken from the 2019 Les Houches Standard Model Working Group Report [12]	80
5.2	Table of phase space cuts used for the ATLAS R_{32} study.	82
5.3	Table of R_{32} values for different definitions of fixed order R_{32} and for HEJ. Calculations are for the central scale choice only and errors quoted are generation errors and not from scale variations. It is known that the generation errors obtained for the NLO pieces are overestimated which affects the errors quoted for the two NLO results presented here.	86
7.1	Table of inclusive cross sections for W plus jets at a range of centre of mass energies and with a selection of minimum jet p_{\perp} cuts. . .	121

Chapter 1

Introduction

Our current understanding of particle physics at the smallest scales comes from the Standard Model, a unification of three out of the four forces of nature: Electromagnetism, the Strong nuclear force and the Weak nuclear force. We describe the fundamental particles in the Standard Model, along with their interactions, as a quantum field theory locally invariant under gauge symmetry

$$SU(3)_c \otimes SU(2)_L \otimes U(1)_Y. \quad (1.1)$$

The first of these groups encodes the colour symmetry of the Standard Model described by the theory of quantum chromodynamics (QCD), which details the interactions of quarks and gluons and is parameterised by the strength of the QCD coupling α_s . Colour confinement tells us that coloured particles do not exist as measurable states, but instead hadronise into colourless objects. These colourless objects can then fragment back into colourless objects which immediately hadronise again, resulting in collimated sprays in energy which we call jets. The cross section for jets at the LHC is generally higher than for interactions of colourless particles from the electroweak $SU(2)_L \otimes U(1)_Y$ sector of the Standard Model [13], so an accurate description of processes involving jets is important to cleanly study electroweak interactions and potential interactions from Beyond the Standard Model (BSM) physics.

To calculate QCD interactions in perturbative quantum field theory, we calculate the S -matrix via the Dyson expansion to a given order in the asymptotic series. Each additional interaction in our scattering process will be suppressed by an

additional power of α_s compared to leading order. For example, if we look at $2 \rightarrow 2$ scattering of QCD particles we can express an observable O as a perturbative series in α_s ,

$$O = \underbrace{O_0 \alpha_s^2}_{\text{Leading order}} + \underbrace{O_1 \alpha_s^3}_{\text{Next-to-leading Order}} + \cdots + \underbrace{O_n \alpha_s^{(n+2)}}_{(\text{Next-to-})^n \text{ Leading Order}} + \dots, \quad (1.2)$$

where O_n is the value of the observable calculated at n -th order in the above expansion. The convergence of this perturbative expansion can be damaged when the suppression by α_s in the $(n+1)$ -th term is not sufficiently smaller than the n -th term. For QCD scattering in the high energy limit where the centre of mass energy s is much larger than the transverse energy scale t , logarithms of the ratio s over t appear to all orders of perturbation theory, damaging the perturbative expansion above.

These logarithms can become enhanced as a direct result of experimental cuts, such as in Vector Boson Fusion (VBF) studies where cuts on the invariant mass and rapidity separation of jets are used to distinguish between actual VBF and QCD gluon fusion. These two components of $pp \rightarrow H + 2j$ are otherwise indistinguishable in the final state, but studying the VBF component allows us to probe the Higgs/vector boson vertex. It is important then to be able to accurately describe the QCD sample which remains after VBF cuts which are logarithmically enhanced.

The High Energy Jets (HEJ) formalism [14–16] captures the leading log behaviour in QCD processes involving jets with the optional emission of a vector boson, including virtual and real corrections to all orders in perturbation theory. Within the HEJ framework, matrix elements are approximated in a form where they are factorised into pieces which are independent of one another without any approximations on the phase space integration. The work presented here builds upon the HEJ formalism using the HEJ2 [17] software, looking at new experimentally relevant processes and adding improvements from looking at experimental setups in ongoing analyses. The HEJ approach has previously been compared with data in experimental analyses involving jets [18–21], W or Z/γ plus jets [22–25] and for H plus jets [26]. As part of the work presented in this thesis, the HEJ2 software now also supports resummation with events containing two same-sign W bosons plus jets [1] relevant for vector boson scattering (VBS)

studies.

We will begin our discussions for this thesis in chapter 2 with a review of the Standard Model using the Lagrangian formulation. We will discuss relevant features of QCD and electroweak theory before moving on to discuss modern technology for performing scattering calculations for hadron colliders. In chapter 3 we will focus on the factorisation of scattering amplitudes in the high energy limit and how we can perform high energy resummation using the HEJ framework. For chapter 4 we will discuss Vector Boson Scattering, focusing on constructing a leading log accurate amplitude for the QCD $\mathcal{O}(\alpha_W^2 \alpha_s^2)$ contribution using the HEJ framework. This result will then be compared to NLO using the setup from a recent CMS analysis [27]. Finally for this study, we will discuss the impact of NLO matching on a selection of experimental observables.

Chapter 5 will discuss the first of two HEJ resummed predictions for ongoing ATLAS analyses, studying jets from QCD scattering at the LHC. We look at the ratio of the inclusive three jet rate to the inclusive two jet rate, R_{32} , against a number of experimentally relevant observables. We compare the leading logarithm resummed HEJ result (including resummation for some subleading configurations) against the LO and NLO approximations for R_{32} . We also calculate the average number of jets against physical observables which are very sensitive to higher jet multiplicities in some regions.

Chapter 6 will discuss the second of the two ATLAS analyses, this time looking at the production of a vector boson plus jets with a large missing transverse energy. This is important in order to cleanly study the signal region of neutrinos + jets relevant for dark matter studies at the LHC. Over the course of producing predictions for this analysis, we developed a framework for performing HEJ resummation when asymmetric jet cuts cause instabilities from unregulated soft divergences. This chapter also provides an introduction to that framework in the context of this analysis. We then compare our predictions with a MEPS@NLO sample provided by ATLAS, discussing where differences are thought to be due to shower effects or due to high energy logarithms.

Finally we will finish our discussion in chapter 7 where we will have a first look at the impact of high energy resummation for W plus jets at a 100 TeV collider using a range of jet p_\perp cuts. Chapter 8 is included as a summary of the content discussed in this thesis, including a brief look at potential future studies.

Chapter 2

Theoretical framework of modern particle physics

2.1 Foundations of Quantum Chromodynamics

2.1.1 From Yang-Mills theory to the QCD Lagrangian

In this section, we will review the fundamentals of QCD needed to frame the content that will appear in later sections. Throughout this section we will be setting up our conventions for the rest of the work presented. We begin our discussion with the Yang-Mills Lagrangian [28] for quark fields $\psi(x)$, $\bar{\psi}(x)$ and for gluon fields A_μ^a in the SU(3) adjoint representation:

$$\mathcal{L}_{\text{YM}} = \bar{\psi}(x) (i\not{D} - m) \psi(x) - \frac{1}{4} F_{\mu\nu}^a F^{a;\mu\nu}, \quad (2.1)$$

where we use the standard convention of writing a slash in variables contracted with the Lorentz matrices and,

- $D^\mu = \partial^\mu - igT^a A_\mu^a(x)$
- $F_{\mu\nu}^a = \partial_\mu A_\nu^a(x) - \partial_\nu A_\mu^a(x) + gf^{abc} A_\mu^b(x) A_\nu^c(x)$
- T^a belongs to the fundamental representation of SU(3)
- f^{abc} is the structure constants of the SU(3) Lie Algebra.

The Lagrangian in eq. (2.1) is invariant under local gauge transformations:

$$A_\mu^a \rightarrow A_\mu'^a(x) = A_\mu^a(x) + f^{abc} A_\mu^b(x) \alpha^c(x) + \frac{1}{g} \partial_\mu \alpha^a(x), \quad (2.2)$$

for any local function $\alpha(x)$. To calculate some observable \mathcal{O} in this theory, naïvely we would consider the ratio,

$$\langle \mathcal{O} \rangle = \frac{\int \mathcal{D}\psi \mathcal{D}\bar{\psi} \mathcal{D}A \mathcal{D}\alpha \mathcal{O} e^{iS[\psi, \bar{\psi}, A]}}{\int \mathcal{D}\psi \mathcal{D}\bar{\psi} \mathcal{D}A \mathcal{D}\alpha e^{iS[\psi, \bar{\psi}, A]}}, \quad (2.3)$$

integrating over all possible $\alpha(x)$. However this will lead to an uncontrolled divergence for large $\alpha(x)$ in both the numerator and the denominator of eq. (2.3) which makes it impossible to calculate the observable. In practice to have something useful for computations, we will impose a gauge-fixing condition $G(A) = 0$. There are a couple of different examples given here to illustrate this:

1. Covariant gauges with $G(A) = \partial^\mu A_\mu^a(x) - w^a(x)$, with a Gaussian $w^a(x)$ with width ξ . This corresponds to introducing a term to the Lagrangian of the form $\mathcal{L}_{\text{gauge fixing}} = -\frac{1}{2\xi} (\partial^\mu A_\mu^a)^2$
2. Axial gauges with $G(A) = n^\mu A_\mu^a(x) - w^a(x)$, again with a Gaussian $w^a(x)$ with width ξ , and introducing a fixed reference vector n^μ . This corresponds to introducing a term to the Lagrangian of the form $\mathcal{L}_{\text{gauge fixing}} = -\frac{1}{2\xi} (n^\mu A_\mu^a)^2$

For the purposes of this document, we will choose to add to the Lagrangian the gauge fixing term,

$$\mathcal{L}_{\text{gauge fixing}} = -\frac{1}{2} (\partial^\mu A_\mu^a)^2, \quad (2.4)$$

which corresponds to the choice of a covariant gauge with $\xi = 1$ (Feynman Gauge).

Finally we must add to our Lagrangian a term including Faddeev-Popov [29] “ghost” terms which appear as a consequence of gauge fixing. When making our gauge choice $G(A) = 0$, we can factor out an integral $\int \mathcal{D}\alpha$ from our path integral introducing a Jacobian factor of $\det \frac{\delta G(A)}{\delta \alpha}$. In the Faddeev-Popov procedure, we associate this factor with a new fields $c(x), \bar{c}(x)$, the exact form of which depends on our choice of Gauge. A full derivation of Faddeev-Popov ghosts is given in reference [30, Chapter 16.2] however for this thesis we will not speak of them

again after eq. (2.5) so we refrain from a deeper discussion here.

Combining everything together gives us the QCD Lagrangian we will use for our theory,

$$\mathcal{L}_{\text{QCD}} = \underbrace{\bar{\psi}(x) (i\not{D} - m) \psi(x) - \frac{1}{4} F_{\mu\nu}^a F^{a\ \mu\nu}}_{\text{Yang-Mills}} - \underbrace{\frac{1}{2} (\partial^\mu A_\mu^a)^2}_{\text{Gauge-Fixing}} - \underbrace{\bar{c}^a(x) (\partial^\mu D_\mu) c^a(x)}_{\text{Ghosts}}. \quad (2.5)$$

This then lets us define the path integral for QCD as a functional of the source fields J , η and $\bar{\eta}$,

$$Z[J, \eta, \bar{\eta}] = \int \mathcal{D}\psi \mathcal{D}\bar{\psi} \mathcal{D}A e^{i \int d^4x [\mathcal{L}_{\text{QCD}} + J^\mu(x) A_\mu(x) + \bar{\eta}(x) \psi(x) + \eta(x) \bar{\psi}(x)]} \quad (2.6)$$

2.1.2 Feynman Rules for QCD

From the QCD Lagrangian given in eq. (2.5), we can deduce the Feynman rules for the theory.

We can determine the quark propagator from looking at the inverse of the kinetic term in the Lagrangian. Further Feynman rules can be computed by taking functional derivatives of the generating function $Z[\eta, \bar{\eta}, J]$. For example we can find the Feynman rule for the quark-gluon vertex by considering,

$$\frac{1}{Z[0, 0, 0]} \frac{\delta}{\delta J_\mu} \frac{\delta}{\delta \eta} \frac{\delta}{\delta \bar{\eta}} Z[J, \eta, \bar{\eta}] \rightarrow ig \gamma^\mu T_{ij}^a. \quad (2.7)$$

Table 2.1 contains all the relevant Feynman rules from QCD that will be used in this thesis.

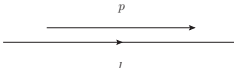
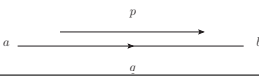
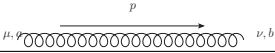
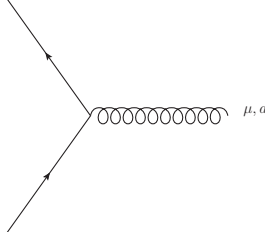
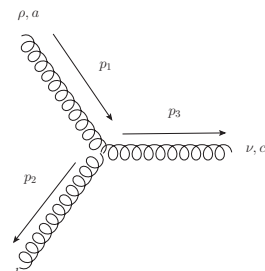
2.1.3 Running of the coupling

It is important at this stage to briefly mention the running of the coupling

$$\alpha_s := \frac{g^2}{4\pi}.$$

The $SU(N)$ beta function governing the strength of the coupling at energy scale μ is typically calculated as a perturbative expansion in α_s . To first order it is

Table 2.1: Relevant QCD Feynman Rules

Type	Diagram	Feynman Rule
Lepton Propagator		$i \frac{\not{p} + m}{p^2 - m^2}$
Quark Propagator		$i \frac{\not{p} + m}{p^2 - m^2} \delta_{ab}$
Gluon Propagator		$-i \left[\frac{g^{\mu\nu}}{p^2} - (1 - \xi) \frac{p^\mu p^\nu}{(p^2)^2} \right] \delta_{ab}$
Quark-Gluon Vertex		$ig\gamma^\mu T_{ij}^a$
3-Gluon Vertex		$gf^{abc} [g^{\mu\nu}(-p_2 + p_3)^\rho + g^{\nu\rho}(-p_3 - p_1)^\mu + g^{\rho\mu}(p_1 + p_2)^\nu]$

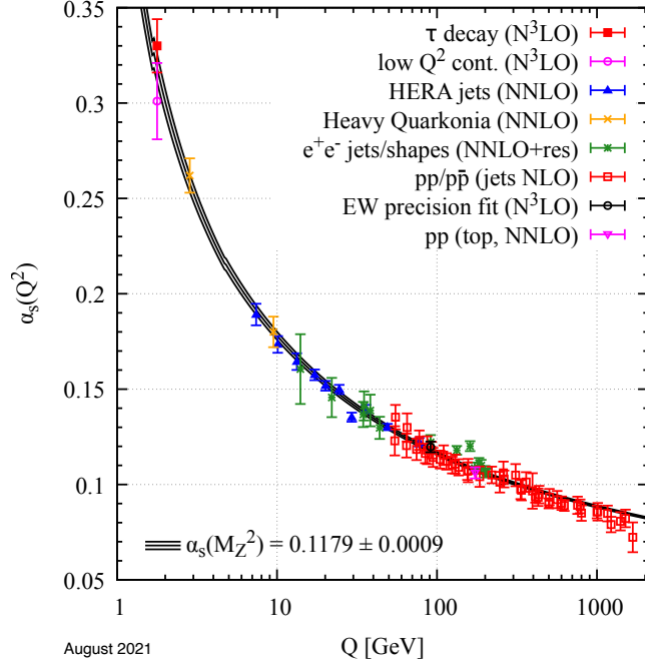


Figure 2.1: Summary of different measurements of α_s as a function of the energy scale Q . As the energy scale increases and the length scale decreases the strength of the coupling is also reduced. Reproduced from 2021 revision of Particle Data Group summary of QCD [5].

given by [30, equation 16.85],

$$\frac{\mu dg(\mu)}{d\mu} := \beta(g) = -\frac{g(\mu)^3}{16\pi^2} \left(\frac{11}{3}C_A - \frac{4}{3}T_R n_f \right) \quad (2.8)$$

where n_f is the number of quarks in the theory and $C_A = N$ is the value of the quadratic Casimir operator in the adjoint representation and T_R is defined to be $\text{Tr}(T_a T_b) = -T_R \delta_{ab}$ and is dependent on the choice of representation. For a large enough n_f , the beta function will be positive and the coupling will increase at large energy scales and will decrease as the energy scale gets smaller. Instead if n_f is small enough then the theory is asymptotically free, meaning that the beta function is negative and the coupling decreases for high energies. For QCD, we restrict our attention to the fundamental representation of $SU(3)$ where the term in the brackets in eq. (2.8) simplifies to,

$$\left(11 - \frac{2}{3}n_f \right). \quad (2.9)$$

So far there have been 6 flavours of quark discovered, which is indeed small enough

for the model to be asymptotically free. This has been experimentally verified, see e.g. fig. 2.1 which plots the coupling α_s as a function of the energy scale as measured through different processes.

2.1.4 Spinor-Helicity notation

Solving the Dirac Equation

It will prove convenient for calculations to introduce a compact notation here for dealing with contractions of (massless¹) Dirac spinors and gamma matrices. Firstly, we look at the solutions to the Dirac equation $(i\not{\partial} - m)\psi = 0$ which take the form,

$$\psi(x) = u_s(p)e^{-ip \cdot x} \quad \& \quad \psi(x) = v_s(p)e^{+ip \cdot x} \quad (2.10)$$

for positive and negative energy solutions respectively, with spin states $s = \pm$. These Dirac spinors, $u_s(p)$ and $v_s(p)$, can then be written in terms of two sets of normalised 2-component spinors, ϕ_\pm and χ_\pm ,

$$u_s(p) = \sqrt{E+m} \begin{pmatrix} \phi_s \\ \frac{\boldsymbol{\sigma} \cdot \mathbf{p}}{E+m} \phi_s \end{pmatrix}, \quad v_s(p) = \sqrt{E+m} \begin{pmatrix} \frac{\boldsymbol{\sigma} \cdot \mathbf{p}}{E+m} \chi_s \\ \chi_s \end{pmatrix}. \quad (2.11)$$

From these explicit formulae for $u_s(p)$ and $v_s(p)$, we can derive the following relationship between the spinors,

$$\sum_s u_s(p) \bar{u}_s(p) = \not{p} + m, \quad \sum_s v_s(p) \bar{v}_s(p) = \not{p} - m. \quad (2.12)$$

Helicity and chirality

We now move on to discussing helicity: the alignment of a particle's spin with its direction of momentum. A particle is said to have positive helicity if said particle's spin is in the direction of its momentum vector, and negative helicity if the spin and momentum point in opposite directions. With the spinors defined

¹Spinor-Helicity notation can be extended to include massive particles as shown in appendix A2 in reference [31], but we will not require this extension for the work presented here.

in eq. (2.11), we can define an operator related to the spin of the particle,

$$\hat{\Sigma}_i = \begin{pmatrix} \sigma_i & 0 \\ 0 & \sigma_i \end{pmatrix} = -\frac{i}{4}\epsilon_{ijk}[\gamma_j, \gamma_k], \quad (2.13)$$

and then use this to define a helicity operator,

$$\hat{h} = \frac{\hat{\Sigma} \cdot \underline{p}}{|\underline{p}|}. \quad (2.14)$$

If we act with this operator on the spinors defined in eq. (2.11), we find that they are indeed eigenstates, with eigenvalues $h = \pm 1$.

We also introduce the concept of chirality which we define through the eigenvalues of the operator γ^5 . For a given fermion ψ we define the particles chirality to be equal to that of the sign of its eigenvalue when acted on by γ^5 . For a general spinor, we can project out the left-handed and right-handed components using the projection operators,

$$P_{\frac{L}{R}} = \left(\frac{1 \pm \gamma^5}{2} \right), \quad (2.15)$$

where $\gamma^5 = i\gamma^0\gamma^1\gamma^2\gamma^3$. From this we define the spinors,

$$u^\pm(p) = P_{\frac{L}{R}}u(p) \quad v^\mp(p) = P_{\frac{R}{L}}v(p). \quad (2.16)$$

The measured masses of the quarks (normally excluding the top quark) are small enough that we will consider the spinors in the massless limit where the Dirac equation is known to decouple into two separate Weyl equations. Furthermore, we now have the equality

$$u^\pm(p) = v^\mp(p), \quad (2.17)$$

allowing us to combine the notations for quarks and anti-quarks.

We now define the brackets,

$$|p^\pm\rangle = u^\pm(p) = v^\mp(p) \quad \langle p^\pm| = \bar{u}^\pm(p) = \bar{v}^\mp(p), \quad (2.18)$$

which will be the notation adopted for the rest of this document. We further use angle and square brackets to distinguish the two helicity products,

$$\langle pq \rangle = \langle p^- || q^+ \rangle, \quad [pq] = \langle p^+ || q^- \rangle. \quad (2.19)$$

From these one can also define mixed bracket products using angled and square brackets, but we will not need to use them here.

Spinor-Helicity identities

In this section we present a small collection of identities for massless theories using the spinor-helicity framework. Firstly, we look at relations purely involving quarks. The following will be useful in later sections:

$$\not{p}_i |p_i\rangle = \langle p_i | \not{p}_i = 0, \quad (2.20)$$

$$\langle p_i p_j \rangle [p_j p_i] = s_{ij} e^{i\pi\phi_{ij}}, \quad (2.21)$$

$$\langle p_i | \gamma^\mu | p_i \rangle = 2p_i^\mu, \quad (2.22)$$

$$\langle p_i | \gamma^\mu | p_j \rangle \langle p_k | \gamma^\mu | p_l \rangle = 2[p_i p_k] \langle p_l p_j \rangle, \quad (2.23)$$

where ϕ_{ij} is a phase factor which is equal to 0 if both particles are outgoing or both incoming and 1 otherwise. The simplest proof of these identities is to prove them in a given representation with a given convention for incoming and outgoing spinors. Here we will use a chiral representation based on Pauli matrices for the gamma matrices which we define in appendix A. As an example we will prove here eq. (2.21) in our choice of representation where p_a is chosen to be incoming and in the positive direction and p_b to be incoming and in the negative direction:

$$\begin{aligned} \langle p_a p_b \rangle [p_b p_a] &= \langle p_a^- p_b^+ \rangle \langle p_b^+ p_a^- \rangle \\ &= \bar{u}^-(p_a) u^+(p_b) \bar{u}^+(p_b) u^-(p_a) \\ &= (u^-(p_a))^\dagger \gamma^0 u^+(p_b) (u^+(p_b))^\dagger \gamma^0 u^-(p_a) \\ &= \sqrt{p_a^+ p_b^-} \sqrt{p_a^+ p_b^-} \quad \text{Using representation in appendix A} \end{aligned} \quad (2.24)$$

Now note that in our setup, all of the momentum of p_a (p_b) will be in the positive (negative) z direction, so we can simplify further by writing our product in terms of the energy of each particle,

$$\langle p_a p_b \rangle [p_b p_a] = (E_a + E_a)(E_b - (-E_b)) = 4E_a E_b = s_{ab}, \quad (2.25)$$

as expected.

Secondly we look at polarisation vectors for external gluons. These can be written

as [31, equation 3.8],

$$\varepsilon_\mu^+(p, k) = + \frac{\langle k^- | \gamma_\mu | p^- \rangle}{\sqrt{2} \langle kp \rangle} \quad (2.26)$$

for positive helicity, and

$$\varepsilon_\mu^-(p, k) = - \frac{\langle k^+ | \gamma_\mu | p^+ \rangle}{\sqrt{2} [kp]} \quad (2.27)$$

for negative helicity. Here p denotes the gluon momenta and k denotes any massless vector not parallel to p . Multiplying two of these together and summing over helicities recovers the usual completeness relation,

$$\sum_{i=\pm} \varepsilon_\mu^i(p, k) \varepsilon_{*\nu}^i(p, k) = -g_{\mu\nu} + \frac{p_\mu k_\nu - p_\nu k_\mu}{p \cdot k}. \quad (2.28)$$

2.2 Fundamental results from Electroweak Theory

We now move on briefly from QCD to talk about some relevant points from electroweak theory. We start by looking at a $SU(2) \times U(1)$ gauge theory as introduced by Glashow, Weinberg and Salam [32–34] which not only described the massless photon but also through the Higgs mechanism [35, 36], a massive W boson (at the time known to be an intermediate particle in weak decay), and a massive neutral vector boson which had not been experimentally observed at the time.

Consider the Lagrangian for a scalar field,

$$\mathcal{L}_{GSW} = (D_\mu \phi)^\dagger D^\mu \phi + \mu^2 \phi^\dagger \phi - \lambda (\phi^\dagger \phi)^2, \quad (2.29)$$

where the covariant derivative is expressed in terms of $SU(2)$ and $U(1)$ gauge bosons A_μ^a and B_μ respectively,

$$D_\mu \phi = (\partial_\mu - igT^a A_\mu^a - ig'Y B_\mu) \phi. \quad (2.30)$$

We now choose the field ϕ to have a vacuum expectation value of

$$\langle \phi \rangle = \frac{1}{\sqrt{2}} \begin{pmatrix} 0 \\ v \end{pmatrix}, \quad (2.31)$$

so that we can expand the field ϕ around this value as,

$$\phi = \frac{1}{\sqrt{2}} \begin{pmatrix} 0 \\ v + h(x) \end{pmatrix}, \quad (2.32)$$

and observe the effect this has on the Lagrangian when the gauge symmetry is spontaneously broken. Choosing the generators of the $SU(2)$ symmetry to be $T^a = \frac{\sigma^a}{2}$, we can rewrite the covariant derivative term in the Lagrangian as [30, equation 20.62],

$$\Delta\mathcal{L} = \frac{1}{2} \frac{v^2}{4} \left[g^2 (A_\mu^1)^2 + g^2 (A_\mu^2)^2 + (-gA_\mu^3 + g'B_\mu)^2 \right]. \quad (2.33)$$

From this, we see that the fields $A_\mu^1, A_\mu^2, (gA_\mu^3 - g'B_\mu)$ have now acquired masses as a result of the gauge symmetry being spontaneously broken. We can now define the three massive bosons to be [30, equation 20.63]:

$$\begin{aligned} W_\mu^\pm &= \frac{1}{\sqrt{2}} (A_\mu^1 \mp iA_\mu^2) & \text{with mass } m_W &= g\frac{v}{2}; \\ Z_\mu^0 &= \frac{1}{\sqrt{g^2 + g'^2}} (gA_\mu^3 - g'B_\mu) & \text{with mass } m_Z &= \sqrt{g^2 + g'^2} \frac{v}{2}. \end{aligned} \quad (2.34)$$

We still have a fourth vector field which remains massless, and we identify this with the photon in this model,

$$A_\mu = \frac{1}{\sqrt{g^2 + g'^2}} (g'A_\mu^3 + gB_\mu). \quad (2.35)$$

We will now add to our Lagrangian a kinetic term for these vector bosons, using the notation that,

$$W_{\mu\nu}^a = \partial_\mu A_\nu^a - \partial_\nu A_\mu^a - ig [A_\mu^a, A_\nu^a] \quad \text{for the generators of } SU(2), \quad (2.36)$$

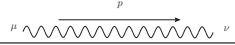
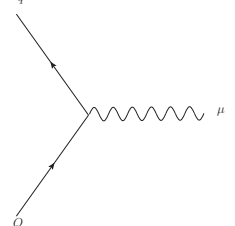
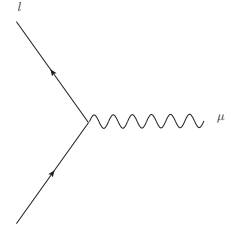
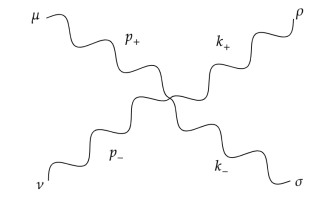
$$B_{\mu\nu} = \partial_\mu B_\nu - \partial_\nu B_\mu \quad \text{for the generators of } U(1). \quad (2.37)$$

The gauge boson kinetic term in the Lagrangian is then,

$$\mathcal{L}_{YM; \text{Bosons}} = -\frac{1}{4} W_{\mu\nu}^a W^{a \mu\nu} - \frac{1}{4} B_{\mu\nu} B^{\mu\nu}. \quad (2.38)$$

From eqs. (2.29) and (2.38) we can calculate the Feynman rules for the W , Z and photon propagators in the theory in the same way as we did for QCD in

Table 2.2: Relevant Electroweak Feynman Rules involving W bosons

Type	Diagram	Feynman Rule
W Propagator		$-i \frac{1}{p^2 - m_W^2 + i m_W \Gamma_W} \left[g^{\mu\nu} - (1 - \xi_W) \frac{p_\mu p_\nu}{p^2 - \xi_W m_W^2} \right]$
W -quark vertex		$-i \frac{g}{2\sqrt{2}} \gamma_\mu (1 - \gamma^5) V_{qQ}$
W -lepton vertex		$-i \frac{g}{2\sqrt{2}} \gamma_\mu (1 - \gamma^5)$
4- W vertex		$ig^2 [2g_{\rho\mu}g_{\sigma\nu} - g_{\rho\sigma}g_{\mu\nu} - g_{\rho\nu}g_{\sigma\mu}]$

section 2.1.2. We will also need to calculate processes where the massive bosons couple to quarks and charged leptons. For this we return to the kinetic terms for the quarks, noting that we will have a similar term for leptons,

$$\mathcal{L}_F = \sum_{\text{quarks}, q} i \bar{q} \not{D} q \quad (2.39)$$

which includes interactions with the gauge boson fields through the covariant derivative. The relevant Feynman rules involving W bosons from this section are summarised in table 2.2, where we have introduced 2 parameters:

- ξ_W is a parameter fixed from the choice of gauge
- V is the relevant component of the CKM matrix[37], accounting for weak flavour mixing.

2.3 Framework for computation of theoretical predictions at fixed order

2.3.1 Fixed order technology

We now discuss how one can use the theory of the Standard Model to calculate predictions for collisions in hadron colliders. The total hadronic cross section for $P_1, P_2 \rightarrow X$ can be expressed as an integral of the partonic cross section $p_a, p_b \rightarrow X$ weighted by parton distribution functions (PDFs) of the Bjorken- x variables $x_a P_1 = p_a, x_b P_2 = p_b$,

$$\sigma(P_1, P_2 \rightarrow X) = \int_0^1 dx_a \int_0^1 dx_b \underbrace{f^{(P_1)}(x_a, Q^2) f^{(P_2)}(x_b, Q^2)}_{\text{PDFs}} \underbrace{d\hat{\sigma}_{ab}(x_a P_1, x_b P_2)}_{\text{Partonic cross section}}. \quad (2.40)$$

The partonic level differential cross section is itself an integral of the squared matrix element:

$$\begin{aligned} d\hat{\sigma}_{ab}(p_a, p_b) &= \int d\Phi \frac{|\bar{\mathcal{M}}|^2}{2\hat{s}} \\ &= \prod_{i, \text{outgoing}} \int \frac{d^3 p_i}{(2\pi)^3 2E_i} \frac{|\bar{\mathcal{M}}|^2}{2\hat{s}} (2\pi)^4 \delta^4 \left(\sum_{\text{outgoing}} p_i - \sum_{\text{incoming}} p_i \right). \end{aligned} \quad (2.41)$$

The squared matrix elements for SM processes can be computed from the Feynman rules listed in tables 2.1 and 2.2, and in-practice these have already been computed by matrix-element generators. It is also convenient for phase-space sampling to rewrite the integral in eq. (2.40) purely in terms of the partonic kinematic variables. In the example following, we will do this for $W + n$ jets as a precursor to the discussion on that process that will follow.

Consider the partonic process $qQ \rightarrow q'Q(W^+ \rightarrow)e^+\nu_e$, where the incoming particles have four-momenta,

$$p_a = \left(\frac{\sqrt{s}}{2} x_a, 0, 0, \frac{\sqrt{s}}{2} x_a \right) \quad p_b = \left(\frac{\sqrt{s}}{2} x_b, 0, 0, -\frac{\sqrt{s}}{2} x_b \right). \quad (2.42)$$

The outgoing particles have momenta p_1, p_2, p_e, p_ν . We start by re-deriving the form of differential cross section in eqs. (2.40) and (2.41). The reciprocal incident

flux for normalised states is given by,

$$\begin{aligned}
\sigma_f &= \frac{1}{4\sqrt{(p_{a\mu}p_b^\mu)^2 - m_a^2 m_b^2}} \\
&= \frac{1}{4\sqrt{(E_a E_b - p_a \cdot p_b)^2}} \quad (\text{massless limit}) \\
&= \frac{1}{2\hat{s}}
\end{aligned} \tag{2.43}$$

Then the total cross section is given by the integral over the degrees of freedom of each particle in the final state including the above flux factor and an integral over the momentum fractions in the incoming state,

$$\begin{aligned}
\sigma &= \int dx_a \int dx_b \int \frac{d^3 p_e}{(2\pi)^3 2E_e} \int \frac{d^3 p_\nu}{(2\pi)^3 2E_\nu} \times \\
&\quad \prod_{\text{outgoing}} \int \frac{d^3 p_i}{(2\pi)^3 2E_i} |\bar{\mathcal{M}}|^2 d\sigma_f f(x_a, Q^2) f(x_b, Q^2) (2\pi)^4 \delta^4 \left(\sum_{\text{outgoing}} p_i - \sum_{\text{incoming}} p_i \right).
\end{aligned} \tag{2.44}$$

For the outgoing momentum we split the spacial integral to isolate the z integral along the beam axis,

$$\int \frac{d^3 p_i}{(2\pi)^3 2E_i} = \int \frac{d^2 p_i}{(2\pi)^3 2} \int \frac{dp_{i,z}}{E_i}. \tag{2.45}$$

Then using the notation $p_{i,z} = p_{i,\perp}(\cosh(y_i), \cos(\phi), \sin(\phi), \sinh(y_i))$, we can instead express our z integral as one over rapidity,

$$\begin{aligned}
\int \frac{dp_{i,z}}{E_i} &= \int dy_i \frac{dp_{i,z}}{dy_i} \frac{1}{E_i} \\
&= \int dy_i p_{i,\perp} \cosh(y_i) \frac{1}{E_i} \\
&= \int dy_i,
\end{aligned} \tag{2.46}$$

where we will define the rapidity of an outgoing particle as a function of its transverse momentum along the beam (z) axis,

$$y_i = \frac{1}{2} \log \left(\frac{E_i + p_{i,z}}{E_i - p_{i,z}} \right). \tag{2.47}$$

We can also split the Dirac-delta into 3 parts: 1 over the transverse momenta components, 1 over the z momenta and 1 over the energy,

$$\begin{aligned} \delta^4 \left(\sum_{\text{outgoing}} p_i - \sum_{\text{incoming}} p_i \right) = & \delta^2 \left(\sum_{\text{outgoing}} p_{i,\perp} - \sum_{\text{incoming}} p_{i,\perp} \right) \times \\ & \delta \left(\sum_{\text{outgoing}} p_{i,z} - \sum_{\text{incoming}} p_{i,z} \right) \times \\ & \delta \left(\sum_{\text{outgoing}} E_i - \sum_{\text{incoming}} E_i \right). \end{aligned} \quad (2.48)$$

We shall leave the transverse delta function alone and focus on the other 2 delta functions. From the definitions of the incoming momenta and momentum conservation, we have the following identities,

$$\frac{\sqrt{s}}{2} (x_a + x_b) = \sum_{\text{outgoing}} E_i, \quad \frac{\sqrt{s}}{2} (x_a - x_b) = \sum_{\text{outgoing}} p_{z,i}. \quad (2.49)$$

Then we can manipulate the delta functions above to instead be expressed as delta functions in the momentum fractions,

$$\begin{aligned} & \delta \left(\sum_{\text{outgoing}} p_{i,z} - \sum_{\text{incoming}} p_{i,z} \right) \delta \left(\sum_{\text{outgoing}} E_i - \sum_{\text{incoming}} E_i \right) \\ &= \delta \left(\frac{\sqrt{s}}{2} (x_a - x_b) - p_{a,z} - p_{b,z} \right) \delta \left(\frac{\sqrt{s}}{2} (x_a + x_b) - E_a - E_b \right) \\ &= \frac{4}{s} \delta \left(x_a - x_b - \frac{2}{\sqrt{s}} (p_{a,z} - p_{b,z}) \right) \delta \left(x_a + x_b - \frac{2}{\sqrt{s}} (E_a - E_b) \right) \\ &\equiv \frac{4}{s} \delta(x_a - x_b - m(p)) \delta(x_a + x_b - n(p)) \\ &= \frac{4x_a x_b}{\hat{s}} \delta(x_a - x_b - m(p)) \delta(x_a + x_b - n(p)) \end{aligned} \quad (2.50)$$

Finally, with the form of the deltas we can perform the integrals over x_a, x_b ,

$$\begin{aligned}
& \int dx_a dx_b \delta(x_a + x_b - m(p)) \delta(x_a - x_b - n(p)) x_a x_b f(x_a, Q^2) f(x_b, Q^2) \\
&= \int dx_b \delta(\underbrace{(-x_b + m(p))}_{\text{From delta}} - x_b - n(p)) \underbrace{(-x_b + m(p))}_{\text{From delta}} x_b f(\underbrace{(-x_b + m(p))}_{\text{From delta}}, Q^2) f(x_b, Q^2) \\
&= \int dx_b \delta(-2x_b + m(p) - n(p)) (-x_b + m(p)) x_b f(-x_b + m(p), Q^2) f(x_b, Q^2) \\
&= \int dx_b \frac{1}{2} \delta(x_b - \frac{m(p) - n(p)}{2}) (-x_b + m(p)) x_b f(-x_b + m(p), Q^2) f(x_b, Q^2) \\
&= \frac{1}{2} \left(\underbrace{-\frac{m(p) - n(p)}{2}}_{\text{From delta}} + m(p) \right) \times \\
&\quad \left(\underbrace{\frac{m(p) - n(p)}{2}}_{\text{From delta}} \right) f \left(\underbrace{-\frac{m(p) - n(p)}{2}}_{\text{From delta}} + m(p), Q^2 \right) f \left(\underbrace{-\frac{m(p) - n(p)}{2}}_{\text{From delta}}, Q^2 \right) \\
&= \frac{1}{2} x_a(p) x_b(p) f(x_a(p), Q^2) f(x_b(p), Q^2)
\end{aligned} \tag{2.51}$$

where we have written $x(p)$ to emphasise that the x_a is calculated as a function of the momenta integrated over. Putting this all together gives,

$$\begin{aligned}
\sigma &= \int dx_a \int dx_b \int \frac{d^3 p_e}{(2\pi)^3 2E_e} \int \frac{d^3 p_\nu}{(2\pi)^3 2E_\nu} \times \\
&\quad \prod_{\text{outgoing}} \int \frac{d^3 p_i}{(2\pi)^3 2E_i} d\sigma_f f(x_a, Q^2) f(x_b, Q^2) (2\pi)^4 \delta^4 \left(\sum_{\text{outgoing}} p_i - \sum_{\text{incoming}} p_i \right) \\
&= \int \frac{d^3 p_e}{(2\pi)^3 2E_e} \int \frac{d^3 p_\nu}{(2\pi)^3 2E_\nu} \prod_{\text{outgoing}} \left(\int \frac{d^2 p_{i,\perp}}{(2\pi)^3} \int \frac{dy_i}{2} \right) \times \\
&\quad |\bar{\mathcal{M}}|^2 \frac{1}{2\hat{s}} \frac{4}{\hat{s}} \frac{1}{2} x_a(p) x_b(p) f(x_a(p), Q^2) f(x_b(p), Q^2) (2\pi)^4 \delta^2 \left(\sum_{\text{outgoing}} p_{i,\perp} - \sum_{\text{incoming}} p_{i,\perp} \right).
\end{aligned} \tag{2.52}$$

Then we have arrived at the equation we will use for numerically computing this

cross section:

$$\sigma(qQ \rightarrow q'Q(W^+ \rightarrow)e^+\nu_e) = \int \frac{d^3p_e}{(2\pi)^3 2E_e} \int \frac{d^3p_\nu}{(2\pi)^3 2E_\nu} \prod_{outgoing} \left(\int \frac{d^2p_i}{(2\pi)^3} \int \frac{dy_i}{2} \right) \times |\bar{\mathcal{M}}|^2 \frac{1}{\hat{s}^2} x_a(p) x_b(p) f(x_a(p), Q^2) f(x_b(p), Q^2) (2\pi)^4 \delta^2 \left(\sum_{outgoing} p_{i,\perp} - \sum_{incoming} p_{i,\perp} \right). \quad (2.53)$$

To calculate eq. (2.53) numerically we will make use of Monte-Carlo sampling methods, where we generate momenta for the outgoing partons by sampling their transverse momentum, angle of emission and rapidity (sampling “phase space”). From there we can calculate the incoming momenta by momentum conservation (delta function), to then evaluate the cross section contribution at that point in phase space. Performing many such samples allows us to construct a numerical estimate for the full cross section, correct in the limit as number of sample points goes to infinity. In practice, for fixed order predictions presented in this study we generate roughly $10^7 - 10^9$ events to achieve smooth differential distributions, but this can vary wildly depending on the process and the phase space sampled which depends on additional cuts and kinematic variables.

2.3.2 Quantifying the structure of the Proton with Parton Distribution Functions

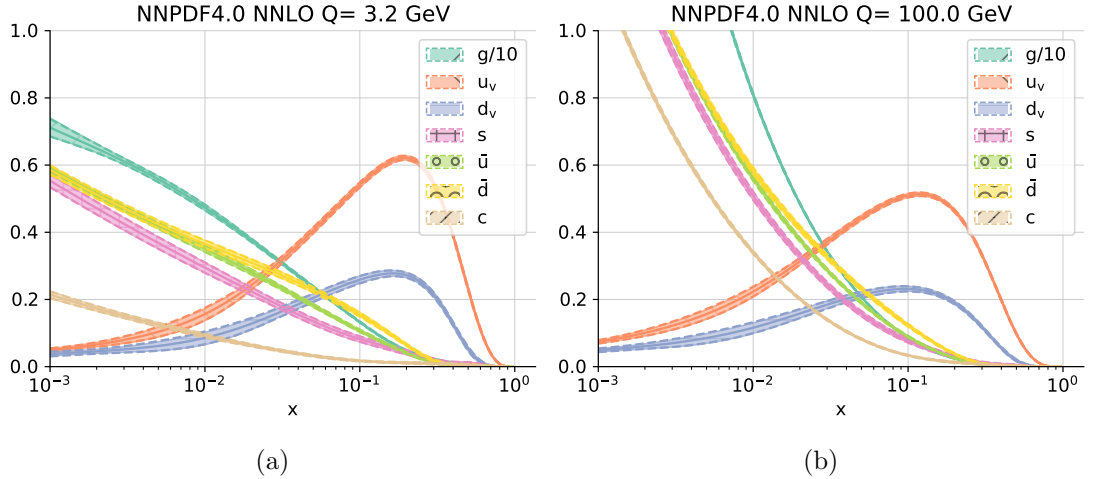


Figure 2.2: Plots showing the NNPDF4.0 fits for the structure of the proton at (a) low (b) high energy scales as a function of momentum fraction x . Taken from reference [6].

As we saw in eq. (2.40), we need to be able to accurately describe the contents of the proton at energy scale Q^2 to be able to compute total cross sections with this technology. These PDF description of the proton (or more generally hadrons) are assumed to be universal, i.e. for a given hadron they are independent of the scattering process and depending only on the momentum fraction x and the energy scale Q^2 . Typically these are then produced in a global fit of many observables simultaneously using a large experimental data set compromising of data from multiple colliders. One example of a recent PDF fit is the NNPDF4.0 PDF set [6], which includes the plots of the proton structure shown in fig. 2.2 for low and high values for Q^2 .

Once a PDF is described at a certain energy scale, it can be evolved to describe the same PDF at other values of Q^2 . This evolution is described using the DGLAP equation [38–40] which to leading order is given by:

$$\underbrace{\frac{\partial}{\partial \log Q^2} \begin{pmatrix} f_q(x, Q^2) \\ f_g(x, Q^2) \end{pmatrix}}_{\text{Vector of quark and gluon PDFs}} = \frac{\alpha_s(Q^2)}{2\pi} \int_x^1 \frac{dz}{z} \underbrace{\begin{pmatrix} P_{qq}(\frac{x}{z}) & P_{qg}(\frac{x}{z}) \\ P_{gq}(\frac{x}{z}) & P_{gg}(\frac{x}{z}) \end{pmatrix}}_{(2n_f + 1) \times (2n_f + 1) \text{ Matrix of Splitting Kernels}} \begin{pmatrix} f_q(x, Q^2) \\ f_g(x, Q^2) \end{pmatrix}, \quad (2.54)$$

where the splitting kernels appearing in the $(2n_f + 1) \times (2n_f + 1)$ matrix as a function of number of fermions (n_f) above encode the kinematics of a quark/gluon splitting into a quark/gluon with momentum fraction z and are given explicitly during the discussion of parton showers in section 2.5.

In practice, we can select a PDF dataset for our calculation by interfacing with the program LHAPDF [41] which allows us to switch PDFs easily to asses dependence on the PDF choice made.

2.3.3 Jet clustering and infrared safety

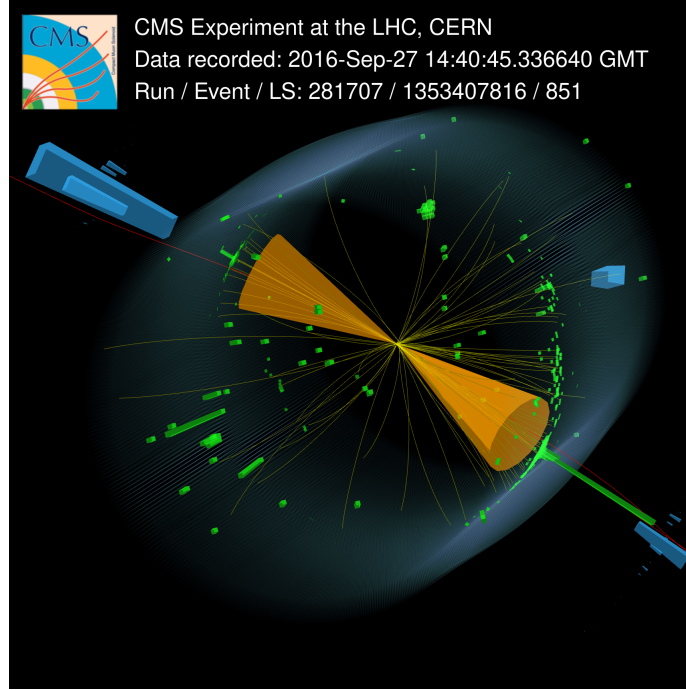


Figure 2.3: Display of a CMS event that occurred in 2016, with two very high energy jets (> 3 TeV) depicted as orange cones. Taken from reference [7].

Colour confinement means that it is impossible to directly observe quarks and gluons, and instead one has to observe the hadrons they are confined to. In high energy collisions it is common to observe collimated sprays of energy where partons are continuously hadronising and then fragmenting back into partons (see for example fig. 2.3). To deal with these quantitatively, we need a jet algorithm which both defines jets and is also “IR safe” meaning that an additional soft or collinear emission does not lead to a change in the set of jets defined. Here, we will mention one such jet algorithm, the anti-kt algorithm, but there are in fact many to choose from. For further discussion of jet algorithms for LHC collisions, see all of reference [42] and further in reference [31, section 2.1.6].

The anti-kt algorithm is an example of a sequential recombination algorithm [42, section 2.2] (c.f. cone algorithms), which combines objects which are within a minimum distance in momentum space. In kt algorithms, we define the distance for each of the objects, i , to be

$$d_{iB} = (p_{i\perp})^{2p}, \quad (2.55)$$

and the distance between two such objects, i and j , as

$$d_{ij} = \min [p_{i\perp}^{2p} p_{j\perp}^{2p}] \frac{\Delta R_{ij}^2}{R_0^2}, \quad (2.56)$$

with $\Delta R_{ij}^2 = (\Delta y_{ij})^2 + (\Delta \phi_{ij})^2$, the sum of the squared rapidity separation and angular separation. These are computed for all particles and if $d_{ij} < d_{iB}$ then we combine i and j into the same jet. We then repeat this until all of the d_{iB} are larger than all of the d_{ij} . The free parameters in this algorithm are the dimensionless p and jet size R_0 . For the anti-kt algorithm, we choose $p = -1$, which corresponds to favouring clustering between hard particles. Anti-kt is typically chosen by ATLAS and CMS with jet size between roughly 0.4 and 0.7 [31, section 2.1.6.5]. In the simulations mentioned later, the jet clustering is done by interfacing with the FASTJET[43] software, where we can input our chosen R_0 and jet algorithm.

2.4 Moving to Next-to-leading order accuracy predictions

The presence of divergences when calculating observables to NLO accuracy poses a problem for Monte-Carlo simulation. Whilst the UV and IR divergences will always cancel according to the KLN [44, 45] theorem, subtracting one infinite integral from another does not work numerically. If we look at the NLO expansion of the total cross section,

$$\sigma^{(NLO)} = \int d\Phi_B (\underbrace{\mathcal{B}}_{\text{born level}} + \underbrace{\mathcal{V}}_{\text{virtual}}) + \int d\Phi_R \underbrace{\mathcal{R}}_{\text{real}}, \quad (2.57)$$

we have two integrals which both need to be evaluated, but both have divergences that need to be controlled. Here we note the difference in the phase space in the two integrals in eq. (2.57), denoted by $d\Phi_B$ for the born-level phase space and by $d\Phi_R$ for the real emission phase space. In order for each of these terms to be finite, and thus numerically integrable, we need to introduce so called “subtraction terms” \mathcal{I} and \mathcal{S} which cancel each other when integrated,

$$0 = \int d\Phi_B \mathcal{I} - \int d\Phi_R \mathcal{S}, \quad (2.58)$$

we can add these terms to our equation for the NLO cross section (eq. (2.57)),

$$\sigma^{(NLO)} = \int d\Phi_B(\mathcal{B} + \mathcal{V} + \mathcal{I}) + \int d\Phi_R(\mathcal{R} - \mathcal{S}). \quad (2.59)$$

Then as long as they are both constructed in a suitable way we can cancel the divergent behaviour of both of the integrals, making them both finite and therefore suitable for numerical integration. In future sections we will refer to the parts of this calculation by single letters B, V, I, R, S . There are many algorithms for creating the subtraction terms, such as Catani-Seymour dipole subtraction [46]. For an example of this see reference [31, section 3.3.3.5]. Equation (2.59) is then the method which is used by Monte Carlo event generators to calculate the NLO cross section for a given process. It is not uncommon for us to need to generate these contributions separately in a calculation where one or more of the parts is numerically unstable.

2.5 All order corrections with Parton Showers

For some regions of phase space, we find that a separation of scales enhances higher order contributions, slowing the convergence of the perturbative description. If we are in a region where higher order terms are enhanced, we can instead look to try and include the enhanced behaviour to all orders in perturbation theory by performing a resummation. This is the underlying idea of parton showers (and in general analytic resummation, see reference [31, Chapter 5.2] for more details). In particular, parton showers (PS) are used to provide all order descriptions of soft and collinear emissions with logarithmic accuracy. Such soft emissions can lead to logarithms in the ratio of final state partons which become large when we compare these emissions with hard emissions. Since we are talking about all orders in perturbation theory, we instead use the language ‘leading log’, ‘next-to-leading log’, etc for labeling the accuracy of our description. We can see explicitly which terms are included to logarithmic accuracy by looking again at our expression for the total inclusive cross section,

$$\begin{aligned} \sigma_{inc} = & \alpha_s^2(\mathcal{K}_0) \\ & + \alpha_s^3(\log(L) \mathcal{K}_{1;1} + \mathcal{K}_{1;0}) \\ & + \alpha_s^4(\log(L)^2 \mathcal{K}_{2;2} + \log(L) \mathcal{K}_{2;1} + \mathcal{K}_{2;0}) \\ & + \mathcal{O}(\alpha_s^5), \end{aligned} \quad (2.60)$$

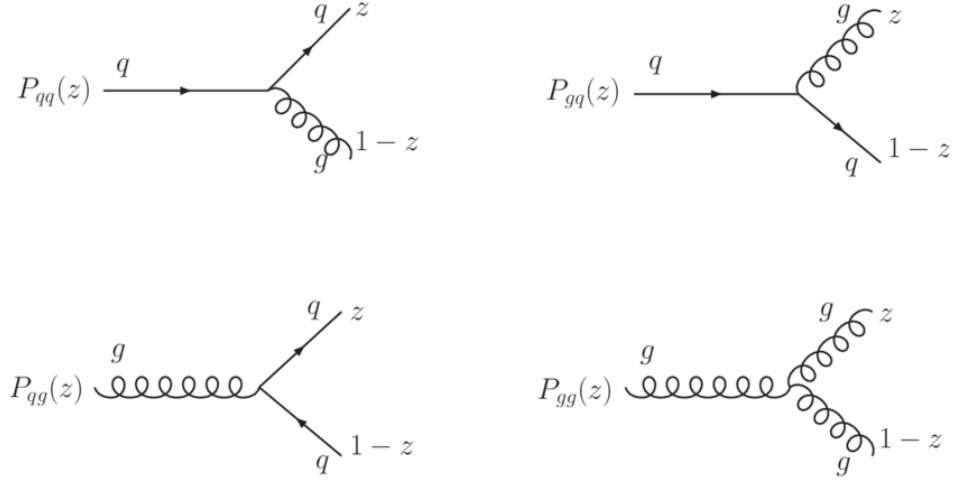


Figure 2.4: Diagrams of the splitting functions. Taken from reference [8].

where L is the enhanced logarithm. The blue terms in eq. (2.60) correspond to the terms included at leading log accuracy (including L0), and the terms in orange contribute at next-to-leading log accuracy. This definition of logarithmic accuracy will again be important in the discussion of the HEJ framework in the next chapter where we resum high energy logarithms in s over t .

We now return to the splitting kernels first mentioned in section 2.3.2 which will become important in our discussion of parton showers. Splitting kernels are universal functions which are included in the kinematics for a QCD particle emitting another QCD particle in the collinear limit. The functions $P_{xy}(z)$ indicate a splitting of $x \rightarrow y$ (which fix the type of the other emitted particle) where y has momentum fraction z . The four splitting functions for QCD involving quarks and gluons can be seen diagrammatically in fig. 2.4 and algebraic expressions are given below.

$$P_{qg}(z) = T_R [z^2 + (1-z)^2], \quad (2.61)$$

$$P_{gq}(z) = C_F \left[\frac{1 + (1-z)^2}{z} \right], \quad (2.62)$$

$$P_{gg}(z) = 2C_A \left[\frac{z}{(1-z)_+} + \frac{1-z}{z} + z(1-z) \right] + \delta(1-z) \frac{11C_A - 4n_f T_R}{6} \quad (2.63)$$

$$P_{qq}(z) = C_F \left(\frac{1+z^2}{1-z} \right)_+, \quad (2.64)$$

where we have introduced the plus prescription to regularise the divergence at

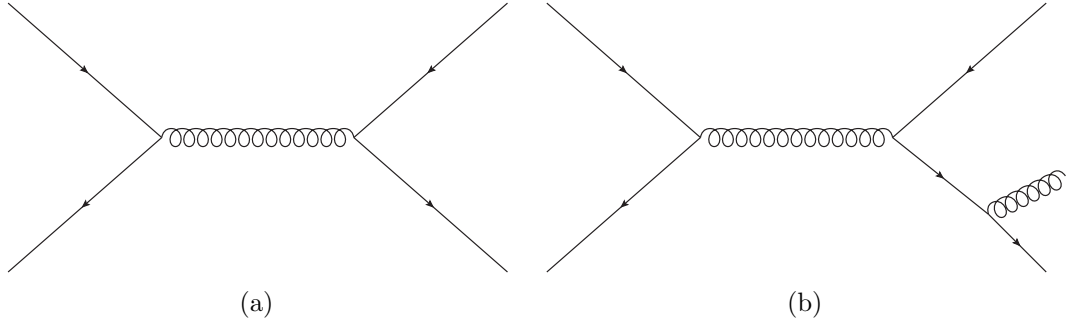


Figure 2.5: (a) Example born level process. (b) Example process which can be reached by both a hard emission from an NLO calculation and from a parton shower algorithm.

$z = 1$:

$$\int_0^1 [g(z)]_+ f(z) = \int_0^1 g(z) f(z) - \int_0^1 g(z) f(1). \quad (2.65)$$

The key point here is that these splitting functions are universal - meaning that they are independent of how we produced particle x in the first place, i.e. the hard scattering process. The splitting kernels allow us to define the Sudakov form factor $\Delta(t, T)$, which is defined to be the probability of no further emissions between t and T . For QCD it is given by the expression,

$$\Delta_{xy}(t, T) = \exp \left\{ - \int_t^T \frac{dt'}{t'} \int_{z_-}^{z_+} dz \frac{\alpha_s}{2\pi} P_{xy}(z) \right\}, \quad (2.66)$$

where z_-, z_+ are the limits on z set by the kinematics. This expression is very useful as it allows us to come up with an algorithm for simulating a parton shower. The basic method is to generate a random number, R , between 0 and 1 and compare that to the Sudakov form factor to determine whether or not we have a resolvable emission. If we do, we can find t_{split} by solving $R = \Delta_{xy}(t_{split}, T)$ to determine the branching then we can repeat this procedure, setting $T = t_{split}$ until there are no longer any resolvable emissions. Doing this, we find a ordered list of emissions $t_1 > t_2 > \dots$ which we will then use in the hadronisation step to form hadrons, which we can then measure properties of and compare with experiment.

2.5.1 Matching and merging

In this section we will look at matching parton showers and NLO matrix element calculations together in a consistent framework - **MC@NLO**, and then conclude this chapter by briefly discussing combining **MC@NLO** samples together to produce a merged sample through the **MEPS@NLO** method. Combining NLO and PS methods is not a straightforward task due to the overlap in the phase spaces between the two methods. For example, a scattering event at NLO includes a correction from one real emission on top of the born level process. But this configuration can also occur from a parton shower simulation with one splitting on one of the born level partons (see fig. 2.5). This overlap can lead to a double counting in the phase space which needs to be accounted for. Therefore a matching procedure between NLO and PS simulations must be defined in such a way that we avoid double counting (or missing) contributions that can appear in either method, thus making sure that the algorithm is accurate at NLO accuracy. In order to ensure this, it is necessary to split the emission phase space into two separate regions, a soft/collinear region where emissions would be dealt with by the parton shower and a hard region where emissions would be dealt with by the NLO matrix element. We then also demand that the transition between these two regions is smooth. Here we will describe the basics of **MC@NLO** matching. We use the notation in [47, equation 4.5] to decompose the partonic differential cross section,

$$d\hat{\sigma}_{ab} = d\hat{\sigma}_{ab}^{(b)} + d\hat{\sigma}_{ab}^{(sv)} + d\hat{\sigma}_{ab}^{(f)} + d\hat{\sigma}_{ab}^{(c+)} + d\hat{\sigma}_{ab}^{(c-)}, \quad (2.67)$$

where the meaning of the superscripts is as follows:

- (b) indicates the Born-level $2 \rightarrow 2$ contribution.
- (sv) indicates the virtual corrections, also $2 \rightarrow 2$ but at order α_S and with the divergences removed via a subtraction term.
- (f) indicates the real emission $2 \rightarrow 3$ contribution with the divergences removed via a subtraction term.
- $(c\pm)$ indicates the contributions from initial state collinear divergences with their appropriate counter terms to ensure they are finite.

Then, similar to eq. (2.59), we differentiate the phase space for $2 \rightarrow 2$ contributions and for $2 \rightarrow 3$ contributions by denoting the former by $d\phi_2$ and

the latter by $d\phi_3$. This allows us to write an expression for the observable O at NLO [47, equation 4.14] in terms of the unintegrated cross sections $\sigma_{ab}(x_1, x_2)$ which include the PDF factors,

$$\begin{aligned} \langle O \rangle = \sum_{ab} \int dx_1 dx_2 d\phi_3 & \left[O(3) \frac{d\sigma_{ab}^{(f)}}{d\phi_3} \Big|_{\text{ev}} + O(2) \frac{1}{\mathcal{I}_2} \left(\frac{d\sigma_{ab}^{(b)}}{d\phi_2} + \frac{d\sigma_{ab}^{(sv)}}{d\phi_2} \right) \right. \\ & + O(\tilde{2}) \frac{1}{\mathcal{I}_2} \left(\frac{d\sigma_{ab}^{(c+)}}{d\phi_2 dx} \Big|_{\text{ev}} + \frac{d\sigma_{ab}^{(c-)}}{d\phi_2 dx} \Big|_{\text{ev}} \right) - O(2) \frac{1}{\mathcal{I}_2} \left(\frac{d\sigma_{ab}^{(c+)}}{d\phi_2 dx} \Big|_{\text{ct}} + \frac{d\sigma_{ab}^{(c-)}}{d\phi_2 dx} \Big|_{\text{ct}} \right) \\ & \left. - \{O(2), O(\tilde{2})\} \frac{d\sigma_{ab}^{(f)}}{d\phi_3} \Big|_{\text{ct}} \right], \end{aligned} \quad (2.68)$$

where the dependence on the $2 \rightarrow n$ phase space is given by the term in brackets in $O(n)$, which represent the observable calculated in $2 \rightarrow n$ kinematics and the \mathcal{I} 's are normalisation factors. The notation of $\{O(2), O(\tilde{2})\}$ indicates that counter-terms need to be evaluated in both the soft and collinear regions.

We then proceed to match with the parton shower by substituting,

$$O(n) \rightarrow I_{\text{MC}}(O, n), \quad (2.69)$$

where $I_{\text{MC}}(O, n)$ is interpreted as the calculation of the observable with the LO + parton shower Monte-Carlo with $2 \rightarrow n$ kinematics. We will also in this procedure add and subtract a term to cancel the low x divergences which takes the form,

$$I_{\text{MC}}(O, \mathbf{n}) \frac{d\bar{\sigma}_{ab}}{d\phi_3} \Big|_{\text{MC}}. \quad (2.70)$$

This lets us define the “master” equation for MC@NLO in QCD [47, equation 4.22],

$$\begin{aligned} \frac{d\sigma}{dO} = \sum_{ab} dz_1 dz_2 d\phi_3 & \left\{ I_{\text{MC}}(O, \mathbf{3}) \left(\frac{d\bar{\sigma}_{ab}^{(f)}}{d\phi_3} \Big|_{\text{ev}} - \frac{d\bar{\sigma}_{ab}}{d\phi_3} \Big|_{\text{MC}} \right) \right. \\ & + I_{\text{MC}}(O, \mathbf{2}) \left[- \frac{d\bar{\sigma}_{ab}^{(f)}}{d\phi_3} \Big|_{\text{ct}} + \frac{d\bar{\sigma}_{ab}}{d\phi_3} \Big|_{\text{MC}} + \frac{1}{\mathcal{I}_2} \left(\frac{d\bar{\sigma}_{ab}^{(b)}}{d\phi_2} + \frac{d\bar{\sigma}_{ab}^{(sv)}}{d\phi_2} \right) \right. \\ & \left. \left. + \frac{1}{\mathcal{I}_2} \left(\frac{d\bar{\sigma}_{ab}^{(c+)}}{d\phi_2 dx} \Big|_{\text{ev}} + \frac{d\bar{\sigma}_{ab}^{(c-)}}{d\phi_2 dx} \Big|_{\text{ev}} \right) - \frac{1}{\mathcal{I}_2} \left(\frac{d\bar{\sigma}_{ab}^{(c+)}}{d\phi_2 dx} \Big|_{\text{ct}} + \frac{d\bar{\sigma}_{ab}^{(c-)}}{d\phi_2 dx} \Big|_{\text{ct}} \right) \right] \right\}. \end{aligned} \quad (2.71)$$

In practice, we can use a procedure where we generate events and counter events,

which we then combine to get the full integral above. In particular, we can then get a prediction for the total integrated cross section by combining [47, equation 4.25],

$$\sigma_{\text{tot}} = I_{\mathbb{S}} + I_{\mathbb{H}}, \quad (2.72)$$

where [47, equations 4.23, 4.24],

$$\begin{aligned} I_{\mathbb{H}} &= \sum_{ab} \int dz_1 dz_2 d\phi_3 \left(\left. \frac{d\bar{\sigma}_{ab}^{(f)}}{d\phi_3} \right|_{\text{ev}} - \left. \frac{d\bar{\sigma}_{ab}}{d\phi_3} \right|_{\text{M}} \right) \\ I_{\mathbb{S}} &= \sum_{ab} \int dz_1 dz_2 d\phi_3 \left[- \left. \frac{d\bar{\sigma}_{ab}^{(f)}}{d\phi_3} \right|_{\text{ct}} + \left. \frac{d\bar{\sigma}_{ab}}{d\phi_3} \right|_{\text{MC}} \right. \\ &\quad + \frac{1}{\mathcal{I}_2} \left(\frac{d\sigma_{ab}^{(b)}}{d\phi_2} + \frac{d\sigma_{ab}^{(sv)}}{d\phi_2} \right) + \frac{1}{\mathcal{I}_2} \left(\left. \frac{d\sigma_{ab}^{(c+)}}{d\phi_2 dx} \right|_{\text{ev}} + \left. \frac{d\sigma_{ab}^{(c-)}}{d\phi_2 dx} \right|_{\text{ev}} \right) \\ &\quad \left. - \frac{1}{\mathcal{I}_2} \left(\left. \frac{d\bar{\sigma}_{ab}^{(c+)}}{d\phi_2 dx} \right|_{\text{ct}} + \left. \frac{d\bar{\sigma}_{ab}^{(c-)}}{d\phi_2 dx} \right|_{\text{ct}} \right) \right]. \end{aligned} \quad (2.73)$$

A full description of the technicalities in implementing this is given in sections 4.5 and 4.6 of reference [47]. Observing that the matrix element calculation will provide the best description of hard emissions, we can try to construct a procedure for using the matrix element calculation when emissions are hard and using the shower when emissions are soft and collinear. This is the main idea behind multijet merging methods, which introduces a cut Q_C on emissions with partons above the cut described by the matrix element and below the cut described by the parton shower.

The **MEPS@NLO** method [48, 49] does this by combining towers of matrix elements with increasing number of jets combined into one inclusive sample. This is depicted pictorially in fig. 2.6. Similar to the construction of **MC@NLO**, one has to be careful to avoid double counting or missing areas of phase space, the details of which can be found in [31, Chapter 5.5.3].

Whilst not relevant for the **HEJ** description detailed in the next chapter, the discussion of parton shower and multijet merged shower formalisms is important in the later chapters for us to distinguish the effects of the parton shower resummation and the resummation of high energy logarithms.

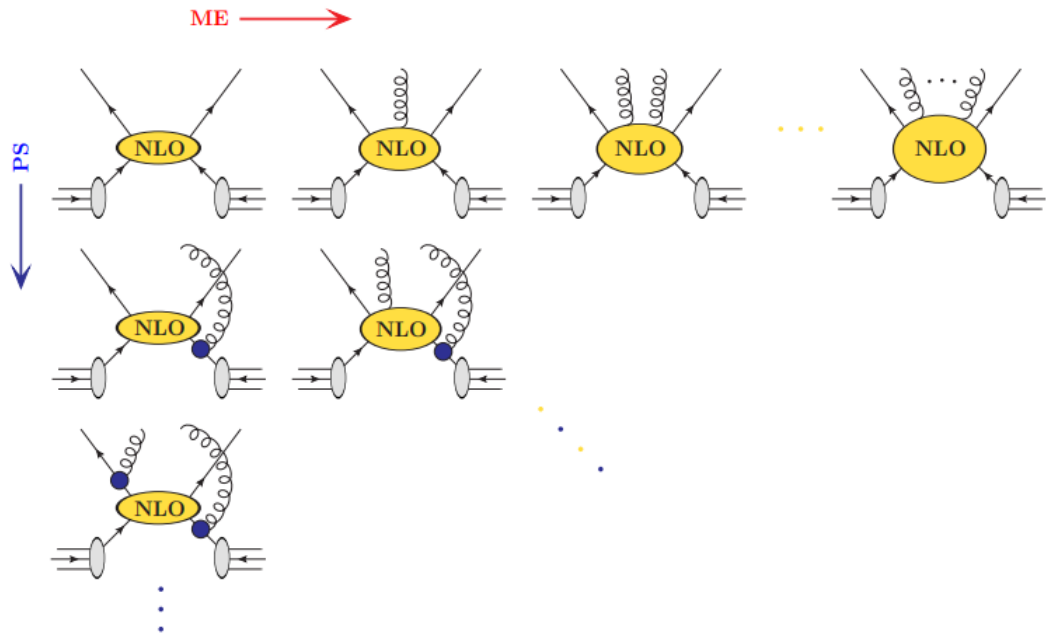


Figure 2.6: Diagrammatic representation of towers of matrix elements calculated at NLO which are combined into one inclusive `MEPS@NLO` sample. Taken from a talk by Stefan Höche [9].

Chapter 3

QCD physics in the high energy limit: An overview of the High Energy Jets framework

In this chapter we discuss the behaviour of QCD amplitudes for $2 \rightarrow n$ scattering in the limit of large separation of energy scales. We begin the discussion by defining what we mean by “high energy limit” of particle scattering by looking at Regge theory[50], a theory which predates the modern theory of QCD. We then go on to show how we can build upon the ideas of Regge theory to construct amplitudes which are accurate at leading logarithm in the high energy limit and how these form the basis of the HEJ formalism. In contrast to what was discussed in chapter 2 the logarithms discussed in this chapter arise in the high energy limit for hard, wide-angled emissions and are thus the basis of a completely separate discussion. Finally, we conclude by discussing how one can implement resummation from fixed order event input using the HEJ2 software package.

3.1 Regge limits

We start by defining the Regge limit of scattering amplitudes where the centre of mass energy is much larger than the transverse energy scale: $\hat{s} \gg \hat{t}$. For $2 \rightarrow 2$ scattering this limit is equivalent to having a large rapidity separation in the final

state as we will demonstrate. Firstly, we will again use the light-cone coordinates

$$p^\pm = E \pm p_z, \quad (3.1)$$

which allows us to re-express particle momenta as

$$p = (p^+, p^-, \underline{p}_\perp), \quad (3.2)$$

with the dot product of two vectors now given by,

$$p \cdot q = \frac{1}{2} (p^+ q^- + p^- q^+) - \underline{p}_\perp \cdot \underline{q}_\perp. \quad (3.3)$$

Given these definitions, we can write the incoming momenta as

$$\begin{aligned} p_a &= (x_a \sqrt{s}, 0, \underline{0}) \\ p_b &= (0, x_b \sqrt{s}, \underline{0}), \end{aligned} \quad (3.4)$$

and the outgoing momenta go from the form

$$p = p_\perp (\cosh(y), \cos(\phi), \sin(\phi), \sinh(y)), \quad (3.5)$$

to

$$\begin{aligned} p_1 &= (|\underline{p}_\perp| e^{y_1}, |\underline{p}_\perp| e^{-y_1}, \underline{p}_\perp) \\ p_2 &= (|\underline{p}_\perp| e^{y_2}, |\underline{p}_\perp| e^{-y_2}, -\underline{p}_\perp). \end{aligned} \quad (3.6)$$

We now explicitly compute expressions for the Mandelstam variables from the expressions for momenta starting with \hat{s} ,

$$\begin{aligned} \hat{s} &= (p_1 + p_2)^2 \\ &= 2p_1 \cdot p_2 \\ &= (p_1^+ p_2^- + p_1^- p_2^+) - 2p_{1;\perp} \cdot p_{2;\perp} \\ &= (|\underline{p}_\perp|^2 e^{y_1 - y_2} + |\underline{p}_\perp|^2 e^{y_2 - y_1}) + 2|\underline{p}_\perp|^2 \\ &= |\underline{p}_\perp|^2 (2 \cosh(\Delta y) + 2) \\ &= 4|\underline{p}_\perp|^2 \cosh^2 \left(\frac{\Delta y}{2} \right). \end{aligned} \quad (3.7)$$

For the other two invariants, we choose to evaluate them in the zero momentum

frame with $x_a = x_b$ and $y_1 = -y_2 = \frac{\Delta y}{2}$,

$$\begin{aligned}
\hat{t} &= (p_a - p_1)^2 \\
&= -2p_1 \cdot p_a \\
&= -p_a^+ p_1^- \\
&= -x_a \sqrt{s} |p_\perp| e^{-y_1} \\
&= -2|p_\perp|^2 e^{\frac{-\Delta y}{2}} \cosh \frac{\Delta y}{2} \\
\hat{u} &= (p_b - p_1)^2 \\
&= -2p_1 \cdot p_b \\
&= -p_b^- p_1^+ \\
&= -x_b \sqrt{s} |p_\perp| e^{y_1} \\
&= -2|p_\perp|^2 e^{\frac{\Delta y}{2}} \cosh \frac{\Delta y}{2}.
\end{aligned} \tag{3.8}$$

If we take the limit of large rapidity separation, $\Delta y \rightarrow \infty$, we can see that

$$\begin{aligned}
\hat{s} &= p_\perp^2 e^{\Delta y} \\
|\hat{t}| &= p_\perp^2 \\
\Rightarrow \Delta y &= \log \left(\frac{\hat{s}}{|\hat{t}|} \right).
\end{aligned} \tag{3.9}$$

Thus the limit of large rapidity separation enforces the Regge limit $\hat{s} \gg \hat{t}$. This logarithm in eq. (3.9) is also the logarithm that causes issues in the perturbative expansion of QCD in the high energy limit which we will discuss shortly. If we want to extend this to $2 \rightarrow n$ scattering, we will use the Multi-Regge-Kinematic (MRK) limit which is the limit of strict rapidity ordering with large separation between all final state particles, which also all have roughly equal transverse momenta [14, section 2]:

$$y_1 \gg y_2 \gg \cdots \gg y_n \quad |p_{i\perp}| \approx p_\perp \forall i. \tag{3.10}$$

Computing the Mandelstam invariants for this process [51, section 3] shows that this limit is equivalent to

$$\hat{s} \gg s_{ij} = 2p_i \cdot p_j \gg p_\perp^2, \tag{3.11}$$

again stressing that the centre-of-mass energy is the largest of the energy scales considered.

3.1.1 Regge limit of scattering amplitudes

In the Regge limit, it can be shown that the amplitude for $2 \rightarrow 2$ scattering, \mathcal{A} , can be written as a function of the energy scales, \hat{s} and \hat{t} [52, equation 5.3],

$$\mathcal{A}(\hat{s}, \hat{t}) \underset{\hat{s} \rightarrow \infty, \hat{t} \text{ fixed}}{\sim} \hat{s}^{\alpha(\hat{t})}, \quad (3.12)$$

where $\alpha(\hat{t})$ is the leading t -channel singularity (singularity with largest real part) of \mathcal{A} , which corresponds to the spin of the exchanged particle of highest spin. For $2 \rightarrow n$ parton scattering in the MRK limit, this corresponds to gluon exchange between the two hardest jets.

We can explicitly write the negative helicity $qQ \rightarrow qQ$ t -channel gluon exchange contribution to the full amplitude using the Feynman rules in table 2.1 (initially neglecting couplings and colour factors),

$$\mathcal{M}_t = \langle p_1 | \mu | p_a \rangle \frac{g^{\mu\nu}}{\hat{t}} \langle p_2 | \nu | p_b \rangle. \quad (3.13)$$

From here we can make use of the identities given in eqs. (2.21) and (2.23) to write this amplitude as,

$$\mathcal{M}_t = 2 \frac{1}{\hat{t}} [p_1 p_2] \langle p_b p_a \rangle \stackrel{\text{High Energy}}{\approx} 2 \frac{\hat{s}}{\hat{t}}, \quad (3.14)$$

where in the last step we have used that in the high energy limit we have

$$p_1 \approx p_A \approx p^+ = (p^+, 0, \underline{0})$$

and

$$p_2 \approx p_B = (0, p^-, \underline{0})$$

to combine the square and angled bracket terms into a \hat{s} . We can then combine the contributions from all helicity configurations to write a square matrix element, now

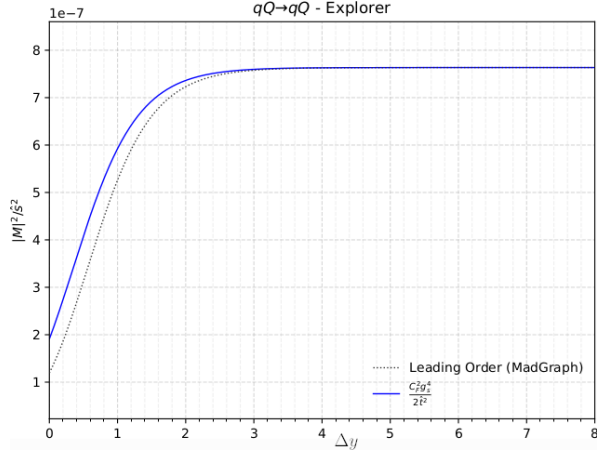


Figure 3.1: Example phase space explorer plot comparing leading order (Madgraph) and the high energy limit given in eq. (3.16) as a function of rapidity separation Δy .

colour and helicity averaged, for quark-quark scattering [31, equation 5.154],

$$|\bar{\mathcal{M}}|^2 = \frac{C_F^2 g_s^4}{4} \frac{\hat{s}^2 + \hat{u}^2}{\hat{t}^2} \quad (3.15)$$

As we saw in eq. (3.7), the invariants \hat{s}^2 and \hat{u}^2 tend to the same value in the MRK limit, which allows us to write the amplitude in a simple form

$$|\bar{\mathcal{M}}|^2 = \frac{C_F^2 g_s^4}{2} \frac{\hat{s}^2}{\hat{t}^2}. \quad (3.16)$$

Numerically we can test this against leading order to make sure that this is indeed the correct limit (fig. 3.1). In fact a consequence of Regge scaling is that when we consider diagrams with t -channel gluon exchange for $pp \rightarrow jj$ scattering, we find that in the high energy limit with $\hat{s} = -\hat{u}$, they are in fact all related by only a constant colour factor, i.e. [31, equation 5.159]

$$\begin{aligned} |\mathcal{M}_{qq' \rightarrow qq'}|^2 &= |\mathcal{M}_{qq \rightarrow qq}|^2 = |\mathcal{M}_{q\bar{q} \rightarrow q\bar{q}}|^2 = \frac{C_F^2 g_s^4}{2} \frac{\hat{s}^2}{\hat{t}^2} \\ |\mathcal{M}_{qg \rightarrow qg}|^2 &= \frac{C_F C_A}{2} g_s^4 \frac{\hat{s}^2}{\hat{t}^2} \\ |\mathcal{M}_{gg \rightarrow gg}|^2 &= \frac{C_A^2 g_s^4}{2} \frac{\hat{s}^2}{\hat{t}^2} \end{aligned} \quad (3.17)$$

3.2 High Energy Jets

We now move on to discuss the High Energy Jets formalism [14–16], and the procedure for which one can obtain a leading log prediction using the software HEJ2 and fixed order event input.

3.2.1 Leading log description

As discussed in the previous sections, the $2 \rightarrow n$ scattering amplitudes are dominated in the MRK limit by t -channel octet exchange. As was shown in reference [53] and as will be demonstrated in this chapter, these amplitudes also factorise at the square matrix element level into a product of spinor string contractions and t -channel pole. We will soon see that this factorisation can be extended to higher multiplicities through use of effective emission vertices [53]. These facts form the basis of the leading log HEJ description of the $2 \rightarrow n$ scattering amplitude depicted in fig. 3.5, and we will use a labelling convention here to match this figure with p_A and p_B incoming and p_i outgoing momentum ordered in increasing/decreasing rapidity

First, we introduce currents which are functions of the incoming momenta, p_A, p_B , and the outgoing momenta with the largest rapidity separation p_1, p_n . For $qQ \rightarrow qQ$ scattering these take the form,

$$\begin{aligned} J_{1;\mu} &= \langle p_1 | \mu | p_A \rangle \\ J_{2;\mu} &= \langle p_n | \mu | p_B \rangle \end{aligned} \tag{3.18}$$

where we will use Greek letters to be shorthand for gamma matrices with that index. For $2 \rightarrow 2$ scattering then the full squared amplitude for quark scattering is proportional to,

$$|\mathcal{M}|^2 \propto \frac{J_{1;\mu} J_2^\mu}{t^2} = \frac{\langle p_1 | \mu | p_A \rangle \langle p_2 | \mu | p_B \rangle}{t^2}. \tag{3.19}$$

A similar amplitude can be written for gluonic amplitudes with currents modified to include gluons and polarisation vectors given in eqs. (2.26) and (2.27). Moving beyond $2 \rightarrow 2$ scattering, for each additional parton in the final state we will include a factor which we will call the Lipatov vertex [54, 55]. We will derive

the form of the Lipatov vertex explicitly in the section which follows.

3.2.2 Motivating the Lipatov Vertex for real emissions

For a concrete example, we will derive the Lipatov vertex here for two to three scattering $qQ \rightarrow qqQ$ in the high energy limit.

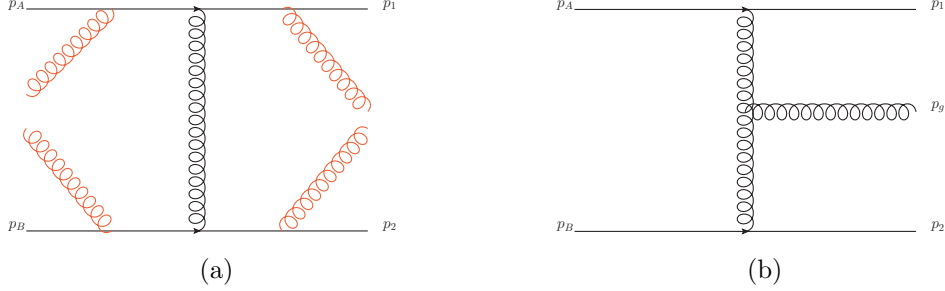


Figure 3.2: Diagrams which contribute to the process $qQ \rightarrow qqQ$ at leading order. (a) shows the 4 possible places where an extra emission (red) can be emitted off of a quark leg and (b) contains the 3 gluon vertex contribution.

At leading order the 5 diagrams which contribute are given in fig. 3.2. Let us first consider the contribution from one of the diagrams in fig. 3.2a, where the additional emission is off of the p_A quark line, which we will call \mathcal{D}_1 . Utilising the spinor-helicity notation defined earlier, we can write the contribution to the amplitude as:

$$\begin{aligned} \mathcal{D}_1 &= T_{1i} T_{ia}^d T_{2b}^d \frac{\langle p_1 | \mu | p_A - p_g | \nu | p_A \rangle}{t_{Ag}} \frac{\langle p_2 | \mu | p_B \rangle}{t_{B2}} (ig_s)^3 \epsilon^\nu(p_g) \\ &= T_{1i} T_{ia}^d T_{2b}^d \frac{\langle p_1 | \mu | p_A | \nu | p_A \rangle - \langle p_1 | \mu | p_g | \nu | p_A \rangle}{t_{Ag}} \frac{\langle p_2 | \mu | p_B \rangle}{t_{B2}} (ig_s)^3 \epsilon^\nu(p_g) \end{aligned} \quad (3.20)$$

Let us examine the long spinor string in the numerator more closely, the first term can be rewritten as:

$$\langle p_1 | \mu | p_A | \nu | p_A \rangle = \langle p_1 | \mu | p_A \rangle \langle p_A | \nu | p_A \rangle = 2p_{A;\nu} \langle p_1 | \mu | p_A \rangle \quad (3.21)$$

And the second term can be written as:

$$\langle p_1 | \mu | p_g | \nu | p_A \rangle = \langle p_1 | \mu | p_g \rangle \langle p_g | \nu | p_A \rangle \quad (3.22)$$

Let us examine how these terms compare in the high energy limit when contracted with $\langle p_2|\mu|p_B\rangle$. Using the Fierz Identity (eq. (2.23)) and writing the products in terms of s invariants (eq. (2.21)) we see:

$$\langle p_2|\mu|p_B\rangle\langle p_1|\mu|p_A\rangle = 2[p_AP_B]\langle p_1p_2\rangle \propto \sqrt{\hat{s}}\sqrt{\hat{s}} = \hat{s} \quad (3.23)$$

and

$$\langle p_2|\mu|p_B\rangle\langle p_1|\mu|p_g\rangle = 2[p_gp_B]\langle p_1p_2\rangle \propto \sqrt{\hat{s}}\sqrt{\hat{s}_{gB}}, \quad (3.24)$$

where $\hat{s}_{gB} = (p_g + p_B)^2$.

From this we see that the second term is suppressed by a factor of $\sqrt{\frac{\hat{s}_{gB}}{\hat{s}}}$. Now if we impose the transverse momentum condition by letting all of the $|p_\perp|$ be roughly equal we then can write this suppression as a function of the rapidity separation of the final state partons. If we let the separation between the (p_1, p_g) and (p_g, p_2) pairs each be Δ then the suppression is:

$$\sqrt{\hat{s}}\sqrt{\hat{s}_{gB}} = \sqrt{\frac{|p_\perp|e^\Delta}{|p_\perp|e^{2\Delta}}} \approx e^{-\frac{\Delta}{2}}. \quad (3.25)$$

Then in the limit of strict rapidity ordering in the final state, $\Delta \rightarrow \infty$ and the second term in the difference of spinor strings in eq. (3.20) is exponentially suppressed in Δ compared to the first.

A similar argument can be made for neglecting one term in each of the diagrams that contribute to fig. 3.2a. This lets us simplify these contributions from,

$$\begin{aligned} \sum_{j=1}^4 \mathcal{D}_j = & (ig_s)^3 T_{1i}^g T_{ia}^d T_{2b}^d \varepsilon_{1\nu} \frac{\langle 1|\nu|g\rangle\langle g|\mu|a\rangle + 2p_1^\nu\langle 1|\mu|a\rangle}{s_{1g}t_{b2}} \langle 2|\mu|b\rangle \\ & + (ig_s)^3 T_{1i}^d T_{ia}^g T_{2b}^d \varepsilon_{1\nu} \frac{2p_a^\nu\langle 1|\mu|a\rangle - \langle 1|\mu|g\rangle\langle g|\nu|a\rangle}{t_{ag}t_{b2}} \langle 2|\mu|b\rangle, \\ & + (ig_s)^3 T_{2i}^g T_{ib}^d T_{1a}^d \varepsilon_{1\nu} \frac{\langle 2|\nu|g\rangle\langle g|\mu|b\rangle + 2p_2^\nu\langle 2|\mu|b\rangle}{s_{2g}t_{a1}} \langle 1|\mu|a\rangle \\ & + (ig_s)^3 T_{2i}^d T_{ib}^g T_{1a}^d \varepsilon_{1\nu} \frac{2p_b^\nu\langle 2|\mu|b\rangle - \langle 2|\mu|g\rangle\langle g|\nu|b\rangle}{t_{bg}t_{a1}} \langle 1|\mu|a\rangle \end{aligned} \quad (3.26)$$

where the blue terms are suppressed compared to the red terms, to:

$$\begin{aligned} \sum_{j=1}^4 \mathcal{D}_j = & -ig_s^3 \langle 1|\mu|a\rangle \langle 2|\mu|b\rangle \varepsilon_{1\nu} \\ & \times \left(\frac{2p_1^\nu}{s_{1g}t_{b2}} T_{1i}^g T_{ia}^d T_{2b}^d + \frac{2p_a^\nu}{t_{ag}t_{b2}} T_{1i}^d T_{ia}^g T_{2b}^d + \frac{2p_2^\nu}{t_{a1}s_{2g}} T_{2i}^g T_{ib}^d T_{1a}^d + \frac{2p_b^\nu}{t_{bg}t_{a1}} T_{2i}^d T_{ib}^g T_{1a}^d \right). \end{aligned} \quad (3.27)$$

At this point, we will again switch to looking at momenta in terms of light cone coordinates. In the high energy limit we can write eq. (3.27) as:

$$\begin{aligned} \sum_{j=1}^4 \mathcal{D}_j = & -ig_s^3 \langle 1|\mu|a\rangle \langle 2|\mu|b\rangle \varepsilon_{1\nu} \\ & \times \left(\frac{p_+^\nu}{(p_+ \cdot p_g)t_{b2}} T_{1i}^g T_{ia}^d T_{2b}^d - \frac{p_+^\nu}{(p_+ \cdot p_g)t_{b2}} T_{1i}^d T_{ia}^g T_{2b}^d + \frac{p_-^\nu}{t_{a1}(p_- \cdot p_g)} T_{2i}^g T_{ib}^d T_{1a}^d - \frac{p_-^\nu}{t_{a1}(p_- \cdot p_g)} T_{2i}^d T_{ib}^g T_{1a}^d \right). \end{aligned} \quad (3.28)$$

At this point we can insert the definition of the Lie algebra,

$$[T^a, T^b]_{ij} = if^{abc}(T_c)_{ij}, \quad (3.29)$$

to express our sum of the first 4 diagrams in the form:

$$\sum_{j=1}^4 \mathcal{D}_j = ig_s^3 \langle 1|\mu|a\rangle \langle 2|\mu|b\rangle \varepsilon_{1\nu} f^{gde} \frac{T_{1a}^e T_{2b}^d}{t_{a1}t_{b2}} \left(\frac{p_+^\nu}{(p_+ \cdot p_g)} t_{a1} + \frac{p_-^\nu}{(p_- \cdot p_g)} t_{b2} \right). \quad (3.30)$$

We notice now that the the colour pre-factor is exactly the same as the pre-factor for the diagram with the three gluon vertex (fig. 3.2b), which will allow us to combine these terms in a simple way. We now turn our attention to what happens to the three gluon contribution in the high energy limit. The diagram

can be expressed as:

$$\mathcal{D}_5 = -ig_s^3 \langle 1|\rho|a\rangle \langle 2|\mu|b\rangle \varepsilon_{1\nu} f^{gde} \frac{T_{1a}^e T_{2b}^d}{t_{a1} t_{b2}} (g^{\rho\mu} (q_1 + q_2)^\nu + 2g^{\mu\nu} p_g^\rho - 2g^{\nu\rho} p_g^\mu) \quad (3.31)$$

$$\rightarrow -ig_s^3 4p_+^\rho p_-^\mu e^{i\alpha} \varepsilon_{1\nu} f^{gde} \frac{T_{1a}^e T_{2b}^d}{t_{a1} t_{b2}} \left(g^{\rho\mu} (q_1 + q_2)^\nu + \frac{4p_+^\mu p_-^\nu + 4p_-^\mu p_+^\nu}{\hat{s}} p_g^\rho - \frac{4p_+^\nu p_-^\rho + 4p_-^\nu p_+^\rho}{\hat{s}} p_g^\mu \right) \quad (3.32)$$

$$= -ig_s^3 4e^{i\alpha} \varepsilon_{1\nu} f^{gde} \frac{T_{1a}^e T_{2b}^d}{t_{a1} t_{b2}} \left((p_+ \cdot p_-) (q_1 + q_2)^\nu + \frac{1}{\hat{s}} \{ 4p_+^\mu p_-^\nu p_+^\rho p_-^\mu p_g^\rho - 4p_+^\nu p_-^\rho p_+^\rho p_-^\mu p_g^\mu \} \right) \quad (3.33)$$

$$= ig_s^3 \langle 1|\mu|a\rangle \langle 2|\mu|b\rangle \varepsilon_{1\nu} f^{gde} \frac{T_{1a}^e T_{2b}^d}{t_{a1} t_{b2}} \left(-(q_1 + q_2)^\nu - \frac{2(p_+ \cdot p_g)}{(p_+ \cdot p_-)} p_-^\nu + \frac{2(p_- \cdot p_g)}{(p_+ \cdot p_-)} p_+^\nu \right), \quad (3.34)$$

where in the last line we extracted a factor of $4(p_+ \cdot p_-) = \langle 1|\mu|a\rangle \langle 2|\mu|b\rangle$ from each of the terms between the brackets. We can now write the full $2 \rightarrow 3$ amplitude in the high energy limit as:

$$A_{qQ \rightarrow qgQ} = \sum_{j=1}^5 \mathcal{D}_j = ig_s^3 \langle 1|\mu|a\rangle \langle 2|\mu|b\rangle \varepsilon_{1\nu} f^{gde} \frac{T_{1a}^e T_{2b}^d}{t_{a1} t_{b2}} \tilde{V}^\nu, \quad (3.35)$$

with V^ν being given by,

$$V^\nu = \frac{p_+^\nu}{(p_+ \cdot p_g)} t_{a1} - \frac{p_-^\nu}{(p_- \cdot p_g)} t_{b2} - (q_1 + q_2)^\nu + \frac{2(p_+ \cdot p_g)}{(p_+ \cdot p_-)} p_-^\nu - \frac{2(p_- \cdot p_g)}{(p_+ \cdot p_-)} p_+^\nu \quad (3.36)$$

Let us compare the squared eq. (3.35) with the squared $qQ \rightarrow qQ$ amplitude. The colour and helicity summed and averaged $qQ \rightarrow qQ$ square matrix element in the high energy limit is given by:

$$|\bar{\mathcal{M}}_{qQ \rightarrow qQ}|^2 = \frac{1}{4(N_C^2 - 1)} \|\langle 1|\mu|a\rangle \langle 2|\mu|b\rangle\|^2 \cdot \left(g_s^2 C_F \frac{1}{t_1} \right) \cdot \left(g_s^2 C_F \frac{1}{t_2} \right), \quad (3.37)$$

whereas also in the high energy limit, the $qQ \rightarrow qgQ$ square matrix element is:

$$|\bar{\mathcal{M}}_{qQ \rightarrow qgQ}|^2 = \frac{1}{4(N_C^2 - 1)} \|\langle 1|\mu|a\rangle \langle 2|\mu|b\rangle\|^2 \cdot \left(g_s^2 C_F \frac{1}{t_1} \right) \cdot \left(g_s^2 C_F \frac{1}{t_2} \right) \cdot \left(-\frac{g_s^2 C_A}{t_{a1} t_{b2}} V^\nu V_\nu \right). \quad (3.38)$$

Thus the $qQ \rightarrow qgQ$ squared matrix element can be written as the product of the

$qQ \rightarrow qQ$ squared matrix element and a term proportional to the square of the V^ν expression, which we will call the “Lipatov Vertex”. In practice we used the symmetrised version of the Lipatov Vertex where we average over the incoming and outgoing momenta:

$$\begin{aligned}
V^\rho(q_1, q_2) = & - (q_1 + q_2)^\rho \\
& + \frac{p_A^\rho}{2} \left(\frac{q_1^2}{p_g \cdot p_A} + \frac{p_g \cdot p_B}{p_A \cdot p_B} + \frac{p_g \cdot p_2}{p_A \cdot p_2} \right) + p_A \leftrightarrow p_1 \\
& - \frac{p_B^\rho}{2} \left(\frac{q_2^2}{p_g \cdot p_B} + \frac{p_g \cdot p_A}{p_B \cdot p_A} + \frac{p_g \cdot p_1}{p_B \cdot p_1} \right) - p_B \leftrightarrow p_2,
\end{aligned} \tag{3.39}$$

From this we generalise to $qQ \rightarrow qg \dots gQ$ square amplitudes by keeping this factorised approach and including an additional Lipatov vertex factor for each additional gluon in the amplitude. This vertex can be verified to be correct by comparing to LO matrix elements in the high energy limit. This forms the basis on how we approximate real corrections to all orders in the MRK limit, we now move on to discuss implementing the MRK limit to the virtual corrections as well.

3.2.3 A brief aside on BFKL resummation

A related formalism for computing cross sections of high energy collisions is that of Balitsky, Fadin, Kuraev and Lipatov (BFKL) [54, 56, 57]. In short, one calculates cross sections using the integral form,

$$\sigma = \int \frac{d^2 k_a}{2\pi k_a^2} \int \frac{d^2 k_b}{2\pi k_b^2} \underbrace{\Phi_a(k_a) \Phi_b(k_b)}_{\text{Impact factors}} \underbrace{G(k_a, k_b)}_{\text{Scattering Green's function}}, \tag{3.40}$$

where the integral is done over process dependent “Impact factors” and process independent Green’s function describing the scattering process. This Green’s function is traditionally calculated by assuming a strong ordering in rapidity in the final state, and integrating over the rapidity differences between interactions. Additional emissions are included through the use of an effective vertex (see next section) appearing inside the Green’s function. Details on how one can perform calculations within the BFKL framework can be found in references [58–60] and in chapter 5 of [31].

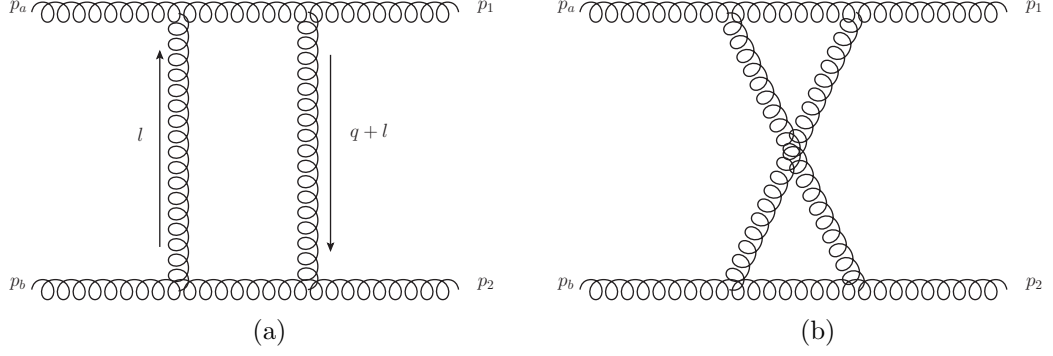


Figure 3.3: The one loop corrections to the gg scattering amplitude that contribute at leading logarithm.

The main reasons to mention the BFKL factorisation is to stress although we will use some of the BFKL terminology in later sections, the approach taken here for the HEJ framework has the advantage of being fully factorisable at the level of the square matrix element, and does not include any approximations on the available phase space from fixed order. In particular we will label configurations as “FKL” if they satisfy the following criteria:

1. The flavour of the most backward outgoing parton has to match the flavour of the backward incoming parton.
2. The flavour of the most forward outgoing parton has to match the flavour of the forward incoming parton.
3. All other outgoing partons have to be gluons.

This is motivated by these being the configurations which permit the maximum number of t -channel gluons, i.e. the LL contribution.

3.2.4 Motivating the Lipatov Ansatz for virtual corrections

To motivate our treatment of the virtual corrections, we will look at the one loop corrections to the $2 \rightarrow 2$ scattering. We will look here at gg , but one can repeat a similar calculation in the other channels with gluon exchange as the important physics here is in the poles of loop momenta.

From the Feynman rules given in table 2.1, we can calculate the the one loop correction by combining the contribution from the diagram with two gluons

exchanged in the t-channel with the contributions from the crossed diagram (see fig. 3.3). Looking at the former first, we can write the amplitude in the high energy limit as a colour piece and a kinematic piece [31, equation 5.187] (neglecting external polarisation vectors),

$$\mathcal{M} \approx \underbrace{g_s^4 f^{aa'c} f^{a'd_0c'} f^{cb'b} f^{c'd_1b'}}_{\text{Colour piece}} \underbrace{\mathcal{I}}_{\text{kinematic piece}}, \quad (3.41)$$

with the kinematic piece being given by an integral over loop momenta l [31, equation 5.189],

$$4\hat{s}^2 \int \frac{d^4 l}{(2\pi^4)} \left[\frac{1}{(p_a + l)^2} \cdot \frac{1}{l^2} \cdot \frac{1}{(p_b - l)^2} \cdot \frac{1}{(q - l)^2} \right]. \quad (3.42)$$

We can then evaluate the integral above, again in the high energy limit, to arrive at a simple form for the diagram,

$$\mathcal{M} \approx \frac{16\pi\alpha_s}{C_A} \cdot f^{aa'c} f^{a'd_0c'} f^{cb'b} f^{c'd_1b'} \cdot \frac{\hat{s}}{-\hat{t}} \log \frac{\hat{s}}{-\hat{t}} \epsilon(\hat{t}), \quad (3.43)$$

where we have introduced the function $\epsilon(\hat{t})^1$ which is given by [31, equation 5.193],

$$\epsilon(\hat{t}) = \alpha_s C_A \hat{t} \int \frac{d^2 l_\perp}{(2\pi)^2} \frac{1}{l_\perp^2 (q - l)_\perp^2}. \quad (3.44)$$

The above integral expression is not finite, so we will need to make use of a regularisation scheme. Introducing a regularisation scale μ to deal with the IR divergence results in the expression we will define as,

$$\omega_0(q) := \epsilon_{\text{reg}}(\hat{t}) = -\frac{\alpha_s C_A}{4\pi} \log \left(\frac{q_\perp^2}{\mu^2} \right). \quad (3.45)$$

Returning to the one loop virtual correction, we can combine the eq. (3.43) with the crossed diagram to obtain the full $\mathcal{O}(\alpha_s)$ virtual correction [51, equation 102],

$$\mathcal{M} \simeq -8\pi\alpha_s \frac{\hat{s}}{\hat{t}} f^{ada'} f^{bdb'} \ln \frac{\hat{s}}{-\hat{t}} \epsilon(\hat{t}). \quad (3.46)$$

¹Note that this function is also commonly called $\alpha(\hat{t})$, but we have used the ϵ notation here to avoid confusion with eq. (3.12)

To extend this description to n -loops, we will employ the use of the Lipatov Ansatz [54], which states that the leading log accurate virtual corrections in $\frac{\hat{s}}{\hat{t}}$ can be included by performing the following replacement,

$$\frac{1}{t_i} \rightarrow \frac{1}{t_i} \exp [\omega_0(q_i)(y_{i-1} - y_i)]. \quad (3.47)$$

One can check that performing this substitution on the $2 \rightarrow 2$ amplitude ($\propto \frac{\hat{s}}{\hat{t}}$), will reproduce the kinematic terms in eq. (3.46) when we truncate the exponential to first order in α_s . It has been checked that this exponential form for the virtual corrections in the high energy limit is valid even for subleading configurations [14, 61–64].

3.2.5 HEJ resummation

In the remainder of this section and in the section which follows we will discuss putting the pieces together in the HEJ formalism. Formally the leading-order matched leading-log HEJ cross section for $(2 \rightarrow 2)$ scattering is given by,

$$\begin{aligned} \sigma_{2j}^{\text{resum,match}} = & \sum_{f_1, f_2} \sum_m \prod_{j=1}^m \left(\int_{p_{j\perp}^B=0}^{p_{j\perp}^B=\infty} \frac{d^2 \mathbf{p}_{j\perp}^B}{(2\pi)^3} \int \frac{dy_j^B}{2} \right) (2\pi)^4 \delta^{(2)} \left(\sum_{k=1}^m \mathbf{p}_{k\perp}^B \right) \\ & \times x_a^B f_{a,f_1}(x_a^B, Q_a^B) x_b^B f_{b,f_2}(x_b^B, Q_b^B) \frac{\left[\mathcal{M}_{\text{LO}}^{f_1 f_2 \rightarrow f_1 g \dots g f_2}(\{p_j^B\}) \right]^2}{(\hat{s}^B)^2} \\ & \times (2\pi)^{-4+3m} 2^m \\ & \times \sum_{n=2}^{\infty} \int_{p_{1\perp}=p_{\perp,\min}}^{p_{1\perp}=\infty} \frac{d^2 \mathbf{p}_{1\perp}}{(2\pi)^3} \int_{p_{n\perp}=p_{\perp,\min}}^{p_{n\perp}=\infty} \frac{d^2 \mathbf{p}_{n\perp}}{(2\pi)^3} \prod_{i=2}^{n-1} \int_{p_{i\perp}=\lambda}^{p_{i\perp}=\infty} \frac{d^2 \mathbf{p}_{i\perp}}{(2\pi)^3} (2\pi)^4 \delta^{(2)} \left(\sum_{k=1}^n \mathbf{p}_{k\perp} \right) \\ & \times \mathbf{T}_y \prod_{i=1}^n \left(\int \frac{dy_i}{2} \right) \mathcal{O}_{mj}^e \left(\prod_{l=1}^{m-1} \delta^{(2)}(\mathbf{p}_{\mathcal{J}_l\perp}^B - \mathbf{j}_{l\perp}) \right) \left(\prod_{l=1}^m \delta(y_{\mathcal{J}_l}^B - y_{\mathcal{J}_l}) \right) \mathcal{O}_{2j}(\{p_i\}) \\ & \times \frac{(\hat{s}^B)^2}{x_a^B f_{a,f_1}(x_a^B, Q_a^B) x_b^B f_{b,f_2}(x_b^B, Q_b^B)} \frac{x_a f_{a,f_1}(x_a, Q_a) x_b f_{b,f_2}(x_b, Q_b)}{\hat{s}^2} \frac{\left[\mathcal{M}_{\text{HEJ}}^{f_1 f_2 \rightarrow f_1 g \dots g f_2}(\{p_i\}) \right]^2}{\left[\mathcal{M}_{\text{HEJ;LO}}^{f_1 f_2 \rightarrow f_1 g \dots g f_2}(\{p_j^B\}) \right]^2}, \end{aligned} \quad (3.48)$$

where,

- The first 2 lines (blue) represent the generation of $f_1 f_2 \rightarrow f_1 g \dots g f_2$, m -jet

input events with outgoing momenta p_j^B (here B is used to denote Born-level rather than parton/jet labelling). In this form we perform the phase space integration over particle transverse momenta and rapidity as described in eq. (2.53) using the HEJ fixed order event generator or we use fixed order input from another generator.

- Line 3 (pink) is simply a factor accounting for the different multiplicities between fixed-order and resummation events.
- Lines 4-5 (red) represent the integration over the resummation phase space. Here we again see integrals over the transverse momenta and rapidity of the particles in the final state. We have also introduced a rapidity ordering operator \mathbf{T}_y , m -jet projector for the resummation phase space \mathcal{O}_{mj}^e , 2-jet projector for the Born phase space \mathcal{O}_{2j} and a soft p_\perp regulator λ for additional radiation. The delta functions fix the relationship between the resummation and fixed order momenta. The first sets each transverse fixed-order jet momentum to be a function of the resummation momenta. The second delta forces the rapidities of resummation and fixed-order jets to be the same.
- Line 6 (purple) contains terms which reweight the PDFs to the resummation phase space.

The helicity and colour summed matrix element $\left| \overline{\mathcal{M}_{\text{HEJ}}^{f_1 f_2 \rightarrow f_1 g \dots g f_2}(\{p_i\})} \right|^2$ is made up of a current piece and Lipatov vertices for any additional emissions and the \hat{t} channel momenta have been replaced using the Lipatov Ansatz.

3.3 Summary of HEJ formalism and performing resummation with the HEJ2 software package

We now discuss how one performs resummation in HEJ2 in practice. As input, HEJ2 requires leading-order (LO) events, generated with e.g. SHERPA [65] or MADGRAPH5_AMC@NLO [66]. For higher jet multiplicities exact fixed-order generation becomes increasingly time consuming. To address this problem, HEJ2 includes the fast HEJ fixed-order generator HEJF0G based on the high-energy approximation of the leading-order matrix elements.

Using the kinematics of each (approximate or exact) input event, we identify whether resummation is possible. Resummable event types include FKL classified events as described in section 3.2.3 which are the configurations which encompass the LL accuracy. We also label an event as resumable for some implemented NLL configurations which will be outlined in the coming sections. For each event that permits resummation, HEJ generates a number of events in the resummation phase space, which include real and virtual corrections to all orders in the high-energy limit using the Lipatov Vertex discussed in section 3.2.2 and the Lipatov Ansatz discussed in section 3.2.4. Together with the unchanged non-resummable (NR) input events, the generated resummation events are then passed on to any number of output event files and/or analyses. This standard control flow is depicted in figure 3.4. It can be modified through HEJ options, such that e.g. non-resummable events are discarded.

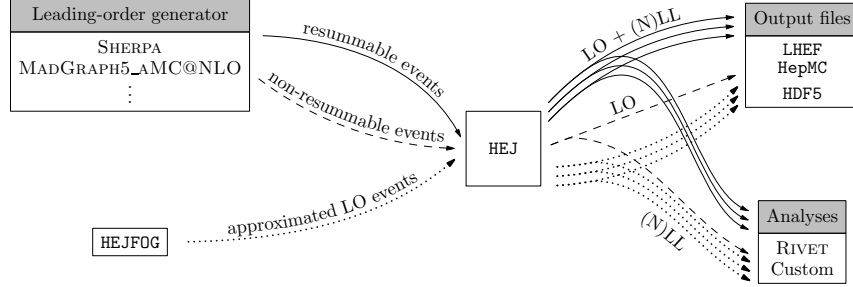


Figure 3.4: Diagram representing the standard HEJ use case. Taken from reference [2].

The first type of event kinematics for which resummation is implemented are leading-logarithmic configurations defined as FKL configurations in section 3.2.3. The criteria given remain the same in processes involving virtual photons and/or Z bosons. For virtual W bosons, the incoming and outgoing flavours in criteria 1 and 2 only have to match up to the change induced by W boson couplings. In the case of a final-state Higgs boson, configurations where the backward (forward) incoming parton is a quark or antiquark and the most backward (forward) outgoing particle is the Higgs boson are formally subleading. Nevertheless, we also implement resummation for such configurations [26]. Depending on the process, resummation is also implemented for two further types of next-to-leading-logarithmic (NLL) configurations. These configurations differ from LL ones as follows.

- *Unordered gluon (UNO)*: Either the most forward or most backward outgoing parton is a gluon, and the next outgoing parton in rapidity order

Process	pure LL	LO + LL	NLL	
			unordered gluon	quark-antiquark
≥ 2 jets	HEJ 2.0	HEJ 2.0	HEJ 2.0	HEJ 2.1
H + 1 jet	—	HEJ 2.2	N/A	N/A
H + ≥ 2 jets	HEJ 2.0	HEJ 2.0	HEJ 2.0	—
W + ≥ 2 jets	HEJ 2.1	HEJ 2.1	HEJ 2.1	HEJ 2.1
Z/ γ + ≥ 2 jets	HEJ 2.2	HEJ 2.1	HEJ 2.1	—
W $^\pm$ W $^\pm$ + ≥ 2 jets	—	HEJ 2.2	—	—

Table 3.1: Implemented processes and higher-order logarithmic corrections in HEJ. The “pure LL” column lists processes implemented in the HEJFOG. The NLL columns include both pure NLL and NLL matched to LO.

is a quark or antiquark whose flavour matches the one of the respective incoming parton.

- *Quark-antiquark (QQBAR)*: A pair of final-state gluons that are adjacent in rapidity is replaced by a quark-antiquark pair.

Formally, these configurations contribute at NLL accuracy as they have one lower power of s compared to strictly gluonic exchanges as seen from eq. (3.12). The current status of the implemented resummation is summarised in table 3.1.

The resummation events generated for the LL and supported NLL configurations are given a final matrix element weight of

$$|\mathcal{M}_{\text{HEJ}}|^2 \frac{|\mathcal{M}_{\text{LO}}|^2}{|\mathcal{M}_{\text{HEJ,LO}}|^2}, \quad (3.49)$$

where \mathcal{M}_{HEJ} is the all-order scattering matrix element in the high-energy approximation, $\mathcal{M}_{\text{HEJ,LO}}$ its leading-order truncation, calculated for the kinematics of the input event and $|\mathcal{M}_{\text{LO}}|^2$ is taken from the LO input and ensures LO accuracy event by event.

To illustrate the structure of the HEJ matrix element, we first focus on LL configurations in pure multijet production. We denote these configurations as $f_a f_b \rightarrow f_a \cdots f_b$, where f_a is the flavour of the incoming parton in the backward direction with momentum p_a . Correspondingly, we use f_b and p_b for the flavour and momentum of the forward incoming parton. The final state contains n partons with momenta p_1, \dots, p_n , which we order by rapidity, viz. $y_1 < \cdots < y_n$. The most backward outgoing parton has flavour f_a , the most forward one flavour

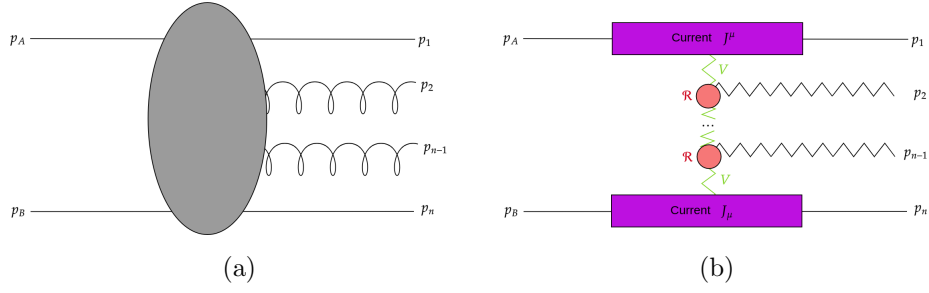


Figure 3.5: $2 \rightarrow n$ scattering (a) in an FKL configuration (b) expressed as a factorised amplitude in the HEJ formalism

f_b , and all other outgoing partons are gluons. Using this notation, we can write the general form of the squared HEJ matrix element as

$$\begin{aligned} \left| \mathcal{M}_{\text{HEJ}}^{f_a f_b \rightarrow f_a \cdots f_b} \right|^2 &= \mathcal{B}_{f_a, f_b}(p_a, p_b, p_1, p_n) \\ &\cdot \prod_{i=1}^{n-2} \mathcal{V}(p_a, p_b, p_1, p_n, q_i, q_{i+1}) \\ &\cdot \prod_{i=1}^{n-1} \mathcal{W}(q_{i\perp}, y_i, y_{i+1}), \end{aligned} \quad (3.50)$$

where $q_i = p_a - \sum_{j=1}^i p_j$ is the t -channel momentum after the emission of parton i . \mathcal{B}_{f_a, f_b} is derived from the modulus square of the Born-level matrix element for the process $f_a f_b \rightarrow f_a f_b$, \mathcal{V} accounts for the real emission of the $n - 2$ gluons in between f_a and f_b , and \mathcal{W} incorporates the virtual and unresolved real corrections. This can be seen diagrammatically in fig. 3.5, where we should stress that these are not Feynman Diagrams but they are still used to express the structure of the amplitudes.

The Born-level function \mathcal{B}_{f_a, f_b} is given by

$$\mathcal{B}_{f_a, f_b}(p_a, p_b, p_1, p_n) = \frac{(4\pi\alpha_s)^n}{4(N_C^2 - 1)} \frac{K_{f_a}}{q_1^2} \frac{K_{f_b}}{q_{n-1}^2} \|S_{f_a f_b \rightarrow f_a \cdots f_b}\|^2, \quad (3.51)$$

where α_s is the strong coupling constant and $N_C = 3$ the number of colours. K_{f_a} and K_{f_b} are generalised colour factors depending on the respective parton flavour and, in the case of gluons, also the parton momentum. For quarks and antiquarks one finds $K_f = C_F = \frac{N_C^2 - 1}{2N_C}$; the factor K_g for gluons is derived in [15].

$S_{f_a f_b \rightarrow f_a \dots f_b}$ denotes the contraction of two currents:

$$\|S_{f_a f_b \rightarrow f_a \dots f_b}\|^2 \equiv \|j^a \cdot j^b\|^2 = \sum_{\substack{\lambda_a=+,- \\ \lambda_b=+,-}} |j^{\mu, \lambda_a}(p_1, p_a) j_{\mu}^{\lambda_b}(p_n, p_b)|^2, \quad (3.52)$$

where j_{μ}^{λ} is the current

$$j_{\mu}^{\lambda}(p, q) = \bar{u}^{\lambda}(p) \gamma_{\mu} u^{\lambda}(q) \quad (3.53)$$

for helicity λ . HEJ employs the symbolic manipulation language FORM [67] to generate compact symbolic expressions for current contractions.

The real corrections are given by contractions of Lipatov vertices [68]:

$$\mathcal{V}(\{p\}) = - \frac{C_A}{q_i^2 q_{i+1}^2} V_{\mu}(\{p\}) V^{\mu}(\{p\}) \quad (3.54)$$

where V_{μ} is given in eq. (3.39) and with $C_A = N_C$.

Finally, the virtual and unresolved real corrections \mathcal{W} can be expressed in terms of the regularised Regge trajectory ω^0 defined in section 3.2.4:

$$\mathcal{W}(q_{j\perp}, y_j, y_{j+1}) = \exp[\omega^0(q_{j\perp})(y_{j+1} - y_j)]. \quad (3.55)$$

The generalisations to NLL configurations and additional non-partonic final state particles are derived in [1, 22, 25, 26, 68–70]. In all cases one finds a factorisation into a Born-level function, resolved real emissions, and virtual and unresolved real corrections. In the absence of interference, one recovers the same structure as in equation (3.50). In particular, the functions \mathcal{V} and \mathcal{W} comprising the all-order corrections are universal, whereas the Born-level function \mathcal{B} is process dependent.

When testing a new process or looking at including higher log corrections inside the HEJ framework we can look at phase space explorer plots such as fig. 3.1 and already published studies comparing to fixed order and data as test of the consistency of the framework. HEJ has been validated against data in experimental studies of pure multijet production [18–21], lepton pair production via a virtual W boson, photon, or Z boson in association with two or more jets [22–25], and Higgs boson production with jets [26].

3.4 NLO bin-by-bin matching

Some observables (e.g. hardest jet p_\perp) are usually described well by fixed order calculation even before adding the higher order logarithms included in HEJ resummation. In order to have valid predictions accross all of phase space, including regions away from the high energy limit, we want to include these fixed order contributions. In order to include the full NLO effects in the HEJ predictions, we can make use of an NLO matching procedure to achieve predictions which are NLO accurate with LL corrections. In this section we derive such a procedure, starting with the total cross sections σ , and then generalising to each bin in each histogram.

Starting with the fixed order results we can write,

$$\sigma_{n\text{-jet}}^{\text{LO}} = f_{n\text{-jet}}^{2\rightarrow n} \alpha_s^n, \quad (3.56)$$

for leading order, and

$$\sigma_{n\text{-jet}}^{\text{NLO}} = \underbrace{f_{n\text{-jet}}^{2\rightarrow n} \alpha_s^n}_{\sigma_{n\text{-jet}}^{\text{LO}}} + (f_{n\text{-jet}}^{2\rightarrow n+1} + f_{n+1\text{-jet}}^{2\rightarrow n+1}) \alpha_s^{n+1}, \quad (3.57)$$

for next-to-leading order. Here we use the notation that $f_{k\text{-jet}}^{2\rightarrow n}$ represents $2 \rightarrow n$ partons clustered into k jets. Note the first term in the brackets in eq. (3.57) contains the virtual one-loop corrections plus the contribution of $2 \rightarrow n+1$ partons clustered into n jets.

The 2-jet inclusive cross section from HEJ contains contributions to all orders in the coupling:

$$\sigma_{n\text{-jet}}^{\text{HEJ}} = \sum_{n=2}^{\infty} \sum_{2 \leq m \leq n} h_{m\text{-jet}}^{2\rightarrow n} \alpha_s^n = h_{2\text{-jet}}^{2\rightarrow 2} \alpha_s^2 + (h_{2\text{-jet}}^{2\rightarrow 3} + h_{3\text{-jet}}^{2\rightarrow 3}) \alpha_s^3 + \mathcal{O}(\alpha_s^4). \quad (3.58)$$

The HEJ results are all currently matched to leading order meaning that for all n , we have the condition,

$$f_{n\text{-jet}}^{2\rightarrow n} = h_{n\text{-jet}}^{2\rightarrow n}. \quad (3.59)$$

For our matching procedure, we will also need to consider HEJ truncated to NLO. That is HEJ limited to 1 loop corrections and with no more than one additional

emission,

$$\sigma_{2\text{-jet}}^{\text{HEJ@NLO}} = f_{2\text{-jet}}^{2\rightarrow 2} \alpha_s^2 + f_{3\text{-jet}}^{2\rightarrow 3} \alpha_s^3 + h_{2\text{-jet}}^{2\rightarrow 3} \alpha_s^3. \quad (3.60)$$

From these definitions, we can define an NLO reweighting factor for 2 jets,

$$\frac{\sigma_{2\text{-jet}}^{\text{NLO}}}{\sigma_{2\text{-jet}}^{\text{HEJ@NLO}}} = \frac{f_{2\text{-jet}}^{2\rightarrow 2} \alpha_s^2 + f_{3\text{-jet}}^{2\rightarrow 3} \alpha_s^3 + h_{2\text{-jet}}^{2\rightarrow 3} \alpha_s^3}{f_{2\text{-jet}}^{2\rightarrow 2} \alpha_s^2 + f_{3\text{-jet}}^{2\rightarrow 3} \alpha_s^3 + h_{2\text{-jet}}^{2\rightarrow 3} \alpha_s^3}. \quad (3.61)$$

This expression can be simplified and expanded in powers of α_s using the standard expansion,

$$\frac{1}{1 + k\alpha_s} = \sum_{n=0}^{\infty} (-k)^n \alpha_s^n, \quad (3.62)$$

which allows us to write,

$$\frac{\sigma_{2\text{-jet}}^{\text{NLO}}}{\sigma_{2\text{-jet}}^{\text{HEJ@NLO}}} = 1 + (f_{2\text{-jet}}^{2\rightarrow 3} - h_{2\text{-jet}}^{2\rightarrow 3}) \left[\sum_{n=0}^{\infty} \frac{(-f_{3\text{-jet}}^{2\rightarrow 3} - h_{2\text{-jet}}^{2\rightarrow 3})^n}{(f_{2\text{-jet}}^{2\rightarrow 2})^{n+1}} \alpha_s^{n+1} \right]. \quad (3.63)$$

When multiplied by the HEJ prediction in eq. (3.58) we get a result which is accurate to next-to-leading order,

$$\sigma_{2\text{-jet}}^{\text{HEJ}} \frac{\sigma_{2\text{-jet}}^{\text{NLO}}}{\sigma_{2\text{-jet}}^{\text{HEJ@NLO}}} = \underbrace{f_{2\text{-jet}}^{2\rightarrow 2} \alpha_s^2 + (f_{2\text{-jet}}^{2\rightarrow 3} + f_{3\text{-jet}}^{2\rightarrow 3}) \alpha_s^3}_{\text{NLO accurate}} + \mathcal{O}(\alpha_s^4). \quad (3.64)$$

We can also show that the reweighting factor in eq. (3.63) allows us to maintain the LL accuracy of HEJ in the high energy limit. In the Regge limit, the HEJ amplitudes tend to the same limit as fixed order and it must be that $(f_{2\text{-jet}}^{2\rightarrow 3} - h_{2\text{-jet}}^{2\rightarrow 3}) \rightarrow 0$. Thus the reweighting factor tends to 1 and we just have the (LL accurate) HEJ result.

Equation (3.64) describes the matching of the total cross sections of HEJ to NLO, but we can also make use of an analogous expression for NLO matching each bin in a two-jet inclusive observable. The only thing then we have not discussed in detail is how to obtain a prediction for HEJ@NLO from fixed order input. As of HEJ2.2, the simplest way of doing this is to add the three jet leading order result to the exclusive 2j HEJ@NLO result obtained from using the following option in the yaml config file:

```
NLO truncation:
  enabled: true
  \NLO order: 2    # number of jets
```


This flag affects the HEJ resummation in two ways: the first is that it changes the number of additional emissions in a resummation phase space point to be chosen as 0 or 1 with equal probability instead of by a Poisson distribution around an estimated mean. The second is that if the number of additional emissions was chosen to be 0, truncate the exponential form of the virtual corrections $\exp\{\hat{\alpha}(q)\Delta y\}$ to linear order $1 + \hat{\alpha}(q)\Delta y$ to account for one-loop corrections. If the number of additional emissions was chosen to be 1, we instead truncate the exponential to 0th order and multiply by 1.

We will see the impact of this matching procedure in the chapters which follow.

Chapter 4

Leading Log description of same-sign WW pair production + jets

This chapter discusses the HEJ implementation of Same-Sign WW pair production in association with jets, available as part of the 2.2 release. Here we start with a discussion of the experimental relevance of this process as a non-removable background to Vector Boson Scattering studies. We then go on to derive the relevant HEJ amplitudes for the process using the groundwork for the construction of leading log accurate amplitudes laid out in the publication *Constructing All-Order Corrections to Multi-Jet Rates*[14]. We then discuss the impact of these logarithms, mirroring the setup of a recent CMS analysis [71]. Finally, we conclude by discussing the impact of NLO matching in the HEJ prediction, using the ideas outlined in section 3.4.

4.1 Vector Boson Scattering and unitarity

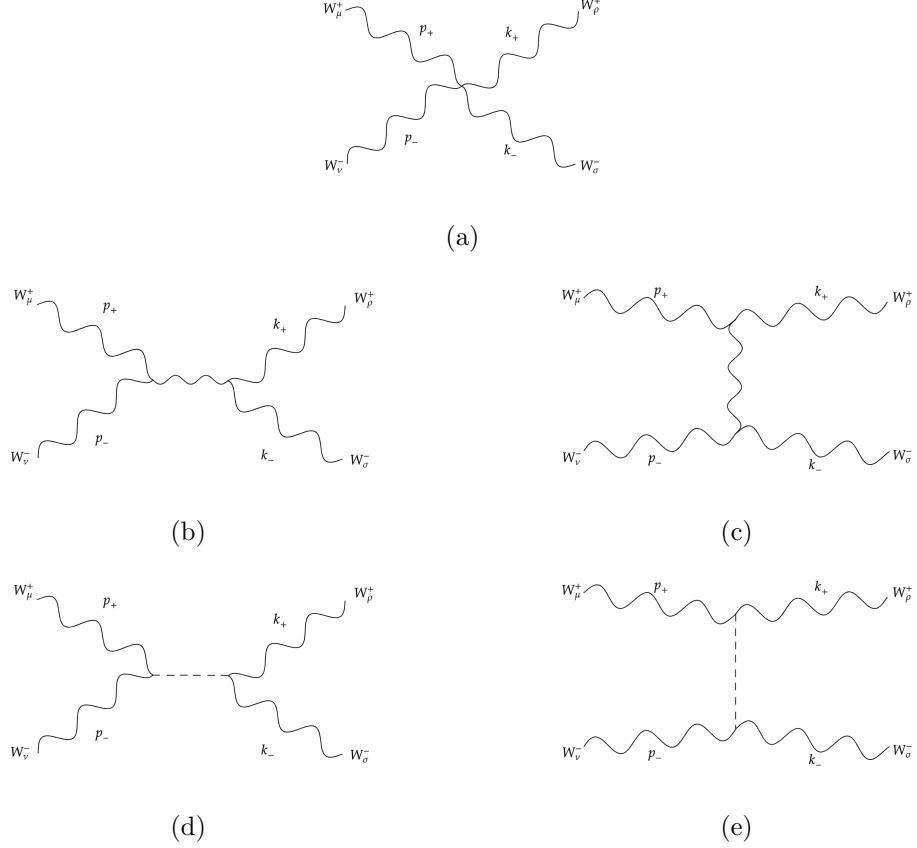


Figure 4.1: Five processes contributing to longitudinally polarised W scattering $W_L^+ W_L^- \rightarrow W_L^+ W_L^-$ at leading order (a) Involving the $4 - V$ vertex (b,c) Involving an intermediate Z boson or photon (d,e) Involving an intermediate Higgs boson

Firstly, we shall briefly discuss Vector Boson Scattering (VBS) as a process which needs the contribution from Higgs couplings in order to be unitary. Vector boson scattering describes the process $VV \rightarrow VV$ plus at least 2 jets where each V may be a W or Z boson, and historically this was used by Lee, Quigg and Thacker [72, 73] to impose an upper bound on the mass of the Higgs boson of $m_h < \left(\frac{8\pi\sqrt{2}}{3G_F} \right)^{1/2} \approx 1 \text{ TeV}$ (where G_F is the Fermi constant). The two jets here are important for the LHC and other pp colliders to be able to access the $VV \rightarrow VV$ vertex. Looking initially at longitudinally polarised W scattering $W_L^+ W_L^- \rightarrow W_L^+ W_L^-$, there are 5 contributions at leading order we need to combine depicted in fig. 4.1. The first comes from the $4 - V$ interaction which we shall label $i\mathcal{M}_{4V}$. The second and third come from an exchange of Z/γ in the s and t channels, labelled $i\mathcal{M}_{Z;s}$ and $i\mathcal{M}_{Z;t}$ respectively. Finally we will have the

contribution with a Higgs boson exchange, again in the s and t channels which we label $i\mathcal{M}_{h,s}$ and $i\mathcal{M}_{h,t}$ respectively. We will study these contributions starting with momenta conventions as set out in reference [74], reproduced in fig. 4.1.

The momenta of the incoming/outgoing polarised W bosons (beam is in z -direction) is given by,

$$\begin{aligned} p_+ &= (E, 0, 0, p), & k_+ &= (E, p \sin \theta, 0, p \cos \theta) \\ p_- &= (E, 0, 0, -p), & k_- &= (E, -p \sin \theta, 0, -p \cos \theta), \end{aligned} \quad (4.1)$$

and the polarisation vectors are given by,

$$\begin{aligned} \varepsilon_L(p_+) &= \frac{1}{m_W}(p, 0, 0, E), & \varepsilon_L(k_+) &= \frac{1}{m_W}(p, E \sin \theta, 0, E \cos \theta) \\ \varepsilon_L(p_-) &= \frac{1}{m_W}(p, 0, 0, -E), & \varepsilon_L(k_-) &= \frac{1}{m_W}(p, -E \sin \theta, 0, -E \cos \theta). \end{aligned} \quad (4.2)$$

Using the Feynman rule for the $4 - V$ vertex given in 2.2, we can write the amplitude for the first diagram as,

$$i\mathcal{M}_{4v} = ig^2 [2g_{\sigma\mu}g_{\rho\nu} - g_{\sigma\rho}g_{\mu\nu} - g_{\sigma\nu}g_{\rho\mu}] \varepsilon_L(p_+)^\mu \varepsilon_L(p_-)^\nu \varepsilon_L(k_+)^\sigma \varepsilon_L(k_-)^\rho. \quad (4.3)$$

Explicit calculation of the contractions of the polarisation vectors above, gives the following expression for the amplitude (no approximations yet),

$$i\mathcal{M}_{4v} = \frac{ig^2}{m_W^4} [2(p^2 - E^2 \cos \theta)^2 - (p^2 + E^2)^2 - (p^2 + E^2 \cos \theta)^2]. \quad (4.4)$$

We can then use the on-shell condition $p^2 = m^2$ to write a high energy approximation of this amplitude,

$$i\mathcal{M}_{4v} = ig^2 \frac{E^4}{m_W^4} [f_1(\theta)] + ig^2 \frac{E^2}{m_W^2} [f_2(\theta)] + \mathcal{O}\left(\frac{E}{m_W}\right)^0 \quad (4.5)$$

where we have taken the limit $E \gg m_W$ and the f_i are functions of the parameter theta. We know that this is not the full amplitude, but if we were to just look at eq. (4.5), we would see a scaling with the fourth power of Energy which means the amplitude would clearly violate unitarity at high energies. Let us now add in the contribution from Z/γ exchange to attempt to repair the unitarity violation.

Calculation of the four diagrams $\mathcal{M}_{Z;s}$, $\mathcal{M}_{Z;t}$ (two diagrams each to account for Z/γ) from the Feynman rules in tables 2.1 and 2.2 is straightforward but tedious. The $\left(\frac{E}{m_W}\right)^4$ terms actually cancel when combining amplitudes and we are left with only a contribution which grows like $\left(\frac{E}{m_W}\right)^2$ in the high energy limit [74, equation 19],

$$i\mathcal{M}_{4v} + i\mathcal{M}_{Z;s} + i\mathcal{M}_{Z;t} = i\frac{g^2}{4m_w^2} [s + t + \mathcal{O}(m_w^2)]. \quad (4.6)$$

However, this amplitude still grows with energy which hints that we are still missing a contribution. Consider now the s -channel Higgs Boson exchange $\mathcal{M}_{h,s}$ which can be written:

$$\mathcal{M}_{h,s} = (igm_W^2)g_{\mu\nu}g^{\rho\sigma}\frac{i}{s^2 - m_h^2 + i\epsilon}\varepsilon^\mu(p_+)\varepsilon^\nu(p_-)\varepsilon_\rho(k_+)\varepsilon_\sigma(k_-) \quad (4.7)$$

which simplifies to a kinematic factor multiplied by a contraction of polarisation vectors,

$$\mathcal{M}_{h,s} = \frac{-ig^2m_W^2}{s^2 - m_h^2 + i\epsilon}\varepsilon^\mu(p_+)\varepsilon_\mu(p_-)\varepsilon^\rho(k_+)\varepsilon_\rho(k_-). \quad (4.8)$$

This can then be simplified further in the high energy limit $E \gg m_W$, to get the result:

$$\mathcal{M}_{h,s} = \frac{-ig^2}{4m_W^2}\frac{s^2}{s^2 - m_h^2 + i\epsilon}. \quad (4.9)$$

So finally when we sum all of the contributions we get something which now does not grow as a function of Energy in the high energy limit

$$i\mathcal{M}_{4v} + i\mathcal{M}_{Z;s} + i\mathcal{M}_{Z;t} + i\mathcal{M}_{h,s} + i\mathcal{M}_{h,t} \sim \mathcal{O}\left(\frac{E^0}{m_W^0}\right). \quad (4.10)$$

Experimentally this is important, as studying vector boson scattering at high energies therefore is a study into not only the 4 vector boson vertex but also the electroweak Higgs couplings that are needed as a necessary background.

4.2 Same-Sign WW production in VBS studies

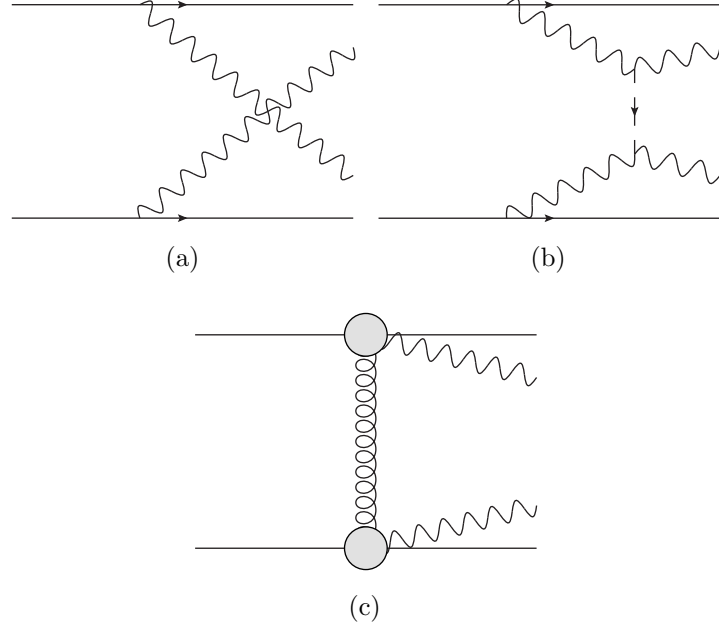


Figure 4.2: Three processes contributing to $pp \rightarrow jjW^\pm W^\pm$ at (a) $\mathcal{O}(g_w^4)$, (b) $\mathcal{O}(g_w^2 g_{HWW}^2)$, (c) $\mathcal{O}(g_w^2 g_s^2)$

Moving on to now include the jets in our discussion of the process $pp \rightarrow jjVV$ in the high energy limit. All possible $V^*V^* \rightarrow VV$ processes can be inserted between two quark lines to give this final state, as shown in fig. 4.2, which provides a key opportunity to study the mechanism of electroweak symmetry breaking. Observations of electroweak WWjj production was reported by both the ATLAS [75] and CMS [76] collaborations. More recently this signal has been analysed in more detail [77, 78] including data for differential distributions of the total cross section.

In order to cleanly study the $\mathcal{O}(g_w^4)$ and $\mathcal{O}(g_w^2 g_{HWW}^2)$ contributions to the amplitude, it is common to introduce VBS cuts to suppress the $\mathcal{O}(g_w^2 g_s^2)$ contribution (hereby also referred to as the QCD contribution). However, introducing such cuts directly leads to large logarithmic corrections to the QCD

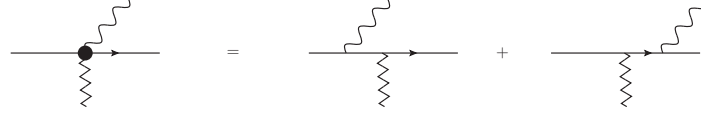


Figure 4.3: Schematic illustration of the current, $j_\mu^W(p_i, p_o, p_\ell, p_{\bar{\ell}})$, defined in Eq. (4.12) to describe the production of a W boson from a quark line with an off-shell gluon (shown as a zigzag line).

contribution which still remains. Common VBS cuts include a restriction to the dijet rapidity separation and dijet invariant mass for the hardest jets in the sample, both of which will directly lead to an increase in the high energy logarithms in s over t that are resummed in the high energy jets framework. In the next section, we will outline how to describe these logs within the HEJ framework.

4.3 Construction of the HEJ leading log amplitude for same-sign WW production

We now begin the process of constructing the HEJ LL amplitude for the Same-Sign WW process. At this point we will explicitly specify the process to be $pp \rightarrow (W_1 \rightarrow \ell_1^\pm \nu_{\ell_1})(W_2 \rightarrow \ell_2^\pm \nu_{\ell_2}) + \geq 2j$, specifying explicitly the decay products of the two W bosons. As described in the previous chapter, for a given multiplicity, a HEJ amplitude is built out of impact factors and Lipatov vertices. These multiplicities are then combined with the Lipatov ansatz for virtual corrections in order to achieve leading logarithmic accuracy in \hat{s}/p_t^2 at all orders in α_s .

We begin with the impact factors which are independent of the number of gluons in the amplitude and hence can be derived from the lowest order process where they occur. The starting point is therefore the L0 process:

$$q(p_a)Q(p_b) \rightarrow (W_1^\pm \rightarrow \ell(p_{\ell_1})\bar{\nu}_\ell(p_{\bar{\ell}_1}))(W_2^\pm \rightarrow \ell'(p_{\ell_2})\bar{\nu}'_\ell(p_{\bar{\ell}_2}))q'(p_1)Q'(p_2), \quad (4.11)$$

where q and Q represent different quark or anti-quark flavours. There are eight diagrams which contribute at L0, each similar to fig. 4.2c, which arise from the $qq'W$ vertices for each boson being assigned to different points on different quark lines.

We define the following current to describe the production of a W boson from a

quark line with an off-shell gluon, $q(p_i) \rightarrow (W \rightarrow \ell \bar{\ell}) q'(p_o) g^*$:

$$j_\mu^W(p_i, p_o, p_\ell, p_{\bar{\ell}}) = \frac{g_W^2}{2} \frac{1}{(p_\ell + p_{\bar{\ell}})^2 - m_W^2 + i\Gamma_W m_W} [\bar{u}^-(p_\ell) \gamma_\alpha v^-(p_{\bar{\ell}})] \\ \times \left(\frac{\bar{u}^-(p_o) \gamma^\alpha (\not{p}_o + \not{p}_\ell + \not{p}_{\bar{\ell}}) \gamma_\mu u^-(p_i)}{(p_o + p_\ell + p_{\bar{\ell}})^2} + \frac{\bar{u}^-(p_o) \gamma_\mu (\not{p}_i - \not{p}_\ell - \not{p}_{\bar{\ell}}) \gamma^\alpha u^-(p_i)}{(p_i - p_\ell - p_{\bar{\ell}})^2} \right), \quad (4.12)$$

as illustrated in fig. 4.3. The exact tree-level result can then be compactly expressed as the following two contractions of two such currents:

$$i\mathcal{M}^{\text{HEJ,tree}} = g_s^2 \left(\frac{j_\mu^W(p_a, p_1, p_{\ell_1}, p_{\bar{\ell}_1}) g^{\mu\nu} j_\nu^W(p_b, p_2, p_{\ell_2}, p_{\bar{\ell}_2})}{q^2} \right. \\ \left. + \frac{j_\mu^W(p_a, p_1, p_{\ell_2}, p_{\bar{\ell}_2}) g^{\mu\nu} j_\nu^W(p_b, p_2, p_{\ell_1}, p_{\bar{\ell}_1})}{\tilde{q}^2} \right), \quad (4.13)$$

where $q = p_a - p_1 - p_{\ell_1} - p_{\bar{\ell}_1}$ and $\tilde{q} = p_a - p_1 - p_{\ell_2} - p_{\bar{\ell}_2}$. This amplitude remains exact at $\mathcal{O}(\alpha_W^2 \alpha_s)$ within the HEJ framework. In particular, our full amplitudes already achieve LO accuracy without the need for further matching with the exception of channels with identical leptons or quarks. The extra contributions arising in these special cases are suppressed in the MRK limit and do not affect the logarithmic accuracy. They are nonetheless included through the fixed-order matching.

We now move on to construct the the Leading Logarithm accurate HEJ result based of the ideas laid out in section 3.2. We write the amplitude as a sum of two skeleton functions, each with its own tower of real and virtual corrections. Interference between these is immediately included upon squaring the amplitude.

These skeleton functions are defined as

$$B = j_\mu^W(p_a, p_1, p_{\ell_1}, p_{\bar{\ell}_1}) g^{\mu\nu} j_\nu^W(p_b, p_n, p_{\ell_2}, p_{\bar{\ell}_2}), \\ \tilde{B} = j_\mu^W(p_a, p_1, p_{\ell_2}, p_{\bar{\ell}_2}) g^{\mu\nu} j_\nu^W(p_b, p_n, p_{\ell_1}, p_{\bar{\ell}_1}), \quad (4.14)$$

which relate to the two possible combinations of leptons and quark lines. These have corresponding planar t -channel momenta:

$$q_1 = p_a - p_1 - p_{\ell_1} - p_{\bar{\ell}_1}, \quad q_i = q_{i-1} - p_i \quad i = 2, \dots, n-1, \\ \tilde{q}_1 = p_a - p_1 - p_{\ell_2} - p_{\bar{\ell}_2}, \quad \tilde{q}_i = \tilde{q}_{i-1} - p_i \quad i = 2, \dots, n-1. \quad (4.15)$$

We refer to the corresponding momenta-squared as $t_i = q_i^2$ and $\tilde{t}_i = \tilde{q}_i^2$ for $i = 1, \dots, n-1$. We also define the rapidity differences of consecutive quarks/gluons

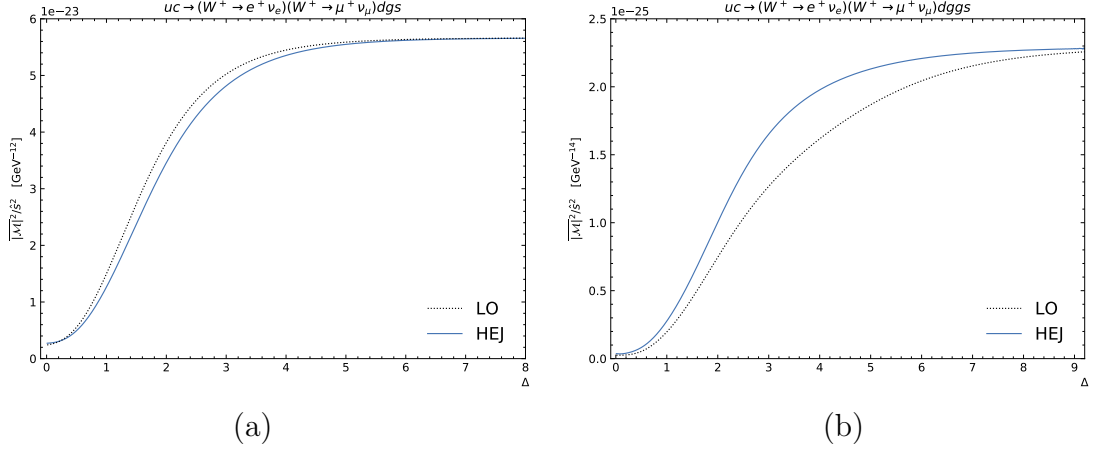


Figure 4.4: Phase space explorer plots for $uc \rightarrow W^+W^+ + n$ jets for (a) 3 jets and (b) 4 jets.

to be $\Delta y_i = y_{i+1} - y_i$. The LL accurate matrix element is then given by

$$\begin{aligned}
& |\mathcal{M}_{qQ \rightarrow W_1^\pm W_2^\pm q'(n-2)gQ'}^{\text{HEJ,reg}}|^2 \\
&= g_s^4 \frac{C_F}{8N_c} (g_s^2 C_A)^{n-2} \\
&\times \left(\frac{|B|^2}{t_1 t_{(n-1)}} \exp(\omega^0(q_{(n-1)\perp}) \Delta y_{n-1}) \prod_{i=1}^{n-2} \frac{-V^2(q_i, q_{(i+1)})}{t_i t_{(i+1)}} \exp(\omega^0(q_{i\perp}) \Delta y_i) \right. \\
&+ \frac{|\tilde{B}|^2}{\tilde{t}_1 \tilde{t}_{(n-1)}} \exp(\omega^0(\tilde{q}_{(n-1)\perp}) \Delta y_{n-1}) \prod_{i=1}^{n-2} \frac{-V^2(\tilde{q}_i, \tilde{q}_{(i+1)})}{\tilde{t}_i \tilde{t}_{(i+1)}} \exp(\omega^0(\tilde{q}_{i\perp}) \Delta y_i) \\
&+ \frac{2\Re\{B\tilde{B}\}}{\sqrt{t_1 \tilde{t}_1} \sqrt{t_{(n-1)} \tilde{t}_{(n-1)}}} \exp(\omega^0(\sqrt{q_{(n-1)\perp} \tilde{q}_{(n-1)\perp}) \Delta y_{n-1}) \\
&\quad \times \left. \prod_{i=1}^{n-2} \frac{-V(q_i, q_{(i+1)}) \cdot V(\tilde{q}_i, \tilde{q}_{(i+1)})}{\sqrt{t_i \tilde{t}_i} \sqrt{t_{(i+1)} \tilde{t}_{(i+1)}}} \exp(\omega^0(\sqrt{q_{i\perp} \tilde{q}_{i\perp}) \Delta y_i) \right), \tag{4.16}
\end{aligned}$$

where V^μ is defined in eq. (3.39). One can immediately check that at $\mathcal{O}(\alpha_W^4 \alpha_s^2)$ this exactly agrees with the summed, averaged and squared amplitude of Eq. (4.13). One can extend this test to higher orders by comparing the result of Eq. (4.16) with the virtual corrections removed (i.e. setting $\omega^0(q_\perp^2) = 0$) at a fixed order in α_s to the corresponding LO result. In the MRK limit, these should match. We illustrate this in figure 4.4 for squared matrix elements for sample channels at $\alpha_W^4 \alpha_s^3$ and $\alpha_W^4 \alpha_s^4$. For the 3 jet final state in figure 4.4(a), we use a

momentum configuration of:

$$\begin{aligned}
p_i &= p_{i;\perp}(\cos(\phi_i), \sin(\phi_i), \sinh(y_i), \cosh(y_i)) \\
p_{d;\perp} &= p_{\ell;\perp} = p_{g;\perp} = 40 \text{ GeV} \\
p_{\nu_\ell;\perp} &= \frac{m_W^2}{2p_{\ell;\perp}(\cosh(y_\ell - y_{\nu_\ell}) - \cos(\phi_\ell - \phi_{\nu_\ell}))} \\
p_{s;\perp} &= -(p_{d;\perp} + p_{e;\perp} + p_{\nu_e;\perp} + p_{\mu;\perp} + p_{\nu_\mu;\perp} + p_{g;\perp}) \\
\phi_d &= 2\pi/3, \quad \phi_e = \pi/4, \quad \phi_\mu = -\pi/2, \\
\phi_{\nu_e} &= -\pi/4, \quad \phi_{\nu_\mu} = +\pi/2, \quad \phi_g = 0.4 \\
y_d &= y_e = y_{\nu_e} = \Delta, \quad y_s = y_\mu = y_{\nu_\mu} = -\Delta, \quad y_g = 0
\end{aligned} \tag{4.17}$$

For the 4 jet final state in figure 4.4(b) we use:

$$\begin{aligned}
p_i &= p_{i;\perp}(\cos(\phi_i), \sin(\phi_i), \sinh(y_i), \cosh(y_i)) \\
p_{d;\perp} &= p_{\ell;\perp} = p_{g_1;\perp} = p_{g_2;\perp} = 40 \text{ GeV} \\
p_{\nu_\ell;\perp} &= \frac{m_W^2}{2p_{\ell;\perp}(\cosh(y_\ell - y_{\nu_\ell}) - \cos(\phi_\ell - \phi_{\nu_\ell}))} \\
p_{s;\perp} &= -(p_{d;\perp} + p_{e;\perp} + p_{\nu_e;\perp} + p_{\mu;\perp} + p_{\nu_\mu;\perp} + p_{g_1;\perp} + p_{g_2;\perp}) \\
\phi_d &= \pi, \quad \phi_e = \pi/4, \quad \phi_\mu = -\pi/2, \quad \phi_{\nu_e} = -\pi/4 \\
\phi_{\nu_\mu} &= +\pi/2, \quad \phi_{g_1} = \pi/2, \quad \phi_{g_2} = -\pi/3 \\
y_d &= y_e = y_{\nu_e} = \Delta, \quad y_s = y_\mu = y_{\nu_\mu} = -\Delta, \quad y_{g_1} = \Delta/3, \quad y_{g_2} = -\Delta/3
\end{aligned} \tag{4.18}$$

The rapidity separation of the quarks and gluons is controlled by the parameter Δ and hence the MRK limit is approached at the right-hand side of the plots. The behaviour seen is not sensitive to the exact values of the transverse momentum or the azimuthal angles. In both plots, we show the squared matrix element divided by \hat{s}^2 , to achieve a finite non-zero value in the MRK limit. The exact **L0** result (black, dotted line) and the approximation within **HEJ** (solid, red line) are very similar throughout the range and converge to the same limiting value at large Δ . The plots also show the rich dynamics of the matrix elements which would be missed at small values of Δ if the limiting value was used throughout phase space.

The LL accurate cross section is then given by the following sum over multiplicities and integration over all phase space (where ℓ_i numbers the four leptons from the

W decays):

$$\begin{aligned}
\sigma_{pp \rightarrow W^\pm W^\pm + 2j}^{\text{LL}} = & \sum_{f^{(A)}, f^{(B)}} \sum_{n=2}^{\infty} \prod_{i=1}^n \left(\int \frac{d^2 \mathbf{p}_{i\perp}}{(2\pi)^3} \int \frac{dy_i}{2} \right) \prod_{l=1}^4 \left(\int \frac{d^2 \mathbf{p}_{l\perp}}{(2\pi)^3} \int \frac{dy_{l_l}}{2} \right) \\
& \times \frac{\left| \mathcal{M}_{qQ \rightarrow W_1^\pm W_2^\pm q' (n-2)gQ'}^{\text{HEJ,reg}} \right|^2}{\hat{s}^2} \\
& \times x_a f^{(A)}(x_a, Q_a) x_b f^{(B)}(x_b, Q_b) (2\pi)^4 \delta^2 \left(\sum_{k=1}^n \mathbf{p}_{k\perp} + \sum_{m=1}^4 \mathbf{p}_{\ell_m\perp} \right) \mathcal{O}_{2j}(\{p_j\}).
\end{aligned} \tag{4.19}$$

We emphasise here that no approximation is made to the phase space being integrated over, only within the matrix element itself. This integral can be efficiently implemented in an exclusive Monte Carlo event generator giving full flexibility to implement experimental cuts and distributions. Before this integration, we first multiply the squared matrix element by reweighting factors to implement fixed-order accuracy, as discussed in the next section.

4.3.1 Matching to Fixed Order

In the previous subsection, we have described how to construct the cross section for $pp \rightarrow W^\pm W^\pm + \geq 2j$ at LL accuracy in \hat{s}/p_t^2 . In order to increase the validity of the approach, we will supplement this with subleading terms which will provide leading-order accuracy at each order in α_s , up to the point where this is computationally feasible. For this process, in this study, that is samples with 2, 3, 4, 5 and 6 jets at LO. We observe that the impact of adding higher multiplicity fixed-order samples decreases with each multiplicity, and in particular that the 6-jet sample has at most a few percent effect in any distribution so we are confident that our results have converged.

The matching is then implemented using the methods of HEJ2 [79] which reorganises the integral over phase space to supplement fixed-order samples at each order with real and virtual corrections such that leading-logarithmic accuracy is maintained at all orders in α_s and additionally leading-order accuracy is achieved for the n -jet components for $n = 2-6$. The fixed-order input is given as Les Houches events and can be taken from any generator. In this study we have used Sherpa [65] to generate the fixed-order input.

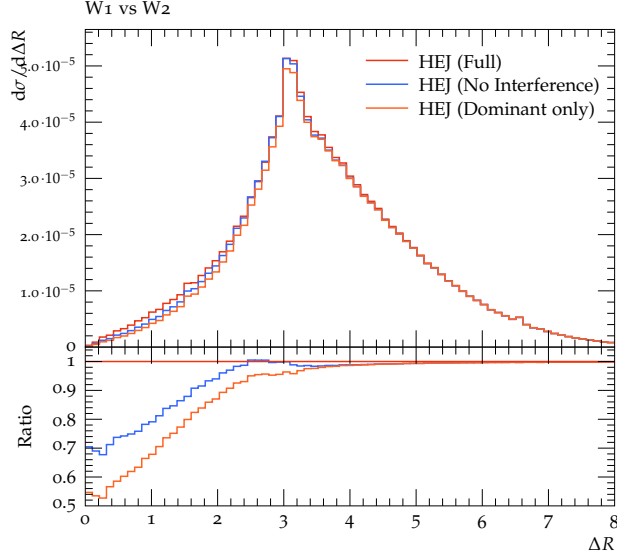


Figure 4.5: Plot of cross section versus ΔR for $pp \rightarrow W^+W^+ + 2j$ using an example experimental setup. In red is the full HEJ amplitude, in blue the interference term from exchanging the two W bosons have been removed and in orange, the subdominant WW configuration is removed.

Finally, we rescale all the final HEJ2 predictions to match the total cross section to the inclusive NLO cross section for each scale choice. However, for the setup described in section 4.4, and as discussed there, this turns out to have a negligible impact in this case.

4.3.2 Impact of interference terms

One immediate question is whether or not we actually need to include the full contribution from swapping the two W bosons from their generated configuration and from the interference between the two configurations, i.e. do we need to include all three of the terms in the brackets in eq. (4.16) in order to obtain a reasonable prediction. Figure 4.5 shows the effect of including these three terms when looking at the difference in R between the two W bosons. In red is the full HEJ amplitude including all three terms, in blue the interference term from exchanging the two W bosons have been removed and in orange, the subdominant WW configuration is removed. From this we see that for regions of phase space with low ΔR we lose as much as 30% in some of the bins from the full HEJ prediction by removing the interference term. Removing the subdominant configuration reduces the HEJ prediction by up to 50%. This makes sense, as for some regions of phase space, where the W 's are close together, the contribution

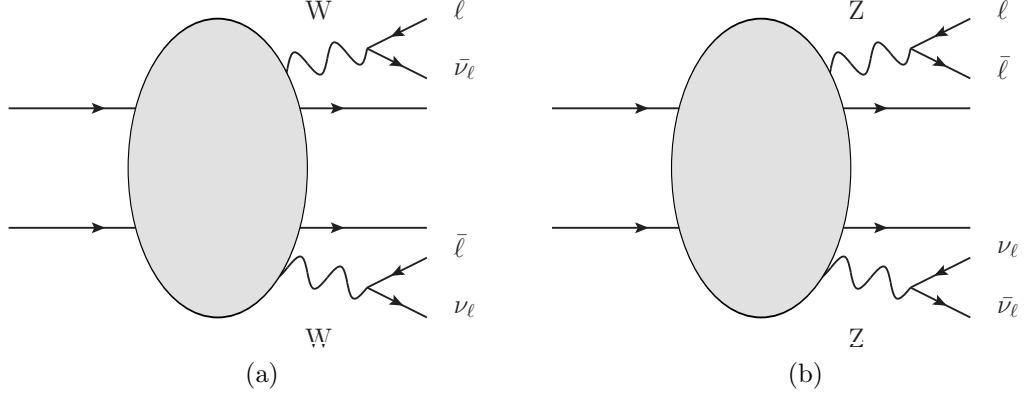


Figure 4.6: Two processes contributing to the amplitude $pp \rightarrow jj\ell\bar{\ell}\nu_\ell\bar{\nu}_\ell$, involving (a) W^+W^- bosons (b) ZZ bosons.

swapping the two bosons will be around half of the full prediction. For this reason, we include the full contribution from swapping the W bosons, including interference, in the HEJ2 amplitude.

4.3.3 A comment on opposite-sign WW production

A natural question then, is can we extend this description to events with two W bosons of different sign?

The problem is that at order $O(\alpha_w^2\alpha_s^2)$ there can be contributions from opposite-sign WW events and from ZZ events, shown in fig. 4.6. In contrast, ZZ events do not contribute at all to the amplitude for same-sign WW events at the same order. We also have events where two W bosons are emitted from the same quark leg. This makes opposite-sign WW more complicated as you necessarily have to also study ZZ production. Therefore, we restricted the scope of this work to solely include descriptions of same-sign WW events. However, the framework for resumming the QCD logarithms is expected to be very similar, so there is no conceptual reason why we couldn't look at this process in the future.

4.4 Impact of Leading-Logarithm corrections

We will now show the predictions constructed and matched as described in the previous section for observables commonly studied at the LHC for the process

$pp \rightarrow W^\pm W^\pm + \geq 2j$, where one W^\pm decays in the electron channel and one in the muon channel. We will compare these with an NLO calculation of the same process (here taken from Sherpa [65] using COMIX [80] with the extension of OpenLoops [81]) to assess the impact of the new LL corrections. Also included for comparison is a calculation including MC@NLO matching [82] with the shower generator CS Shower [83] packaged with Sherpa. We use the NNPDF3.0 NLO PDF set [84] as provided by LHAPDF6 [85]. We choose the central factorisation and renormalisation scale as the geometric mean of the transverse momenta of the two leading jets, $\mu_F = \mu_R = \sqrt{p_{\perp;j_1} p_{\perp;j_2}}$. These scales are varied independently by a factor of two around this central value, with the constraint that their ratio is kept between 0.5 and 2. The uncertainty bands shown in the plots are obtained from the envelope of these variations.

In figures 4.9–4.13 we show distributions measured in a recent CMS analysis [27]. It is not meaningful to compare to the data points in that study as these include the large $\mathcal{O}(\alpha_W^4)$ contributions. The cuts applied to the predictions are listed in Table 4.1. Those in the first group form the inclusive cuts which are applied to all plots. The additional three criteria (below the second horizontal line) give the extra cuts on leading dijet invariant mass, leading jet pseudorapidity separation and the Zeppenfeld variable [86]

$$z_l = \frac{\eta_l - \frac{1}{2}(\eta_{j_1} + \eta_{j_2})}{|\eta_{j_1} - \eta_{j_2}|}, \quad (4.20)$$

where j_1 and j_2 are the two hardest jets in the event. These cuts are used to try to suppress the QCD contribution to this process. We will refer to them as “VBS cuts” and will show results before and after these extra criteria. The output of HEJ is exclusive in the momenta of all outgoing particles. Here we have used the functionality of linking HEJ directly with Rivet[87] to apply the cuts and fill the histograms.

Before discussing the distributions, we give the cross sections obtained at NLO, with MC@NLO and with HEJ2 before and after the application of VBS cuts in Table 4.2 for the central scale choice above. Both before and after VBS cuts the values are remarkably similar for the central value of the renormalisation and factorisation scales. This is a marked difference to other processes where similar cuts have been applied. For example in $pp \rightarrow H + \geq 2j$ despite relative agreement at the inclusive level, the HEJ2 predictions were significantly more suppressed by VBF cuts than those at NLO (by about a factor of 2) [69]. This result is sensitive

Variable	Selection Cut
Lepton pseudorapidity	$ \eta_l < 2.5$
Jet pseudorapidity	$ \eta_j < 4.7$
Leading/subleading lepton p_T	$p_T > 25/20$ GeV
Missing transverse momentum	$E_T^{\text{miss}} > 30$ GeV
Jet p_T	$p_T > 50$ GeV
Lepton isolation	$\Delta R(l, \text{jet}) > 0.4$ o/w jet is removed
Di-lepton mass	$m_{ll} > 20$ GeV
Di-lepton mass restriction	$ m_{ll} - m_Z > 15$ GeV
Di-jet mass	$m_{j_1 j_2} > 500$ GeV
Jet rapidity separation	$ \Delta\eta_{j_1 j_2} > 2.5$
Max lepton Zeppenfeld variable (Eq. 4.20)	$\max(z_l) < 0.75$

Table 4.1: The selection cuts used in the analysis where the lepton cuts apply only to the charged leptons. The last three rows define the additional VBS cuts.

Cross Section (fb)	<i>without</i> VBS cuts, σ_{incl}	<i>with</i> VBS cuts, σ_{VBS}	$\sigma_{\text{VBS}}/\sigma_{\text{incl}}$
HEJ2 W^+W^+	1.428 ± 0.002	0.1219 ± 0.0004	0.0854 ± 0.0003
NLO W^+W^+	1.41 ± 0.05	0.12 ± 0.07	0.08 ± 0.02
MC@NLO W^+W^+	1.285 ± 0.003	0.1033 ± 0.0006	0.0804 ± 0.0005
HEJ2 W^-W^-	0.6586 ± 0.0003	0.0402 ± 0.0001	0.0610 ± 0.0002
NLO W^-W^-	0.68 ± 0.02	0.04 ± 0.01	0.06 ± 0.02
MC@NLO W^-W^-	0.6186 ± 0.0004	0.0371 ± 0.0002	0.0600 ± 0.0002

Table 4.2: This table gives the total cross section calculated with the new HEJ2 LO + LL predictions in this paper compared to the result at NLO accuracy, both before and after the VBS cuts given in the text.

to the scale choice; in the window of variations we studied, the ratio between the HEJ2 and NLO cross sections varies by as much as 22% in either direction. It is also clear from the distributions that follow that this agreement is not flat in phase space (even for the central scale choice), but arises from different regions where the HEJ2 result is greater and less than NLO. In figure 4.7, we show the exclusive jet rates. For only the inclusive selection criteria, we see a steady decrease at each multiplicity, but in the HEJ2 predictions the 4-, 5- and 6-jet rates remain at 21%, 6% and 2% of the exclusive 2-jet rate respectively. After VBS cuts, the relative importance of the higher multiplicity rates in the HEJ2 predictions is enhanced with the 2-jet and 3-jet rates being very similar and the 4-, 5- and 6-jet rates now increasing to 40%, 13% and 3% of the exclusive 2-jet rate respectively. In the NLO sample after VBS cuts, the 3-jet rate is a third larger than the 2-jet rate for the central scale choice. The scale variation bands here are very large; however, for any one choice the 3-jet was always comparable to or greater than the 2-jet rate. This is already one measure of the importance of the higher-order corrections in

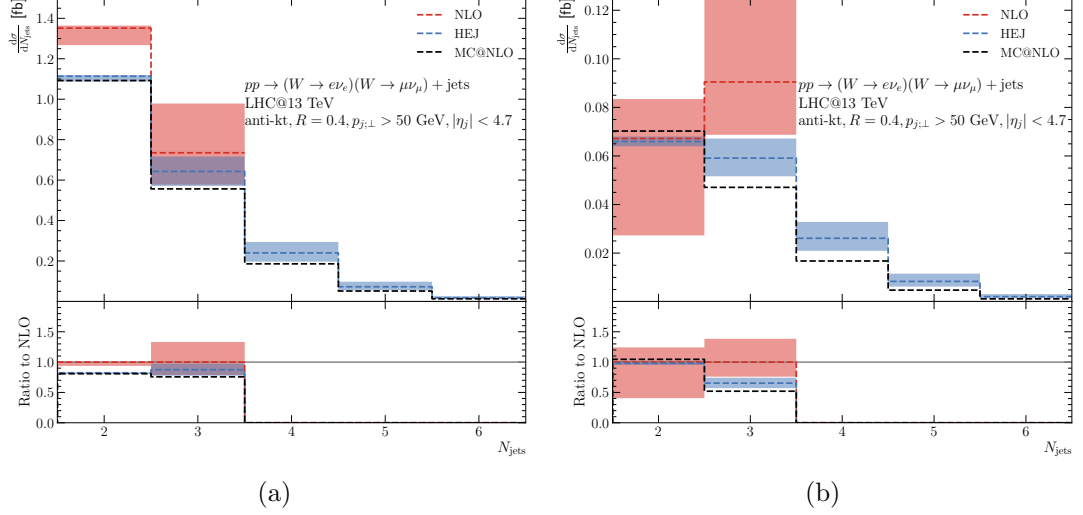


Figure 4.7: Exclusive jet rates for $pp \rightarrow W^\pm W^\pm + \geq 2j$, (a) without and (b) with additional VBS cuts. In this figure and the remaining figures in this chapter, the bands shown are scale variation bands obtained from varying the renormalisation and factorisation scales around the central value.

α_s (i.e. α_s^4 and above). The MC@NLO predictions show that the effect of adding a parton shower to the NLO predictions is to distribute the 3-jet component among the higher jet-rate bins. The large contribution to the cross section from events with three or more jets suggests that additional jet vetoes could be used to further suppress the relative QCD contribution to $pp \rightarrow VV + 2j$.

The jet rate plots are affected by the lepton isolation cut (see table 4.1). Any jet which satisfies $\Delta R(l, \text{jet}) < 0.4$ for any charged lepton is removed from the event, but the event is still kept provided there are at least two further jets. This means that events which arise from a theoretical calculation with e.g. 4 jets can appear in the plot in the 2-jet or 3-jet bin. For comparison, we show the equivalent plots from HEJ2 without lepton isolation applied in fig. 4.8. The differences with only inclusive cuts are modest, with a slight decrease in the first bin and slight increases in the higher bins. After VBS cuts, the effect is more pronounced. The 3-jet rate is now slightly above the 2-jet rate and there is then a bigger step down to the 4, 5 and 6 jet rates which have each risen slightly from the values after lepton isolation cuts. They are now 47%, 16% and 4% respectively of the exclusive 2-jet rate compared to 40%, 13% and 3% after the lepton isolation cut is applied.

Figure 4.9 shows the comparison for the difference in pseudorapidity between

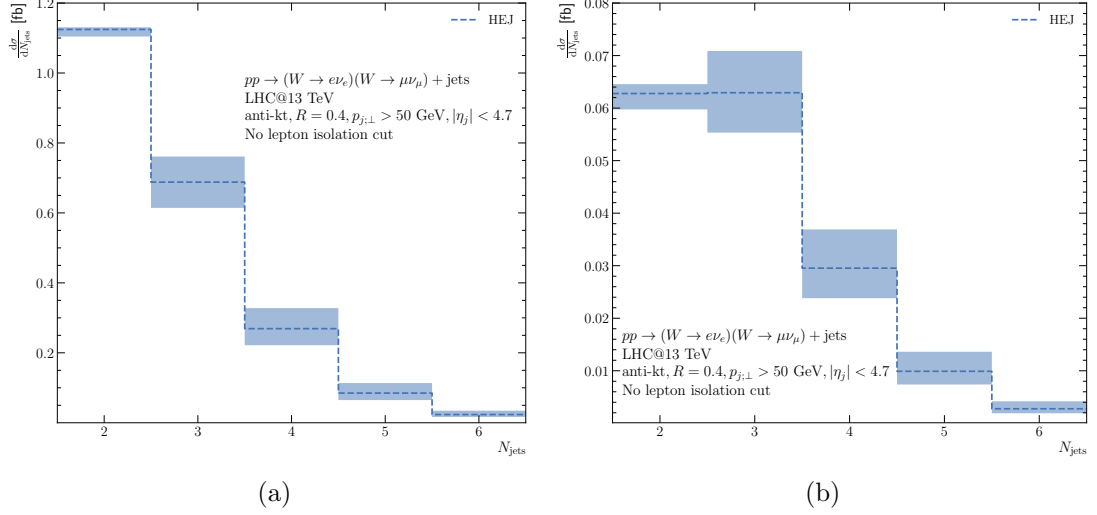


Figure 4.8: Exclusive jet rates for $pp \rightarrow W^\pm W^\pm + \geq 2j$ where the jet isolation cut has been removed, (a) without and (b) with additional VBS cuts.

the two leading jets¹. Here we see only modest differences in shape between the two descriptions which are slightly enhanced once VBS cuts are applied in the right-hand plot. However, any differences lie mostly within the scale variation bands. Here, and in the remaining distributions, we observe only a small impact of adding a parton shower to the pure NLO calculation, with no significant changes in shapes of distributions.

Figure 4.10 exhibits greater differences in shape in the distribution of the transverse momentum of the leading jet. For the inclusive cuts in (a), the HEJ2 prediction starts much lower than the NLO prediction but increases with respect to it until the predictions cross around 200 GeV. Above this value the prediction from HEJ2 falls more slowly leading to a prediction of a harder spectrum in $p_{j1,\perp}$. A very similar behaviour is seen in (b) after the application of VBS cuts. This distribution clearly emphasises that the close agreement of the total cross section values is a coincidence of the experimental setup used. If the transverse momentum requirement of the jets had been larger, the HEJ2 cross section would have also been correspondingly larger than that from NLO.

Similarly, in figure 4.11 we see that the HEJ2 and NLO predictions for the invariant mass distribution of the two leading jets have a different shape with a ratio which increases steadily from 0.5 at $m_{j1j2} = 0$ GeV to 1.4 by $m_{j1j2} = 2$ TeV where it

¹We use pseudorapidity to match the convention in the Ref. [27]. In practice, there is little difference in NLO and HEJ2 predictions when one chooses to use rapidity or pseudorapidity as the parton multiplicity within a jet is relatively low in each case.

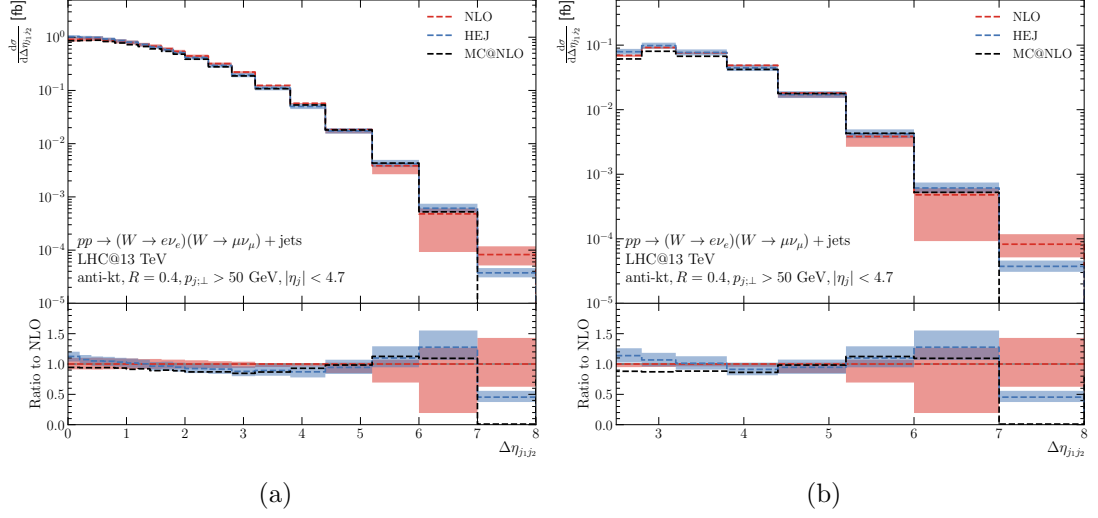


Figure 4.9: The differential distribution in the pseudorapidity separation of the two leading jets in $pp \rightarrow W^\pm W^\pm + \geq 2j$, (a) without and (b) with additional VBS cuts.

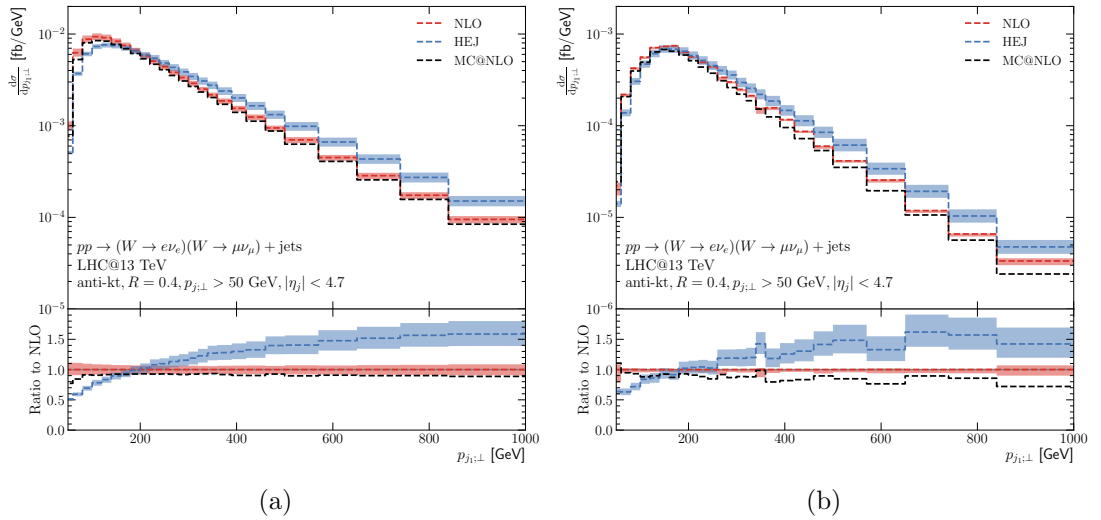


Figure 4.10: The differential distribution in the transverse momentum of the hardest jet in $pp \rightarrow W^\pm W^\pm + \geq 2j$, (a) without and (b) with additional VBS cuts.

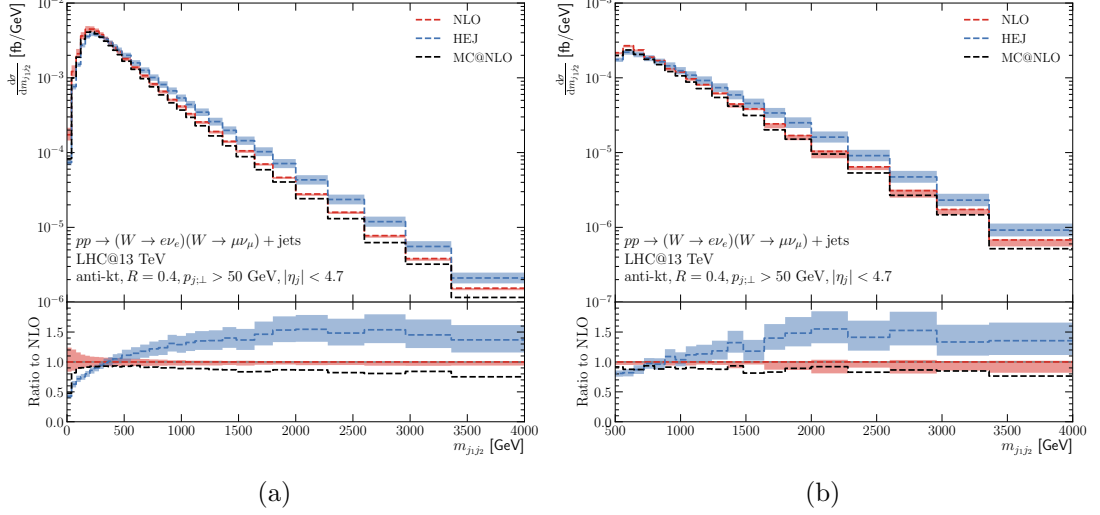


Figure 4.11: The differential distribution in the invariant mass of the two leading jets in $pp \rightarrow W^\pm W^\pm + \geq 2j$, (a) without and (b) with additional VBS cuts.

roughly plateaus. A similar effect is seen after VBS cuts are imposed, although of course here the lower region has been removed. The point where the predictions cross has moved to a slightly higher value of $m_{j_1 j_2}$ as a result of the cuts on the other variables which form part of the VBS cuts.

In figure 4.12, we show the distributions in the invariant mass of the two charged leptons from the decays of the W bosons. This is related to the invariant mass of the jets if one considers event topologies where the W bosons follow the direction of the associated quark lines. For modest transverse momenta, the invariant mass between particles is driven by their rapidity difference. The leptons, though, are required to be more central than the jets and we see more modest differences between the NLO and HEJ2 predictions.

The final distribution we show in this section is the Zeppenfeld variable z_e of the electron, defined in Eq. (4.20). This measures the relative position of the electron in these events with respect to the jet system. Both before and after VBS cuts, the predictions from NLO and from HEJ2 are in very close agreement, and the ratio between the two remains largely flat throughout the region showing that this variable is largely insensitive to the logarithmic corrections at higher orders in α_s .

In this section, we have compared the new predictions for $pp \rightarrow e^\pm \nu_e \mu^\pm \nu_\mu + \geq 2j$ available in HEJ2 (which include the leading logarithmic corrections in \hat{s}/p_\perp^2 at all orders in α_s) with those obtained at next-to-leading order in QCD. We have

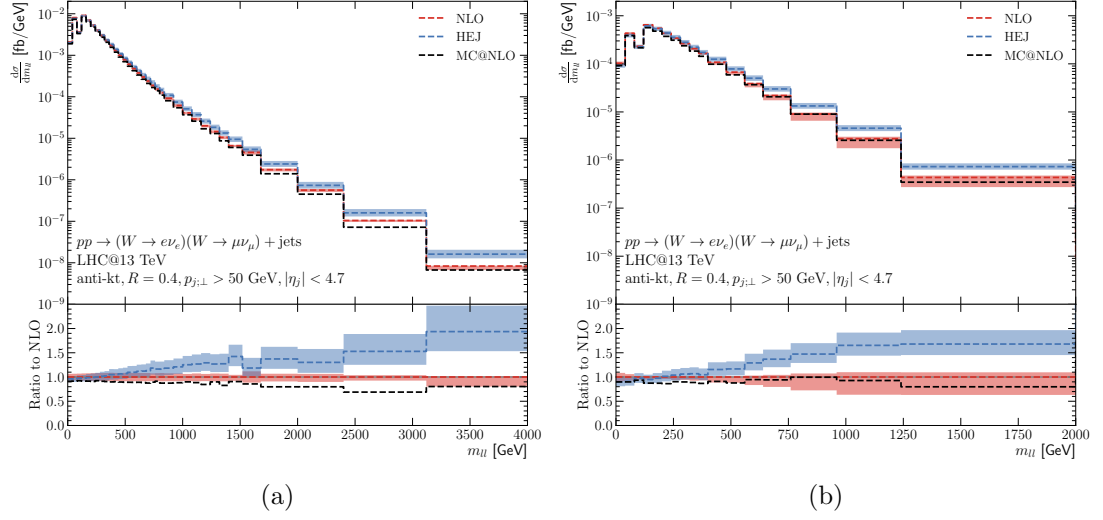


Figure 4.12: The differential distribution in the invariant mass of the two charged leptons in $pp \rightarrow W^\pm W^\pm + \geq 2j$, (a) without and (b) with additional VBS cuts.

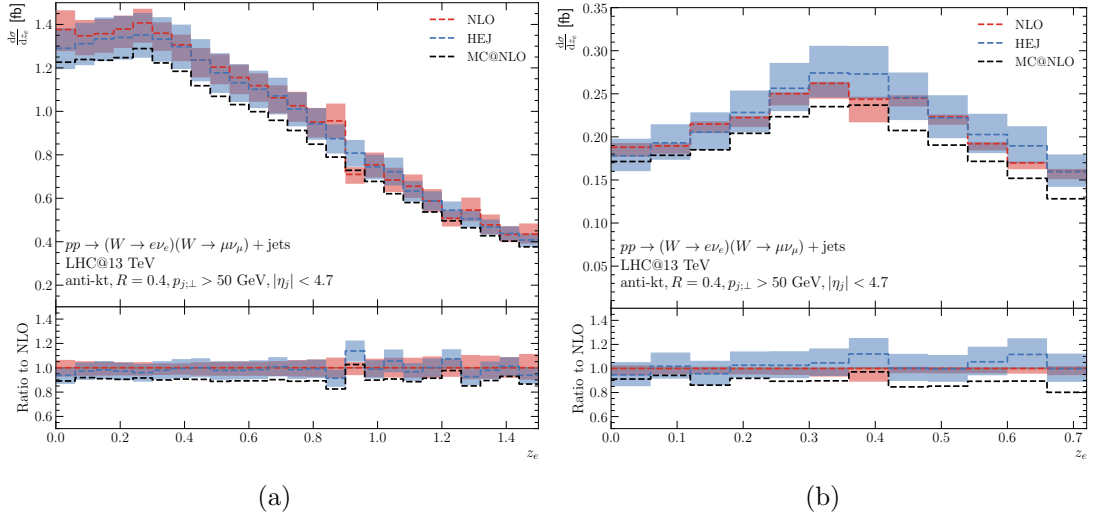


Figure 4.13: The differential distribution in the Zeppenfeld variable for the electron in $pp \rightarrow W^\pm W^\pm + \geq 2j$, without and with additional VBS cuts.

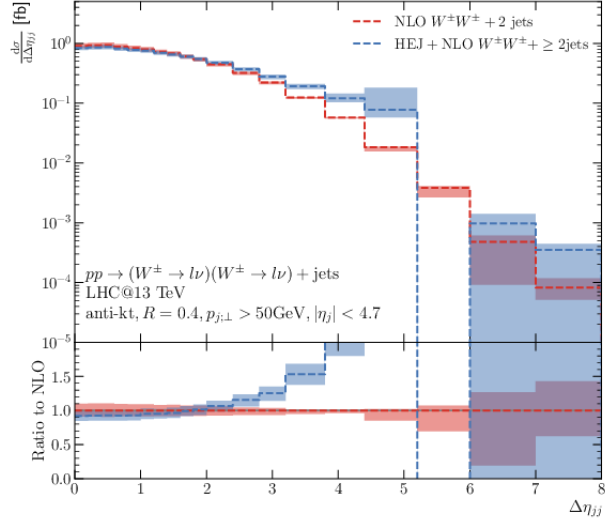
seen close agreement in the total cross sections obtained in the two approaches at the central scale choice, but a study of distributions in $p_{j1;\perp}$, m_{j1j2} and m_{ll} show large differences in shape which make this agreement appear to be a coincidence of the specific values chosen in the experimental cuts.

4.5 Impact of NLO matching

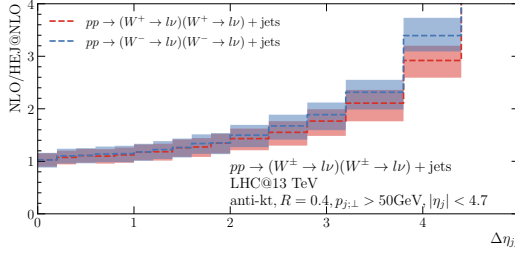
We will now go on to briefly discuss the impact of the including full NLO accuracy bin-by-bin in the HEJ LL prediction through NLO matching. The procedure is the same as in section 3.4 and was first published in reference [10]. In this section we will also compare the reweighting factors obtained here versus those included in that study.

In practice, the W^+W^+ and W^-W^- contributions were matched to NLO separately but we found little difference between the two, so here only the combined result is presented for each distribution, however both lines are included in the plots of the reweighting factors. Presented in figs. 4.14, 4.16, 4.18 and 4.20 are the NLO matched HEJ predictions compared to pure NLO for various kinematic observables of experimental interest. Included for each distribution is a plot of the reweighting factors, $\frac{\sigma_{2\text{-jet}}^{\text{NLO}}}{\sigma_{2\text{-jet}}^{\text{HEJ@NLO}}}$ and $\frac{\sigma_{2\text{-jet}}^{\text{HEJ}}}{\sigma_{2\text{-jet}}^{\text{HEJ@NLO}}}$ to make clear the differences between full NLO, HEJ@NLO and LL.

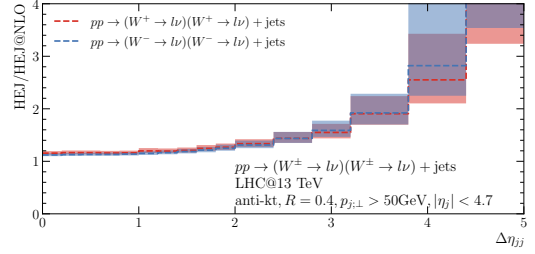
Firstly, let us look at the matching for the dijet (pseudo-)rapidity separation shown in fig. 4.14 and fig. 4.15. Looking at the NLO matched HEJ prediction, we see that the result becomes very unstable beyond 5 units of rapidity, and diverges from the NLO result. The reasons for this can be deduced from the plots of the ratios $\frac{\sigma_{2\text{-jet}}^{\text{NLO}}}{\sigma_{2\text{-jet}}^{\text{HEJ@NLO}}}$ and $\frac{\sigma_{2\text{-jet}}^{\text{HEJ}}}{\sigma_{2\text{-jet}}^{\text{HEJ@NLO}}}$. Looking at the first of these, we see that the ratio grows rapidly as a function of rapidity separation. There are a few reasons contributing to why this is the case, some of which we explain in more detail in chapter 6. Whilst there are shared components between NLO and HEJ@NLO calculations, they differ in both the treatment of the poles in the virtual corrections and the real-collinear pieces. We also have to question to validity of the factorised approach to describing the matrix element when the W boson is close to the opposite quark/gluon line meaning that we no longer have distinct forward and backwards pieces. This poses a problem for the NLO matching procedure as the rapidity separation gets very large, but we expect that this will be solved once a full treatment of NLL corrections (including impact factors) is included in HEJ2. In the



(a)



(b)



(c)

Figure 4.14: The (a) differential distribution in the pseudorapidity separation of the two leading jets in $pp \rightarrow W^\pm W^\pm + \geq 2j$ without additional VBS cuts. The HEJ result here has been matched to NLO using the procedure outlined in section 3.4. (b) ratio $\frac{\sigma_{2\text{-jet}}^{\text{NLO}}}{\sigma_{2\text{-jet}}^{\text{HEJ@NLO}}}$ and (c) ratio $\frac{\sigma_{2\text{-jet}}^{\text{HEJ}}}{\sigma_{2\text{-jet}}^{\text{HEJ@NLO}}}$

HEJ prediction, we also only generate additional emissions with rapidity between the forward and backwards jets, which is not the case for the NLO prediction which can have a large impact depending on the phase space region.

Such corrections we predict will be important in improving the description this observable. Looking at the ratio $\frac{\sigma_{2\text{-jet}}^{\text{HEJ}}}{\sigma_{2\text{-jet}}^{\text{HEJ@NLO}}}$, shows that the higher order log corrections contribute significantly, meaning that the best prediction relies on both NLO and LL corrections. This is a similar conclusion to what was seen in the single W study shown in fig. 4.15 which is a good example of the universality of QCD.

Secondly, we look at the transverse momentum of the leading jet in the event. Figure 4.16 shows the differential distribution after the NLO matching alongside the reweighting factors. In previous studies, the observable $p_{1,\perp}$ has not shown

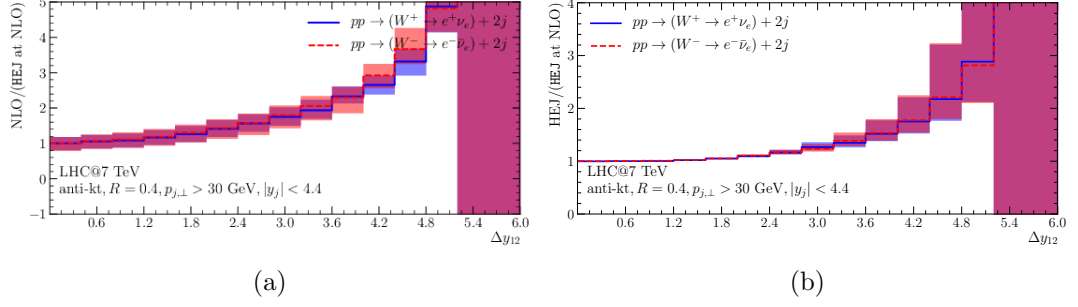
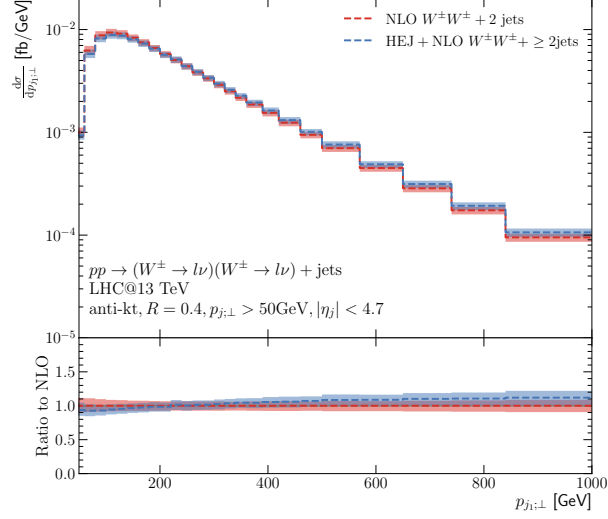


Figure 4.15: Reweighting factors for dijet rapidity separation in single W plus jets production, taken from reference² [10]

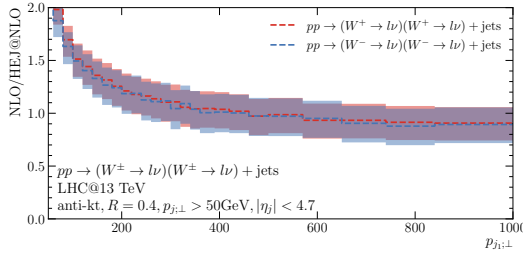
strong dependence on higher order corrections from high energy logarithms, and is thus described well at next-to-leading order. We can see this explicitly in fig. 4.16c where the ratio which probes the effects of higher order HEJ corrections, $\frac{\sigma_{2\text{-jet}}^{\text{HEJ}}}{\sigma_{2\text{-jet}}^{\text{HEJ@NLO}}}$, rises very slowly as a function of $p_{1;\perp}$. This leads to a HEJ matched prediction which is very similar to the NLO prediction in fig. 4.16a, with the ratio between the two being almost flat. Compare this to the equivalent plot in the single W study, fig. 4.17b, where the ratio is also flat but falls as p_{\perp} increases rather than increasing slightly. This could be due to a number of factors - for the single W study, the centre of mass energy is lower at 7 TeV compared to 13 TeV in the WW study and the selection cuts are different between the two studies. Also the single W study includes subleading corrections described in section 5.3. The ratio of $\frac{\sigma_{2\text{-jet}}^{\text{NLO}}}{\sigma_{2\text{-jet}}^{\text{HEJ@NLO}}}$ is very similar between the two studies (figs. 4.16b and 4.17a) with the ratio starting large at low $p_{1;\perp}$ before falling and flattening out for larger $p_{1;\perp}$, indicating the biggest differences between the two predictions is in the region of phase space where the jets are close the jet cut.

Figure 4.18 shows the effect of NLO matching on the HEJ predictions for the cross section as a function of dijet invariant mass. Here there is still a clear difference between the HEJ and NLO predictions, with the HEJ line ending up roughly 50% larger than NLO at large m_{jj} . Looking at the $\frac{\sigma_{2\text{-jet}}^{\text{HEJ}}}{\sigma_{2\text{-jet}}^{\text{HEJ@NLO}}}$ reweighting factor in fig. 4.18c, we can see that there is a large impact from including contributions from higher order logarithms when m_{jj} gets large.

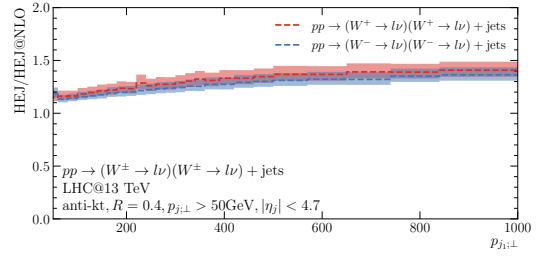
Finally we look at the invariant mass between the two charged leptons shown in fig. 4.20. This distribution requires at least two charged leptons so cannot compare to single W results here. What we see from the ratio factor in fig. 4.20b is that this observable is similar to the p_{\perp} observable in that it is less dependent on the higher order logs than the rapidity observables and dijet invariant mass.



(a)

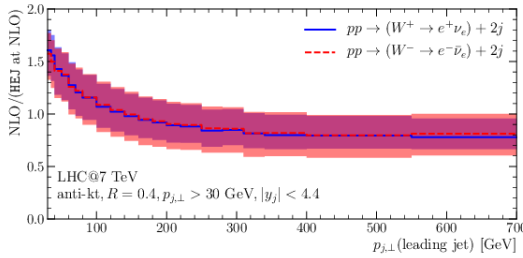


(b)

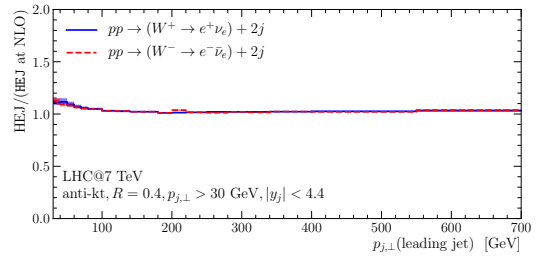


(c)

Figure 4.16: The (a) differential distribution in the hardest jet transverse momentum in $pp \rightarrow W^\pm W^\pm + \geq 2j$ without additional VBS cuts. The HEJ result here has been matched to NLO using the procedure outlined in section 3.4. (b) ratio $\frac{\sigma_{2\text{-jet}}^{\text{NLO}}}{\sigma_{2\text{-jet}}^{\text{HEJ@NLO}}}$ and (c) ratio $\frac{\sigma_{2\text{-jet}}^{\text{HEJ}}}{\sigma_{2\text{-jet}}^{\text{HEJ@NLO}}}$

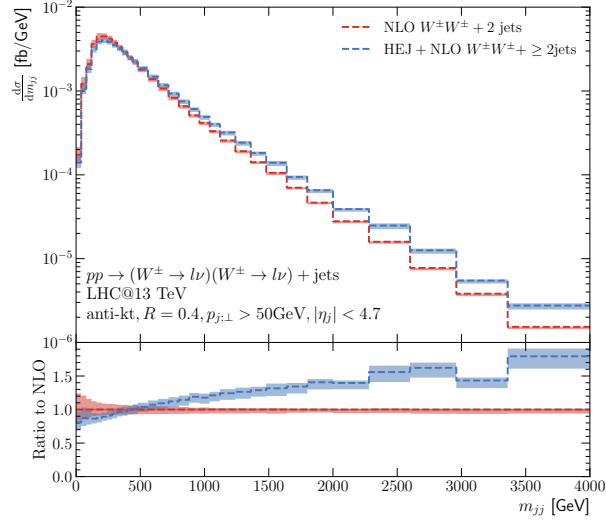


(a)

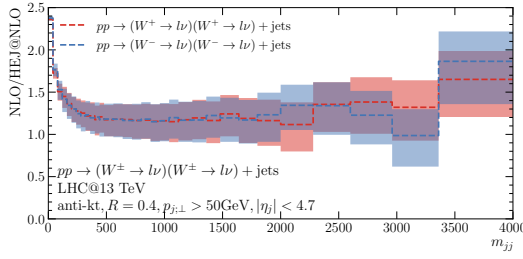


(b)

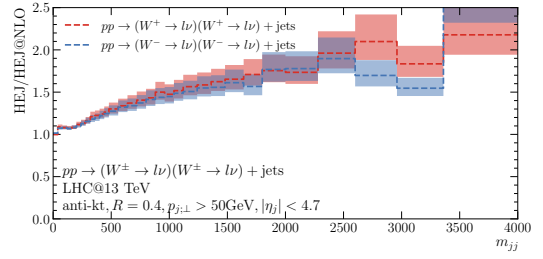
Figure 4.17: Reweighting factors for hardest jet transverse momentum in single W plus jets production, taken from reference² [10]



(a)



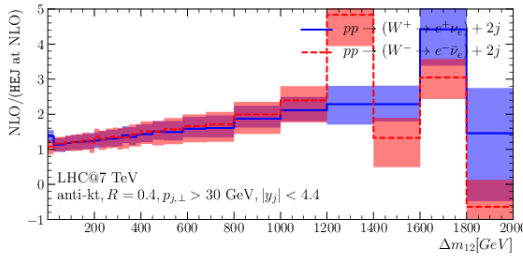
(b)



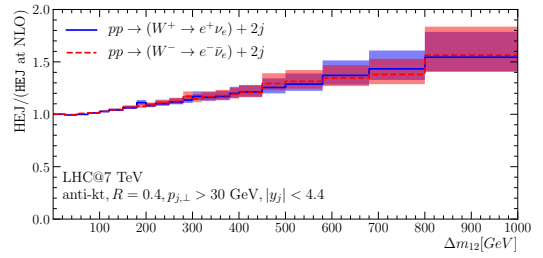
(c)

Figure 4.18: The (a) differential distribution in the dijet invariant mass of the two leading jets in $pp \rightarrow W^\pm W^\pm + \geq 2j$ without additional VBS cuts. The HEJ result here has been matched to NLO using the procedure outlined in section 3.4.

(b) ratio $\frac{\sigma_{2\text{-jet}}^{\text{NLO}}}{\sigma_{2\text{-jet}}^{\text{HEJ@NLO}}}$ and (c) ratio $\frac{\sigma_{2\text{-jet}}^{\text{HEJ}}}{\sigma_{2\text{-jet}}^{\text{HEJ@NLO}}}$

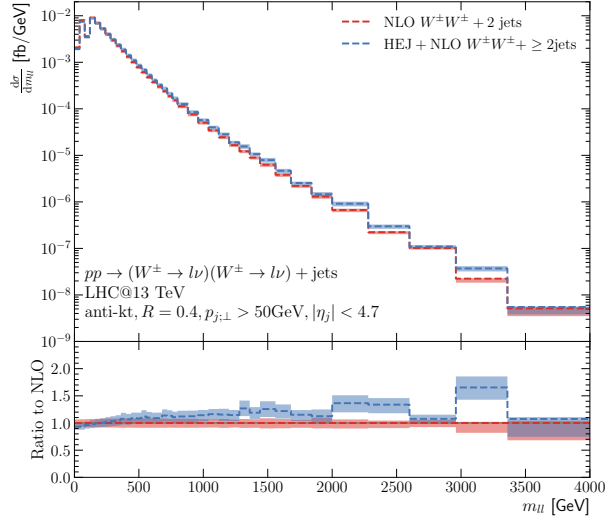


(a)

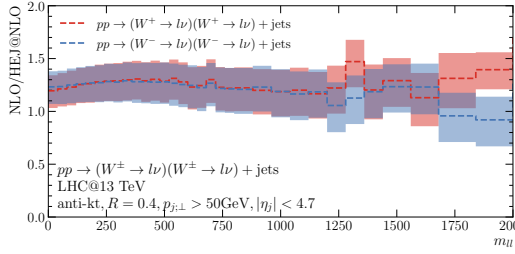


(b)

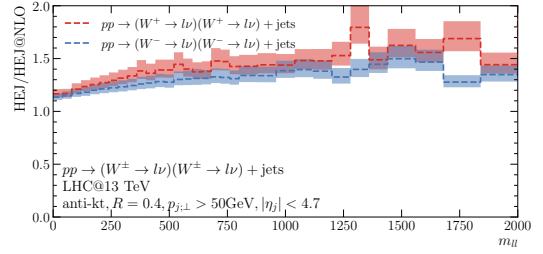
Figure 4.19: Reweighting factors for dijet invariant mass in single W plus jets production, taken from reference² [10]



(a)



(b)



(c)

Figure 4.20: The (a) differential distribution in the invariant mass of the two charged leptons in $pp \rightarrow W^\pm W^\pm + \geq 2j$ without additional VBS cuts. The HEJ result here has been matched to NLO using the procedure outlined in section 3.4. (b) ratio $\frac{\sigma_{2\text{-jet}}^{\text{NLO}}}{\sigma_{2\text{-jet}}^{\text{HEJ@NLO}}}$ and (c) ratio $\frac{\sigma_{2\text{-jet}}^{\text{HEJ}}}{\sigma_{2\text{-jet}}^{\text{HEJ@NLO}}}$

This leads to a matched HEJ prediction in fig. 4.20a which is very similar to next-to-leading order and it is expected that these results will both be close to data.

What is clear from looking directly at a leptonic observable in figs. 4.20b and 4.20c is that there is a slight charge asymmetry between the final states that we don't see in the jet based observables. As the treatment of the charged leptons is the same in HEJ2 for each charge, it is expected that this is directly an effect from the differing PDFs for the allowed channels in each case.

²Note that the HEJ/HEJ@NLO ratio plots did not appear in the citation, but were included as part of the study.

4.6 Conclusions and future work

In this chapter, we have presented the first calculation of all leading logarithmic contributions which scale as $\alpha_W^4 \alpha_s^{k+2} \log^k(\hat{s}/p_t^2)$ to the production of a same-sign W -pair which decays leptonically, i.e. the QCD contribution to the process $pp \rightarrow e^\pm \nu_e \mu^\pm \nu_\mu + \geq 2j$. In order to separate the electroweak and QCD contributions to this process, so-called VBS cuts are usually applied to require large invariant mass and rapidity separation of the tagging jets. These cuts exactly select regions of phase space where the logarithms above become important. To assess their impact in $pp \rightarrow e^\pm \nu_e \mu^\pm \nu_\mu + \geq 2j$, we have compared our new predictions to those obtained at NLO within the experimental setup of a recent 13 TeV CMS analysis.

We have found that the HEJ2 cross section is very close to the NLO prediction both for inclusive cuts, and after VBS cuts have been applied. However, it is clear from the distributions that this agreement arises from cancellations across phase space rather than being true throughout. The distributions in transverse momentum of the leading jet in figure 4.10, in invariant mass of the leading jets in figure 4.11 and in invariant mass of the charged leptons in figure 4.12 show clear differences in shape with differences of up to 50% between HEJ2 and NLO. There are other distributions, $\Delta\eta_{j_1 j_2}$ and z_e where the two sets of predictions show close agreement, indicating that these distributions are more stable with respect to higher-order logarithmic corrections.

Previous studies of this process have seen that the 3-jet component is significant in typical experimental analyses, enhanced within VBS cuts. We also find this, and that it extends beyond 3-jets. The exclusive jet components within HEJ2 are matched to leading-order accuracy for 2–6 jets. We showed in figure 4.7 that the VBS cuts do indeed increase the significance of the 3–6-jet components relative to the 2-jet component. The contribution from 3-jets is similar to 2-jet in HEJ2 and greater than the 2-jet at NLO. The 4–6-jet components steadily decrease but such that the 6-jet components still contributed at the order of a few percent in some distributions.

We also isolated the effects of higher order corrections from next-to-leading order corrections by using a matching procedure to match HEJ2 to NLO. By doing this we showed we can reproduce the NLO behaviour well in observables where the higher order corrections beyond next-to-leading order have a small effect on the distributions (p_\perp and leptonic observables), but highlight the importance of these

corrections in other observables (rapidity observables and dijet invariant masses).

We therefore conclude that logarithmic corrections of the form $\alpha_W^4 \alpha_s^{k+2} \log^k(\hat{s}/p_t^2)$ are numerically significant at the 13 TeV LHC, and should be included in accurate modelling of the QCD background to vector boson scattering.

Chapter 5

High Energy predictions for QCD jets at LHC: A study with ATLAS R_{32} team

This chapter includes the first of two LHC studies involving HEJ and ATLAS, looking at the quantity R_{32} vs various observables of experimental interest. We discuss here the motivation behind doing this study, the theoretical and computational tools that went into making the HEJ predictions, and finally a comparison to data and other Monte-Carlo predictions.

5.1 Measurements of experimental interest

5.1.1 The quantity R_{32}

We define R_{32} as the ratio of the 3-jet inclusive cross section to the 2-jet inclusive cross section:

$$R_{32} = \frac{\sigma_{3j}^{\text{inc}}}{\sigma_{2j}^{\text{inc}}}. \quad (5.1)$$

Whilst this quantity makes sense to define for an inclusive prediction (e.g. HEJ or using a multijet merged sample), one question that can immediately be asked is how this quantity is defined at fixed order in α_s ? The simplest approximation one can make is to calculate both the 2-jet cross section, σ_{2j}^{exc} , and 3-jet cross

process	known	desired
$pp \rightarrow 2 \text{ jets}$	NNLO _{QCD}	
	NLO _{QCD} + NLO _{EW}	
$pp \rightarrow 3 \text{ jets}$	NLO _{QCD} + NLO _{EW}	NNLO _{QCD}

Table 5.1: Precision wish list for jet final states, taken from the 2019 Les Houches Standard Model Working Group Report [12]

section, σ_{3j}^{exc} , to leading order in α_s and then take the ratio of the two,

$$R_{32}^{\text{LO}} = \frac{\sigma_{3j}^{\text{exc}}}{\sigma_{2j}^{\text{exc}}}. \quad (5.2)$$

This is useful as a first approximation but as we will see, this approximation can end up giving very different results from the NLO results or the all-orders resummed results. The second approximation we will make is to perform the two jet calculation of the cross section at next-to-leading order, σ_{2j}^{NLO} , which will let us calculate the ratio,

$$R_{32}^{\text{LO/NLO}} = \frac{\sigma_{3j}^{\text{exc}}}{\sigma_{2j}^{\text{NLO}}}. \quad (5.3)$$

Finally we will also compare fixed order results with the three jet cross section calculation also performed at next-to-leading order. This will let us calculate the ratio,

$$R_{32}^{\text{NLO}} = \frac{\sigma_{3j}^{\text{NLO}}}{\sigma_{2j}^{\text{NLO}}}, \quad (5.4)$$

and compare these to our other fixed order calculations to discern the stability of the result. The NLO calculations presented here were performed using Sherpa [88] and Openloops [89], which at time of writing includes NLO libraries for up to and including three jets in pp collisions. Whilst 2-jet calculations at NNLO_{QCD} are available at time of writing, the NNLO_{EW} corrections for 2 jets and both the NNLO_{QCD} and NNLO_{EW} are not yet known for 3 jets (and above). $pp \rightarrow 3 \text{ jets}$ was highlighted in the 2019 Les Houches Standard Model Working Group Report [12] as one of the processes which was desired to be calculated at higher accuracy by the physics community (see table 5.1 for a summary). Once the analysis discussed in this chapter is published, it will be interesting to see the effects of NNLO corrections to the fixed order predictions.

5.1.2 Profiles of average number of jets

Included also as part of the analysis is a study of the average number of jets versus kinematic observables. Similar to the R_{32} ratio, these distributions will be highly sensitive to higher jet multiplicities making them a good study of the accuracy of physical predictions beyond leading order. For leading order two jets, the average number of jets as a function of cross section or any kinematic observable will of course always just be two, so we will focus here on how we can define this in a consistent manor for NLO calculations and for all-order HEJ predictions.

For HEJ, the averaging is straightforward over the jet multiplicities:

$$\langle N \rangle_{XS} = \frac{2\sigma_{2j}^{HEJ} + 3\sigma_{3j}^{HEJ} + 4\sigma_{4j}^{HEJ} + \dots}{\sigma_{2j}^{HEJ} + \sigma_{3j}^{HEJ} + \sigma_{4j}^{HEJ} + \dots} = \frac{\sum_{n=2}^{\infty} n\sigma_{nj}^{HEJ}}{\sum_{n=2}^{\infty} \sigma_{nj}^{HEJ}}, \quad (5.5)$$

where each of the sigma represent the *exclusive* contribution to the total cross section at that multiplicity. One can then extend this definition to be instead for each bin in a distribution being studied, i.e. for each bin we can look at the contribution to that observable from each jet multiplicity to calculate the average number of jets versus the observable.

For NLO two jet calculations we first split the inclusive cross section into exclusive 2j and 3j pieces:

$$\sigma_{2j-inc}^{NLO} = \sigma_{2j-exc}^{2jNLO} + \sigma_{3j-exc}^{2jNLO}, \quad (5.6)$$

and then go on to define the average number of jets as,

$$\langle N \rangle_{XS} = \frac{2\sigma_{2j-exc}^{2jNLO} + 3\sigma_{3j-exc}^{2jNLO}}{\sigma_{2j-inc}^{NLO}} = 2 + \frac{\sigma_{3j-exc}^{2jNLO}}{\sigma_{2j-inc}^{NLO}}. \quad (5.7)$$

Nately, one may expect the average number of jets using eq. (5.7) to be bound by 2 below and 3 above. This however is not guaranteed to be the case. Looking at the final expression in the equation,

$$\frac{\sigma_{3j-exc}^{2jNLO}}{\sigma_{2j-inc}^{NLO}} = \frac{\sigma_{3j-exc}^{2jNLO}}{\sigma_{2j-exc}^{2jNLO} + \sigma_{3j-exc}^{2jNLO}}, \quad (5.8)$$

this term is no longer bounded by one if σ_{2j-exc}^{2jNLO} ends up being less than zero, which

Variable	Value
Jet p_{\perp}	$> 60 \text{ GeV}$
Jet R	0.4
Jet $ \eta_{\max} $	4.4
H_{T2}	$> 250 \text{ GeV}$

Table 5.2: Table of phase space cuts used for the ATLAS R_{32} study.

can happen in an NLO calculation depending on the choice of subtraction terms, factorisation scale and renormalisation scale. Whilst this behaviour is clearly unphysical, it is unavoidable when looking at this sort of quantity in numerical simulations.

5.2 Experimental and simulation setups

Before looking at the comparison of fixed order predictions, we will first go into detail of the experimental setup for this analysis. The experimental cuts are summarised in table 5.2. For each fixed order, jet clustering was performed using the anti-kt algorithm [90] with jet parameter $R = 0.4$. Jets were required to have transverse momentum greater than 60 GeV and have an absolute value of rapidity less than 4.4. In addition, there was a requirement that each event must have at least 2 jets passing the cuts described and the sum of the transverse momentum of the hardest 2 jets must be above 250 GeV.

For the predictions shown in this section, the factorisation scale, μ_F , and renormalisation scale μ_R were both chosen to be $\frac{H_T}{2}$ (in Sherpa one sets $\mu_F^2 = \mu_R^2 = \frac{H_T^2}{4}$). To assess the impact of the scale choice, the central scale choices (not squared) were independently varied by factors of 2 or 1/2, but with the ratio between μ_F and μ_R being no more than 2. The interface to the parton distribution was provided by LHAPDF [41], and the set used was NNPDF31_nlo_as_0118 (LHAPDF number 303400) provided by the part of the 3.1 release of NNPDF [91]. The analysis was performed using the Sherpa interface to rivet [92], using a custom analysis.

In practice, a rapidity cut was introduced to improve the sampling over a large rapidity range. In the Sherpa runcards, the difference in rapidity was restricted to be below 5.2 units of rapidity for one sample and above 5.2 for a second sample which were then combined. For the final predictions in this chapter it was

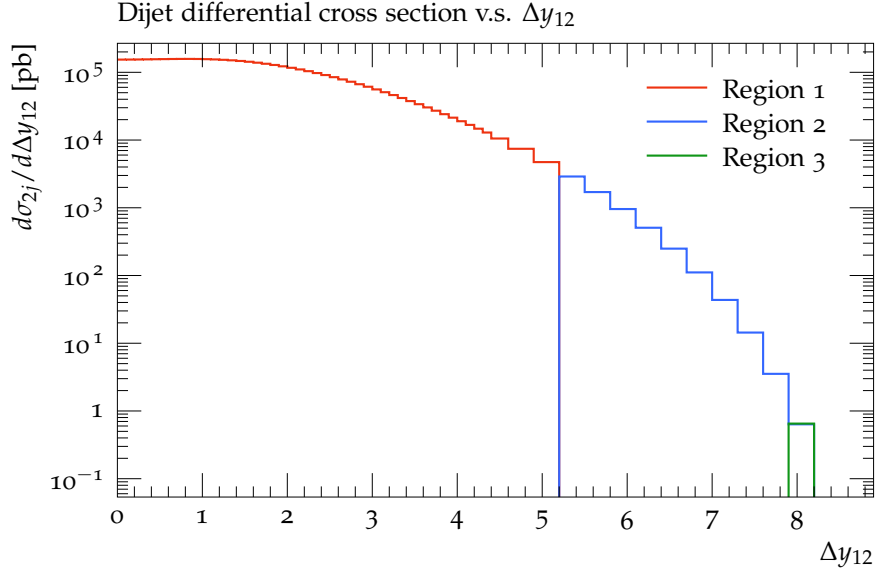


Figure 5.1: Plot of the rapidity separation between the two hardest jets for 2 jet fixed order sample split into three regions: $(0, 5.2)$, $(5.2, 7.9)$, $(7.9+)$.

convenient to split this rapidity range further into $(0, 5.2)$, $(5.2, 7.9)$, $(7.9+)$, as shown in fig. 5.1 for the two jet sample. From this figure we see that the cross section falls sharply as a function of dijet rapidity separation, spanning 6 orders of magnitude which is difficult for the phase space sampler to sample effectively in one go. For the HEJ resummation discussed later, this method of splitting of the phase space at born level and then combining is still valid as it is equivalent to splitting a rapidity integral in eq. (3.48),

$$\int_0^{8.8} dy_{12} = \left(\int_0^{5.2} dy_{12} + \int_{5.2}^{7.9} dy_{12} + \int_{7.9}^{8.8} dy_{12} \right). \quad (5.9)$$

5.3 Logarithmically accurate predictions with High Energy Jets

To perform high energy resummation with HEJ2, one starts with the fixed order events taken from the Sherpa event generator and passes them to the main HEJ2 executable (discussed in detail in section 3.3. For this study the jets in the fixed order events were clustered at 60 GeV to match the cut in the analysis, but no additional requirement on H_{T2} was added at this stage. Starting with leading order events for $pp \rightarrow jj$, one then also generates leading order events

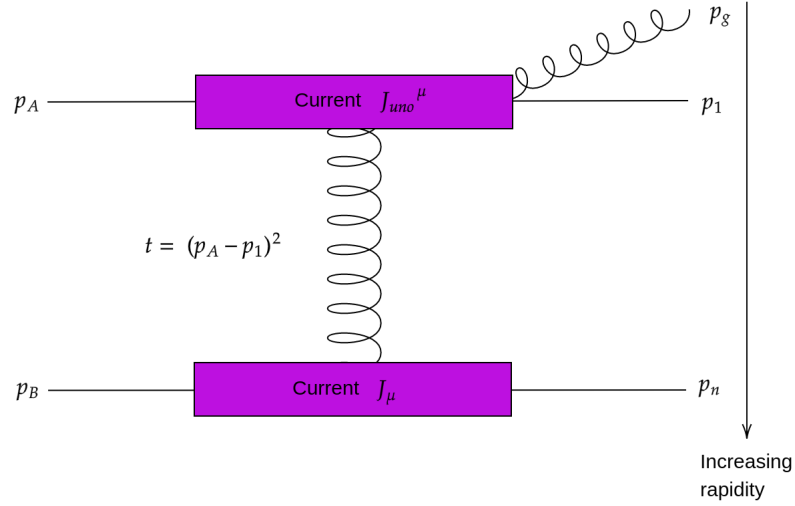


Figure 5.2: HEJ2.1 includes support for resumming unordered emissions where one parton is emitted outside of the forward backwards rapidity range of the quarks.

for $pp \rightarrow \underbrace{j \dots j}_n$ for $n = 3, 4, 5, \dots$ to also be passed to HEJ2. Typically one sees the percentage contribution from each fixed order multiplicity to the *inclusive* HEJ cross section decreases as you go to higher multiplicity¹. For this study, it was found that the contribution from the 6j fixed order events contributed about 0.12% to the inclusive HEJ prediction and did not have a discernible effect on any of the shapes of the differential distributions. Therefore, we did not include any corrections from 7 jet samples or above.

For each of the fixed order events passed to HEJ2, the event was classified as being FKL, with a strict rapidity ordering between final state jets, being a *NLL correction* with the rapidity ordering broken in one place else being labelled as *non-resummable* and being passed directly to the analysis. For the FKL events, HEJ2 generates a number of resummation phase space points with extra emissions and calculates the square amplitude using the rules outlined in section 3.2. As of HEJ2.1, resummation for diagrams including an unordered emission (fig. 5.2) or a quark-antiquark vertex can be included.

In unordered events, the rapidity ordering is broken only by the unordered emission but is otherwise intact. For the $q\bar{q}$ emissions, there is a spin 1/2 particle exchange in the t -channel which we know from the discussion on the Regge limit in

¹An example we see where this isn't quite true is VBS/VBF processes where the 3j contribution can be higher than the 2j contribution.

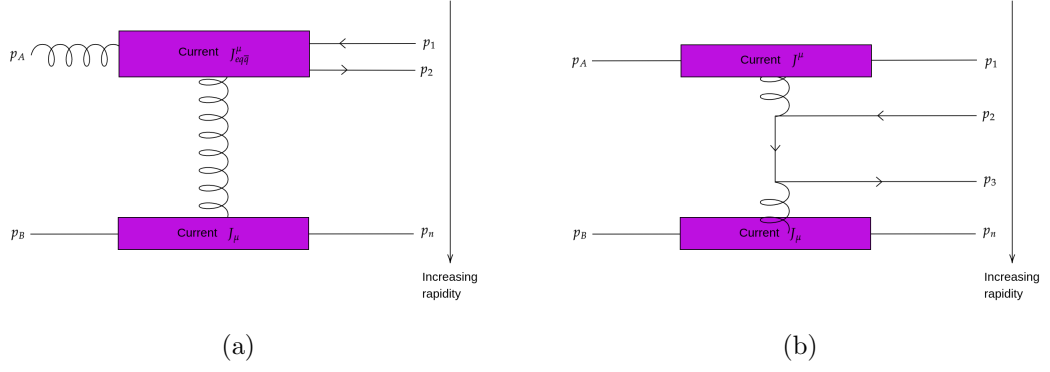


Figure 5.3: Two processes involving $q\bar{q}$ vertices that contribute to next-to-leading logarithm which are included in the HEJ resummation.

section 3.1.1 is subleading compared to only spin 1 exchanges. These unordered and quark-antiquark contributions thus are part of the NLL corrections to the prediction.

Once these resummation events are generated, they are passed to the analysis handler to be analysed further.

5.3.1 Lower energy jet contributions

For each fixed order event passed to HEJ2, a number of corresponding resummation events will be generated depending on the user input. Whilst it is guaranteed that the number of jets in the resummation event and the rapidity of these jets matches that in the fixed order input event, this is not generally the case for the transverse momenta of jets nor the rapidity of other final state particles. The reason for this is that the resummation events will include additional emissions corresponding to the all order real corrections to the process.

A consequence of this is that there will be a contribution to the resummed prediction from events where the resummation jets pass the transverse momentum cuts, but the fixed order events contain jets which are slightly below the cuts. Empirically, depending on the study we expect the contribution from these events to be the order of a few percent per multiplicity, and at most about 10%. In practice, one can include these contributions by setting the jet p_\perp cut in the fixed order input to be lower than the analysis p_\perp cut, but doing this is very inefficient for phase space sampling. The total cross section typically decays exponentially as a function of jet p_\perp , so the sampling will favour events with lower jet p_\perp .

R_{32} Measurement	Value
R_{32}^{LO}	0.30999 ± 0.00003
$R_{32}^{LO/NLO}$	0.43 ± 0.13
R_{32}^{NLO}	0.28 ± 0.27
R_{32}^{HEJ}	0.271 ± 0.005

Table 5.3: Table of R_{32} values for different definitions of fixed order R_{32} and for HEJ. Calculations are for the central scale choice only and errors quoted are generation errors and not from scale variations. It is known that the generation errors obtained for the NLO pieces are overestimated which affects the errors quoted for the two NLO results presented here.

which will lead to a large number of discarded events that don't pass the analysis cuts. Instead, it is more efficient to generate a low statistics, lower p_{\perp} fixed order sample separately from the main high statistics sample where the jet p_{\perp} cut for the fixed order sample matches the analysis. As of HEJ2.2 [2] there is a flag,

```
require low pt jet: true
```

which is used to signal to HEJ2 to discard events where the fixed order event jets all pass the p_{\perp} cuts in the analysis. For this study, the contribution from low p_{\perp} events was expected to be small as the analysis has an additional requirement that $H_{T2} > 250$ GeV already requires that 2 jet events contain jets with transverse momentum above the 60 GeV cut.

5.4 Comparison of fixed order and HEJ results

5.4.1 Comparison of R_{32} Measurements

The calculated central values for R_{32} are given in table 5.3. The scale errors on the NLO calculations are known to be vastly overestimated and come from a known issue in the way Rivet2 and Sherpa2 deal with errors in NLO calculations (this has been fixed as part of 2.2.15 release). As we will see in the integrated distributions, the NLO lines are actually pretty stable but do sometimes still have large scale variation bands. We see from looking at the analysis data that the two jet and three jet cross section are actually 30% smaller at NLO, which explains the large increase in the value of $R_{32}^{LO/NLO}$ versus the other R_{32} measurements presented. From LO to NLO we see a decrease in the predicted R_{32} value of about 9% coming from the decrease in the 3j cross section going from LO to NLO being

larger than the decrease in the 2j cross section. Comparing HEJ and fixed order, we see that the inclusive HEJ R_{32} central predicted value is about 12% lower than that of LO and 4% lower than NLO.

5.4.2 Comparison of differential distributions for R_{32}

Presented in figs. 5.4 to 5.6 are comparisons of R_{32} versus various kinematic observables for LO, NLO and HEJ. For the leading order and HEJ predictions, the scale variation bands tend to be of order a few percent, but in some regions can increase to of order 10%. In contrast, the NLO scale variation errors are very large, often encompassing the whole plot. This is due to a large scale error in the three jet NLO sample from Sherpa, and a large scale error in the two jet NLO sample at high energy (large Δy_{12} and m_{12}) indicating a perturbative instability. As such, the plots shown in the rest of this chapter have the NLO scale bands omitted, leaving only the central value.

Presented first in fig. 5.4 are rapidity distributions for Δy_{12} and Δy_{fb} respectively. For the Δy_{12} distribution, the lines are somewhat similar, with the HEJ prediction being slightly lower than LO and very similar to LO until we get to high rapidities, where the LO prediction falls sharply. The cross section as a function of Δy_{12} falls sharply when the hard jets are no longer central, and even more sharply when looking at more than 2 jets. This leads to the LO result in R_{32} falling to 0 as we reach the maximum allowed rapidity separation. For the Δy_{fb} we see very different behaviour where all three predictions are similar for $\Delta y_{fb} < 2$ but while the HEJ and NLO results level off, the LO result continues to rise sharply. This shows that at large Δy_{fb} , there is a large contribution to the inclusive cross section from events with more than two jets which is not accounted for at two jet LO. Also the scale variation bands for the HEJ prediction end up being very small for large Δy_{fb} , signifying a very stable prediction in this region.

Figure 5.5 shows R_{32} as a function of invariant mass using the two hardest jets in fig. 5.5a and the maximum of the invariant masses in fig. 5.5b. For m_{12} , the central lines are all very similar in shape for LO, NLO and HEJ, with the HEJ result being lower than the fixed order results and the difference increasing as the invariant mass increases. For fig. 5.5b, this difference between LO and HEJ is much larger with both results starting to fall by 7 TeV. This could be explained as a lack of energy available for jets beyond the first two jets when the invariant mass of the hardest 2 jets is so high. For this plot in particular, the NLO expansion

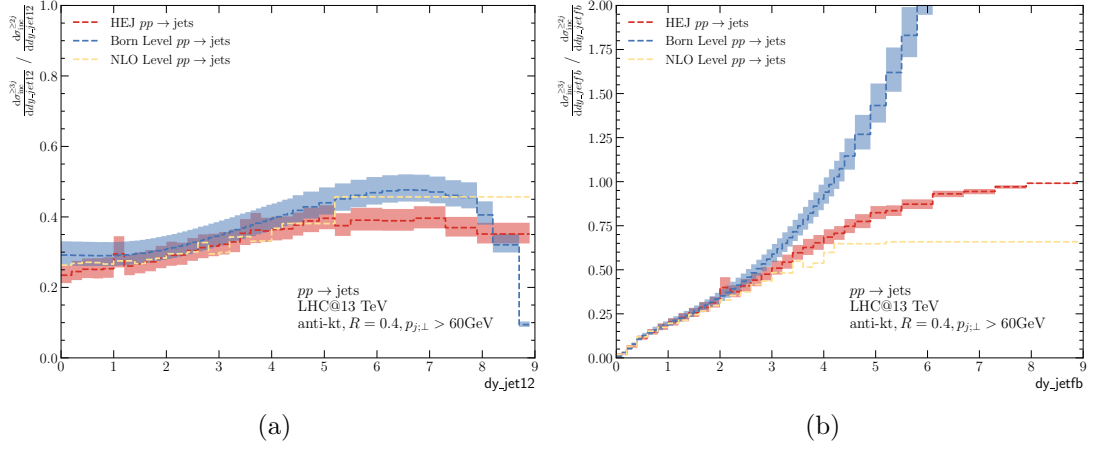


Figure 5.4: Plot of R_{32} as a function of jet rapidity separation between jets for (a) hardest two jets (b) most forward and backward jets. In red is the HEJ result at LL with some NLL corrections included, in blue ratio of R_{32}^{LO} defined in eq. (5.2) and in yellow the ratio R_{32}^{NLO} defined in eq. (5.4). The NLO lines have an adjusted binning in the large rapidity regions to account for poor statistics.

struggles to give a stable result.

The plot of R_{32} versus H_{T2} is split into several regions depending on the transverse momentum of the third hardest jet. The six plots in Figure 5.6 show these six regions, with the y-axis scaled in each of the plots to see the behaviour clearly. For each of these plots, there is a region at low H_{T2} which is not filled as the jet clustering is done at 60 GeV which imposes a lower limit on the transverse momentum of the third hardest jet. This is most prominent in fig. 5.6a which shows behaviour down to $H_{T2} = 1200$ GeV. The differences in the predictions are most pronounced in the first few of these plots where the p_{\perp} of the third jet is lowest. In figure (a), the lines all start to plateau in the limit of large H_{T2} , with a clear hierarchy throughout $LO > NLO > HEJ$. As the limits on $p_{3,\perp}$ increase, there becomes a clear peak in the distribution. This makes sense as the cross section for three jets is known to sharply decrease as a function of $p_{3,\perp}$, so we would expect to see the biggest values of R_{32} around where the third jet is near its minimum value. For fig. 5.6b for example, at $H_{T2} = 1200$ GeV, the lower bound on $p_{3,\perp}$ becomes the same as the jet cut and the upper bound is 120 GeV. The integral of this region in $p_{3,\perp}$ should be larger than the integrals of other regions the same size - leading to a peak in R_{32} . As the H_{T2} bands increase further the NLO and HEJ lines start to become a lot more similar, until by fig. 5.6d the differences between all three lines becomes minimal.

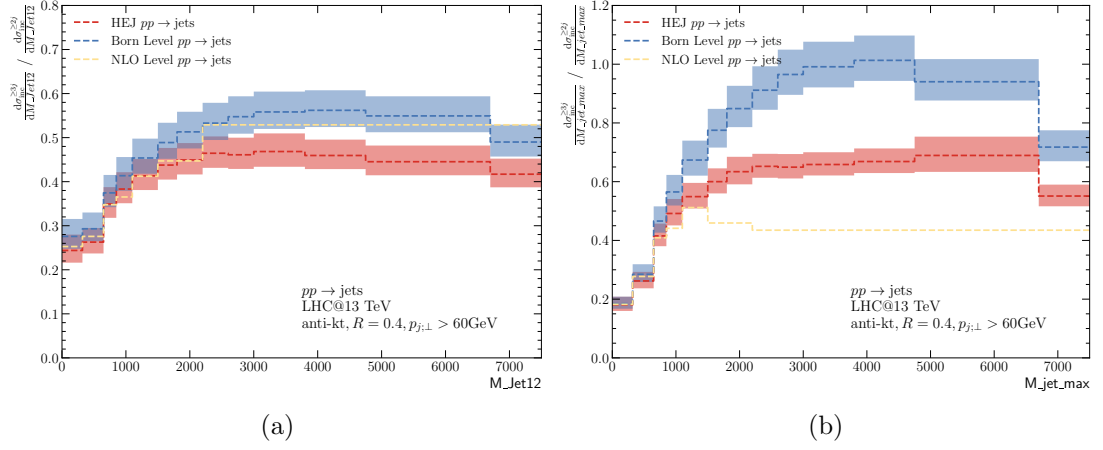


Figure 5.5: Plot of R_{32} as a function of dijet invariant mass between jets for (a) hardest two jets (b) jet pair with the largest invariant mass. In red is the HEJ result at LL with some NLL corrections included, in blue ratio of R_{32}^{LO} defined in eq. (5.2) and in yellow the ratio R_{32}^{NLO} defined in eq. (5.4). The NLO lines have an adjusted binning in the large invariant mass regions to account for poor statistics.

5.4.3 Comparison of differential distributions for average number of jets

Presented in this section in figs. 5.7 to 5.10 are plots of the average number of jets in a prediction versus kinematic variables of experimental interest. To start with, we again look at the rapidity distributions before moving on to looking at the invariant mass distributions and concluding with H_{T2} and angular separation.

Figure 5.7 shows the average number of jets as a function of for Δy_{12} and Δy_{fb} respectively. For the chosen scale choice at $y_{12} = 5.2$ units of rapidity, we see exactly the behaviour discussed around eq. (5.8) where the exclusive two jet rate in the two jet NLO prediction becomes negative and the average number of jets gets larger than 3 which is unphysical behaviour for a two jet NLO prediction. This is driven by a large negative VI component in the two jet rate which is not cancelled by the Born level result. At this point, the NLO scale variation bands also become very large which can be seen in both fig. 5.7a and also in fig. 5.4a. For the Δy_{fb} profile, we see the average number of jets rise almost linearly reaching around $\langle N \rangle = 4$ at 9 units of rapidity separation. This behaviour from about 4.5 to 9 units of rapidity can't be predicted by pure NLO as it strongly depends on contributions from higher jet multiplicities which can be captured with HEJ.

Figure 5.8 shows the average number of jets as a function of dijet invariant mass. For both fig. 5.8a and fig. 5.8b, the exclusive two jet rate becomes negative at

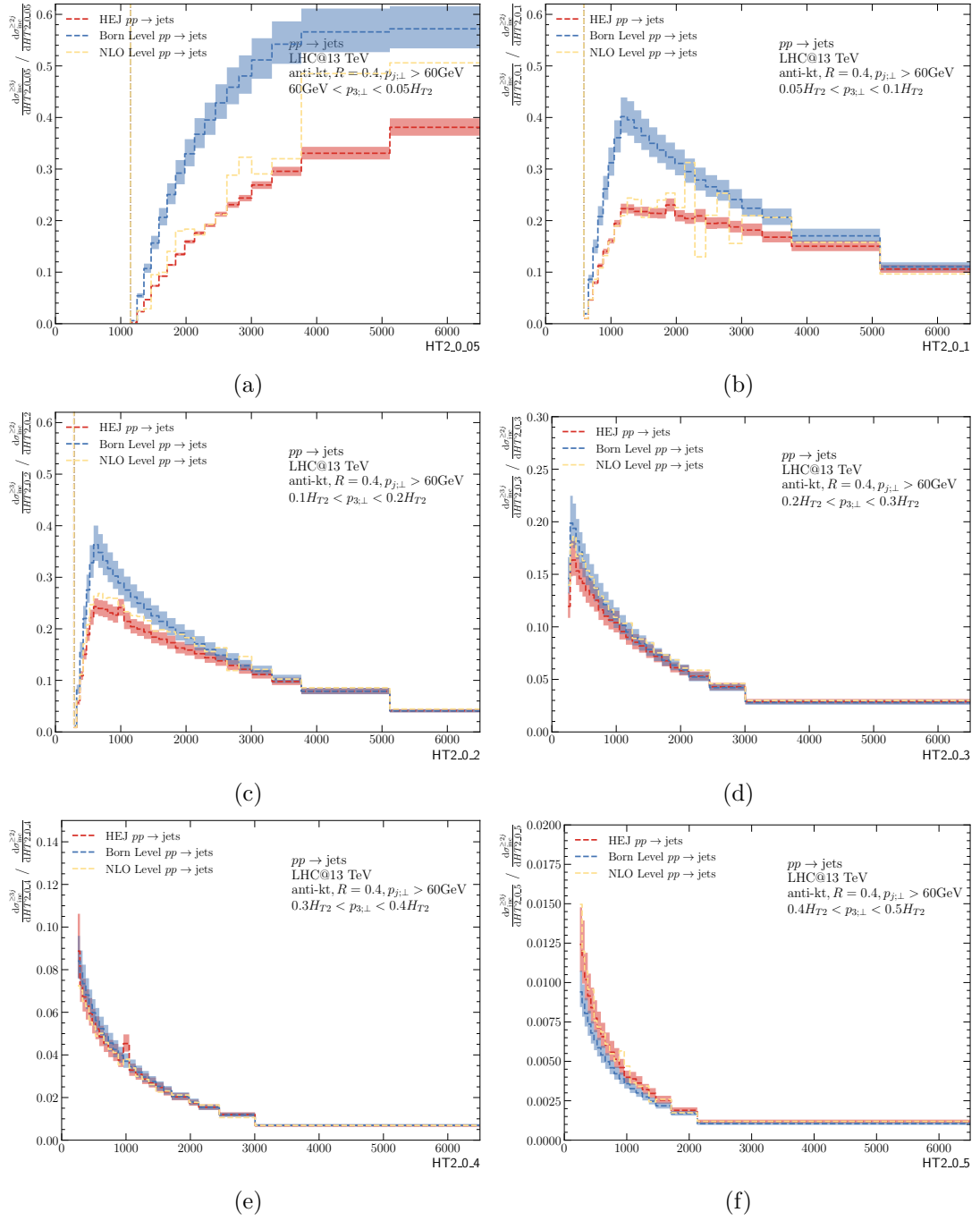


Figure 5.6: Plot of R_{32} as a function of sum of transverse momenta of the hardest two jets, H_{T2} , for (a) $60 \text{ GeV} < p_{3,\perp} < 0.05 H_{T2}$ (b) $0.05 H_{T2} < p_{3,\perp} < 0.1 H_{T2}$ (c) $0.1 H_{T2} < p_{3,\perp} < 0.2 H_{T2}$ (d) $0.2 H_{T2} < p_{3,\perp} < 0.3 H_{T2}$ (e) $0.3 H_{T2} < p_{3,\perp} < 0.4 H_{T2}$ (e) $0.4 H_{T2} < p_{3,\perp} < 0.5 H_{T2}$. In red is the HEJ result at LL with some NLL corrections included, in blue ratio of R_{32}^{LO} defined in eq. (5.2) and in yellow the ratio R_{32}^{NLO} defined in eq. (5.4).

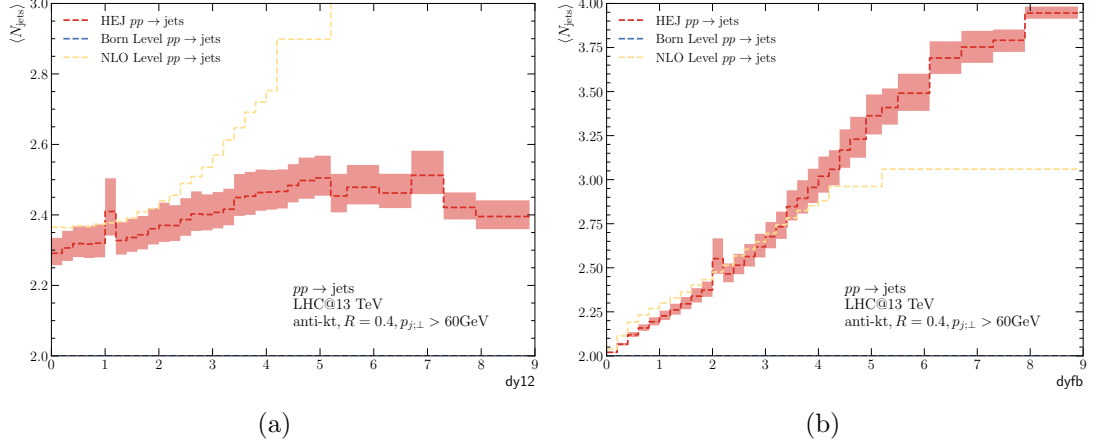


Figure 5.7: Plot of average number of jets as a function of jet rapidity separation between jets for (a) hardest two jets (b) most forward and backward jets. In red is the HEJ result at LL with some NLL corrections included and in yellow the NLO mean number of jets defined in eq. (5.7). The NLO lines have an adjusted binning in the large rapidity regions to account for poor statistics.

around 2 TeV which leads to an NLO prediction which goes above 3 for this region. Before this point, the NLO prediction rises sharply as a function of invariant mass for both plots. For m_{12} , the HEJ prediction rises less sharply, softly peaking at about 2.7 between 3 TeV and 4 TeV before slowly falling again. For $\max m_{jj}$, the HEJ result initially rises at a similar rate to the NLO result before peaking slightly above 3 before falling below 3 again at 7 TeV.

Figure 5.9 shows the average number of jets versus H_{T2} displayed here as one plot instead of the 6 different regions discussed when looking at R_{32} . Here there is closer agreement between HEJ and NLO compared to the other profiles discussed here, with both peaking softly at $\langle N \rangle = 3$ when $H_{T2} = 2$ TeV before falling slowly.

Finally, we look at the average number of jets as a function of the angular separation of the hardest two jets ϕ_{12} . Figure 5.10 shows this for only the HEJ prediction as the average number of jets goes above 3 almost immediately going from either the left or right hand side of the plot. This plot is very sensitive to higher order corrections, peaking at almost $\langle N \rangle = 5$ which is far beyond what is accessible to next-to-leading order. The reason for this sensitivity to higher multiplicity is that the central $\phi_{12} \approx 0$ are not kinematically accessible at low multiplicity.

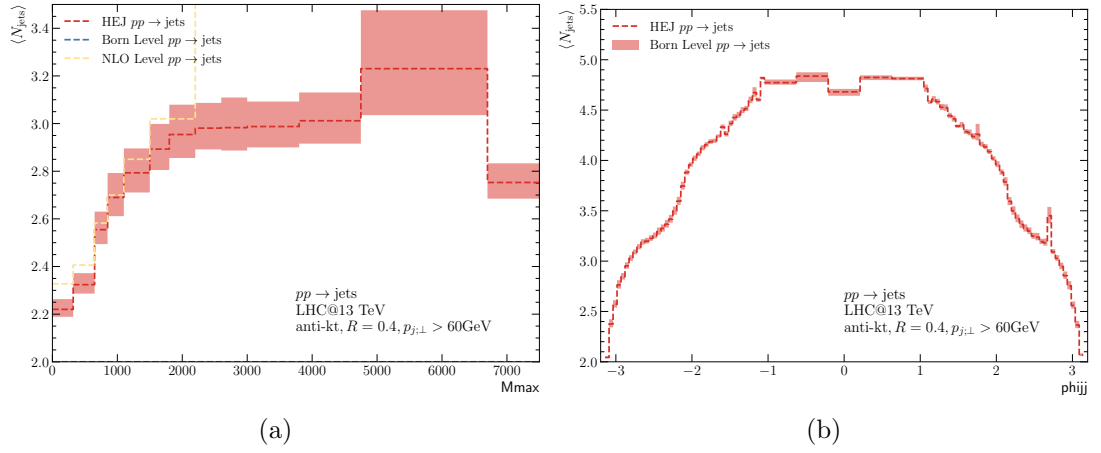


Figure 5.8: Plot of average number of jets as a function of dijet invariant mass between jets for (a) hardest two jets (b) jet pair with the largest invariant mass. In red is the HEJ result at LL with some NLL corrections included and in yellow the NLO mean number of jets defined in eq. (5.7). The NLO lines have an adjusted binning in the large rapidity regions to account for poor statistics.

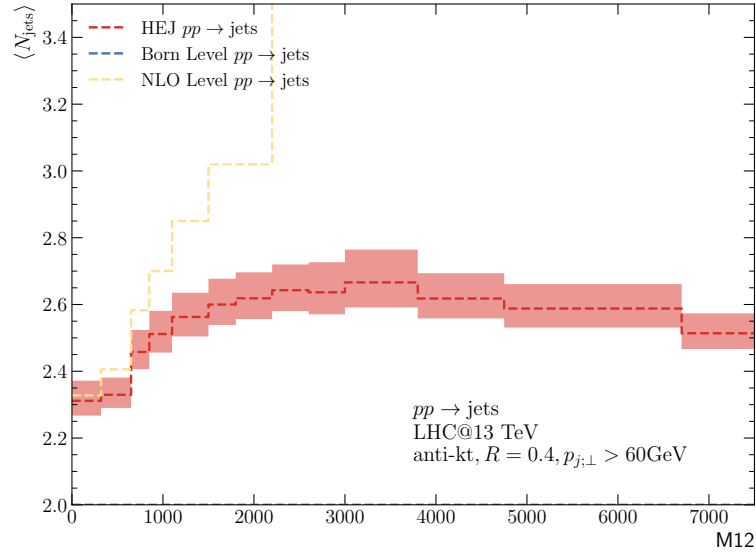


Figure 5.9: Plot of average number of jets as a function of the sum of the transverse momenta of the hardest two jets, H_{T2} . In red is the HEJ result at LL with some NLL corrections included and in yellow the NLO mean number of jets defined in eq. (5.7).

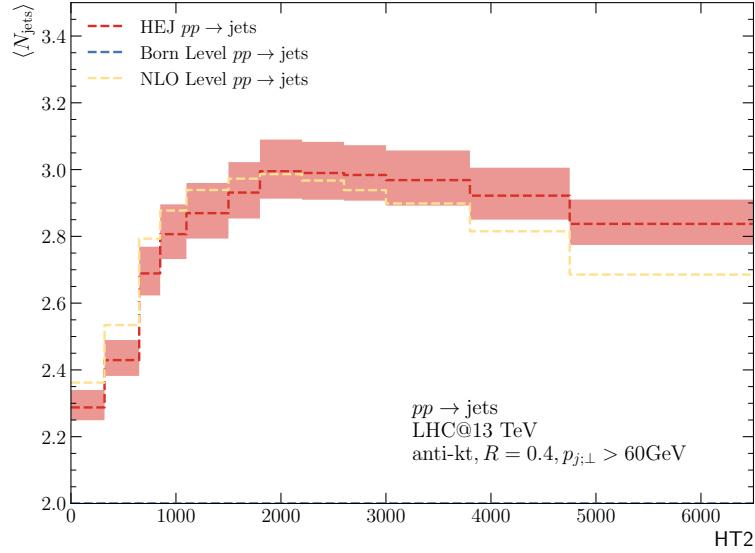


Figure 5.10: Plot of average number of jets as a function of the angular separation of the hardest two jets. In red is the HEJ result at LL with some NLL corrections included.

5.5 Final thoughts and conclusions

In this chapter we presented the HEJ predictions for the 2023 ATLAS study looking at the ratio R_{32} for QCD jets at the LHC, as well as looking at profiles of the average number of jets versus various kinematic observables. Due to delays in the analysis being published, we can only compare versus leading order or next-to-leading order predictions where possible but even there we have seen some significant deviations from the fixed order results for some distributions. In the rapidity and the invariant mass distributions, the predictions were very different at large rapidity separations/ large invariant mass with the ratio R_{32} making clear the differences between the lines are not just from scale variation errors. Some of the average number of jets plots also clearly highlight the dependence on higher order corrections where the average number of jets goes above 3. These corrections are included in HEJ in the leading log description of the process which includes contributions from all jet multiplicities. We are keenly awaiting for the analysis to be published to be able to compare with experimental data and for theoretical physicists working on higher fixed order predictions to be able to compare our predictions in regions where the higher order corrections are needed.

Chapter 6

High energy predictions for Vector Boson plus jets at LHC: A study with ATLAS_MET_JETS analysis team

This chapter details the HEJ predictions for the ATLAS study involving jets with a large missing transverse energy ($E_{\perp;missing}$, or “MET”), highlighting in particular the differences in the methodology from chapters 4 and 5. For this study, the HEJ predictions were initially $\approx 40\%$ larger than NLO or MEPS@NLO, which turned out to be a result of treatment of events with the heterogeneous jet p_{\perp} cuts used in the analysis. This chapter then also serves as a summary of the work done extending the HEJ description to analyses with heterogeneous jet cuts, with the promise of a better prediction once NLL impact factors are derived and implemented in the HEJ2 code.

6.1 Setup of the experimental measurement

The goal of this ongoing experimental analysis is to produce a measurement of large missing energy plus jets at a centre of mass energy of 13 TeV. “Large” here is defined to be the region where the missing p_{\perp} is greater than 200 GeV. In order to constrain the signal region of $\nu\nu$ plus jets which is an important probe of dark matter physics at the LHC[93], ATLAS also measured the control regions of dilepton (ee and $\mu\mu$) plus jets and single-lepton ($e\nu$, $\mu\nu$) plus jets. The

	≥ 1 jet	≥ 2 jet	VBF
p_T^{miss}	> 200 GeV		
$\Delta\phi(\text{jet}_i, p_T^{\text{miss}})$	> 0.4 , where $i = 1, \dots, 4$ runs over the four highest p_T jets		
(Additional) muons	None with $p_T > 7$ GeV, $ \eta < 2.5$		
(Additional) electrons	None with $p_T > 7$ GeV, $0 < \eta < 1.37$ or $1.52 < \eta < 2.47$		
Hadronic taus	None with $p_T > 20$ GeV, $0 < \eta < 1.37$ or $1.52 < \eta < 2.47$		
lead jet $ y $	< 4.4		
lead jet p_T	> 120 GeV	> 110 GeV	> 80 GeV
sub-lead jet $ y $	N/A	< 4.4	< 4.4
sub-lead jet p_T	N/A	> 50 GeV	> 50 GeV
lead jet $ \eta $	< 2.4		
m_{jj}	N/A	N/A	> 200 GeV
$ \Delta y_{jj} $	N/A	N/A	> 1
In-gap jets	N/A	N/A	None with $p_T > 30$ GeV, $ y < 4.4$

(a)

	1 ℓ +jets	2 ℓ +jets
lepton $ \eta $ (muons)	$ \eta < 2.5$	
lepton $ \eta $ (electrons)	$0 < \eta < 1.37$ or $1.52 < \eta < 2.47$	
leading lepton p_T	> 30 GeV for e , > 7 GeV for μ	> 80 GeV
sub-leading lepton p_T	N/A	> 7 GeV
di-lepton mass	N/A	$66 < m_{\ell\ell} < 116$ GeV
transverse mass	$30 < m_T < 100$ GeV for e only	N/A
true p_T^{miss}	> 60 GeV for e only	N/A

(b)

Figure 6.1: Tables outlining the experimental setup for the large missing p_\perp study focusing on selection cuts to (a) jets (b) leptons

measurement looks at a number of regions:

- An inclusive one-jet region
- An inclusive two-jet region
- An inclusive two-jet region with additional VBF cuts,

although we will only be looking at HEJ predictions for the two-jet inclusive and VBF regions as the HEJ2 formalism requires at least 2 jets in the final state for W and Z/γ plus jets predictions.

Outlined in fig. 6.1 is the experimental setup for the measurement which is dependent on the number of identified leptons and the analysis region. The two jet and VBF regions both require a missing p_\perp (p_\perp of identified leptons and

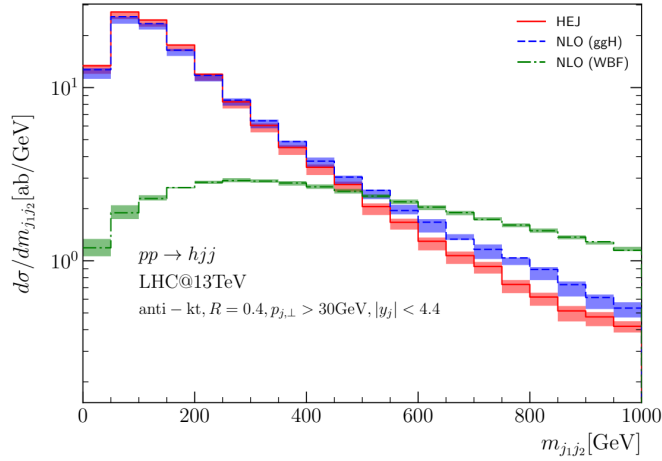


Figure 6.2: Plot of cross section as function of dijet invariant mass from a study of Higgs Boson plus jets comparing HEJ with vector boson fusion and gluon fusion calculated at NLO. Reproduced from reference [11].

true “missing” momenta) to be larger than 200 GeV. There is also a requirement that the missing momenta vector and each of the four hardest jets be separated by more than 0.4 in azimuthal angle.

Jets are required to have an absolute rapidity less than 4.4 and the leading jet is required to be above 110 GeV in the two-jet region and above 80 GeV in the VBF region. The second hardest jet is required to be above 50 GeV and all additional jets are counted above 30 GeV. Jets are classified in the analysis according to the anti-kt algorithm with a jet parameter $R = 0.4$.

Furthermore, in the VBF region we have the additional restrictions that the dijet invariant mass of the hardest two jets is above 200 GeV and the absolute value of the rapidity separation of the hardest two jets is above 1. Both of these cuts are known in VBF studies to restrict the phase space to a region where QCD contributions are suppressed compared to the electroweak contribution. See fig. 6.2 for an example of this from a recent review [11].

Then leptons are identified with absolute (pseudo-)rapidity below 2.5 for muons and in the intervals $0 < |\eta| < 1.37$ and $1.52 < |\eta| < 2.47$ for electrons to account for gaps in the detector. For one identified charged lepton, the transverse momentum of an electron was required to be above 30 GeV and for a muon it was required to be above 7 GeV. The ATLAS muon detector has two p_{\perp} triggers, a large p_{\perp} trigger at 20 GeV and a low p_{\perp} trigger at 6 GeV, so this analysis ends up pushing close to the limits of what is possible with the detector [94]. For the region with 2 identified charged leptons the hardest lepton was required to

have transverse momentum above 80 GeV and the second lepton was required to be above 7 GeV. In addition for the two lepton region there was a restriction that the dilepton invariant mass was between 66 GeV and 116 GeV in order to restrict the contribution from photons decaying into lepton-antilepton pairs. Finally for the one lepton region, there was a restriction on the transverse mass of the electron to be between 30 GeV and 100 GeV, and for the (actual) missing transverse momenta to be above 60 GeV for the electron channel.

The selection cuts used in this study for the charged leptons are very close to the limits what is recorded with the triggers available. The reason for this is to try and study the signal region of pure missing energy plus jets as cleanly as the hardware will allow, with as much of the events as possible with identified charged leptons included as part of the control regions.

6.2 Initial HEJ2 predictions for ATLAS_MET_JETS analysis

In this section, we will look at the steps involved in making the HEJ predictions for this analysis. Later on in this chapter, we will go into detail about some of the changes to this methodology for two jet inclusive observables, which came from an investigation into HEJ resummation with heterogeneous jet p_{\perp} cuts.

For this study, we look at making predictions for the one identified lepton and two identified lepton regions. This meant looking at HEJ2 predictions for W plus jets and Z plus jets, although cuts on leptons meant that there would be some Z events where only one lepton would pass the analysis cuts and be classified as an event with only one charged lepton. This effect was only possible in the muon channel and was observed to be small compared to the contribution from W events to these observables. Figure 6.3 shows the impact on an example experimental observable. In red is the contribution from generated W plus jets events, in blue is the contribution from Z plus jet events with only one identified lepton in the analysis and in black is the combined result. For this distribution, the contribution from Z events was exactly 0 for the electron channel and around two percent for the muon channel. The highest we saw this contribution in any bin in any of the observables studied was around 3%.

We start our procedure with fixed order input from Sherpa (2.2.12) [65] using

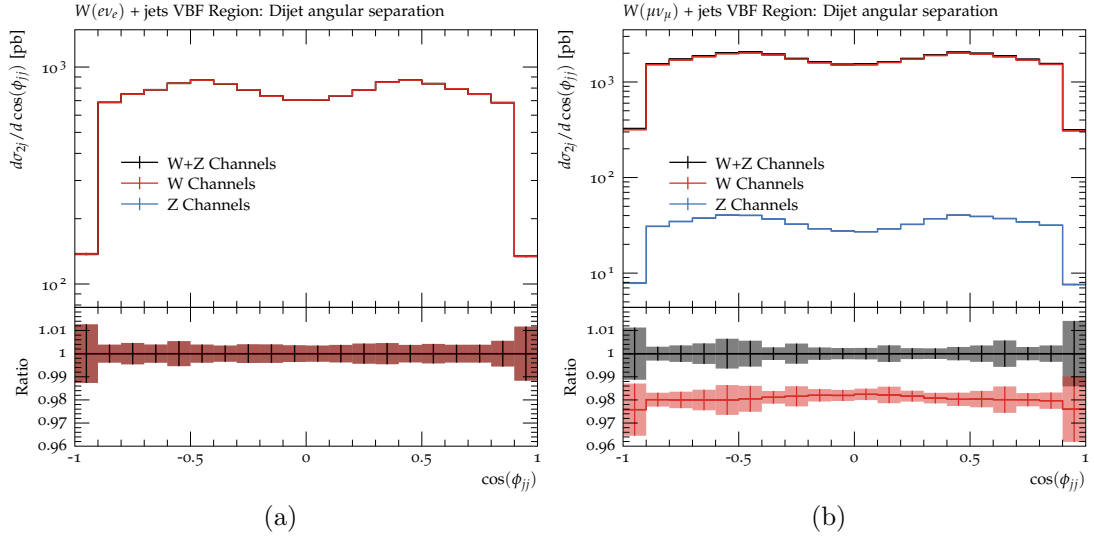


Figure 6.3: Plots of the cross section as a function of dijet angular separation highlighting the contribution of lepton isolation cuts in (a) electron channel (b) muon channel.

matrix elements obtained from COMIX [80] given as Les Houches events. The PDF used was NNPDF31_nlo_as.0118 taken from the Sherpa interface to LHAPDF [85]. For both W plus jets and Z plus jets, fixed order samples were taken with number of jets ranging from two to five. Each of these jets were required to have transverse momentum above 30 GeV and have an absolute value of rapidity less than 4.4. Electron and muon decay channels were included at the same time by using the particle containers 90 and 91 after removing the Tau lepton channel from these containers.

The central scale choice used was,

$$\mu_F = \mu_R = \frac{\sqrt{H_T^2} - p_{\perp \ell_1} - p_{\perp \ell_2} + m_{\perp \ell_1 \ell_2}}{2}, \quad (6.1)$$

where ℓ_1, ℓ_2 are the W decay products in W plus jets events and the charged leptons in Z plus jets events and H_T is the scalar sum of the transverse momenta of all final state particles. When the transverse momenta of the charged leptons and invariant mass of the leptons is small, this reduces to the commonly used scale choice of $H_T/2$. This scale choice was chosen by ATLAS for speed of calculation and to reduce the fraction of events with negative weights, so we chose the same central scale for the HEJ predictions. Since we knew this was the scale choice used for the other predictions in this analysis, we used the same choice here to ensure consistency across the predictions for a fair comparison. For scale variation bands

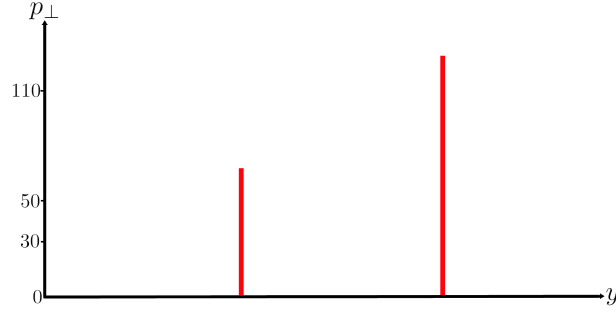


Figure 6.4: Example fixed-order event jets with one jet passing the $p_{\perp} > 110$ GeV requirement and one passing the $p_{\perp} > 50$ GeV requirement.

shown in this chapter, the central factorisation and renormalisation scale choice was varied independently by factors of 2.

In HEJ2, for each fixed order event in a resumable configuration, we attempt to generate a number of events in the resummation phase space. Resumable events currently include FKL events, events with an unordered gluon and $W +$ jets events with a $q\bar{q}$ vertex. Any non-resumable events were passed directly onto the analysis through the rivet (Rivet 3.1.5)[87] interface. Jet clustering was done at 30 GeV using the kt algorithm [90] in the analysis before looking at a higher p_{\perp} requirement on the leading and subleading jets. There was also a contribution from so called “low pt” events discussed in section 5.3.1, where the fixed order input jets were below 30 GeV but the resummation jets were above 30 GeV. Whilst this contribution has been important to include in previous studies, the higher jet p_{\perp} cut on the leading and subleading jets in the analysis greatly reduced this component in this study and was never seen to be more than 1% of the combined result.

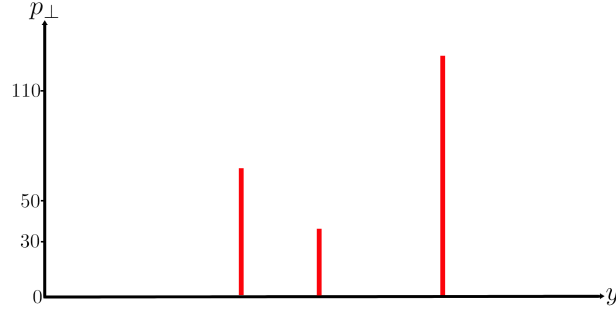


Figure 6.5: Example correction to the born level event (fig. 6.4) with an additional emission above 30 GeV between jets.

6.3 HEJ Resummation with heterogeneous jet samples

6.3.1 Classifying additional FKL emissions

Hard process and inclusive corrections

Let us begin this discussion by clearly defining what we mean by the hard process and what should be included as inclusive corrections to the hard process. For the examples shown here we define the hard process to be $pp \rightarrow W(\rightarrow e\nu_e)jj$ with one jet required to have transverse momentum over 110 GeV and the other above 50 GeV (see fig. 6.4). Then any additional emissions will be part of the corrections to the hard process. Depending on where we choose to cut the momentum of the additional jets, the corrections can move between the bins in the exclusive jet rates.

Suppose for example we have a correction in the form of an additional > 30 GeV emission with rapidity somewhere between the two outer jets (see fig. 6.5). If the jet clustering and resummation limit were set to below 30 GeV, then that emission would be part of the 3 jet ME correction and would contribute towards the 3j bin in the exclusive jet rates. However if one were to do jet clustering at a value above 30 GeV, for example at 50 GeV, this emission would be part of the HEJ resummation depicted in fig. 6.6b. In this case this would contribute to the 2j bin in the exclusive jet rates.

However for the second case with the emission below the resummation cut, we

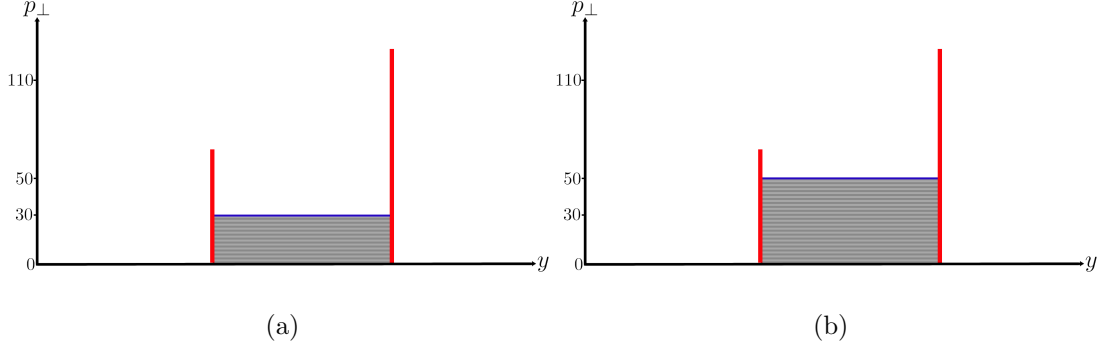


Figure 6.6: Diagrams indicating the regions of phase space where HEJ will produce extra emissions, Starting from the fixed order input in fig. 6.4, resummation is allowed in the grey shaded area when the jet p_{\perp} in the HEJ config is set to (a) 30 GeV (b) 50 GeV.

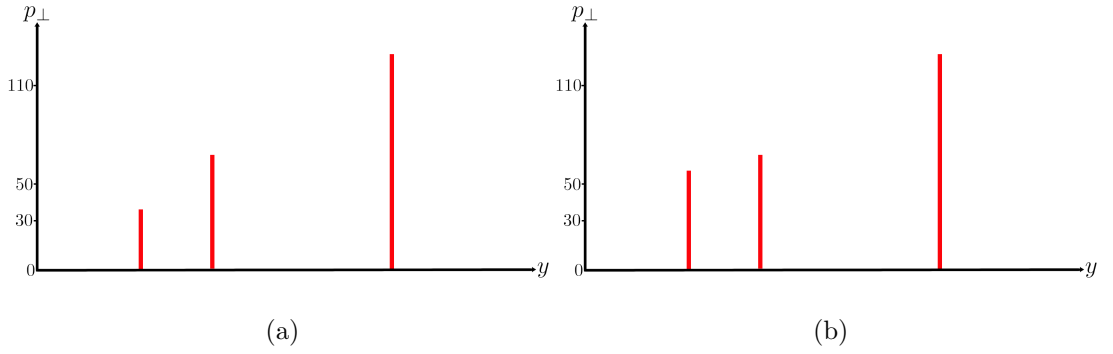


Figure 6.7: Diagrams showing an extra emission outside of the rapidity region between the hardest jets at (a) 30 GeV (b) 50 GeV. Allowing the third jet to have a low p_{\perp} will lead to a divergence which is not currently cancelled in the HEJ procedure due to missing virtual corrections.

need to be sure we include the full virtual corrections to cancel the divergence that occurs when that emission becomes infinitely soft. For the FKL emission described here with the emission between the outer jets in rapidity, this is taken care of in HEJ as the virtual corrections are included to cancel emissions between the outer jets depicted by the shaded region in fig. 6.6.

Jets outside the y_{jj} rapidity interval

This is not though the full picture as we can also have additional jets generated outside of the region between the two hardest jets. Figure 6.7 depicts an additional jet outside of the rapidity separation of the two leading jets. Allowing the additional jet to get arbitrarily small will lead to a divergence in the prediction as the virtual corrections required to cancel said divergence are not

```

// get anti-kT 0.4 jets
Jets jets = apply<FastJets>(event, "Jets").jetsByPt(Cuts::pT > 10*GeV && ↵
↵ Cuts::absrap < 4.4);

Jets rapjets = jets;
sort(rapjets.begin(), rapjets.end(), rapOrder);

// Middle jet cut
size_t snjets = rapjets.size();
double j_pt1 = rapjets[0].pT();
double j_pt2 = rapjets[snjets-1].pT();

if ((j_pt1 < 50 * GeV || j_pt2 < 50 * GeV ) || (j_pt1 < 110 * GeV && ↵
↵ j_pt2 < 110 * GeV)){ vetoEvent; }

```

Figure 6.8: Code snippet from the modified ATLAS_MET_JETS analysis which restricted the sample to only include events where the outer jets in rapidity are above 50 GeV and at least one is above 110 GeV.

yet implemented (c.f. fig. 6.6). Requiring the p_{\perp} cut on the third jet to be the same as the cut on the second leading jet (see fig. 6.7b) however, can lead to an event where the outer jets are still above 50 and 110 GeV, and thus has the appropriate virtual corrections included.

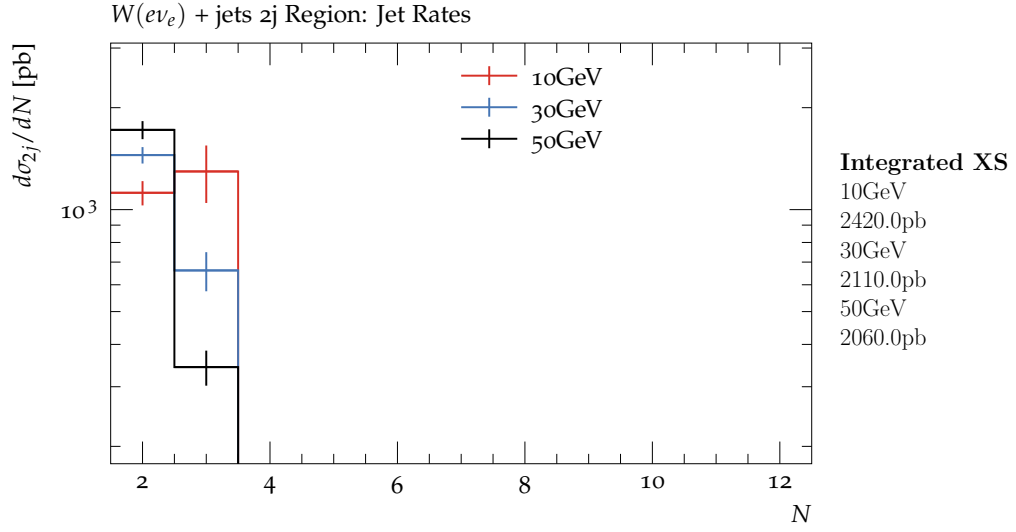
For a consistent, numerically stable HEJ prediction we need to include in the resummation events where the outer jets in rapidity meet the jet p_{\perp} cuts of 50 and 110 GeV to ensure the virtual corrections are included for when the additional jet(s) become soft. In the next section we look at how we can do this in practice and the effect that different p_{\perp} cuts on the additional emissions have on the exclusive jet rates.

6.3.2 Numerical testing of the HEJ descriptions

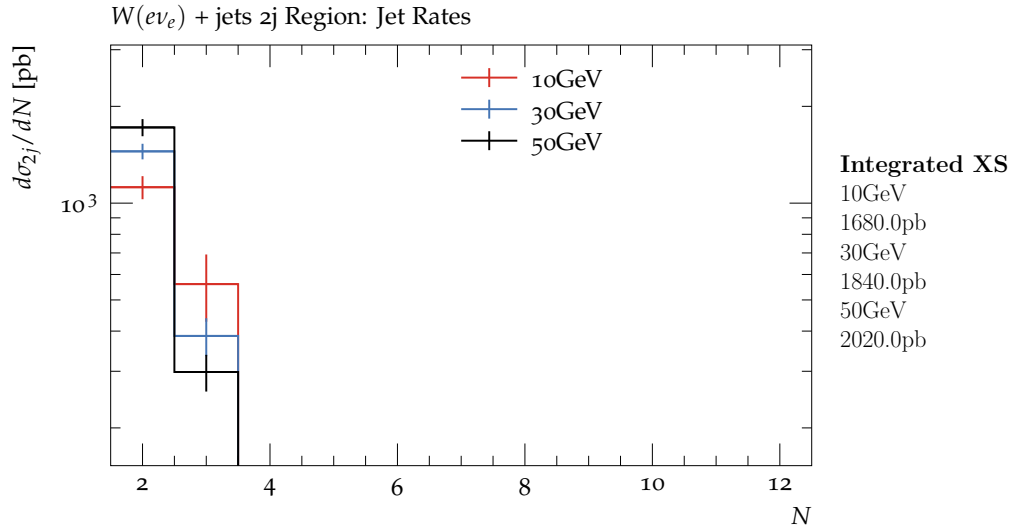
Testing the FKL description

To see the contribution from FKL events where the third jet is in a region without the full virtual corrections like in fig. 6.7a, we first create a modified version of the analysis with an additional requirement that the outer jets in rapidity are above 50 GeV, and that at least one of those is above 110 GeV. Figure 6.8 gives an example of how this can be done for the 10 GeV analysis.

Figure 6.9a is a plot of the exclusive jet rates for three different jet p_{\perp} samples - 10 GeV, 30 GeV, 50 GeV where the requirements on the outer jets are unchanged.



(a)



(b)

Figure 6.9: Combined two and three-jet exclusive jet rates from HEJ2, reweighing the FKL events and discarding everything else. The N GeV line uses a fixed order sample at N GeV and has the HEJ resummation jets at N GeV. (a) Uses a modified version of the `ATLAS_MET_JETS` analysis, with the jet cut adjusted (b) Requires that the outer jets in rapidity satisfy the cuts on the two jet sample.

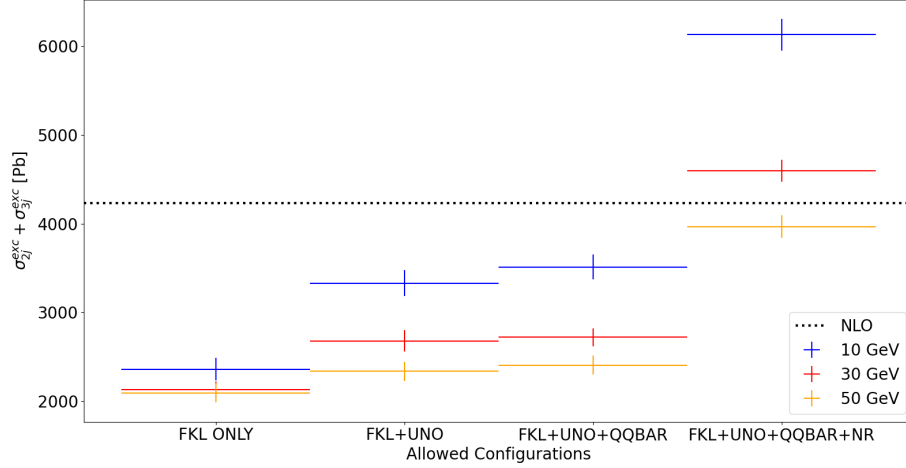


Figure 6.10: Combined $\sigma_{2j}^{exc} + \sigma_{3j}^{exc}$ jet rates against configuration options for 10, 30 and 50 GeV jets. The FKL, FKL+UNO and FKL+QQBAR differ only in the 3j contribution, whereas there are contributions from non-resummable events to both the 2j and 3j rate.

The fixed order input jet p_{\perp} minimum is set to the same value as the resummation jet p_{\perp} minimum which is the same value as what is used in the jet clustering in the analysis. Shown on the righthand side of the plot are the integrated rates for each line. We compare this with Figure 6.9b which has the additional restriction on the rapidity of the third jet. The difference between the plots is that in (b) events are removed when a third jet causes the outer jets to not pass the 110/50 GeV cuts. We see that as the p_{\perp} used in the jet clustering decreases, the contribution from such events increases so that at 10 GeV this contributes as much as 30% of the combined two and three jet rates. We see from figure (a) that the three jet rate (and thus the cross section) starts to rise significantly at 10 GeV and we expect that if we lowered the p_{\perp} cut further that we would see rapid growth as we approach the uncontrolled soft divergence.

Checking the stability of the NLL and non-resummable descriptions

We now move on to discuss the impact of restricting the third jet to be between the hardest two jets in rapidity for reweighting unordered and qqbar events, and for adding back in the non-resummable component. We continue to focus here on the process of W plus jets where resummation is implemented for UNO and QQBAR event types.

Figure 6.10 shows the combined $\sigma_{2j}^{exc} + \sigma_{3j}^{exc}$ jet rates against configuration options for three different choices of minimum jet p_{\perp} . From left to right we start with the FKL description {FKL: reweight, UNO: discard, QQBAR: discard, NR: discard} and then add in the unordered emissions {FKL: reweight, UNO: reweight, QQBAR: discard, NR: discard}, and then further add in the qqbar emissions {FKL: reweight, UNO: reweight, QQBAR: reweight, NR: discard}. Then finally for the farthest right bin, we add back in the non-resummable contributions {FKL: reweight, UNO: reweight, QQBAR: reweight, NR: Keep}, matching the NLL config options used in the full HEJ prediction. Included also is the total NLO cross section as a dotted black line. This is not used here as part of the HEJ prediction, and we do not expect to reproduce the NLO cross section in HEJ, but this is included to show how using a low jet p_{\perp} cut takes the prediction far away from NLO.

For this particular setup, going from the FKL only configurations to FKL + UNO, we see an increase of 10% for the 50 GeV jets, increasing to 26% for 30 GeV jets and to 41% for the 10 GeV jets. Adding in the QQBAR events sees a further increase of a few percent for all of the jet p_{\perp} cuts shown.

Looking at the final FKL+UNO+QQBAR+NR bin (the full NLLHEJ prediction) clearly illustrates that there is a divergence currently unaccounted for, with the combined jet rates going from ≈ 4000 pb for 50 GeV jets, to ≈ 4600 pb for 30 GeV jets, and finally to ≈ 6100 pb for 10 GeV jets. This is clearly an effect from uncontrolled soft (and collinear) divergences. The question is, can we make our prediction more stable by changing which events we attempt to resum in HEJ ?.

Figure 6.11 is the same plot as fig. 6.10, but with the additional requirement on the rapidity of the third jet (see fig. 6.8). With this additional requirement, the increase from FKL only to FKL+UNO is still 10% for the 50 GeV jets, but is now only an increase of 13% for 30 GeV jets and 6% for 10 GeV indicating a much more stable prediction compared to fig. 6.10. Indeed, when we look at the full FKL+UNO+QQBAR+NR configuration (the full HEJ NLL prediction), we see remarkable agreement between the three lines which are all within errors of each other. This indicates a very stable prediction and is evidence that previously we were sensitive to an uncontrolled soft divergence which was severely damaging the convergence of the HEJ predictions.

A full breakdown of contributions from different configurations without this additional requirement on the rapidity of the third jet is given in the table in

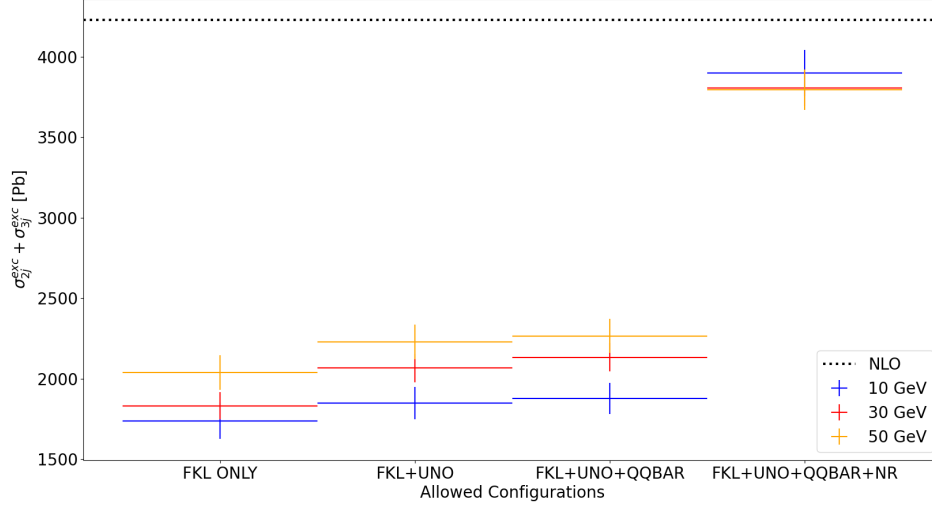


Figure 6.11: Combined $\sigma_{2j}^{exc} + \sigma_{3j}^{exc}$ jet rates against configuration options for 10, 30 and 50 GeV jets with the additional requirement that the third hardest jet be between the two hardest jets in rapidity. The FKL, FKL+UNO and FKL+QQBAR differ only in the 3j contribution, whereas there are contributions from non-resummable events to both the 2j and 3j rate.

fig. 6.12.

6.3.3 Correct treatment of non-FKL events

In creating the lines for fig. 6.11, we assumed that the treatment for NLL events (UNO/QQBAR) should be the same as that of the FKL events. In this section we look at these classifications in more detail, to try to come up with the closest equivalent treatment. If we are looking to study the corrections to the hard

Jet Cut FKL	Config Option				Exclusive 3j-rate*	Error
	UNO	qqbar	Non-Resummable			
30 Reweight	Discard	Discard	Discard		675	87
30 Reweight	Reweight	Discard	Discard		1026	66
30 Reweight	Reweight	Reweight	Discard		1456	365
30 Reweight	Reweight	Reweight	Keep		1874	368
30 Reweight	Discard	Discard	Keep		1094	132
30 Reweight	Keep	Keep	Discard		1532	164
30 Reweight	Reweight	Discard	Keep		1445	104
30 Reweight	Reweight	Keep	Discard		1239	121
50 Reweight	Discard	Discard	Discard		357	29
50 Reweight	Reweight	Discard	Discard		582	52
50 Reweight	Reweight	Reweight	Discard		612	50
50 Reweight	Reweight	Reweight	Keep		869	45
50 Reweight	Discard	Discard	Keep		615	40
50 Reweight	Keep	Keep	Discard		770	42
50 Reweight	Reweight	Discard	Keep		840	58
50 Reweight	Reweight	Keep	Discard		703	57

* Includes contribution to 2j rate from jet isolation cuts

Figure 6.12: Table of exclusive 3j rates using the `ATLAS_MET_JETS` analysis with modified p_{\perp} in jet clustering.

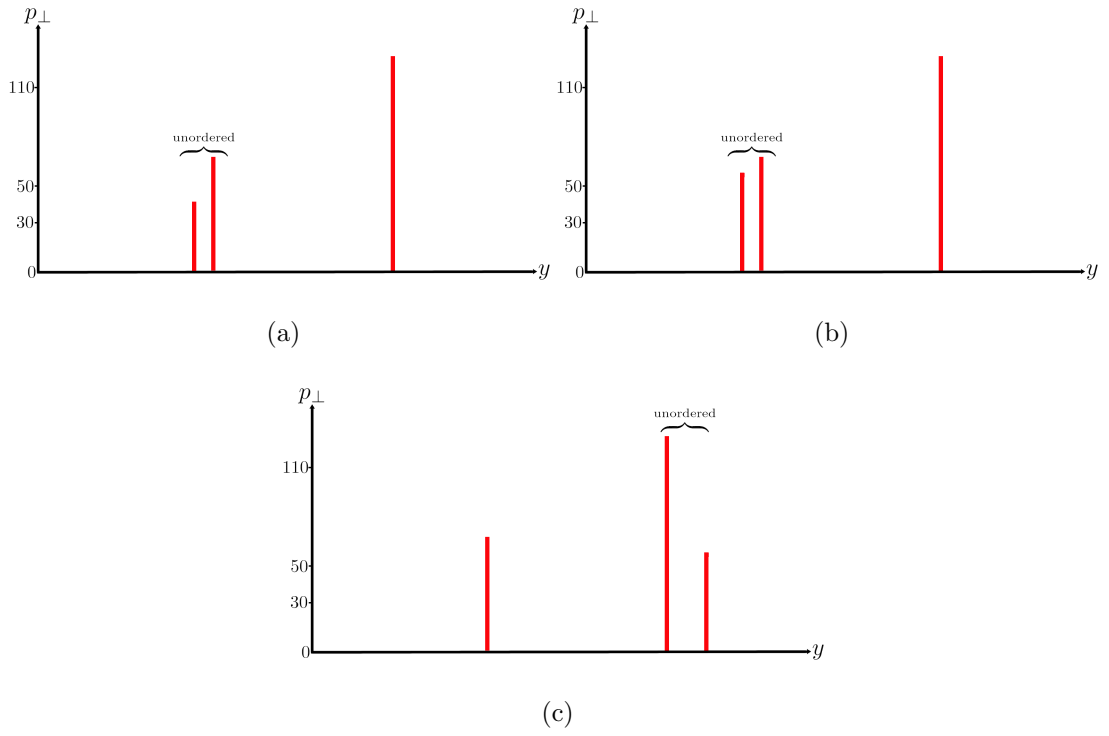


Figure 6.13: Example 3j unordered events, with the cut on the third jet being (a) lower than that of the other jets, leading to an impact factor with non-uniform cuts, (b,c) the same as the other jets, leading to an impact factor with uniform jet p_{\perp} cuts.

process described in section 6.3.1 and in fig. 6.4, then an unordered correction to this process should have the same jet p_{\perp} cuts as the jets in the hard process.

This means for our example of 50 GeV jets with one jet also above 110 GeV, we should allow unordered events with the additional jet also above 50 GeV. This would then exclude events with a third jet below 50 GeV like the one depicted in fig. 6.13a, but include events with a 50 GeV jet as part of an unordered current with either the other > 50 GeV jet (fig. 6.13b) or with the > 110 GeV jet (fig. 6.13c). As there is no resummation allowed between the component jets in an unordered current, we don't need to worry about the divergences which arose in the FKL case. We do, however, need to make sure that the p_{\perp} limit for resummation matches that of the 2j event and the FKL events in the 3j sample.

In practice, this means we should generate the fixed order samples with a minimum p_{\perp} , then match that p_{\perp} in the HEJ config file to be the same value, but then we can use the 50 GeV analysis for the unordered 3j events, regardless of this p_{\perp} choice. This ensures that all jets (the two hardest and the additional jet) are above 50 GeV for the unordered description.

This will lead to events which look like fig. 6.13a, but then in the analysis get classified as 2 jet events. We have choice here to add in an extra restriction that there still be 3 jets in the final sample or just look at the 3j rate in the analysis output. Both options will distort the result of the jet isolation cuts in the ATLAS_MET_JETS analysis, but this effect was found to be very small: around 0.6% of the exclusive 2j rate was coming from 3j events with one jet vetoed.

In practice then, we implement a custom HEJ analysis which filters events from the HEJ resummation before they reach the rivet analysis. We define a set of “test jets” which we require to pass the jet cuts and then add to this set jets depending on the identified configuration. For backward unordered emissions and backward $q\bar{q}$ emissions, we look at the first 2 and the final jet (ordered by rapidity), and for forward unordered emissions and forward $q\bar{q}$ emissions we look at the first jet and final two jets (again ordered by rapidity). For central $q\bar{q}$ emissions we require the $q\bar{q}$ jets to be above 50 GeV and then only test the outer jets in rapidity. Then we demand that all of the test jets are above 50 GeV and at least one of the test jets is above 110 GeV (80 GeV for VBF region), and give any of the events which pass this restriction to the rivet analysis to be analysed further.

Correct treatment of non-resummable events

At this stage we accept any non-resummable event which passes the analysis, with the jet clustering set to match the fixed order input and the HEJ resummation.

6.3.4 Full breakdown of best ATLAS_MET_JETS description

To summarise this section and the previous section. For a fixed order input of $p_{\perp;in}$ jets. At leading log for all n -jet samples we have

FKL events

- Resummation $p_{\perp}, p_{\perp;r} = p_{\perp;in}$.
- In analysis, $p_{\perp;analysis} = p_{\perp;r}$,
- $p_{\perp,y_{max}}, p_{\perp,y_{min}} > 50$ GeV,
- $\max(p_{\perp,y_{max}}, p_{\perp,y_{min}}) > 110$ GeV.

Non-Resummable events

- $p_{\perp;analysis} = p_{\perp;in}$,
- $p_{\perp,leading} > 110$ GeV,
- $p_{\perp,subleading} > 50$ GeV.

UNO/QQBAR events

- Resummation $p_{\perp}, p_{\perp;r} = p_{\perp;in}$.
- In analysis, $p_{\perp;analysis} = p_{\perp;r}$,
- $\max(\{p_{\perp} \text{ for jets in currents}\}) > 110$ GeV,
- $\min(\{p_{\perp} \text{ for jets in currents}\}) > 50$ GeV,
- (if central $q\bar{q}$) $\min(\{p_{\perp} \text{ for jets in } q\bar{q} \text{ vertex}\}) > 50$ GeV,

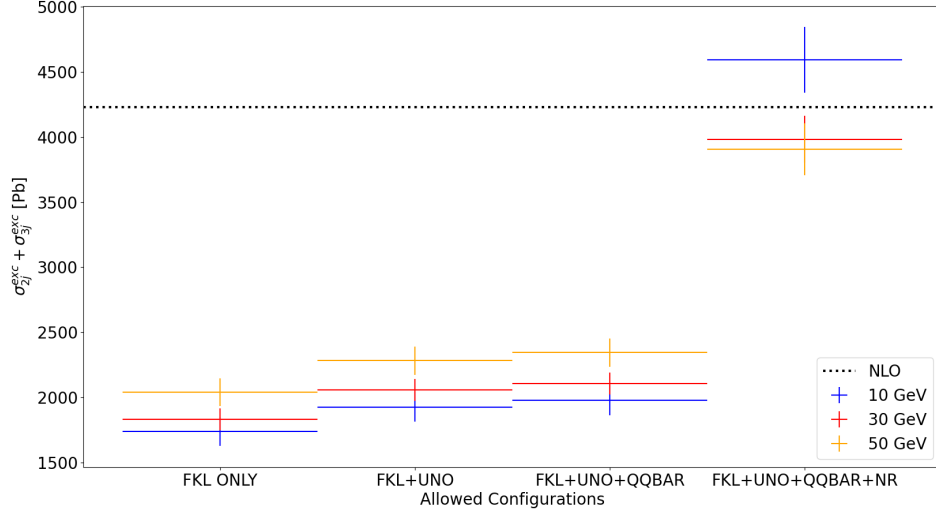


Figure 6.14: Combined $\sigma_{2j}^{exc} + \sigma_{3j}^{exc}$ jet rates against configuration options for 10, 30 and 50 GeV jets using the breakdown of HEJ configurations in section 6.3.4. The FKL, FKL+UNO and FKL+QGBAR differ only in the 3j contribution, whereas there are contributions from non-resummable events to both the 2j and 3j rate.

6.3.5 Quantitative changes to the jet rates

Figure 6.14 shows the combined $\sigma_{2j}^{exc} + \sigma_{3j}^{exc}$ jet rates against configuration options for three different choices of minimum jet p_{\perp} with the configuration breakdown outlined in the previous section. Shown also again is a black dashed line representing the total NLO cross section. The non-resummable contribution here includes contribution from 2j and 3j non-resummable events.

Looking at the full HEJ description on the furthest right, we see that the 50 GeV and 30 GeV lines are very similar in value and are below NLO. Adding in the 4 and 5 jet FKL and non-resummable contributions increases the 30 GeV cross section by roughly 10%, making the HEJ prediction 5% large than NLO (but easily within error bars of each other with the current level of statistics). This is similar agreement to what we have seen for other processes. The 10 GeV line however is already much larger than NLO, but is still much smaller than it was in fig. 6.10 indicating that there is a divergence in the non-resummable events as one jet becomes soft. However as this is in the non-resummable contribution, we do not have direct control over this divergence except to possibly remove the 3 jet non-resummable contribution entirely. Any difference in the non resumable contributions of the 30 and 50 GeV samples cancels partly with the differences

in the HEJ descriptions of those lines (in the third bin) leading to a very similar result for 30 and 50 GeV jets.

6.4 Comparison of HEJ and multijet merged predictions for selected experimental observables

We now return to the initial task of making predictions for the `ATLAS_MET_JETS` analysis. The setup for the analysis is given in section 6.1 and the setup for the fixed order input is unchanged from what was described in section 6.2. From the fixed order, we perform the resummation using HEJ2 calculating the FKL, unordered/ $q\bar{q}$ and non-resummable components separately for both 2j and VBF regions using the procedure outlined in section 6.3.4. These contributions were then combined together to form the full HEJ prediction.

For some observables which we have previously seen to be minimally impacted by resummation, we performed a matching to NLO using the procedure outlined in section 3.4. This includes the two p_\perp observables and the missing energy, leaving the jet rates, dijet rapidity separation, dijet angular separation and dijet invariant mass observables matched only to LO. Figures 6.15 and 6.16 shows the reweighting factors of $\frac{\sigma_{2\text{-jet}}^{\text{NLO}}}{\sigma_{2\text{-jet}}^{\text{HEJ@NLO}}}$ and $\frac{\sigma_{2\text{-jet}}^{\text{HEJ}}}{\sigma_{2\text{-jet}}^{\text{HEJ@NLO}}}$ respectively for the three NLO matched observables. For each we see that the behaviour seen is similar to that of fig. 4.16 with the NLO ratio being flat for large p_\perp , showing that the HEJ prediction is not missing any physics present in the NLO calculation in this region. For the HEJ ratios, we see all the ratios rise slowly as p_\perp increases showing that these observables are less sensitive to higher order corrections from high energy logarithms.

In this section we will compare the differences seen between HEJ and `MEPS@NLO` for a selection of observables from this study. There are 52 plots we made predictions for as part of this analysis: 2 different number of leptons \times 2 different lepton flavours \times 2 different regions (2j/VBF) \times 7 observables - 4 as they didn't look at rapidity plots in the 2j region. As such only a sample of each observable is shown in this chapter. A full prediction with all of the plots is given as appendix B.

We start our discussion by looking at the cross section as a function of exclusive jet rates depicted in fig. 6.17. In red is the `MEPS@NLO` line provided by ATLAS and in

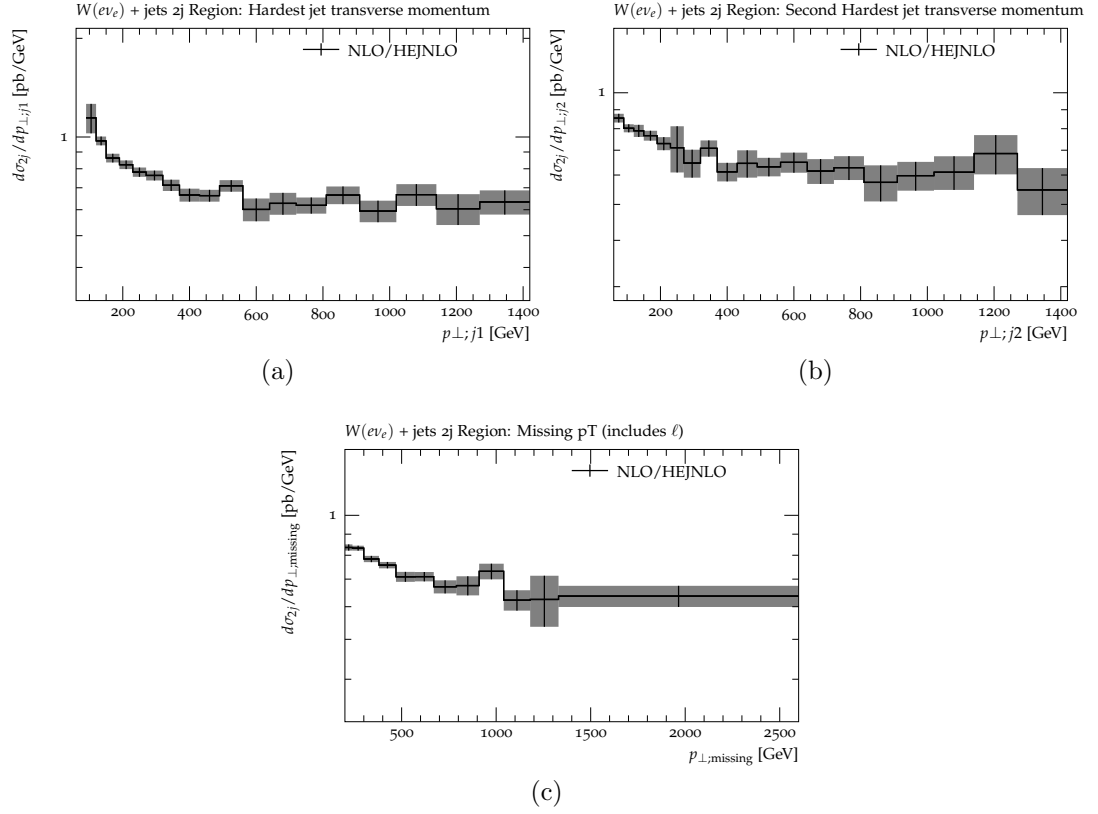


Figure 6.15: Plot of the ratio $\frac{\sigma_{2\text{-jet}}^{\text{NLO}}}{\sigma_{2\text{-jet}}^{\text{HEJ@NLO}}}$ for one identified electron in the final state in the 2 jet region for (a) hardest jet transverse momentum (b) second hardest jet transverse momentum (c) missing transverse momentum.

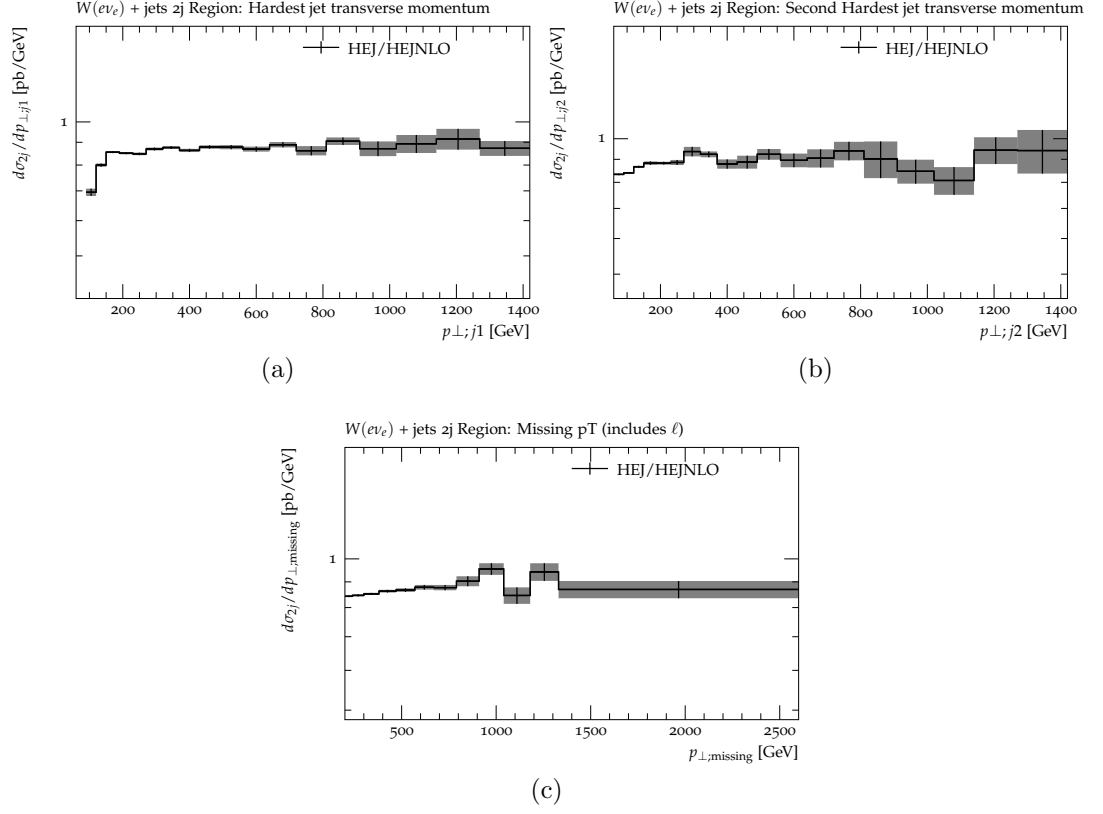


Figure 6.16: Plot of the ratio $\frac{\sigma_{2\text{-jet}}^{\text{HEJ}}}{\sigma_{2\text{-jet}}^{\text{HEJ@NLO}}}$ for one identified electron in the final state in the 2 jet region for (a) hardest jet transverse momentum (b) second hardest jet transverse momentum (c) missing transverse momentum.

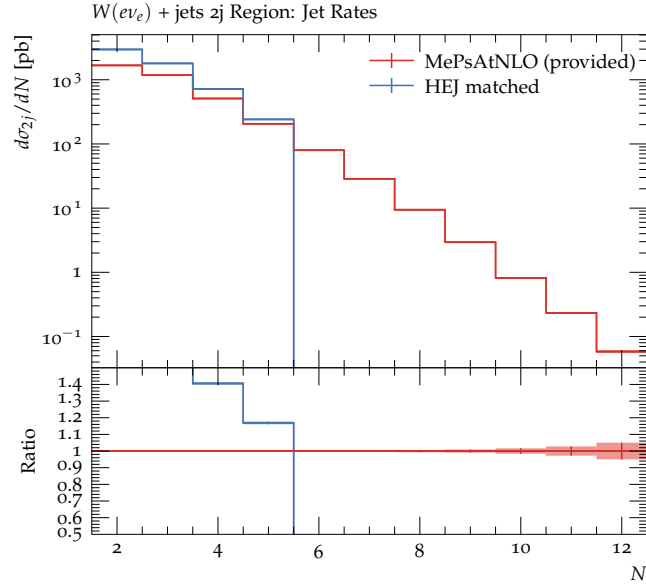


Figure 6.17: Plot of the total cross section as a function of number of jets for the ATLAS_MET_JETS study comparing HEJ and MEPS@NLO with one identified charged lepton in the final state. Decay is in the electron channel and in the 2j region.

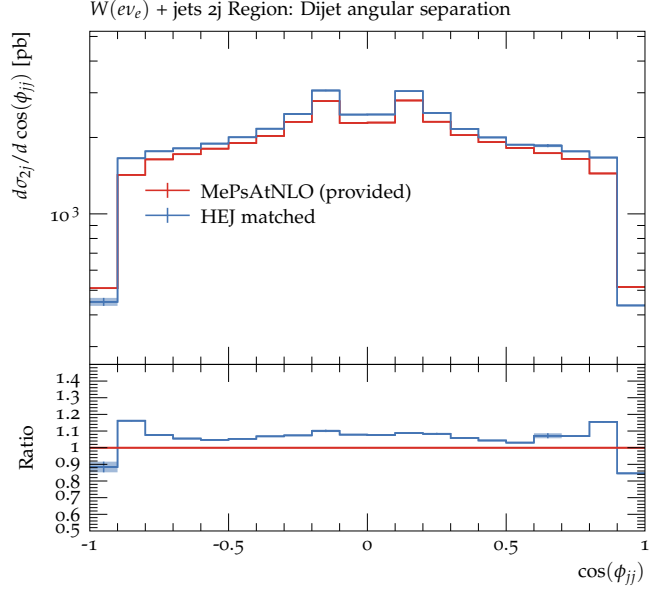


Figure 6.18: Plot of the total cross section as a function of dijet angular separation for the hardest two jets in the `ATLAS_MET_JETS` study comparing HEJ and `MEPS@NLO` with one identified charged lepton in the final state. Decay is in the electron channel and in the 2j region.

blue is the HEJ prediction. Note that although the `MEPS@NLO` matching procedure is unitary - i.e. it doesn't change the total cross section, the matching is done for inclusive W and Z production and not inclusive W/Z plus two jet production. This is important as contributions move between 0 and 1 jet rates to 2+ jet rates and vice-versa. As a consequence of this and the requirement of having at least two jets in the analysis, we do not expect that the `MEPS@NLO` and pure NLO lines in any of these distributions to integrate to the same values. For this distribution, each bin in the HEJ prediction will contain contributions from FKL and non-resummable events, with the rates from three jets onwards also including contributions from subleading configurations. The HEJ result is truncated at five jets as it was found that the contribution from five jets to the total HEJ prediction was around or below a percent. While we include contributions from higher jet multiplicities using the HEJ fixed order generator, they are not shown on this plot as they do not include contributions from non-resummable configurations which cannot be generated by the `HEJFOG` so are not LO accurate. In each of the regions studied, the jet rates (and thus the total cross section) was found to be higher in HEJ compared to `MEPS@NLO`, despite the HEJ cross section being similar to pure NLO.

This difference in the cross sections is the reason for the difference in the

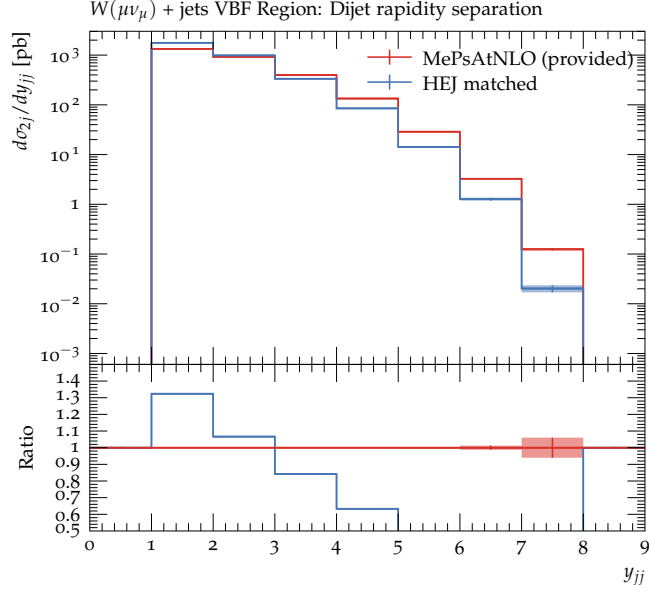


Figure 6.19: Plot of the total cross section as a function of dijet rapidity separation for the ATLAS_MET_JETS study comparing HEJ and MEPS@NLO in the VBF region with leptonic decay into muon + neutrino in the VBF region.

dijet angular separation observables depicted for one channel in fig. 6.18, which otherwise has a flat ratio between HEJ and NLO. The angular separation plots were found to be peaked either side of 0 for the 2j region with the VBF cuts pushing the peaks further from the centre.

Figure 6.19 shows the cross section as a function of the dijet rapidity separation. The authors of the analysis decided only to measure this distribution in the VBF region so this is what we present here. In this plot we see a big difference in the HEJ and MEPS@NLO predictions which we have come to expect from previous studies. This is down to a number of factors - rapidity separation is known to be highly sensitive to higher order logarithms that we resum in the HEJ framework (see the discussion around fig. 4.14), especially when the separation becomes large. This difference becomes more apparent when we introduce VBF cuts which we have shown directly lead to an increase in the impact of the high energy logarithms.

As shown in previous studies, the ratio between HEJ and NLO remains flat as a function of jet transverse momenta away from low values. It is interesting to see then that the ratio remains roughly flat between HEJ and MEPS@NLO depicted in fig. 6.20 for both the hardest jet p_{\perp} and the second hardest jet p_{\perp} . This shows that these observables (away from low values of p_{\perp}) are not particularly sensitive to the corrections from high energy logarithms or from the corrections from the parton shower. The latter case is not particularly surprising as the physics from

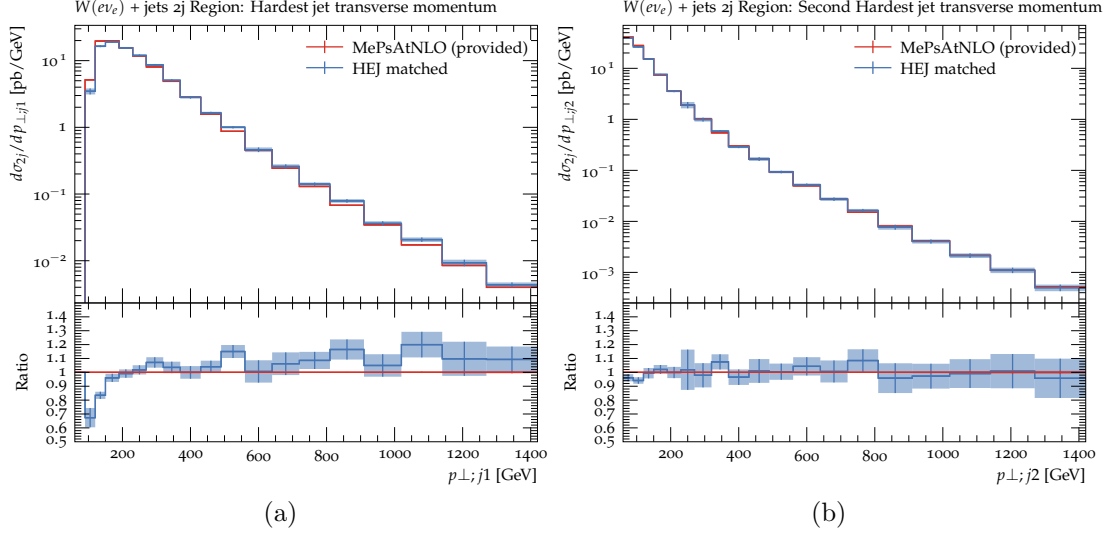


Figure 6.20: Plot of the total cross section as a function of the transverse momentum of the (a) hardest jet (b) second hardest jet for the `ATLAS_MET_JETS` study comparing HEJ and `MEPS@NLO` with one identified charged electron in the final state. Decay is in the electron channel and in the 2j region.

the parton shower are most relevant for soft and collinear emissions.

Included also here is the same plot of transverse momenta of the hardest jets, except this time for Z plus jets. Figure 6.21 shows the cross section as a function of the hardest and second hardest jet momenta for the Z decaying in the electron channel. Compared to the flat ratio we observed in the W plus jet plots discussed previously, we see that the ratio here is almost linearly decreasing between the two predictions. The `MEPS@NLO` line also peaks one bin earlier than the HEJ prediction.

At this point we have to ask the question if this difference is mainly due to effects of high energy logarithms resummed by HEJ or due to parton shower merging. Indeed we look at the difference between HEJ and pure NLO we see that the ratio is again flat at high values of p_{\perp} , similar to what was observed previously. The difference here is really due to a difference in the NLO and `MEPS@NLO` predictions, and the cause is not immediately obvious. It could perhaps be explained by looking at the effect of the lower multiplicity samples included in the `MEPS@NLO` calculation (which is based off of inclusive V production, not inclusive V plus jets production) where tuning the parameters can move contributions between jet multiplicities. Another explanation of the difference in behaviour here between W and Z emissions could involve the large difference in the lepton cuts highlighted in fig. 6.1b. Finally, we may need to look at PDF effects and the allowed channels for W and Z production to further investigate the differences in these processes.

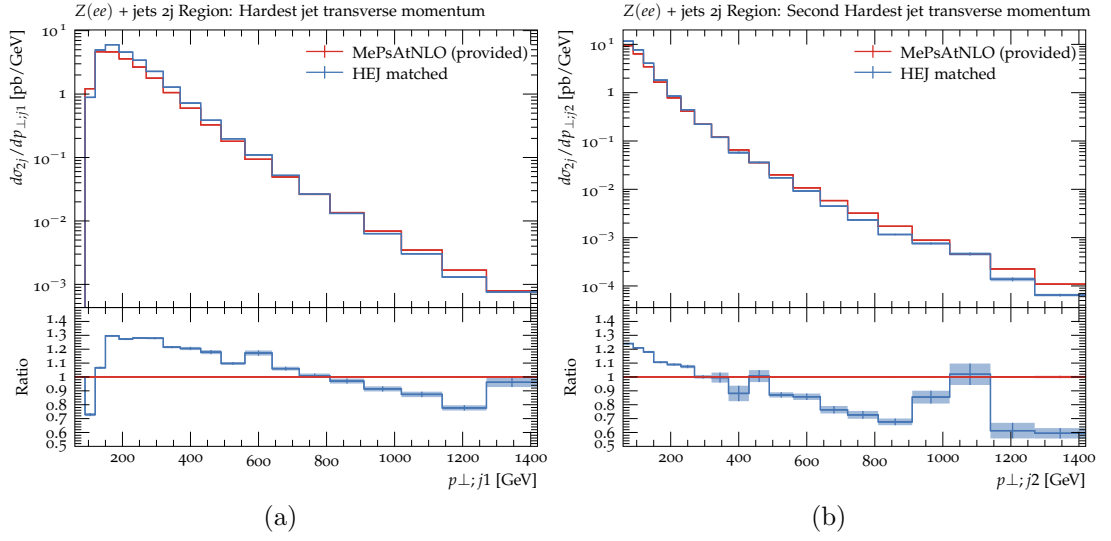


Figure 6.21: Plot of the total cross section as a function of the transverse momentum of the (a) hardest jet (b) second hardest jet for the `ATLAS_MET_JETS` study comparing HEJ and `MEPS@NLO` with two identified charged electrons in the final state. Decay is in the electron channel and in the 2j region.

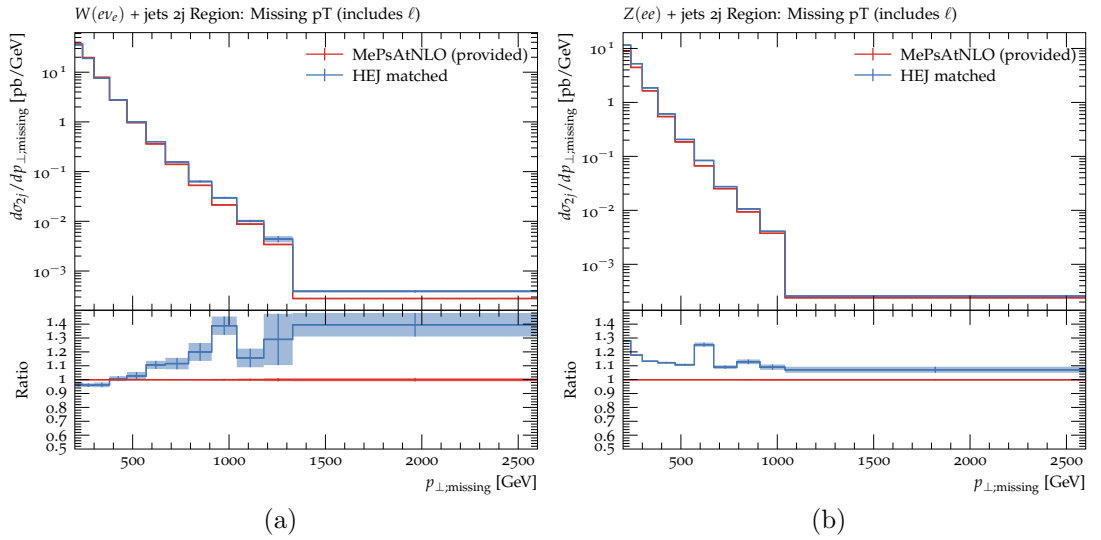


Figure 6.22: Plot of the total cross section as a function of the missing transverse momentum for the `ATLAS_MET_JETS` study comparing HEJ and `MEPS@NLO` with (a) one (b) two identified charged lepton in the final state. Decay is in the 2j region.

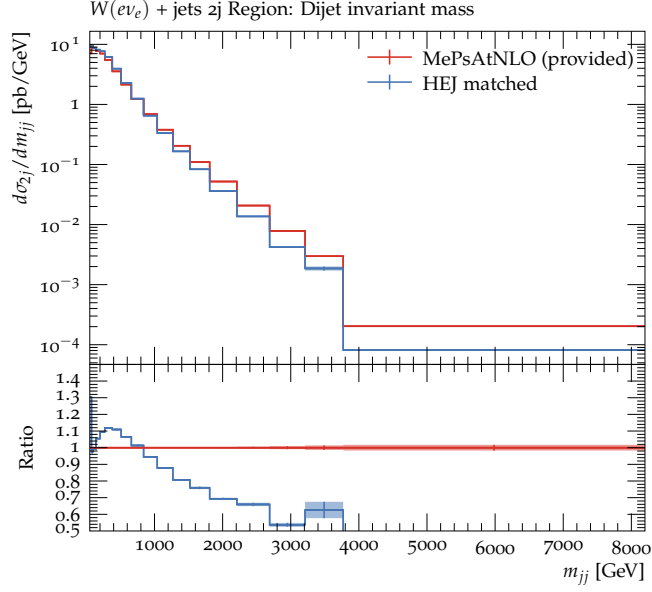


Figure 6.23: Plot of the total cross section as a function of the dijet invariant mass for the `ATLAS_MET_JETS` study comparing HEJ and `MEPS@NLO` with one identified charged lepton in the final state. Decay is in the electron channel and in the 2j region.

Next, we look at the cross section as a function of the “missing transverse momentum” which in this case has been defined to be the combined contribution from all neutrinos and all charged leptons identified in the event. Figure 6.22 shows this observable plotted for both W plus jets and Z plus jets to highlight the differences between the two. For W plus jets we see the ratio rise significantly with p_{\perp} whereas for Z plus jets the ratio falls and remains relatively flat.

Looking a little deeper, we can show that the ratio between HEJ and pure NLO is actually pretty flat for both W and Z plus jets, but the ratio between NLO and `MEPS@NLO` changes significantly for W plus jets instead of staying roughly flat for Z plus jets. This difference then is mainly due to the effects of merging with the parton shower and an asymmetry between the W and Z predictions, similar to what was seen above in the p_{\perp} observables.

Finally, we look at the plot of the dijet invariant mass depicted in fig. 6.23. The dijet invariant mass is an observable sensitive to both the p_{\perp} of the jets as well as their rapidity difference, so in principle we should see effects here from both high energy logarithms and logarithms resummed by the shower which will grow with a large separation of transverse scales. In the large m_{jj} region we are going to see an impact from events with large rapidity separation which leads to large high energy logarithms resummed in HEJ, but also we will have the impact from events

with more than two jets where all the transverse momenta is clustered in two jets, leaving further jets to be softer. This large difference in scales will lead to large logarithms in the transverse scales which are resummed in the parton shower. So the ideal prediction for this observable should really include contributions resumming both high energy logarithms and logarithms in the transverse scales.

There is work ongoing on matching the HEJ formalism and parton shower formalism in HEJ +Pythia [95], which has sometimes proved necessary to produce the best possible predictions for observables like discussed above which are sensitive to both effects.

6.5 Conclusions and summary of ATLAS_MET_JETS study

In this chapter we have presented changes to the HEJ formalism for dealing effectively with asymmetric jet cuts in the fixed order sample. We presented a formalism for dealing with each of the identified types of kinematic configurations and discussed how we can combine these together to consistently deal with the HEJ resummation methods and the treatment of poles. It should be stated that some of the shortcomings will be addressed by a full next-to-leading logarithm resummation planned as part of an upcoming HEJ release.

We then discussed the impact of high energy corrections for an ongoing ATLAS study into jets at the LHC with large missing energy due to the presence of a W or Z/γ emission. This study in particular looked at multiple regions where the jet cuts on the hardest jets were asymmetric requiring one to be above 50 GeV and the other to be above 80/110 GeV depending on the region. For this study we looked at comparing the HEJ prediction using the formalism for dealing effectively with asymmetric jet cuts we have constructed with the parton shower matched result provided by ATLAS. In some observables we saw a significant difference between the two which we sometimes deduced as the effect of high energy logarithms, sometimes from the effect of the shower and sometimes the effect of both.

We deduce then that both the shower corrections and high energy logarithms are important for the best predictions for this analysis. Work is ongoing to construct a framework for combining both of these corrections into one software package.

Chapter 7

Impact of high energy resummation at a future circular collider

In this chapter, we wrap up our discussion on High Energy Jets by having a first look at the effect of HEJ resummation at a future circular collider (FCC). We start by discussing briefly some of the relevant engineering predictions for a detector in a future circular collider from recent reports [96–99] and how these will be important in defining new limits on the phase space we can probe in experiment. We then discuss the impact of high energy logarithms at such an FCC by looking at the effect on distributions for $W + \text{jets}$ as we increase the centre of mass energy.

7.1 Considerations on construction of a future circular collider

Proposed plans for a FCC [96] estimate a potential to reach a centre of mass energy of 100 TeV and beyond with an integrated luminosity of around $20ab^{-1}$ [97]. Such a collider would be used to search for and study BSM particles with masses beyond what is capable of being produced at the LHC. However as we have already seen at the LHC, QCD interactions are extremely important in describing the phenomena at a pp collider, even whilst trying to probe the electroweak sector [98]. Important QCD effects include both “initial state” effects probing the structure of the proton through the PDFs in the “ultra-low x region” of $x < 10^{-5}$ [99], and “final state” effects from enhanced QCD logarithmic corrections.

CoM Energy and Jet cut	σ_{HEJ} [pb]	σ_{NLO} [pb]	$\sigma_{\text{HEJ}}/\sigma_{\text{NLO}}$
13 TeV, $p_{\perp} > 30$ GeV	2.68×10^5 $\pm 4.76 \times 10^4$	2.83×10^5 $\pm 1.08 \times 10^4$	0.95 ± 0.17
50 TeV, $p_{\perp} > 30$ GeV	1.61×10^6 $\pm 2.93 \times 10^5$	1.46×10^6 $\pm 4.92 \times 10^4$	1.11 ± 0.20
100 TeV, $p_{\perp} > 30$ GeV	3.55×10^6 $\pm 6.45 \times 10^5$	3.10×10^6 $\pm 1.21 \times 10^5$	1.14 ± 0.21
100 TeV, $p_{\perp} > 60$ GeV	1.00×10^5 $\pm 1.66 \times 10^5$	1.01×10^6 $\pm 2.77 \times 10^4$	0.99 ± 0.17
100 TeV, $p_{\perp} > 80$ GeV	5.62×10^5 $\pm 8.95 \times 10^4$	6.02×10^5 $\pm 1.68 \times 10^4$	0.93 ± 0.15

Table 7.1: Table of inclusive cross sections for W plus jets at a range of centre of mass energies and with a selection of minimum jet p_{\perp} cuts.

When discussing future colliders, it is also important to discuss the impact of the additional phase space which proposed detectors will be able to probe. Proposed targets for jet tracking have the desired rapidity detection as high as $|y| \approx 6$ units of rapidity in order to study the tails of distributions in VBF studies [97]. This increase in rapidity will allow us to probe the very high Δy separation between jets where we have seen significant differences between HEJ resummed predictions and fixed order where the high energy logarithms are enhanced.

Targets for the lepton calorimeters include detection of leptons with rapidity $|y| < 5$, which will allow the study of collisions where there is a large separation in rapidity between an emitted W boson and its parent quark line. This is a significant increase from the LHC where region for lepton detection was quite narrow. This increase will allow for a probe of the dependence on the prediction of the position of W boson in rapidity relative to the QCD interactions.

With an increase to centre of mass energy also comes an increase in the pileup at the collider, which will make signals of interest more difficult to cleanly study. This will lead to the need for triggers which start at a higher energy than what was needed at the LHC.

7.2 Impact of HEJ resummation at large centre-of-mass energies

In this section we look at the HEJ leading log predictions for W plus jets at a potential future circular collider at $\sqrt{s} = 100$ TeV. The setup was designed to have minimal

selection cuts on the phase space to be similar to a potential detector. Jets were clustered with jet parameter $R = 0.4$ and with a range of minimum p_\perp cuts. Jets were only counted if they had an absolute value of rapidity less than 4.7. W bosons were required to decay in the electron channel where the electrons were restricted to having p_\perp above 20 GeV and were required to have an absolute value of rapidity less than 2.5.

The central scale choice was chosen to be $\mu_F = \mu_R = H_T/2$ and scale errors shown in this section are estimated by varying μ_F and μ_R independently by factors of 2, similar to what was done in other chapters.

The generation was done in a similar way to section 4.4, using Sherpa [65] and COMIX [80] with the extension of OpenLoops [81] for NLO calculations. We used the NNPDF3.1 NLO PDF set [91] as provided by LHAPDF6 [85].

Table 7.1 shows the total inclusive integrated cross section for HEJ, NLO and the ratio between the two with errors quoted being from scale variations around the central scale. From this table we can see the effect on the cross section when we increase the centre of mass energy keeping the minimum jet p_\perp the same as well as the effect of changing the jet p_\perp whilst keeping the centre of mass energy fixed at 100 TeV. Referring back to eq. (2.53), the only part of the phase space integral that is going to change if we increase the centre of mass energy is,

$$x_a(p)x_b(p)f(x_a(p), Q^2)f(x_b(p), Q^2). \quad (7.1)$$

Another way of saying this is that changing our centre of mass energy will not change our result for the matrix element calculation, but will allow us to both probe a different region of the PDFs, and probe configurations which were not kinematically accessible at 13 TeV. From fig. 2.2 we know that in the low x limit the gluon PDF dominates over the u and d PDFs and increases sharply as x decreases further. This explains why in table 7.1 we see the HEJ and NLO cross sections increase as we increase the centre of mass energy. What is interesting is that the HEJ result increases slightly more than the NLO result as we increase the centre of mass energy. Going from 13 TeV to 100 TeV, the HEJ result increases by a factor of about 13 whereas the NLO result increases by a factor of about 11.

This is in contrast to the effect of increasing the jet p_\perp cut at 100 TeV, where the HEJ result falls faster as a function of jet p_\perp than NLO and we can see that at $p_\perp = 80$ GeV the ratio of HEJ to NLO is the same (within errors) as the ratio at

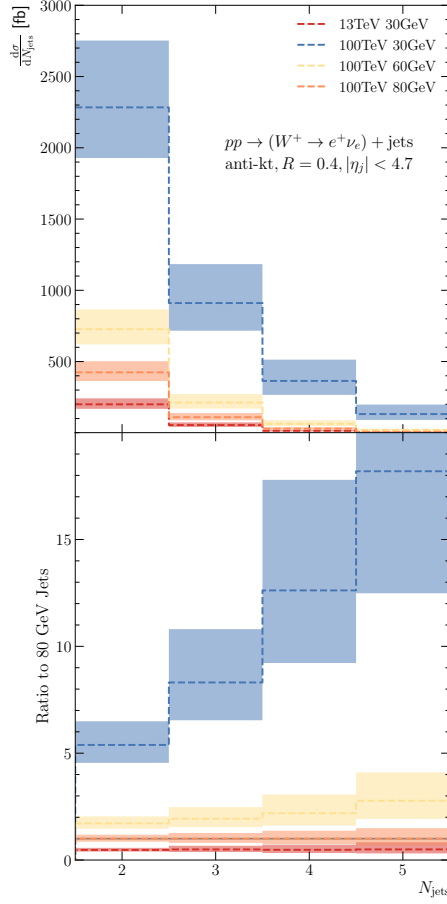


Figure 7.1: Plot of two, three and four jet rates in leading log resummed HEJ prediction for W plus jets where jets are clustered at $R = 0.4$. The red line is at $\sqrt{s} = 13$ TeV with jets counted above 30 GeV, whilst the other lines are at $\sqrt{s} = 100$ TeV with jets counted above (dark blue) 30 GeV (yellow) 60 GeV (light blue) 80 GeV.

13 TeV with a 30 GeV jet cut. Since most of the cross section in p_{\perp} distributions appears in the low p_{\perp} region, it makes sense that the cross section decreases sharply as we increase the jet p_{\perp} cut. Since HEJ will typically have more jets counted than NLO, it makes sense that the HEJ prediction falls faster than NLO as we increase the jet cut.

Figure 7.1 shows the cross section as a function of jet rates for HEJ calculated at $\sqrt{s} = 13$ TeV with 30 GeV jets and $\sqrt{s} = 100$ TeV with 30, 60 and 80 GeV jets. The ratio plot shown is the ratio to the $\sqrt{s} = 100$ TeV, $p_{\perp} > 80$ GeV line. Immediately we see that ratio between the blue line and orange line increases for higher jet multiplicities which is due to most of the cross section being concentrated in the low p_{\perp} region. With each additional jet we are requiring above 80 GeV, we are excluding the jets that would be counted 30-80 GeV range

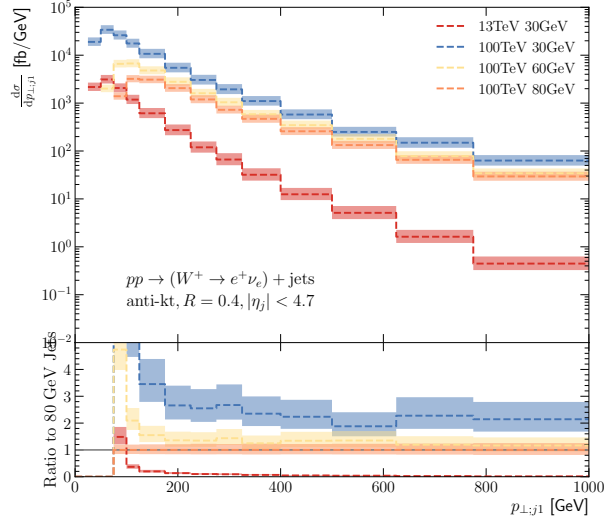


Figure 7.2: Plot of transverse momentum of the hardest jet in leading log resummed HEJ prediction for W plus jets where jets are clustered at $R = 0.4$. The red line is at $\sqrt{s} = 13$ TeV with jets counted above 30 GeV, whilst the other lines are at $\sqrt{s} = 100$ TeV with jets counted above (dark blue) 30 GeV (yellow) 60 GeV (light blue) 80 GeV.

which contains a significant contribution to the cross section. We can also see that the ratio between the $\sqrt{s} = 13$ TeV with 30 GeV jets line and the $\sqrt{s} = 100$ TeV with 80 GeV jets line is roughly constant across the different jet multiplicities, showing that the higher p_{\perp} cut ends up compensating for the increase in the centre of mass energy.

Figure 7.2 shows the cross section as a function of the p_{\perp} of the hardest jet. As we saw in table 7.1, the total cross section increased as a function of centre of mass energy, so we expect the blue line to be much larger than the red line and this is the case here with a similar shape between the two but with a slightly different slope. Increasing the jet p_{\perp} cut going from the blue line to the yellow and orange line shifts the peak of the distribution further from zero, but ultimately the ratio between these 3 lines tends to a constant value for large enough p_{\perp} . Similar behaviour can be seen in fig. 7.3 when looking at the cross section as a function of dijet invariant mass. We see biggest differences between the lines occur in the low m_{jj} region with the ratios tending to a flat value in the large m_{jj} region despite the fact that there are clear differences between the setups when there is a large rapidity separation between jets (fig. 7.4). One could argue that the reason that we don't see significant differences at large m_{jj} is due to the computation limits of our simulation. At $m_{jj} < 4$ TeV we are already spanning 6 orders of magnitude in the cross section, and including contributions with an

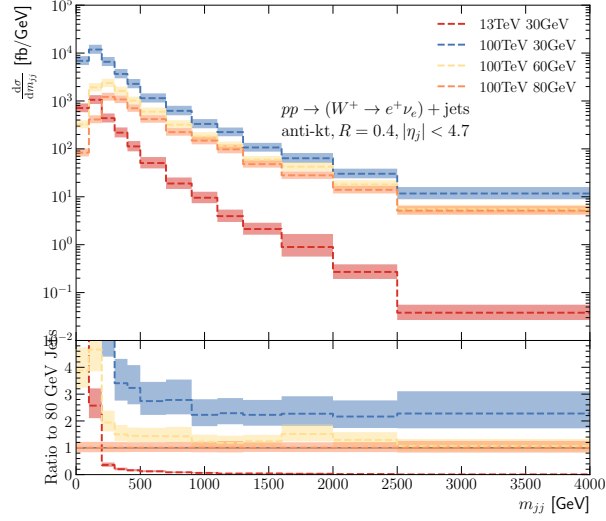


Figure 7.3: Plot of invariant mass between the hardest two jets in leading log resummed HEJ prediction for W plus jets where jets are clustered at $R = 0.4$. The red line is at $\sqrt{s} = 13$ TeV with jets counted above 30 GeV, whilst the other lines are at $\sqrt{s} = 100$ TeV with jets counted above (dark blue) 30 GeV (yellow) 60 GeV (light blue) 80 GeV.

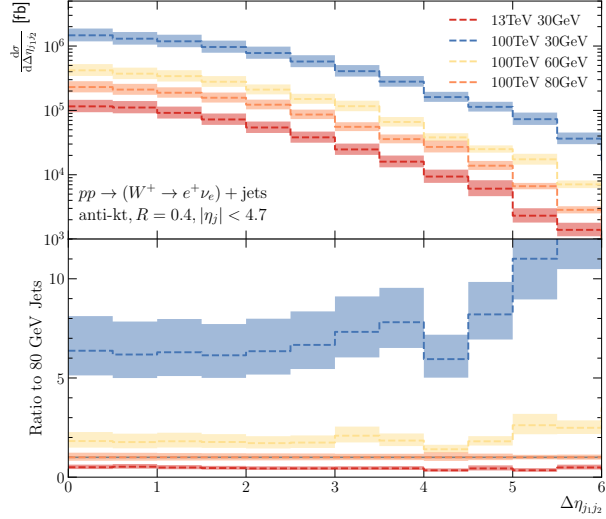


Figure 7.4: Plot of rapidity separation between the hardest two jets in leading log resummed HEJ prediction for W plus jets where jets are clustered at $R = 0.4$. The red line is at $\sqrt{s} = 13$ TeV with jets counted above 30 GeV, whilst the other lines are at $\sqrt{s} = 100$ TeV with jets counted above (dark blue) 30 GeV (yellow) 60 GeV (light blue) 80 GeV.

high enough invariant mass where we see significant impact from large Δy_{jj} jets would be computationally challenging.

7.3 Conclusions and final remarks

In this chapter we discussed the impact of the increase in centre of mass energy in going from the LHC to a potential FCC. Such an upgrade will hopefully also come with improvements to detectors allowing us to probe never before accessible regions of phase space which are important for certain physical processes. In comparing HEJ and fixed order, we saw larger differences in the total integrated cross sections between the two as we increased the centre of mass energy but this difference was reduced as we increased the jet p_{\perp} cut.

This increase in available phase space will be particularly important for VBS and VBF studies, where we have seen a large impact of high energy logarithms at high jet rapidity separation. We expect that similar to the LHC, studies of VBS/VBF at a FCC will see that high energy logs from QCD topologies will be important in accurately describing the tails of differential distributions.

Chapter 8

Summary and future studies

In order to cleanly study electroweak interactions and search for BSM physics at hadron colliders, an accurate description of QCD phenomena is necessary. In this thesis we have studied the perturbative stability of QCD in the limit of high energy scattering using the High Energy Jets formalism. Our discussions began in chapter 2 where we presented a brief overview of the Standard Model and the technology required for performing amplitude calculations. We presented our conventions and tools that would be important for framing the work presented in the following chapters in a broader context. In chapter 3 we presented an overview of the HEJ methodology for resumming large logarithms in $\frac{\hat{s}}{t}$ that appear to all orders in perturbation theory and which can damage the QCD perturbative expansion. We discuss how to construct amplitudes which are exact in the high energy MRK limit including leading log accurate contributions from all order real and virtual corrections. It is this framework that we build upon in chapters 4 to 6 where we look at extending the HEJ description to include resummation for new, experimentally relevant processes and setups.

In chapter 4, we presented an approach to resumming logarithms of the form $\alpha_W^4 \alpha_s^{k+2} \log^k(\hat{s}/p_t^2)$ which appear in the QCD contribution to same sign WW pair production as a form of vector boson scattering. In studies of vector boson scattering it is common to introduce cuts on the rapidity separation and invariant mass between the hardest jets in order to try and separate the contribution from pure electroweak interactions and those involving QCD interactions. However these cuts directly enhance the logarithmic contributions in the QCD perturbative expansion, making them important to include in the QCD contribution that

remains after the cuts. To study the effect of these logs we implemented same sign W pair resummation in the latest version of HEJ2 and compared the resummed predictions to that of next-to-leading order for the process $pp \rightarrow e^\pm \nu_e \mu^\pm \nu_\mu + \geq 2j$ using the setup of a recent CMS analysis. We found that although the total cross sections of the two methods were very similar, this was due to cancellations across phase space with this particular setup. When we looked at distributions of experimental observables, we found that there were some that were sensitive to higher order corrections, particularly in the tails of the distributions. We further found that the effect of the VBS cuts was significant in the breakdown of the perturbative expansion. We saw that for this study the three jet rate (without lepton isolation cuts) was now slightly larger than the two jet rate with the four jet rate only being suppressed by a factor of about a half compared to the two jet rate. Finally, we looked at the impact of matching the HEJ resummed predictions to NLO in order to include full NLO accuracy as well as the LL accuracy. We concluded the chapter by discussing which of the observables studied were sensitive to NLO corrections, which were sensitive to LL corrections and which were sensitive to both or neither.

In chapter 5 we presented the results for the first of two ongoing ATLAS analyses sensitive to higher order corrections beyond next-to-leading order. We described the way in which we can produce a ratio of the inclusive 3-jet rate to the inclusive 2-jet rate, R_{32} for a HEJ leading log accurate resummed prediction and for fixed order to compare the two as a function of a selection of experimental observables. Due to delays in the analysis being published outside of our control, we were not able to compare with data at the time of writing so could only compare against fixed order calculations. However this still proved interesting to discuss as there were distributions where there were significant differences in shape between HEJ and fixed order where the errors from varying the central scale choice typically underwent a large amount of cancellation when taking the ratio R_{32} for HEJ predictions, leading to a line with relatively small variation bands. We also studied as part of this analysis the effect of the setup on predicting the average number of jets as a function of the same experimental observables discussed in the R_{32} distributions. Here we again saw significant differences in shape between HEJ and NLO, even when restricting the scope of the comparison to where the lines stayed below what was physical of the NLO prediction ($\langle N \rangle = 3$). We also saw that some observables were sensitive to corrections from events with up to 5 jets, well beyond what is currently achievable with fixed order methodology.

The results from the second of these studies was presented in chapter 6, where we looked at the effect on vector boson (W or Z/γ) plus jets where there is large missing energy in the event. This setup is important to accurately describe as it is a necessary background to the signal process of neutrinos + jets (or any other unseen particle), used as a probe of dark matter at the LHC. As with the previous chapter, due to delays in the analysis being published, we were not able to compare with data at the time of writing. We were however able to compare with a high statistics multijet merged sample provided by members of the ATLAS collaboration. This study was important to discuss as initially it highlighted the need for a improved HEJ prescription for dealing with setups with heterogeneous jet cuts. Therefore we spent some time in this chapter discussing these changes in detail for future studies. We then moved on to discuss the differences between the HEJ resummed prediction and the multijet merged prediction. Due to the large number of observables and regions of interest in this analysis, we discussed a representative selection of distributions in the main text, but included the full array of distributions as an appendix. In the discussions around the plots, we aimed to describe where differences were due to enhanced high energy logarithms and which were due to shower corrections included in the multijet merged sample. In particular we looked at a region where VBF cuts were applied (similar to the VBS cuts discussed in chapter 4), which as we have already seen, directly increase the impact from high energy logarithms in damaging the QCD perturbative expansion.

Finally, in chapter 7 we presented a short look at the impact of high energy logarithms at a future circular collider with centre of mass energy of 100 TeV. Such a collider will allow us to probe never before accessible regions of phase space, extending the upper bounds of various kinematic observables where we see the biggest differences between HEJ and fixed order calculations. We found that directly increasing the centre of mass energy whilst keeping everything else in the setup the same lead to the the HEJ prediction moving further away from the next-to-leading order prediction, but increasing the jet p_{\perp} requirement brought the predictions for jet rates back together. We finished this chapter by looking at how some experimentally relevant distributions were affected by the change in centre of mass energy and jet p_{\perp} cut to probe how we expect our resummed prediction to be affected going from the LHC to a future collider.

The work presented in this thesis goes towards improving the logarithmic description of QCD scattering processes using the high energy jets framework

at both the LHC and at future hadron colliders. Myself and my collaborators eagerly await the results from the experimental analyses discussed in chapters 5 and 6 which will hopefully be published in the near future. We hope that the results presented here will help to accurately describe QCD topologies needed as a background to probes of both the electroweak sector of the Standard Model and beyond the Standard Model, where new physics is waiting to be discovered.

Appendix A

Spinor representations

We use the following (chiral) representation for the spinors similar to reference [14]. Note that the sign conventions here make this representation different from the chiral representation found in other texts, e.g in reference [30, Appendix A2]. For outgoing particles with 4-momentum $p, p^\pm = E \pm p_z$ and $p_\perp = p_x + ip_y$, we use

$$u^+(p) = \begin{pmatrix} \sqrt{p^+} \\ \sqrt{p^-} \frac{p_\perp}{|p_\perp|} \\ 0 \\ 0 \end{pmatrix} \quad \text{and} \quad u^-(p) = \begin{pmatrix} 0 \\ 0 \\ \sqrt{p^-} \frac{p_\perp^*}{|p_\perp|} \\ -\sqrt{p^+} \end{pmatrix}. \quad (\text{A.1})$$

For incoming particles with 4-momentum p moving in the $+$ direction, we use:

$$u^+(p) = \begin{pmatrix} \sqrt{p^+} \\ 0 \\ 0 \\ 0 \end{pmatrix} \quad \text{and} \quad u^-(p) = \begin{pmatrix} 0 \\ 0 \\ 0 \\ -\sqrt{p^+} \end{pmatrix}. \quad (\text{A.2})$$

For incoming particles with 4-momentum p moving in the $-$ direction, we use:

$$u^+(p) = \begin{pmatrix} 0 \\ -\sqrt{p^-} \\ 0 \\ 0 \end{pmatrix} \quad \text{and} \quad u^-(p) = \begin{pmatrix} 0 \\ 0 \\ -\sqrt{p^-} \\ 0 \end{pmatrix}. \quad (\text{A.3})$$

We use the following representation for the gamma matrices:

$$\begin{aligned}\gamma^0 &= \begin{pmatrix} 0 & 0 & 1 & 0 \\ 0 & 0 & 0 & 1 \\ 1 & 0 & 0 & 0 \\ 0 & 1 & 0 & 0 \end{pmatrix}, & \gamma^1 &= \begin{pmatrix} 0 & 0 & 0 & -1 \\ 0 & 0 & -1 & 0 \\ 0 & 1 & 0 & 0 \\ 1 & 0 & 0 & 0 \end{pmatrix}, \\ \gamma^2 &= \begin{pmatrix} 0 & 0 & 0 & i \\ 0 & 0 & -i & 0 \\ 0 & -i & 0 & 0 \\ i & 0 & 0 & 0 \end{pmatrix}, & \gamma^3 &= \begin{pmatrix} 0 & 0 & -1 & 0 \\ 0 & 0 & 0 & 1 \\ 1 & 0 & 0 & 0 \\ 0 & -1 & 0 & 0 \end{pmatrix}.\end{aligned}\tag{A.4}$$

From this, we can write the fifth gamma matrix as

$$\gamma^5 = i\gamma^0\gamma^1\gamma^2\gamma^3 = \begin{pmatrix} 1 & 0 & 0 & 0 \\ 0 & 1 & 0 & 0 \\ 0 & 0 & -1 & 0 \\ 0 & 0 & 0 & -1 \end{pmatrix}\tag{A.5}$$

Appendix B

Full collection of predictions for the ATLAS_MET_JETS analysis

Presented here is the full HEJ prediction for the ATLAS_MET_JETS study. Please refer to chapter 6 for a discussion of a representative sample of the plots shown here and a discussion some of the behaviour seen.

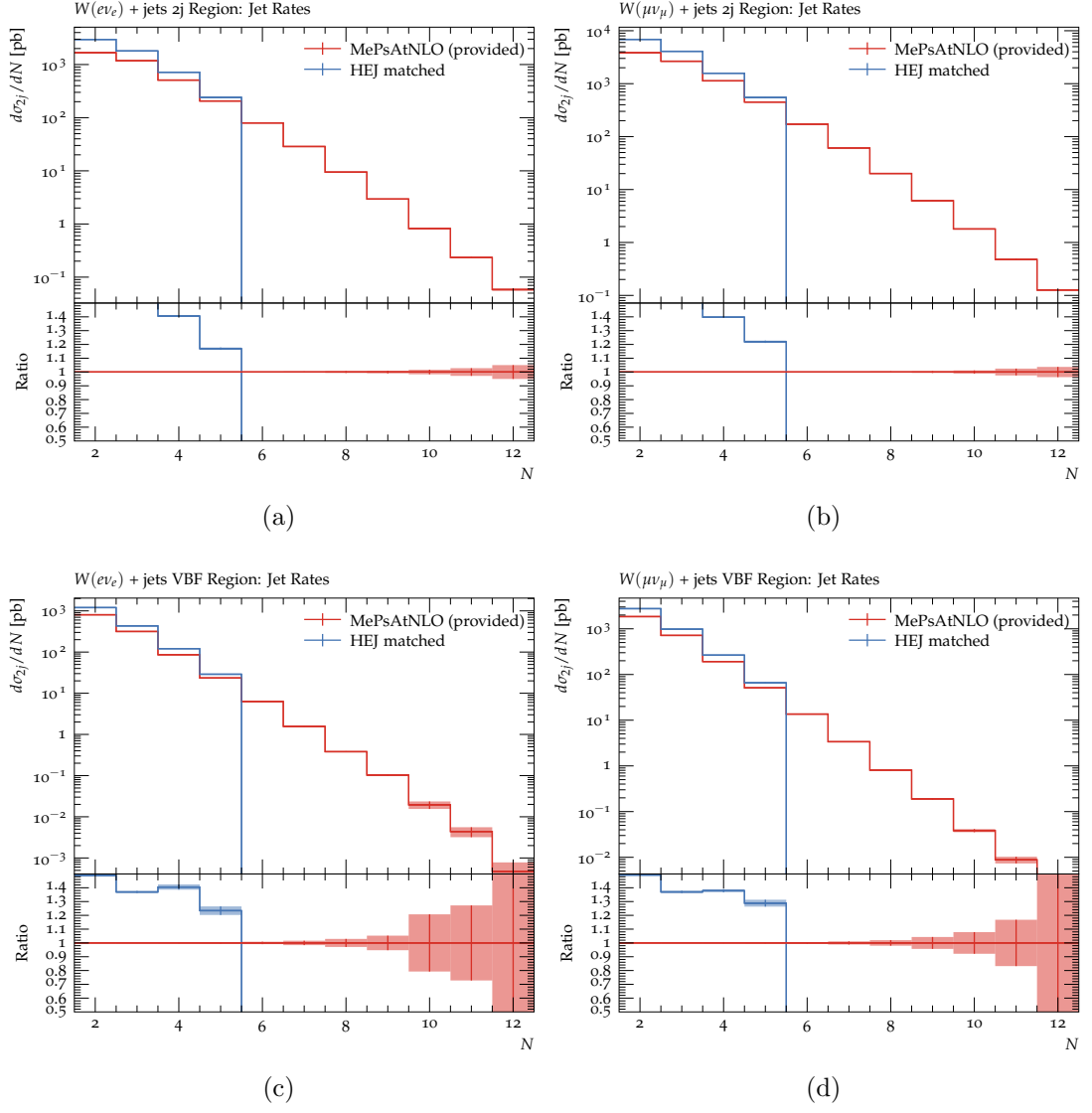


Figure B.1: Plot of the total cross section as a function of number of jets for the ATLAS MET JETS study comparing HEJ and MEPS@NLO with one identified charged lepton in the final state. Decay is in the (a) electron channel, 2j region (b) muon channel, 2j region (c) electron channel VBF region (d) muon channel, VBF region

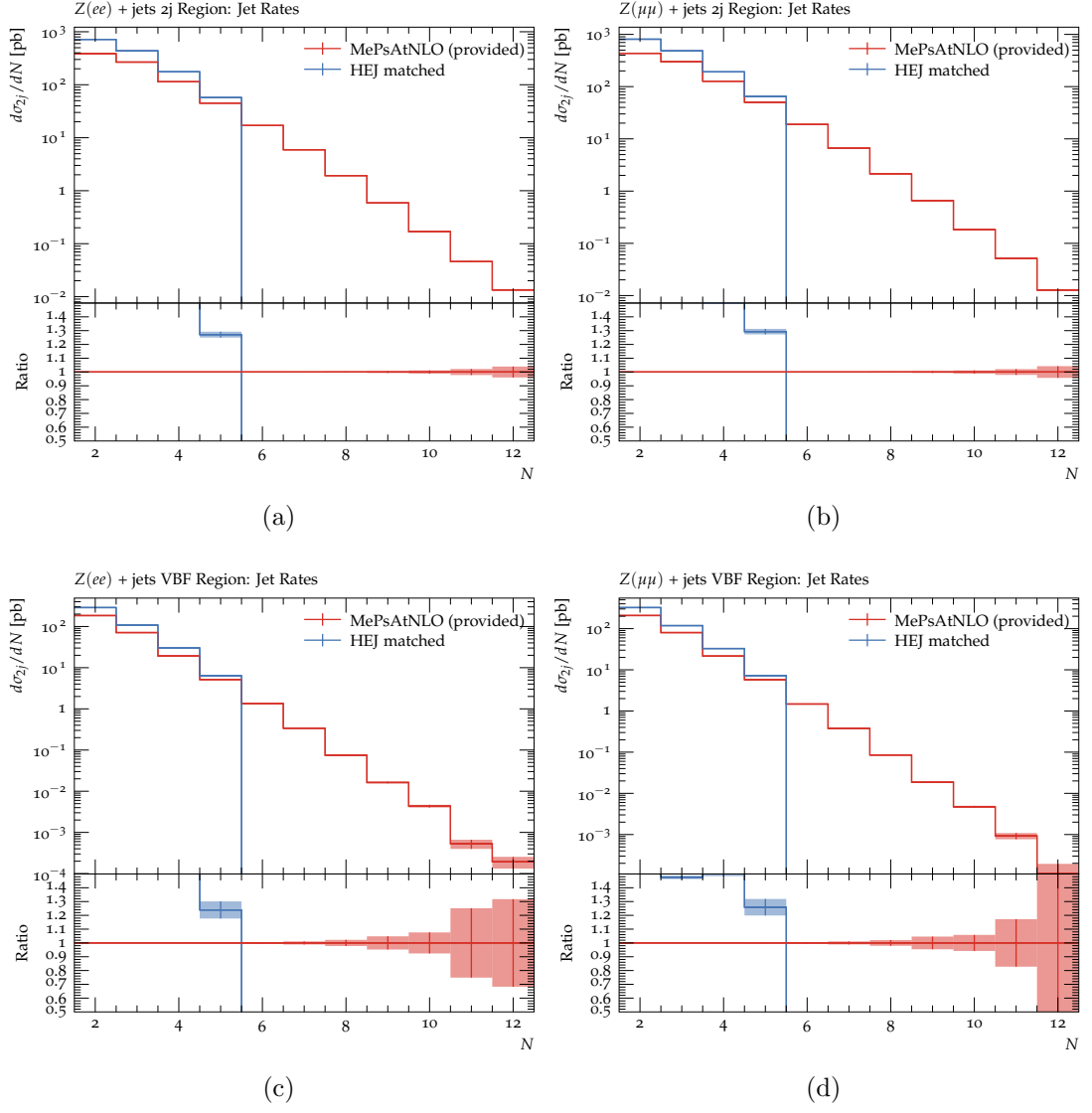


Figure B.2: Plot of the total cross section as a function of number of jets for the ATLAS MET JETS study comparing HEJ and MEPS@NLO with two identified charged leptons in the final state. Decay is in the (a) electron channel, 2j region (b) muon channel, 2j region (c) electron channel VBF region (d) muon channel, VBF region

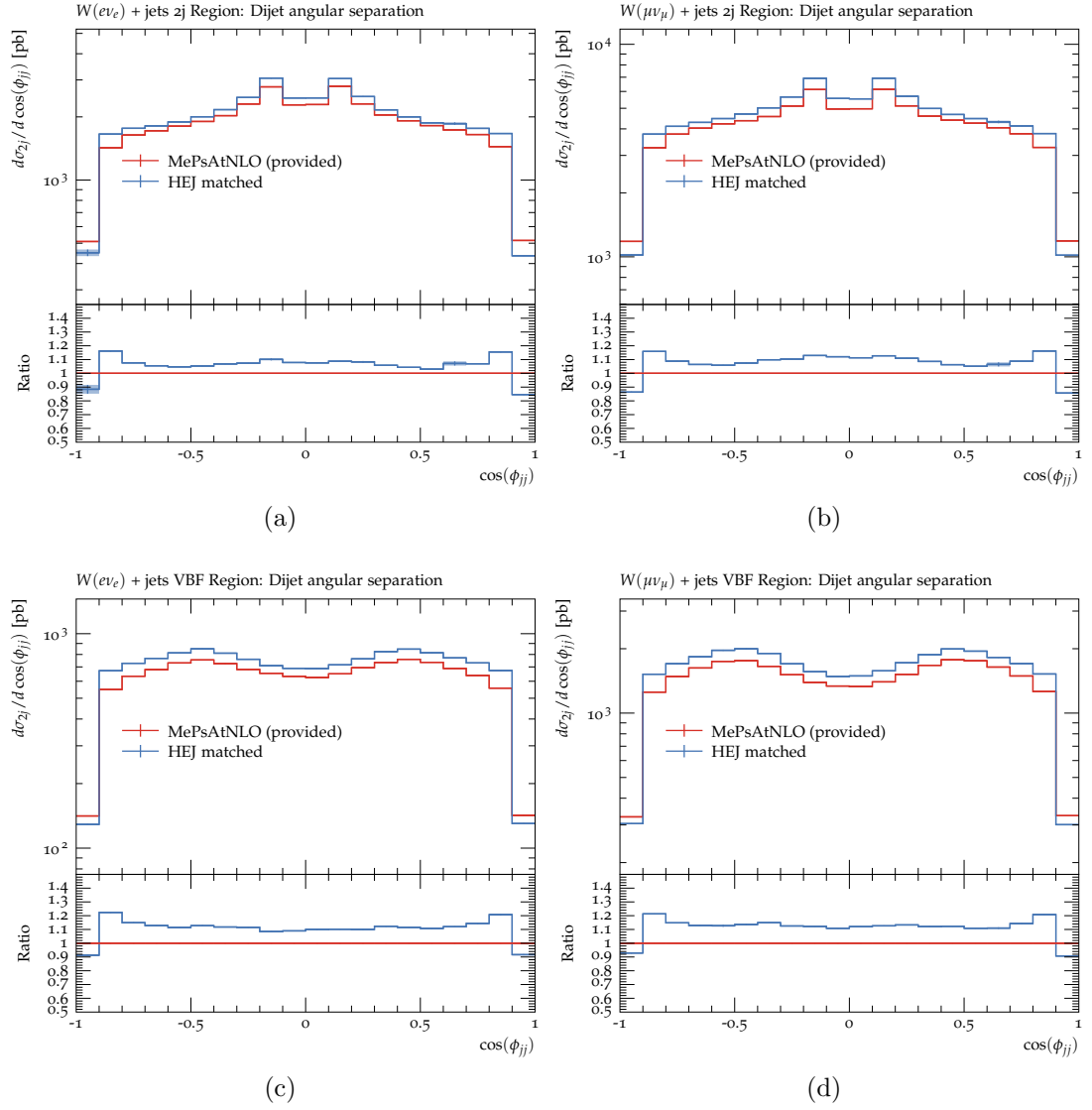


Figure B.3: Plot of the total cross section as a function of dijet angular separation for the ATLAS MET JETS study comparing HEJ and MEPS@NLO with one identified charged lepton in the final state. Decay is in the (a) electron channel, 2j region (b) muon channel, 2j region (c) electron channel VBF region (d) muon channel, VBF region

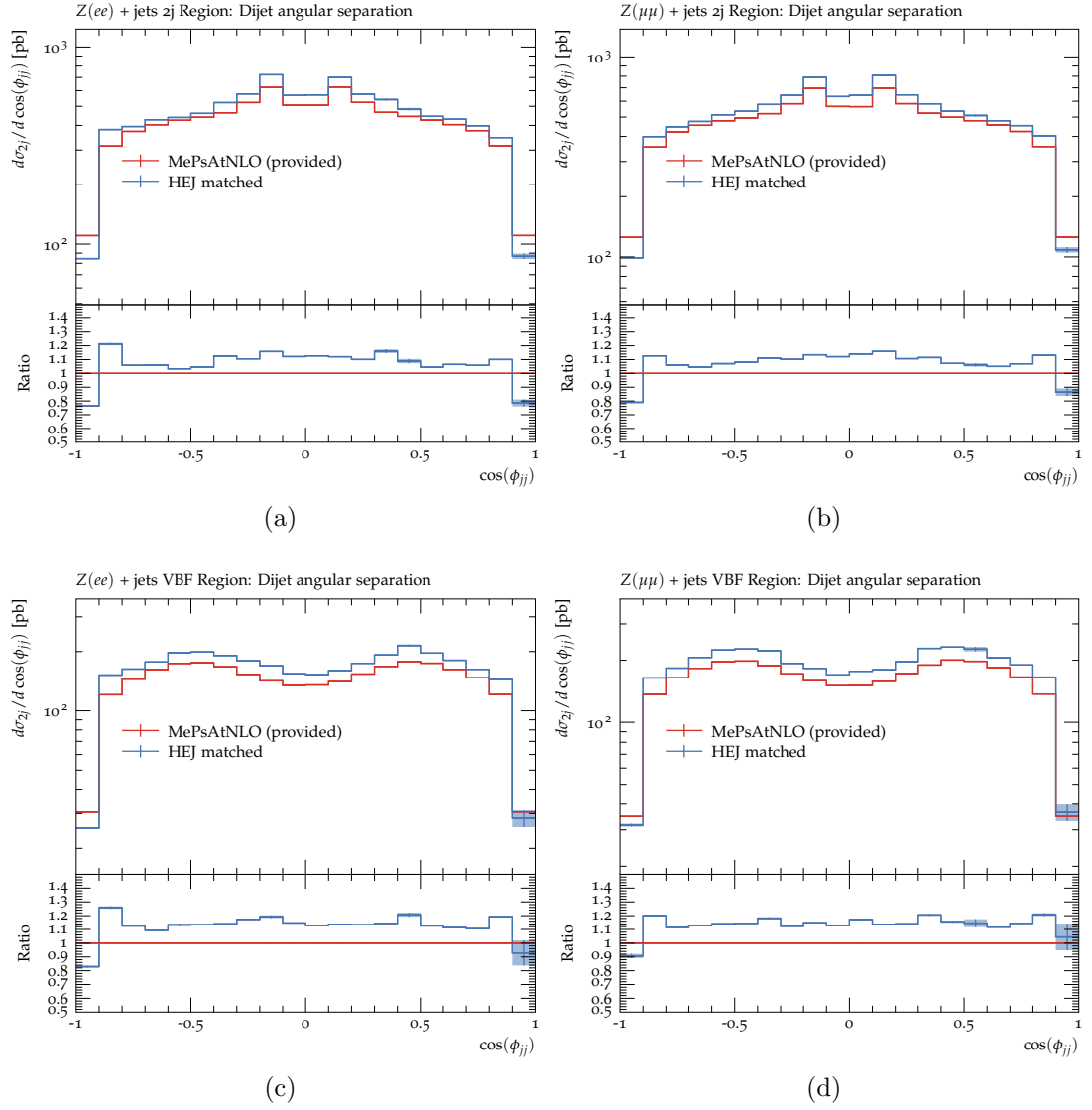


Figure B.4: Plot of the total cross section as a function of dijet angular separation for the ATLAS MET JETS study comparing HEJ and MEPS@NLO with two identified charged leptons in the final state. Decay is in the (a) electron channel, 2j region (b) muon channel, 2j region (c) electron channel VBF region (d) muon channel, VBF region

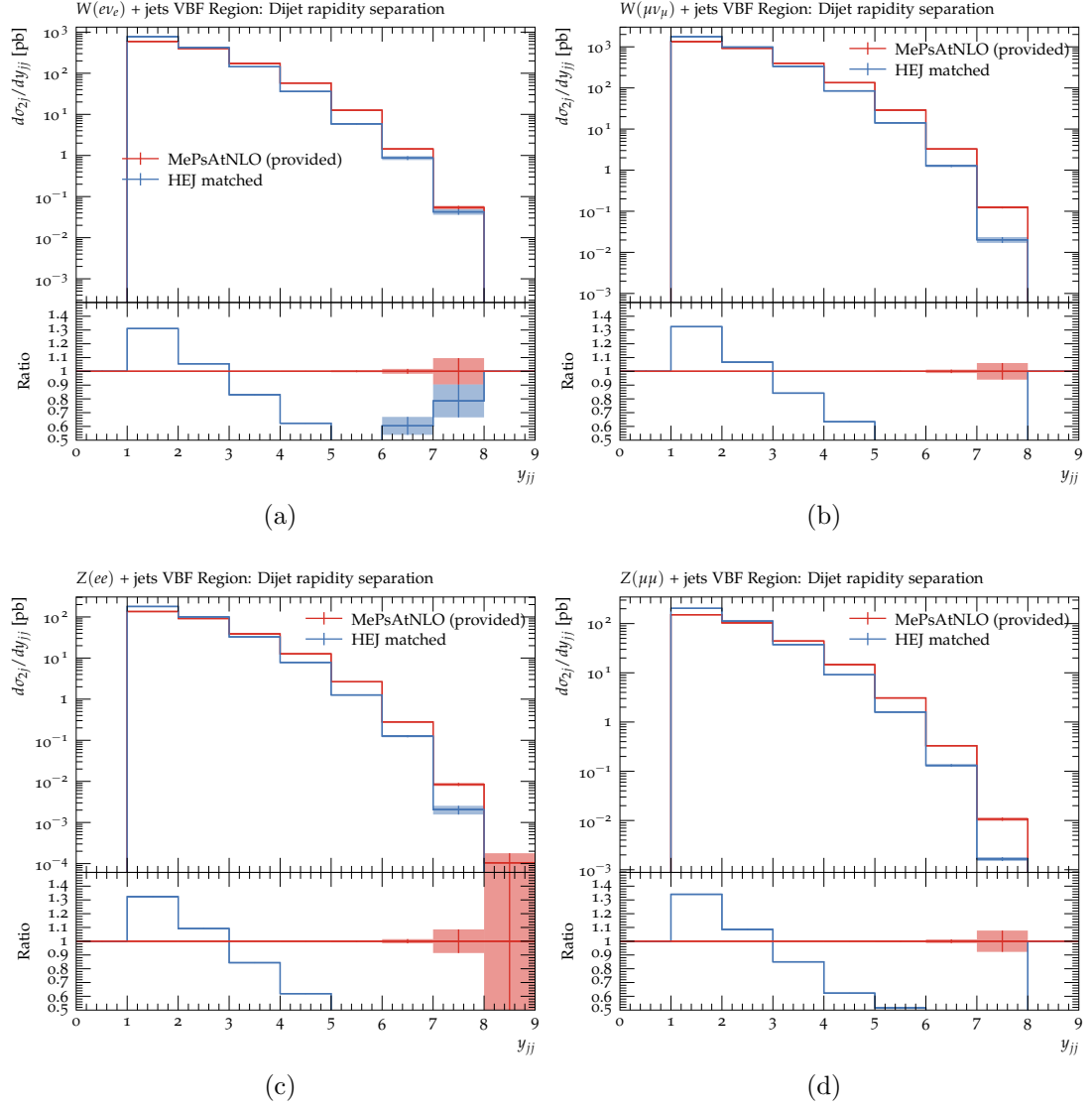


Figure B.5: Plot of the total cross section as a function of dijet rapidity separation for the ATLAS MET JETS study comparing HEJ and MEPS@NLO in the VBF region with leptonic decay into (a) electron + neutrino (b) muon + neutrino (c) electron + antielectron (d) muon + antimuon

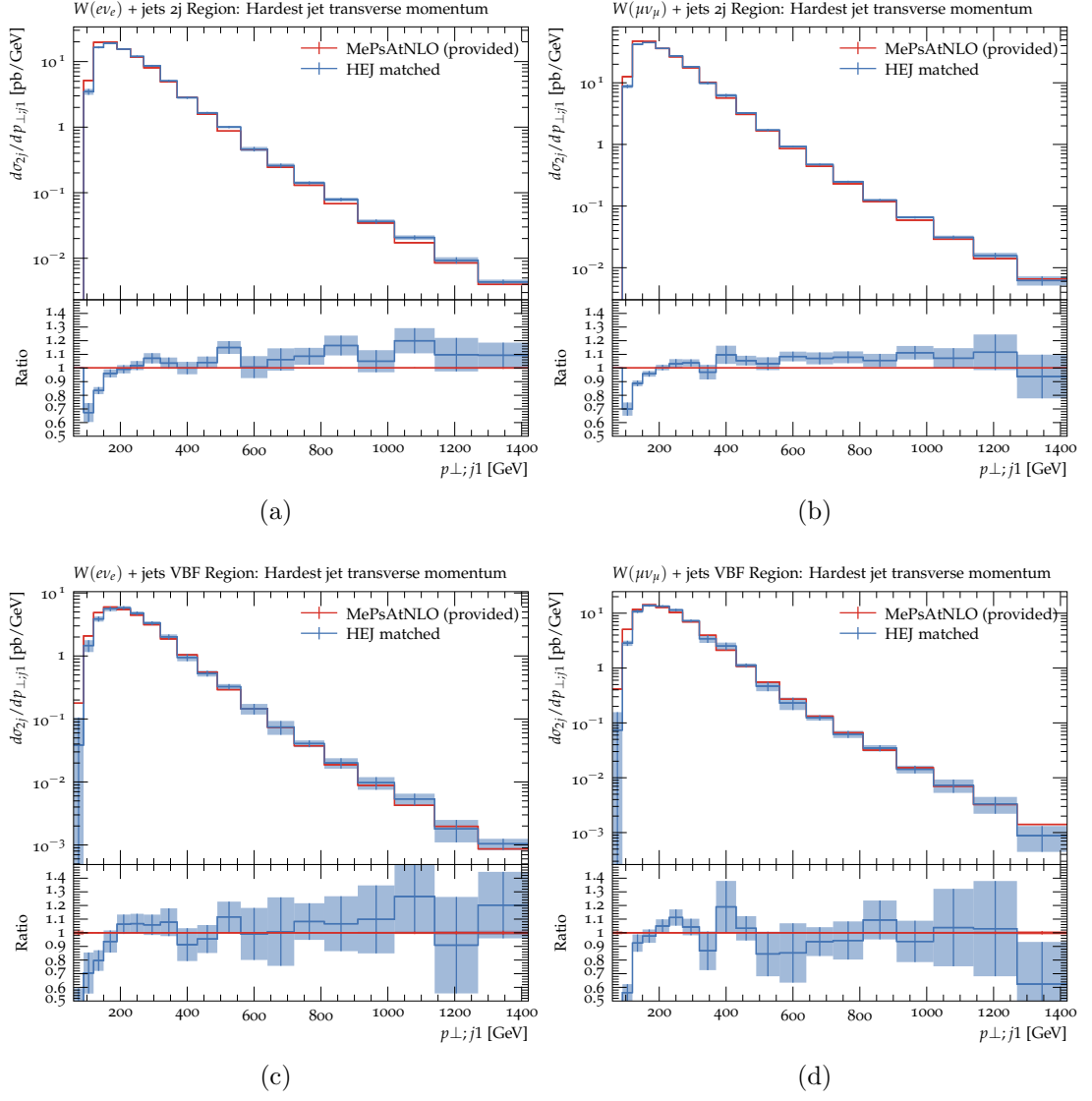


Figure B.6: Plot of the total cross section as a function of the transverse momentum of the hardest jet for the ATLAS MET JETS study comparing HEJ and MEPS@NLO with one identified charged lepton in the final state. Decay is in the (a) electron channel, 2j region (b) muon channel, 2j region (c) electron channel VBF region (d) muon channel, VBF region

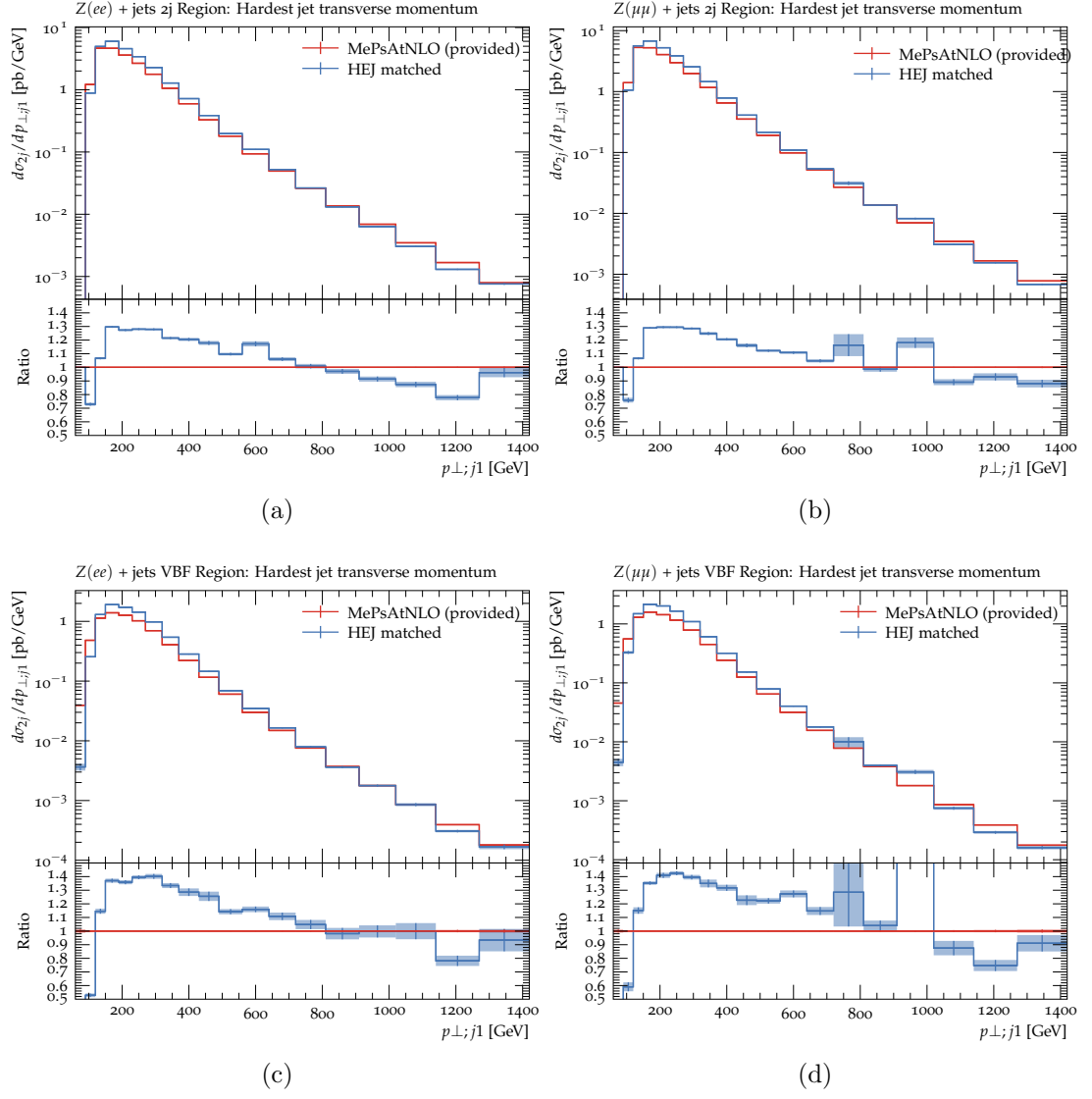


Figure B.7: Plot of the total cross section as a function of the transverse momentum of the hardest jet for the ATLAS MET JETS study comparing HEJ and MEPS@NLO with two identified charged leptons in the final state. Decay is in the (a) electron channel, 2j region (b) muon channel, 2j region (c) electron channel VBF region (d) muon channel, VBF region

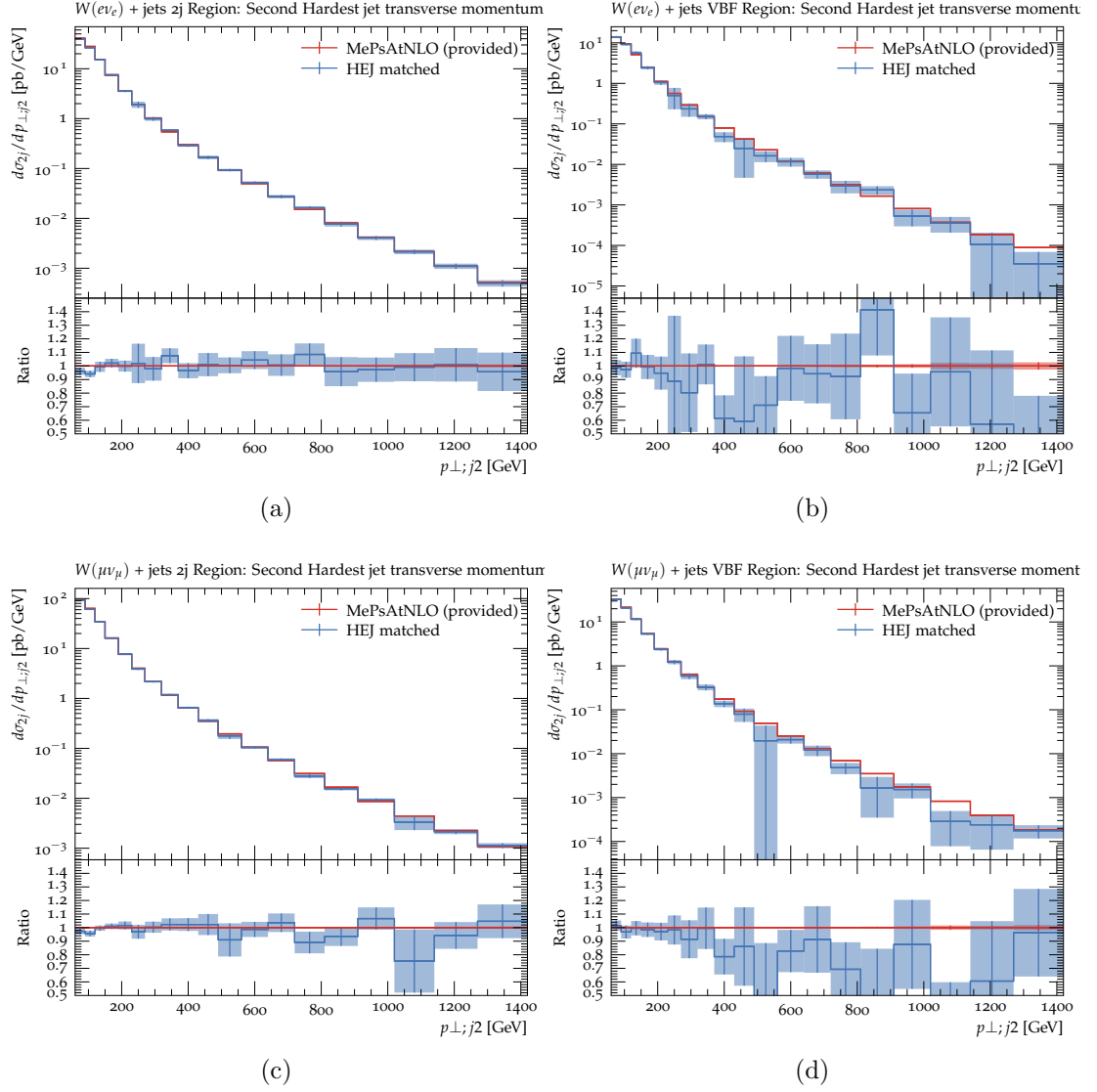


Figure B.8: Plot of the total cross section as a function of the transverse momentum of the second hardest jet for the ATLAS MET JETS study comparing HEJ and MEPS@NLO with one identified charged lepton in the final state. Decay is in the (a) electron channel, 2j region (b) muon channel, 2j region (c) electron channel VBF region (d) muon channel, VBF region

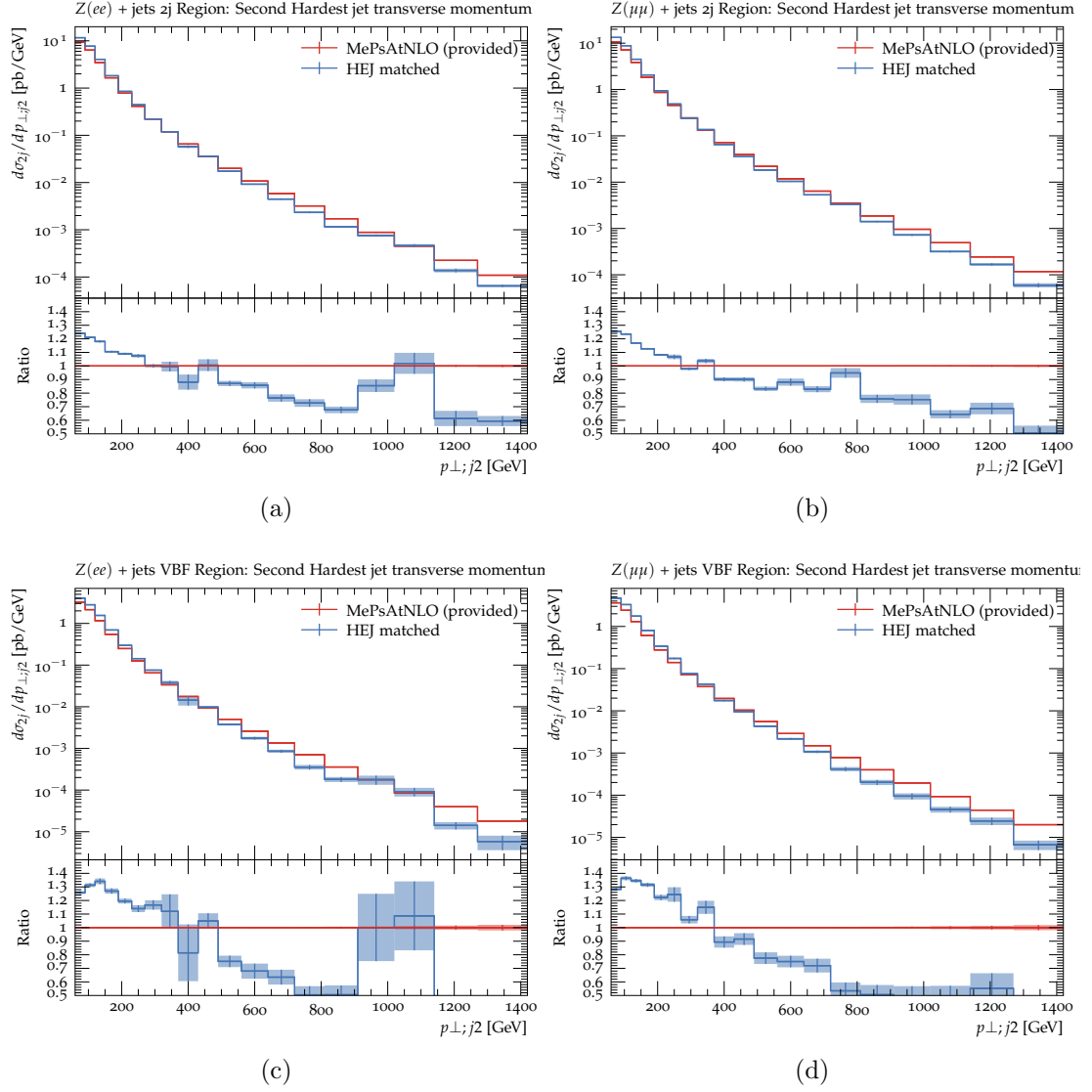


Figure B.9: Plot of the total cross section as a function of the transverse momentum of the second hardest jet for the ATLAS MET JETS study comparing HEJ and MEPS@NLO with two identified charged leptons in the final state. Decay is in the (a) electron channel, 2j region (b) muon channel, 2j region (c) electron channel VBF region (d) muon channel, VBF region

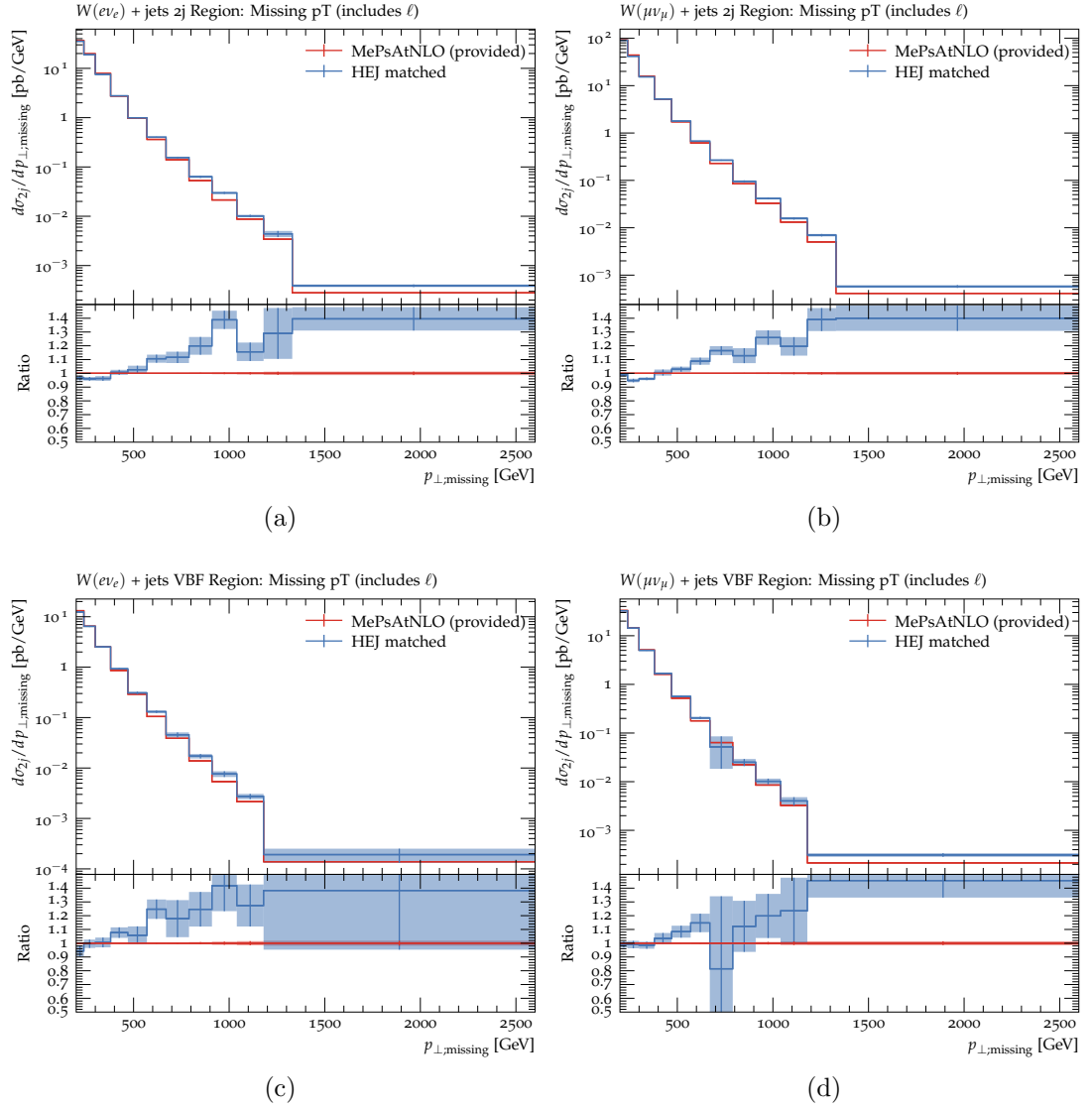


Figure B.10: Plot of the total cross section as a function of the missing transverse momentum for the ATLAS MET JETS study comparing HEJ and MEPS@NLO with one identified charged lepton in the final state. Decay is in the (a) electron channel, 2j region (b) muon channel, 2j region (c) electron channel VBF region (d) muon channel, VBF region

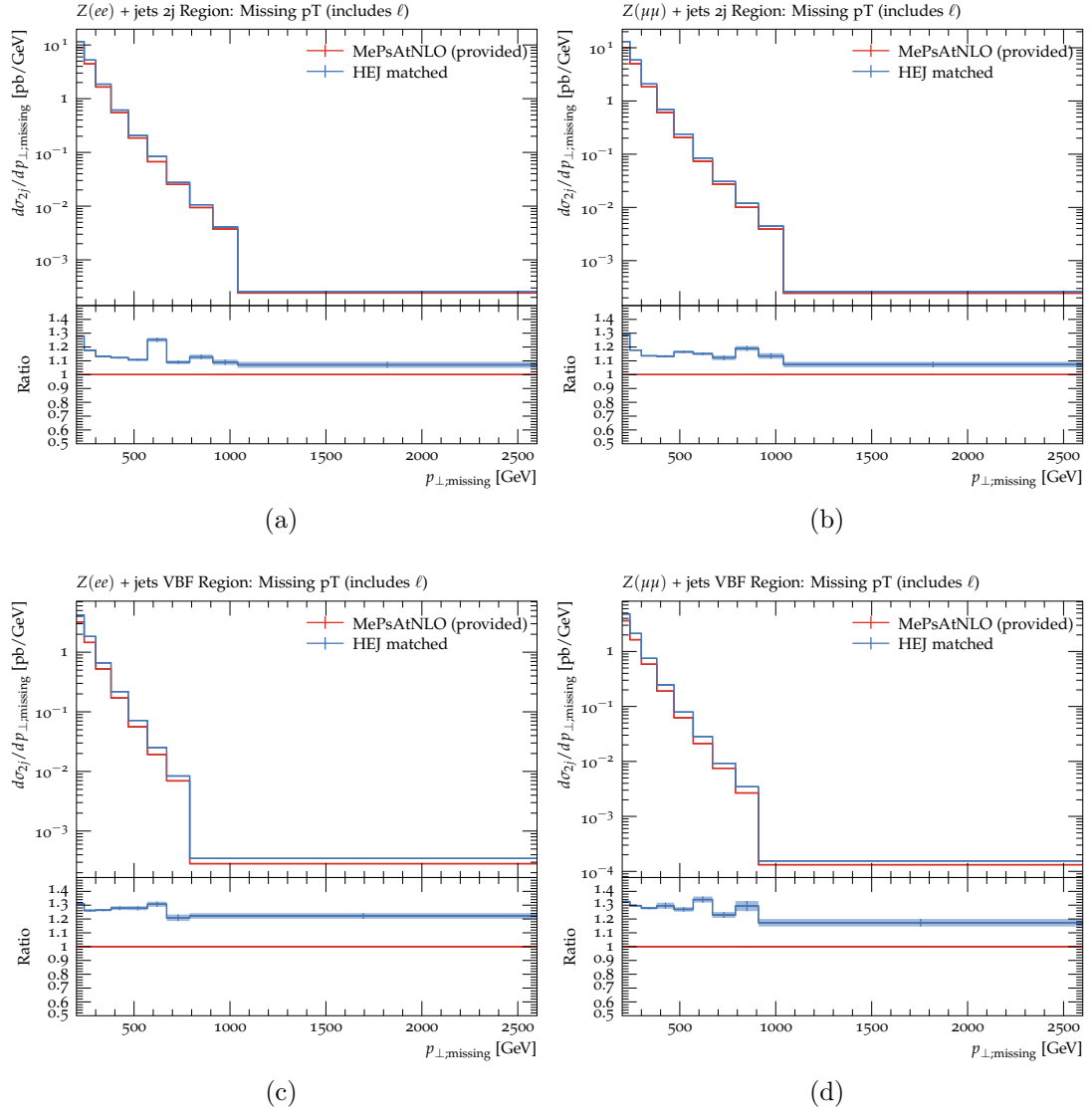


Figure B.11: Plot of the total cross section as a function of the missing transverse momentum for the ATLAS MET JETS study comparing HEJ and MEPS@NLO with two identified charged leptons in the final state. Decay is in the (a) electron channel, 2j region (b) muon channel, 2j region (c) electron channel VBF region (d) muon channel, VBF region

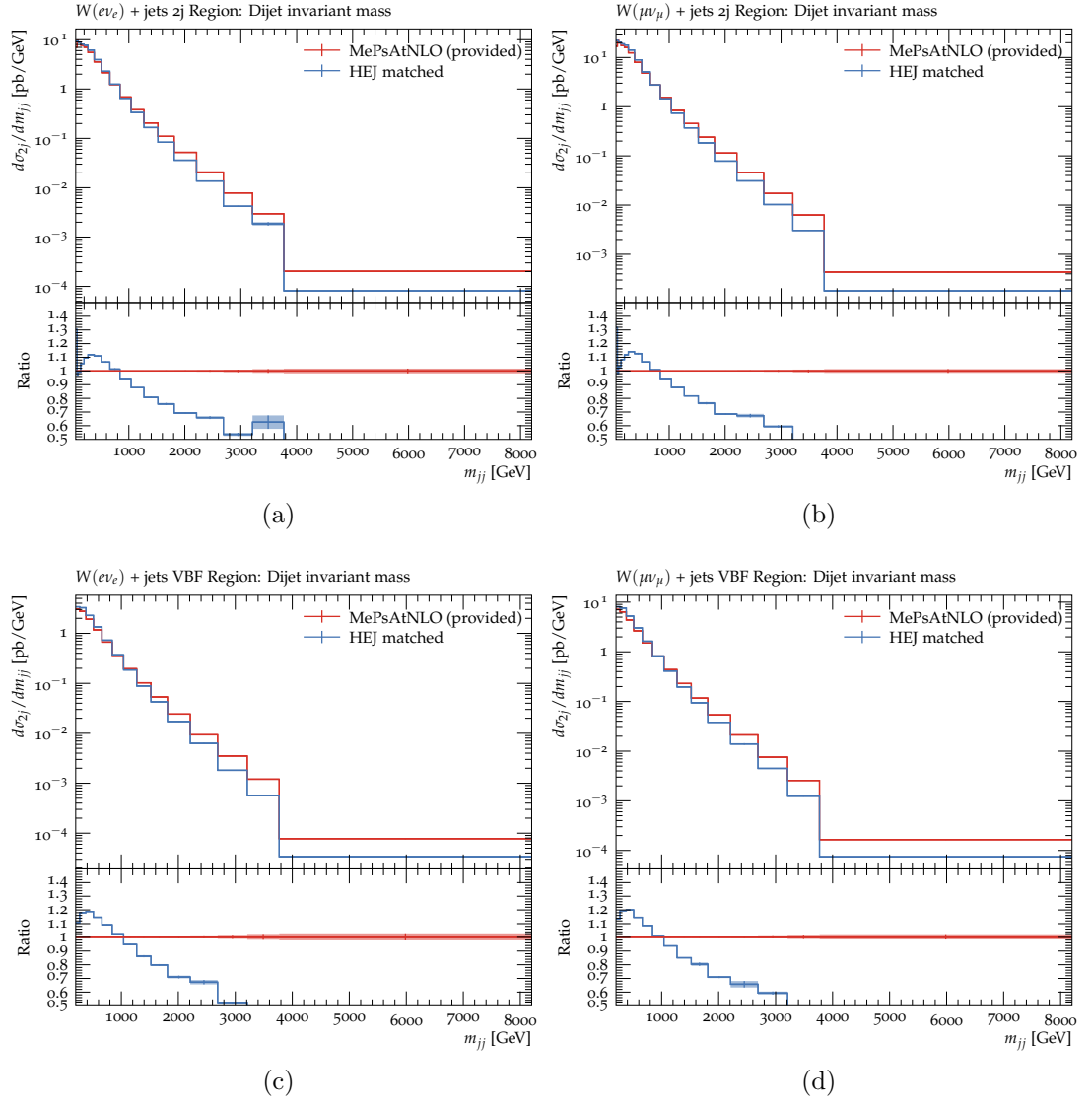


Figure B.12: Plot of the total cross section as a function of the dijet invariant mass for the ATLAS MET JETS study comparing HEJ and MEPS@NLO with one identified charged lepton in the final state. Decay is in the (a) electron channel, 2j region (b) muon channel, 2j region (c) electron channel VBF region (d) muon channel, VBF region

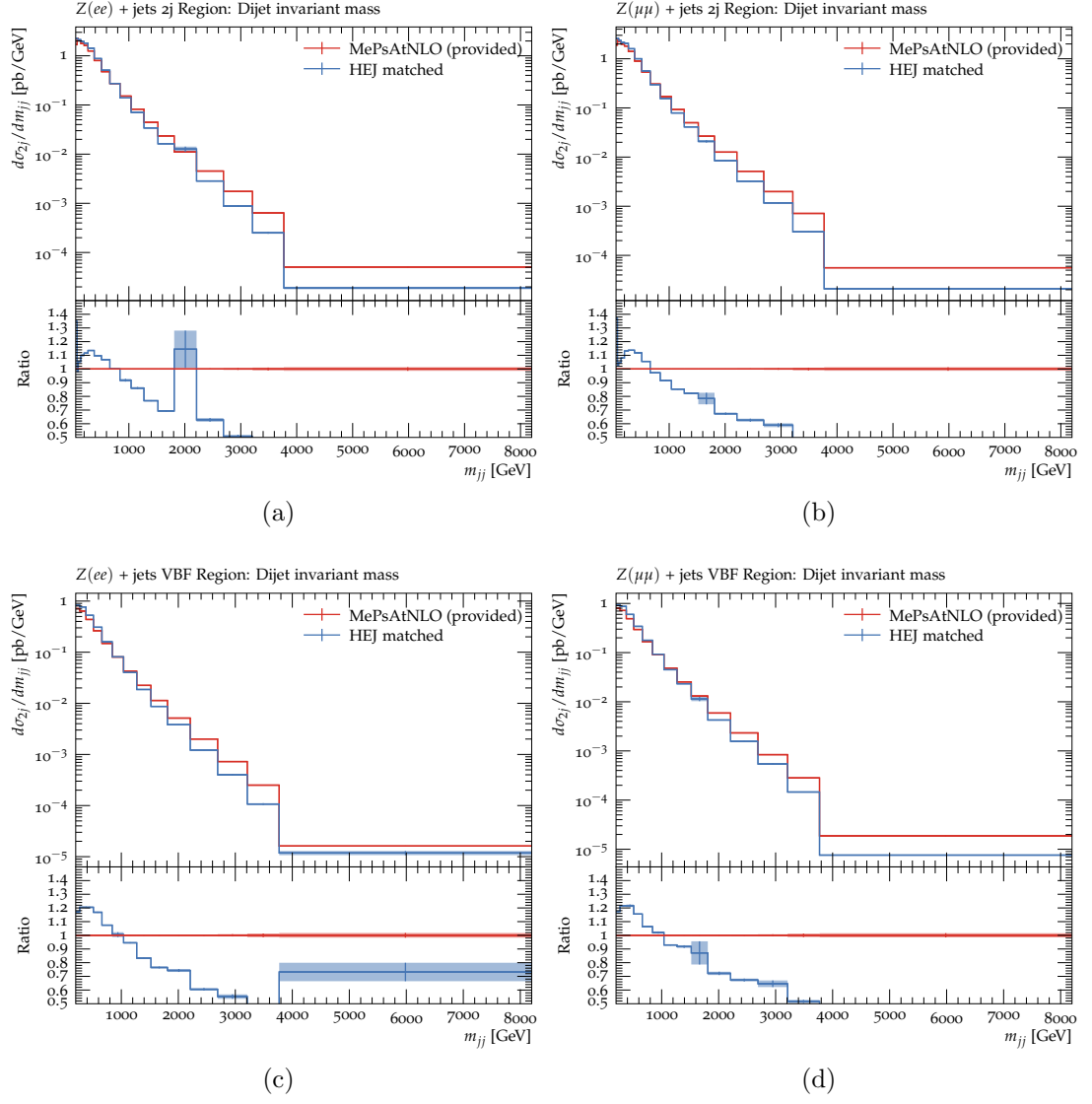


Figure B.13: Plot of the total cross section as a function of the dijet invariant mass for the ATLAS MET JETS study comparing HEJ and MEPS@NLO with two identified charged leptons in the final state. Decay is in the (a) electron channel, 2j region (b) muon channel, 2j region (c) electron channel VBF region (d) muon channel, VBF region

Bibliography

- [1] J. R. Andersen, B. Ducloué, C. Elrick, A. Maier, G. Nail, J. M. Smillie, Logarithmic corrections to the QCD component of same-sign W-pair production for vector boson scattering studies, *Phys. Rev. D* 104 (11) (2021) 114008. [arXiv:2107.06818](#), [doi:10.1103/PhysRevD.104.114008](#).
- [2] J. R. Andersen, B. Duclou, H. Hassan, C. Elrick, A. Maier, G. Nail, J. Paltrinieri, A. Papaefstathiou, J. M. Smillie, Hej 2.2: W boson pairs and higgs boson plus jet production at high energies (2023). [arXiv:2303.15778](#).
- [3] The GridPP Collaboration, GridPP: Development of the UK Computing Grid for Particle Physics, *J. Phys. G* 32 (2006) N1–N20.
URL <http://dx.doi.org/10.1088/0954-3899/32/1/N0138>
- [4] D. Britton, et al., GridPP: the UK grid for particle physics, *Phil. Trans. R. Soc. A* 367 (2009) 2447–2457.
URL <http://dx.doi.org/10.1098/rsta.2009.0036>
- [5] P. D. Group, R. L. Workman, V. D. Burkert, V. Crede, E. Klempt, U. Thoma, L. Tiator, K. Agashe, G. Aielli, B. C. Allanach, C. AMSler, M. Antonelli, E. C. Aschenauer, D. M. Asner, H. Baer, S. Banerjee, R. M. Barnett, L. Baudis, C. W. Bauer, J. J. Beatty, V. I. Belousov, J. Beringer, A. Bettini, O. Biebel, K. M. Black, E. Blucher, R. Bonventre, V. V. Bryzgalov, O. Buchmuller, M. A. Bychkov, R. N. Cahn, M. Carena, A. Ceccucci, A. Cerri, R. S. Chivukula, G. Cowan, K. Cranmer, O. Cremonesi, G. D’Ambrosio, T. Damour, D. de Florian, A. de Gouvá, T. DeGrand, P. de Jong, S. Demers, B. A. Dobrescu, M. D’Onofrio, M. Doser, H. K. Dreiner, P. Eerola, U. Egede, S. Eidelman, A. X. El-Khadra, J. Ellis, S. C. Eno, J. Erler, V. V. Ezhela, W. Fetscher, B. D. Fields, A. Freitas, H. Gallagher, Y. Gershtein, T. Gherghetta, M. C. Gonzalez-Garcia, M. Goodman, C. Grab, A. V. Gritsan, C. Grojean, D. E. Groom, M. Grnewald, A. Gurtu, T. Gutsche, H. E. Haber, M. Hamel, C. Hanhart, S. Hashimoto, Y. Hayato, A. Hebecker, S. Heinemeyer, J. J. Hernandez-Rey, K. Hikasa, J. Hisano, A. Hcker, J. Holder, L. Hsu, J. Huston, T. Hyodo, A. Ianni, M. Kado, M. Karliner, U. F. Katz, M. Kenzie, V. A. Khoze, S. R. Klein, F. Krauss, M. Kreps, P. Krian, B. Krusche, Y. Kwon, O. Lahav, J. Laiho, L. P. Lellouch, J. Lesgourgues, A. R. Liddle, Z. Ligeti, C.-J. Lin, C. Lippmann, T. M. Liss, L. Littenberg, C. Loureno, K. S.

Lugovsky, S. B. Lugovsky, A. Lusiani, Y. Makida, F. Maltoni, T. Mannel, A. V. Manohar, W. J. Marciano, A. Masoni, J. Matthews, U.-G. Meiner, I.-A. Melzer-Pellmann, M. Mikhasenko, D. J. Miller, D. Milstead, R. E. Mitchell, K. Mnig, P. Molaro, F. Moortgat, M. Moskvic, K. Nakamura, M. Narain, P. Nason, S. Navas, A. Nelles, M. Neubert, P. Nevski, Y. Nir, K. A. Olive, C. Patrignani, J. A. Peacock, V. A. Petrov, E. Pianori, A. Pich, A. Piepke, F. Pietropaolo, A. Pomarol, S. Pordes, S. Profumo, A. Quadt, K. Rabbertz, J. Rademacker, G. Raffelt, M. Ramsey-Musolf, B. N. Ratcliff, P. Richardson, A. Ringwald, D. J. Robinson, S. Roesler, S. Rolli, A. Romaniouk, L. J. Rosenberg, J. L. Rosner, G. Rybka, M. G. Ryskin, R. A. Ryutin, Y. Sakai, S. Sarkar, F. Sauli, O. Schneider, S. Schnert, K. Scholberg, A. J. Schwartz, J. Schwiening, D. Scott, F. Sefkow, U. Seljak, V. Sharma, S. R. Sharpe, V. Shiltsev, G. Signorelli, M. Silari, F. Simon, T. Sjstrand, P. Skands, T. Skwarnicki, G. F. Smoot, A. Soffer, M. S. Sozzi, S. Spanier, C. Spiering, A. Stahl, S. L. Stone, Y. Sumino, M. J. Syphers, F. Takahashi, M. Tanabashi, J. Tanaka, M. Taevsk, K. Terao, K. Terashi, J. Terning, R. S. Thorne, M. Titov, N. P. Tkachenko, D. R. Tovey, K. Trabelsi, P. Urquijo, G. Valencia, R. Van de Water, N. Varelas, G. Venanzoni, L. Verde, I. Vivarelli, P. Vogel, W. Vogelsang, V. Vorobyev, S. P. Wakely, W. Walkowiak, C. W. Walter, D. Wands, D. H. Weinberg, E. J. Weinberg, N. Wermes, M. White, L. R. Wiencke, S. Willocq, C. G. Wohl, C. L. Woody, W.-M. Yao, M. Yokoyama, R. Yoshida, G. Zanderighi, G. P. Zeller, O. V. Zenin, R.-Y. Zhu, S.-L. Zhu, F. Zimmermann, P. A. Zyla, Review of Particle Physics, Progress of Theoretical and Experimental Physics 2022 (8), 083C01. [arXiv:https://academic.oup.com/ptep/article-pdf/2022/8/083C01/49175558/ptac097_19_miscellaneous_searches_and_searches_in_other_sections.pdf](https://academic.oup.com/ptep/article-pdf/2022/8/083C01/49175558/ptac097_19_miscellaneous_searches_and_searches_in_other_sections.pdf), doi:10.1093/ptep/ptac097. URL <https://doi.org/10.1093/ptep/ptac097>

- [6] R. D. Ball, S. Carrazza, J. Cruz-Martinez, L. D. Debbio, S. Forte, T. Giani, S. Iranipour, Z. Kassabov, J. I. Latorre, E. R. Nocera, R. L. Pearson, J. Rojo, R. Stegeman, C. Schwan, M. Ubiali, C. Voisey, M. Wilson, The path to proton structure at 1% accuracy, The European Physical Journal C 82 (5). doi:10.1140/epjc/s10052-022-10328-7. URL <https://doi.org/10.1140%2Fepjc%2Fs10052-022-10328-7>
- [7] C. Collaboration, T. Mc Cauley, Displays of an event with two jets with transverse momentum of more than 3 TeV as seen in the CMS detector, CMS Collection. (2021). URL <http://cds.cern.ch/record/2775841>
- [8] M. Kollar, Top-quark and top-squark production at hadron colliders at electroweak nlo.
- [9] S. Hoche, Merging matrix elements with parton showers. URL <https://link.aps.org/doi/10.1103/PhysRev.133.B1549>
- [10] J. R. Andersen, J. A. Black, H. M. Brooks, E. P. Byrne, A. Maier, J. M.

Smillie, Combined subleading high-energy logarithms and NLO accuracy for w production in association with multiple jets, *Journal of High Energy Physics* 2021 (4). doi:10.1007/jhep04(2021)105.
 URL <https://doi.org/10.1007%2Fjhep04%282021%29105>

- [11] J. Bendavid, F. Caola, V. Ciulli, R. Harlander, G. Heinrich, J. Huston, S. Kallweit, S. Prestel, E. Re, K. Tackmann, J. Thaler, K. Theofilatos, J. R. Andersen, J. Bellm, N. Berger, D. Bhatia, B. Biedermann, S. Bruer, D. Britzger, A. G. Buckley, R. Camacho, G. Chachamis, S. Chatterjee, X. Chen, M. Chiesa, J. R. Currie, A. Denner, F. Dreyer, F. Driencourt-Mangin, S. Forte, M. V. Garzelli, T. Gehrmann, S. Gieseke, E. W. N. Glover, P. Gras, N. Greiner, C. Gtschow, C. Gwenlan, M. Heil, M. Herndon, V. Hirschi, A. H. Hoang, S. Hche, A. Huss, S. P. Jones, D. Kar, A. Karlberg, Z. Kassabov, M. Kerner, J. Klappert, S. Kuttimalai, J. N. Lang, A. Larkoski, J. M. Lindert, P. Loch, K. Long, L. Lnnblad, G. Luisoni, A. Maier, P. Maierhofer, D. Matre, S. Marzani, J. A. McFayden, I. Moul, M. Mozer, S. Mrenna, B. Nachman, D. Napoletano, C. Pandini, A. Papaefstathiou, M. Pellen, L. Perrozzi, J. Pires, S. Pltzer, S. Pozzorini, S. Quackenbush, K. Rabbertz, M. Rauch, C. Reuschle, P. Richardson, A. G.-D. Ridder, G. Rodrigo, J. Rojo, R. Rntsch, L. Rottoli, D. Samitz, T. Samui, G. Sborlini, M. Schnherr, S. Schumann, L. Scyboz, S. Seth, H. S. Shao, A. Sidmok, P. Z. Skands, J. M. Smillie, G. Soyez, P. Sun, M. R. Sutton, F. J. Tackmann, S. Uccirati, S. Weinzierl, E. Yazgan, C. P. Yuan, F. Yuan, Les houches 2017: Physics at tev colliders standard model working group report (2018). arXiv:1803.07977.
- [12] S. Amoroso, P. Azzurri, J. Bendavid, E. Bothmann, D. Britzger, H. Brooks, A. Buckley, M. Calvetti, X. Chen, M. Chiesa, L. Cieri, V. Ciulli, J. Cruz-Martinez, A. Cueto, A. Denner, S. Dittmaier, M. Doneg, M. Dhrssen-Debling, I. Fabre, S. Ferrario-Ravasio, D. de Florian, S. Forte, P. Francavilla, T. Gehrmann, A. G.-D. Ridder, L. Gellersen, E. W. N. Glover, P. Gras, C. Gwenlan, Y. Haddad, G. Heinrich, J. Hessler, T. J. Hobbs, M. Hfer, A. Huss, J. Huston, T. Jeo, S. P. Jones, S. Kallweit, M. Klasen, G. Knippen, A. Larkoski, M. LeBlanc, P. Loch, K. Long, D. Matre, S. Marzani, J. Mazzitelli, J. A. Mcfayden, E. Metodiev, J. K. L. Michel, M. M. Llcer, B. Nachman, P. Nadolsky, D. Napoletano, E. R. Nocera, C. Oleari, C. Pandini, M. Pellen, S. Pigazzini, J. Pires, S. Pltzer, S. Prestel, K. Rabbertz, E. Re, P. Richardson, F. Ringer, J. Rojo, J. Roloff, R. Rntsch, M. Schnherr, C. Schwan, F. Siegert, D. Soper, G. Soyez, M. Spira, M. R. Sutton, F. J. Tackmann, V. Theeuwes, S. L. Villani, J. Whitehead, H. T. Yang, J. Zhou, Les houches 2019: Physics at tev colliders: Standard model working group report (2020). arXiv:2003.01700.
- [13] Standard Model Summary Plots February 2022, Tech. rep., CERN, Geneva, all figures including auxiliary figures are available at <https://atlas.web.cern.ch/Atlas/GROUPS/PHYSICS/PUBNOTES/ATL-PHYS-PUB-2022-009> (2022).
 URL <https://cds.cern.ch/record/2804061>

- [14] J. R. Andersen, J. M. Smillie, Constructing All-Order Corrections to Multi-Jet Rates, JHEP 01 (2010) 039. [arXiv:0908.2786](#), [doi:10.1007/JHEP01\(2010\)039](#).
- [15] J. R. Andersen, J. M. Smillie, The Factorisation of the t-channel Pole in Quark-Gluon Scattering, Phys.Rev. D81 (2010) 114021. [arXiv:0910.5113](#), [doi:10.1103/PhysRevD.81.114021](#).
- [16] J. R. Andersen, J. M. Smillie, Multiple Jets at the LHC with High Energy Jets, JHEP 1106 (2011) 010. [arXiv:1101.5394](#), [doi:10.1007/JHEP06\(2011\)010](#).
- [17] J. R. Andersen, T. Hapola, M. Heil, A. Maier, J. Smillie, HEJ 2: High Energy Resummation for Hadron Colliders, Comput.Phys.Commun. 245. [arXiv:1902.08430](#), [doi:10.1016/j.cpc.2019.06.022](#).
- [18] G. Aad, et al., Measurement of dijet production with a veto on additional central jet activity in pp collisions at $\sqrt{s} = 7$ TeV using the ATLAS detector, JHEP 09 (2011) 053. [arXiv:1107.1641](#), [doi:10.1007/JHEP09\(2011\)053](#).
- [19] S. Chatrchyan, et al., Measurement of the inclusive production cross sections for forward jets and for dijet events with one forward and one central jet in pp collisions at $\sqrt{s} = 7$ TeV, JHEP 06 (2012) 036. [arXiv:1202.0704](#), [doi:10.1007/JHEP06\(2012\)036](#).
- [20] S. Chatrchyan, et al., Ratios of dijet production cross sections as a function of the absolute difference in rapidity between jets in proton-proton collisions at $\sqrt{s} = 7$ TeV, Eur. Phys. J. C 72 (2012) 2216. [arXiv:1204.0696](#), [doi:10.1140/epjc/s10052-012-2216-6](#).
- [21] G. Aad, et al., Measurements of jet vetoes and azimuthal decorrelations in dijet events produced in pp collisions at $\sqrt{s} = 7$ TeV using the ATLAS detector, Eur. Phys. J. C 74 (11) (2014) 3117. [arXiv:1407.5756](#), [doi:10.1140/epjc/s10052-014-3117-7](#).
- [22] J. R. Andersen, T. Hapola, J. M. Smillie, W Plus Multiple Jets at the LHC with High Energy Jets, JHEP 1209 (2012) 047. [arXiv:1206.6763](#), [doi:10.1007/JHEP09\(2012\)047](#).
- [23] V. M. Abazov, et al., Studies of W boson plus jets production in $p\bar{p}$ collisions at $\sqrt{s} = 1.96$ TeV, Phys. Rev. D 88 (9) (2013) 092001. [arXiv:1302.6508](#), [doi:10.1103/PhysRevD.88.092001](#).
- [24] G. Aad, et al., Measurements of the W production cross sections in association with jets with the ATLAS detector, Eur. Phys. J. C 75 (2) (2015) 82. [arXiv:1409.8639](#), [doi:10.1140/epjc/s10052-015-3262-7](#).
- [25] J. R. Andersen, J. J. Medley, J. M. Smillie, Z/γ^* plus multiple hard jets in high energy collisions, JHEP 05 (2016) 136. [arXiv:1603.05460](#), [doi:10.1007/JHEP05\(2016\)136](#).

- [26] J. R. Andersen, H. Hassan, A. Maier, J. Paltrinieri, A. Papaefstathiou, J. M. Smillie, High Energy Resummed Predictions for the Production of a Higgs Boson with at least One Jet [arXiv:2210.10671](#).
- [27] A. M. Sirunyan, et al., Measurements of production cross sections of WZ and same-sign WW boson pairs in association with two jets in proton-proton collisions at $\sqrt{s} = 13$ TeV, *Phys. Lett. B* 809 (2020) 135710. [arXiv:2005.01173](#), doi:10.1016/j.physletb.2020.135710.
- [28] C. N. Yang, R. L. Mills, Conservation of isotopic spin and isotopic gauge invariance, *Phys. Rev.* 96 (1954) 191–195. doi:10.1103/PhysRev.96.191. URL <https://link.aps.org/doi/10.1103/PhysRev.96.191>
- [29] L. Faddeev, V. Popov, Feynman diagrams for the yang-mills field, *Physics Letters B* 25 (1) (1967) 29–30. doi:[https://doi.org/10.1016/0370-2693\(67\)90067-6](https://doi.org/10.1016/0370-2693(67)90067-6). URL <https://www.sciencedirect.com/science/article/pii/0370269367900676>
- [30] M. Peskin, D. Schroeder, An introduction to quantum field theory, CRC press, 2018.
- [31] J. Campbell, J. Huston, F. Krauss, The black book of quantum chromodynamics: a primer for the LHC era, Oxford University Press, 2018.
- [32] S. L. Glashow, The renormalizability of vector meson interactions, *Nuclear Physics* 10 (1959) 107–117. doi:[https://doi.org/10.1016/0029-5582\(59\)90196-8](https://doi.org/10.1016/0029-5582(59)90196-8). URL <https://www.sciencedirect.com/science/article/pii/0029558259901968>
- [33] A. Salam, J. C. Ward, Weak and electromagnetic interactions, *Il Nuovo Cimento* (1955-1965) 11 (1959) 568–577.
- [34] S. Weinberg, A model of leptons, *Phys. Rev. Lett.* 19 (1967) 1264–1266. doi:10.1103/PhysRevLett.19.1264. URL <https://link.aps.org/doi/10.1103/PhysRevLett.19.1264>
- [35] F. Englert, R. Brout, Broken symmetry and the mass of gauge vector mesons, *Physical review letters* 13 (9) (1964) 321.
- [36] P. W. Higgs, Broken symmetries and the masses of gauge bosons, *Physical review letters* 13 (16) (1964) 508.
- [37] M. Kobayashi, T. Maskawa, CP-Violation in the Renormalizable Theory of Weak Interaction, *Progress of Theoretical Physics* 49 (2) (1973) 652–657. [arXiv:https://academic.oup.com/ptp/article-pdf/49/2/652/5257692/49-2-652.pdf](#), doi:10.1143/PTP.49.652. URL <https://doi.org/10.1143/PTP.49.652>

- [38] G. Altarelli, G. Parisi, Asymptotic freedom in parton language, Nuclear Physics B 126 (2) (1977) 298–318. doi:[https://doi.org/10.1016/0550-3213\(77\)90384-4](https://doi.org/10.1016/0550-3213(77)90384-4).
URL <https://www.sciencedirect.com/science/article/pii/0550321377903844>
- [39] Y. L. Dokshitzer, Calculation of the Structure Functions for Deep Inelastic Scattering and $e^+ e^-$ Annihilation by Perturbation Theory in Quantum Chromodynamics., Sov. Phys. JETP 46 (1977) 641–653.
- [40] V. N. Gribov, L. N. Lipatov, Deep inelastic $e p$ scattering in perturbation theory, Sov. J. Nucl. Phys. 15 (1972) 438–450.
- [41] A. Buckley, J. Ferrando, S. Lloyd, K. Nordström, B. Page, M. Rfenacht, M. Schnherr, G. Watt, LHAPDF6: parton density access in the LHC precision era, The European Physical Journal C 75 (3). doi:[10.1140/epjc/s10052-015-3318-8](https://doi.org/10.1140/epjc/s10052-015-3318-8).
URL <https://doi.org/10.1140/2Fepjc%2Fs10052-015-3318-8>
- [42] G. P. Salam, Towards jetography, The European Physical Journal C 67 (3-4) (2010) 637–686. doi:[10.1140/epjc/s10052-010-1314-6](https://doi.org/10.1140/epjc/s10052-010-1314-6).
URL <https://doi.org/10.1140/2Fepjc%2Fs10052-010-1314-6>
- [43] M. Cacciari, G. P. Salam, G. Soyez, FastJet user manual, The European Physical Journal C 72 (3). doi:[10.1140/epjc/s10052-012-1896-2](https://doi.org/10.1140/epjc/s10052-012-1896-2).
URL <https://doi.org/10.1140/2Fepjc%2Fs10052-012-1896-2>
- [44] T. D. Lee, M. Nauenberg, Degenerate systems and mass singularities, Phys. Rev. 133 (1964) B1549–B1562. doi:[10.1103/PhysRev.133.B1549](https://doi.org/10.1103/PhysRev.133.B1549).
URL <https://link.aps.org/doi/10.1103/PhysRev.133.B1549>
- [45] T. Kinoshita, Mass singularities of feynman amplitudes, Journal of Mathematical Physics 3 (4) (1962) 650–677.
- [46] S. Catani, M. Seymour, A general algorithm for calculating jet cross sections in nlo qcd, Nuclear Physics B 485 (1-2) (1997) 291419. doi:[10.1016/S0550-3213\(96\)00589-5](https://doi.org/10.1016/S0550-3213(96)00589-5).
URL [http://dx.doi.org/10.1016/S0550-3213\(96\)00589-5](http://dx.doi.org/10.1016/S0550-3213(96)00589-5)
- [47] S. Frixione, B. R. Webber, Matching nlo qcd computations and parton shower simulations, Journal of High Energy Physics 2002 (06) (2002) 029029. doi:[10.1088/1126-6708/2002/06/029](https://doi.org/10.1088/1126-6708/2002/06/029).
URL <http://dx.doi.org/10.1088/1126-6708/2002/06/029>
- [48] T. Gehrmann, S. Höche, F. Krauss, M. Schönherr, F. Siegert, Nlo qcd matrix elements+ parton showers in $e^+ e^-$ hadrons, Journal of High Energy Physics 2013 (1) (2013) 1–22.
- [49] S. Höche, F. Krauss, M. Schönherr, F. Siegert, Qcd matrix elements+ parton showers. the nlo case, Journal of High Energy Physics 2013 (4) (2013) 1–22.

- [50] T. Regge, Introduction to complex orbital momenta, *Il Nuovo Cimento* (1955-1965) 14 (1959) 951–976.
- [51] V. Del Duca, An introduction to the perturbative qcd pomeron and to jet physics at large rapidities, arXiv preprint hep-ph/9503226.
- [52] V. Barone, E. Predazzi, *Regge Theory*, Springer Berlin Heidelberg, Berlin, Heidelberg, 2002, pp. 83–121. doi:10.1007/978-3-662-04724-8_5.
URL https://doi.org/10.1007/978-3-662-04724-8_5
- [53] J. R. Andersen, J. M. Smillie, Factorization of the t-channel pole in quark-gluon scattering, *Physical Review D* 81 (11) (2010) 114021.
- [54] L. N. Lipatov, Reggeization of the Vector Meson and the Vacuum Singularity in Nonabelian Gauge Theories, *Sov. J. Nucl. Phys.* 23 (1976) 338–345.
- [55] E. A. Kuraev, L. N. Lipatov, V. S. Fadin, Multi - Reggeon Processes in the Yang-Mills Theory, *Sov. Phys. JETP* 44 (1976) 443–450.
- [56] E. A. Kuraev, L. Lipatov, V. S. Fadin, Pomeron singularity in nonabelian gauge theories, *Sov. Phys.-JETP (Engl. Transl.);(United States)* 45 (2).
- [57] Y. Y. Balitsky, L. Lipatov, The pomeron singularity in quantum chromodynamics, *Yad. Fiz.* 28 (1978) 1597–1611.
- [58] J. R. Andersen, A. S. Vera, Solving the BFKL equation in the next-to-leading approximation, *Physics Letters B* 567 (1-2) (2003) 116–124. doi:10.1016/s0370-2693(03)00871-2.
URL <https://doi.org/10.1016%2Fs0370-2693%2803%2900871-2>
- [59] C. R. Schmidt, Review of bflk (2001). arXiv:hep-ph/0106181.
- [60] V. S. Fadin, Bflk news (1998). arXiv:hep-ph/9807528.
- [61] V. Fadin, R. Fiore, M. Kozlov, A. Reznichenko, Proof of the multi-regge form of qcd amplitudes with gluon exchanges in the nla, *Physics Letters B* 639 (2) (2006) 74–81.
- [62] A. Bogdan, V. Fadin, A proof of the reggeized form of amplitudes with quark exchanges, *Nuclear Physics B* 740 (1-2) (2006) 36–57.
- [63] V. S. Fadin, M. G. Kozlov, A. Reznichenko, Radiative corrections to qcd amplitudes in quasi-multi-regge kinematics, *Physics of Atomic Nuclei* 67 (2004) 359–375.
- [64] V. Fadin, The gluon reggeization in perturbative qcd at nlo, arXiv preprint hep-ph/0511121.
- [65] E. Bothmann, et al., Event Generation with Sherpa 2.2, *SciPost Phys.* 7 (3) (2019) 034. arXiv:1905.09127, doi:10.21468/SciPostPhys.7.3.034.

- [66] J. Alwall, R. Frederix, S. Frixione, V. Hirschi, F. Maltoni, O. Mattelaer, H. S. Shao, T. Stelzer, P. Torrielli, M. Zaro, The automated computation of tree-level and next-to-leading order differential cross sections, and their matching to parton shower simulations, JHEP 07 (2014) 079. [arXiv:1405.0301](#), doi: 10.1007/JHEP07(2014)079.
- [67] J. A. M. Vermaseren, New features of FORM [arXiv:math-ph/0010025](#).
- [68] J. R. Andersen, T. Hapola, A. Maier, J. M. Smillie, Higgs Boson Plus Dijets: Higher Order Corrections, JHEP 09 (2017) 065. [arXiv:1706.01002](#), doi: 10.1007/JHEP09(2017)065.
- [69] J. R. Andersen, J. D. Cockburn, M. Heil, A. Maier, J. M. Smillie, Finite Quark-Mass Effects in Higgs Boson Production with Dijets at Large Energies, JHEP 04 (2019) 127. [arXiv:1812.08072](#), doi:10.1007/JHEP04(2019)127.
- [70] J. R. Andersen, J. A. Black, H. M. Brooks, E. P. Byrne, A. Maier, J. M. Smillie, Combined subleading high-energy logarithms and NLO accuracy for W production in association with multiple jets, JHEP 04 (2021) 105. [arXiv:2012.10310](#), doi:10.1007/JHEP04(2021)105.
- [71] A. M. Sirunyan, et al., Measurements of production cross sections of WZ and same-sign WW boson pairs in association with two jets in proton-proton collisions at $\sqrt{s} = 13$ TeV, Phys. Lett. B 809 (2020) 135710. [arXiv:2005.01173](#), doi:10.1016/j.physletb.2020.135710.
- [72] B. W. Lee, C. Quigg, H. B. Thacker, Weak Interactions at Very High-Energies: The Role of the Higgs Boson Mass, Phys. Rev. D 16 (1977) 1519. doi:10.1103/PhysRevD.16.1519.
- [73] B. W. Lee, C. Quigg, H. B. Thacker, The Strength of Weak Interactions at Very High-Energies and the Higgs Boson Mass, Phys. Rev. Lett. 38 (1977) 883–885. doi:10.1103/PhysRevLett.38.883.
- [74] H. E. Logan, Lectures on perturbative unitarity and decoupling in higgs physics (2022). [arXiv:2207.01064](#).
- [75] A. Collaboration, Observation of electroweak production of a same-sign w boson pair in association with two jets in pp collisions at $\sqrt{s} = 13$ TeV with the atlas detector, Phys. Rev. Lett. 123 (2019) 161801. doi:10.1103/PhysRevLett.123.161801.
URL <https://link.aps.org/doi/10.1103/PhysRevLett.123.161801>
- [76] C. collaboration, et al., Observation of electroweak production of same-sign w boson pairs in the two jet and two same-sign lepton final state in proton-proton collisions at $\sqrt{s} = 13$ tev, [arXiv preprint arXiv:1709.05822](#).
- [77] C. collaboration, Measurements of production cross sections of WZ and same-sign WW boson pairs in association with two jets in proton-proton

- collisions at $\sqrt{s} = 13$ tev, Physics Letters B 809 (2020) 135710. doi:10.1016/j.physletb.2020.135710.
URL <https://doi.org/10.1016%2Fj.physletb.2020.135710>
- [78] A. collaboration, et al., Atlas conference note, ATLAS-CONF-2023-023, 2023.
 - [79] J. R. Andersen, T. Hapola, M. Heil, A. Maier, J. M. Smillie, Higgs-boson plus Dijets: Higher-Order Matching for High-Energy Predictions, JHEP 08 (2018) 090. arXiv:1805.04446, doi:10.1007/JHEP08(2018)090.
 - [80] T. Gleisberg, S. Hche, Comix, a new matrix element generator, Journal of High Energy Physics 2008 (12) (2008) 039039. doi:10.1088/1126-6708/2008/12/039.
URL <http://dx.doi.org/10.1088/1126-6708/2008/12/039>
 - [81] F. Buccioni, S. Pozzorini, M. Zoller, On-the-fly reduction of open loops, Eur. Phys. J. C 78 (1) (2018) 70. arXiv:1710.11452, doi:10.1140/epjc/s10052-018-5562-1.
 - [82] S. Frixione, B. R. Webber, Matching NLO QCD computations and parton shower simulations, JHEP 06 (2002) 029. arXiv:hep-ph/0204244, doi:10.1088/1126-6708/2002/06/029.
 - [83] S. Schumann, F. Krauss, A Parton shower algorithm based on Catani-Seymour dipole factorisation, JHEP 03 (2008) 038. arXiv:0709.1027, doi:10.1088/1126-6708/2008/03/038.
 - [84] R. D. Ball, et al., Parton distributions for the LHC Run II, JHEP 04 (2015) 040. arXiv:1410.8849, doi:10.1007/JHEP04(2015)040.
 - [85] A. Buckley, J. Ferrando, S. Lloyd, K. Nordström, B. Page, M. Rüfenacht, M. Schönherr, G. Watt, LHAPDF6: parton density access in the LHC precision era, Eur. Phys. J. C 75 (2015) 132. arXiv:1412.7420, doi:10.1140/epjc/s10052-015-3318-8.
 - [86] D. L. Rainwater, R. Szalapski, D. Zeppenfeld, Probing color singlet exchange in $Z + \text{two jet}$ events at the CERN LHC, Phys. Rev. D 54 (1996) 6680–6689. arXiv:hep-ph/9605444, doi:10.1103/PhysRevD.54.6680.
 - [87] A. Buckley, J. Butterworth, D. Grellscheid, H. Hoeth, L. Lnnblad, J. Monk, H. Schulz, F. Siegert, Rivet user manual, Computer Physics Communications 184 (12) (2013) 28032819. doi:10.1016/j.cpc.2013.05.021.
URL <http://dx.doi.org/10.1016/j.cpc.2013.05.021>
 - [88] E. Bothmann, et al., Event Generation with Sherpa 2.2, SciPost Phys. 7 (3) (2019) 034. arXiv:1905.09127, doi:10.21468/SciPostPhys.7.3.034.
 - [89] F. Buccioni, J.-N. Lang, J. M. Lindert, P. Maierhofer, S. Pozzorini, H. Zhang, M. F. Zoller, OpenLoops 2, The European Physical Journal C 79 (10). doi:

10.1140/epjc/s10052-019-7306-2.

URL <https://doi.org/10.1140/2Fepjc%2Fs10052-019-7306-2>

- [90] M. Cacciari, G. P. Salam, G. Soyez, The anti- k_t jet clustering algorithm, JHEP 04 (2008) 063. [arXiv:0802.1189](#), [doi:10.1088/1126-6708/2008/04/063](#).
- [91] R. D. Ball, V. Bertone, S. Carrazza, L. D. Debbio, S. Forte, P. Groth-Merrild, A. Guffanti, N. P. Hartland, Z. Kassabov, J. I. Latorre, E. R. Nocera, J. Rojo, L. Rottoli, E. Slade, M. Ubiali, Parton distributions from high-precision collider data, The European Physical Journal C 77 (10). [doi:10.1140/epjc/s10052-017-5199-5](#).
URL <https://doi.org/10.1140/2Fepjc%2Fs10052-017-5199-5>
- [92] A. Buckley, J. Butterworth, D. Grellscheid, H. Hoeth, L. Lnnblad, J. Monk, H. Schulz, F. Siegert, Rivet user manual, Computer Physics Communications 184 (12) (2013) 2803–2819. [doi:10.1016/j.cpc.2013.05.021](#).
URL <https://doi.org/10.1016/2Fj.cpc.2013.05.021>
- [93] J. M. Lindert, S. Pozzorini, R. Boughezal, J. M. Campbell, A. Denner, S. Dittmaier, A. G.-D. Ridder, T. Gehrmann, N. Glover, A. Huss, S. Kallweit, P. Maierhofer, M. L. Mangano, T. A. Morgan, A. Mck, F. Petriello, G. P. Salam, M. Schnherr, C. Williams, Precise predictions for $v + \text{jets}$ dark matter backgrounds, The European Physical Journal C 77 (12). [doi:10.1140/epjc/s10052-017-5389-1](#).
URL <https://doi.org/10.1140/2Fepjc%2Fs10052-017-5389-1>
- [94] L. Pontecorvo, The ATLAS Muon Spectrometer Revised version number 1 submitted on 2003-07-27 16:31:16. [doi:10.1140/epjcd/s2004-04-013-y](#).
URL <https://cds.cern.ch/record/676896>
- [95] J. R. Andersen, H. Hassan, S. Jaskiewicz, All Order Merging of High Energy and Soft Collinear Resummation, in: 51st International Symposium on Multiparticle Dynamics, 2022. [arXiv:2210.06898](#).
- [96] T. Group, et al., Deliberation document on the 2020 update of the european strategy for particle physics, Tech. rep., Tech. Rep. CERN-ESU-014, Geneva (2020).
- [97] A. Abada, M. Abbrescia, S. S. AbdusSalam, I. Abdyukhanov, J. Abelleira Fernandez, A. Abramov, M. Aburaia, A. Acar, P. Adzic, P. Agrawal, et al., Fcc-hh: The hadron collider, The European Physical Journal Special Topics 228 (4) (2019) 755–1107.
- [98] A. Abada, M. Abbrescia, S. S. AbdusSalam, I. Abdyukhanov, J. A. Fernandez, A. Abramov, M. Aburaia, A. Acar, P. Adzic, P. Agrawal, et al., Fcc physics opportunities, The European Physical Journal C 79 (6) (2019) 1–161.

- [99] CERN, Cern yellow reports: Monographs, vol 3 (2017): Physics at the fcc-hh, a 100 tev pp collider (2017). doi:10.23731/CYRM-2017-003.
URL <https://e-publishing.cern.ch/index.php/CYRM/issue/view/35>